DISTRIBUTED FEEDBACK LASER DIODES

Principles and Physical Modelling

H. GHAFOURI-SHIRAZ
B. S. K. LO

WILEY

DISTRIBUTED FEEDBACK LASER DIODES

Principles and Physical Modelling

H. Ghafouri-Shiraz
B.S.K. Lo

University of Birmingham, UK

JOHN WILEY & SONS
Chichester • New York • Brisbane • Toronto • Singapore

CONTENTS

GLOSSARY OF ABBREVIATIONS

1PS	single phase shift
3PS	three phase shift
ASK	amplitude-shift keying
AlGaAs	aluminium gallium arsenide
BER	bit error rate
BC	buried crescent
BH	buried heterostructure
CP	corrugation position
CPM	continuous-pitch-modulated
CSP	channelled substrate planar
CW	continuous wave
DBR	distributed Bragg reflector
DCC	distributed coupling coefficient
DD	direct detection
DFB	distributed feedback
DPSK	differential phase shift keying
EDFA	erbium-doped fibre amplifier
EIM	effective index method
FDM	frequency division multiplexing
FP	Fabry–Perot
FSK	frequency-shift keying
GaAs	gallium arsenide
GP	geometric progression
HE/CP	heterodyne receiver with coherent post-detection
HE/IP	heterodyne receiver with incoherent post-detection
IF	intermediate frequency
IM	intensity modulation
InGaAsP	indium gallium arsenide phosphide

InP	indium phosphide
ISDN	integrated service digital network
ISI	inter-symbolic interference
LD	laser diode
MOCVD	metal–organic chemical vapour deposition
MPS	multiple-phase shift
MQW	multiple quantum well
NRZ	non-return to zero
OEIC	optoelectronic integrated circuit
PS	phase-shifted
PSK	phase-shift keying
PSP	phase-shift position
QW	quantum well
QWS	quarterly wavelength shifted
RG	rectangular grating
RW	ridge waveguide
RZ	return to zero
SCH	separate confinement heterostructure
SHB	spatial hole burning
SLA	semiconductor amplifiers
SLM	single longitudinal mode
SMF	single mode fibre
SMSR	side mode suppression ratio
TG	triangular grating
TLM	transmission line matrix
TE	transverse electric field
TM	transverse magnetic field
TMM	transfer matrix method
WDM	wavelength division multiplex
WG	waveguide

GLOSSARY OF SYMBOLS

A_0	differential gain
A_1	parameters governing the base width of the gain spectrum or the gain curvature
A_2	wavelength shifting coefficient or differential peak wavelength
B	radiative bimolecular recombination
A_{21}	Einstein coefficient of spontaneous emission
B_{21}	Einstein coefficient of stimulated emission
c	free space velocity
c.c.	complex conjugate
C	Auger recombination coefficient
C_N	weighted function
C_S	weighted function
d	active layer thickness
dn/dN	differential index
D, D_{FF^*}	diffusion coefficient
e or exp	exponential
$\boldsymbol{E}$	electric field vector
E, E^{-1}	self-explanatory parameters
E_a	occupied conduction band at energy E_a
E_b	occupied valence band at energy E_b
E_f	equilibrium Fermi level
E_c, E_v	conduction and valence band edge, respectively
E_{Fc}, E_{Fv}	quasi-Fermi levels in the conduction band and valence band, respectively
E_g	energy gap
$E_R(z)$	complex forward propagating wave at z
$E_S(z)$	complex backward propagating wave at z
E_i	intrinsic Fermi level
E_1	occupied valence band at energy E_1
E_2	occupied conduction band at energy E_2

$E_\omega(z)$	complex Fourier component of the electric field
f	optical frequency
$f(E)$	Fermi–Dirac distribution function
F	flatness
$F_\omega(z)$	Langevin noise term
f_{ij}	matrix elements (for $i, j = 1, 2$) of the matrix $\mathbf{F}$
$\mathbf{F}$	forward transfer matrix
$\mathbf{F}^{(k)}$	($k = 1$ to N) forward transfer matrix $= \mathbf{T}^{(m)}\mathbf{P}^{(m)}$
g	material gain
$g(E_{21})$	gain parameter
g_{peak}	peak material gain
g_{th}	threshold gain
g_{ij}	matrix elements (for $i, j = 1, 2$) of the matrix $\mathbf{G}$
$\mathbf{G}$	backward transfer matrix
$G^{(k)}$	($k = 1$ to N) backward transfer matrix
G	amplifying term
$G(z, z')$	Green's function
h	Planck's constant (6.63×10^{-34} J s)
$hf = hc/\lambda$	photon energy
$\mathbf{I}$	identity matrix
$\boldsymbol{I}$	injection current
I_{avg}	average field intensity
I_{th}	threshold current
$I(z)$	local field intensity
j	$\sqrt{-1}$
J_{th}	nominal threshold current density
$H_\omega(z)$	complex Fourier component of the magnetic field
k	propagation constant
k'	complex propagation constant
k_0	free space propagation constant
$\mathbf{k}$	Boltzmann's constant (1.38×10^{-23} J/K)
k_{un}	complex propagation constant for unperturbed structure
$K_{(1)}$	self-explained parameter
$K_{(2)}$	self-explained parameter
$K_{(3)}$	self-explained parameter
K_{tn}	local frequency tuning efficiency
L	overall laser cavity length
m	order of Bragg diffraction
m_0	mass of electron
m_n	effective mass of electron
m_p	effective mass of hole
$\mathbf{M_b}$	average matrix element of the Bloch states
$\mathbf{M_{env}}$	slowing varying envelope function
$\mathbf{M_{21}}$	momentum matrix of the carrier transition
$n = \sqrt{(\varepsilon/\varepsilon_0)}$	refractive index

n_0	steady-state refractive index at threshold
n_1	active layer refractive index
n_2	cladding layer refractive index
n_{act}	active layer refractive index
n_{clad}	cladding layer refractive index
n_g	group refractive index
n_{ini}	refractive index at zero current injection
n_{sp}	population inversion factor
N	carrier concentration (or electron density)
N_0	carrier concentration at transparency
N_1	carrier concentration at energy E_1 inside the valence band
N_2	carrier concentration at energy E_2 inside the conduction band
N_{th}	carrier concentration or density at threshold
P	optical power
$\boldsymbol{P}^{(m)}$	phase shift matrix
P_{num}	total number of photons found inside the laser cavity
P_{mut}	mutual interaction between the coupled waves $R(z)$ and $S(z)$
P_N	amplified spontaneous emission power
q	electronic charge
r	coupling ratio κ_1/κ_2
r_1, r_2	complex reflection coefficients at the left and right facets, respectively
$\hat{r}_1, \hat{r}_2$	amplitude reflection coefficients at the left and right facets, respectively
$r_{spon}(E_{21})$	spontaneous emission rate
$r_{stim}(E_{21})$	stimulated emission rate
R	rate of non-coherent carrier recombination
$R(N)$	carrier recombination rate excluding stimulated emission
$R(z)$	complex amplitude term
R'	first-order derivative of $R(z)$
R''	second-order derivative of $R(z)$
R_1, R_2	complex coefficients
R_{sp}	rate of spontaneous emission
R_{st}	rate of stimulated emission
$R_{a\to b}$	overall downward transition between two energy bands
$R_{b\to a}$	overall upward transition between two energy bands
$R_{a\to b}(\text{net})$	net downward transition between two energy bands
S	photon density
S'	first-order derivative of $S(z)$
S''	second-order derivative of $S(z)$
$S(z)$	complex amplitude term

S_1, S_2	complex coefficients
$\hat{t_1}, \hat{t_2}$	amplitude transmission coefficients at laser facets
t_{ij}	matrix elements (for $i, j = 1, 2$) of the matrix $\mathbf{T}$
$\mathbf{T}$	forward transfer matrix
$\mathbf{T}^{(k)}$	($k = 1$ to N) forward transfer matrix
T	temperature in degrees Kelvin
u_{ij}	matrix elements (for $i, j = 1, 2$) of the matrix $\mathbf{U}$
$\mathbf{U}$	backward transfer matrix
$\mathbf{U}^{(k)}$	($k = 1$ to N) backward transfer matrix
V	volume of the active volume
v_g	group velocity
w	active layer width
W	Wronskian term
$\boldsymbol{W}$	distance spans by the rising and the dropping edges of the corrugation
W_B	distance spans by the bottom width of the corrugation
W_T	distance spans by the top width of the corrugation
x	transverse direction
y	lateral direction
y_{ij}	matrix elements (for $i, j = 1, 2$) of the matrix $\mathbf{Y}$
$\mathbf{Y}$	overall transfer matrix chain using the forward propagation matrix
z	longitudinal direction
$Z_1(x), Z_2(x)$	corrugation functions
$Z_1(z), Z_2(z)$	solutions of the homogeneous wave equation satisfying the boundary conditions at the left and right facets, respectively
z_{ij}	matrix elements (for $i, j = 1, 2$) of the matrix $\mathbf{Z}$
$\mathbf{Z}$	overall transfer matrix chain using backward propagation matrix
α	amplitude gain coefficient
α_0	steady-state amplitude gain
α_a	absorption loss in the active layer
α_c	absorption loss in the cladding layer
α_{eff}	effective linewidth enhancement factor
α_H	intrinsic linewidth enhancement factor
α_{loss}	internal cavity loss
α_{sca}	scattering loss at heterostructure interface
$\overline{\alpha}$	average amplitude gain
$\overline{\alpha}_L$	average amplitude gain for the lasing mode
$\overline{\alpha}_{SM}$	average amplitude gain for the most probable side mode
β	propagation constant
β_0	the Bragg propagation constant
γ	complex propagation constant

Γ	optical confinement factor
δ	detuning coefficient
$\overline{\delta}_{ij}$	Kronecker delta function
$\overline{\delta}$	average detuning coefficient gain
$\overline{\delta}_L$	average detuning coefficient for the lasing mode
δ_{SM}	average detuning coefficient for the most probable side mode
Δ	spin–orbit splitting
$\Delta\alpha$	gain margin
$\Delta\varepsilon$	perturbed relative permittivity induced by the corrugation
ε	non-linear gain coefficient
ε_{ini}	average relative permittivity
ε'	complex permittivity
ε_0	permittivity of free space (8.854×10^{-12} F/m)
η_i	internal quantum efficiency
θ	relative phase difference between perturbation of the refractive index and the amplitude gain
θ_ε	effective phase shift
θ_k	complex electric field phase shift between section k and $(k-1)$
κ	coupling coefficient
κ_{avg}	average coupling coefficient used in a DCC laser structure
κ_i	index coupling coefficient
κ_g	gain coupling coefficient
κ_{RS}	forward coupling coefficient
κ_{SR}	backward coupling coefficient
λ	lasing wavelength
λ_B	the Bragg wavelength
λ_c	complex wavelength $\lambda_c = \lambda + \lambda_i$
λ_i	imaginary wavelength
λ_{th}	lasing wavelength at threshold
λ_0	peak wavelength at zero gain transparency
Λ	corrugation period
$\Delta\upsilon$	spectral linewidth
$\Delta\upsilon_{sp}$	spectral linewidth due to spontaneous emission
$\Delta\upsilon_{NN}$	spectral linewidth due to local fluctuation of the carrier density
$\Delta\upsilon_{NS}$	spectral linewidth due to the correlation between the local carrier and photon changes
π	mathematical constant
ρ	self-explained parameter, $\rho = jk/(\alpha - j\delta + \gamma)$
τ	linear recombination lifetime

τ_N	carrier recombination lifetime
Ψ	position factor
Ψ_1, Ψ_2	complex corrugation phase terms associated with r_1 and r_2
ω	angular frequency
Ω	corrugation phase at z origin

1

INTRODUCTION

Communication is a process in which messages, ideas and information are exchanged between two individuals. From the early days when languages were developed, the methods people use to communicate have experienced a dramatic evolution. Nowadays, the rapid transmission of information over long distances and instant access to various information sources have become conspicuous and important features of our society.

The rapidly growing information era has been augmented by a global network of optical fibres [1]. By offering an enormous transmission bandwidth of about 10^{14} Hz and a low signal attenuation, the low-cost, glass-based, single-mode optical fibre (SMF) provides an ideal transmission medium. In order that information can be carried along the SMF, information at the transmitter side is first converted into a stream of coherent photons. Using a specially designed semiconductor junction diode with heavy doping concentration, semiconductor lasers have been used to provide a reliable optical source required in fibre-based lightwave communication. With its miniature size — compatible with the SMF — the semiconductor laser diode has played a crucial role in the success of optical fibre communication systems.

This chapter is organised as follows: In section 1.1, the historical progress of optical communication is presented. Before exploring the characteristics of semiconductor lasers, various configurations of optical-fibre-based communication systems are discussed in section 1.2. Depending on the type of detection method used, both direct and coherent detection schemes are discussed. On the basis of the characteristics of the coherent optical communication systems, the performance requirements of semiconductor lasers are presented at the end of the chapter. In particular, the significance of having an optical source that oscillates at a single frequency while having a narrow spectral linewidth is reviewed.

1.1 HISTORICAL PROGRESS

In the early days of human civilisation, simple optical communication in terms of signal fires and smoke was used. In those days, only limited information

could be transferred within line of sight distances. And of course, the transmission quality was strongly restricted by atmospheric disturbances. This form of visual communication was extended and used in the form of flags and signal lamps until the early 1790s, when a French scientist, Claude Chappe [2], suggested a system of semaphore stations. Messages were first translated into a sequence of visual telegraphs. The message was then transmitted between tall towers each perhaps 32 km apart. These towers acted as regenerators or repeaters so that messages could be transmitted over a longer distance. However, this method was slow and costly since messages had to be verified between each tower.

With the beginning of the modern understanding of electricity in the nineteenth century, scientists started to investigate how electricity might be used in long distance communication. The invention of the telegraph [3] and the telephone [4] in the nineteenth century were the two products that best represent this early stage of the electrical communication era. During that period of time, optical communication in the atmosphere received less attention and any systems that were developed were slow and inefficient. The lack of suitable optical sources and transmission mediums were two factors that hindered the development of optical communication. It was not until the early 1960s that the invention of the laser [5] once again stimulated interest in optical communication. A laser source provides a highly directional light source in which photons generated are in phase with one another. By modulating the laser, the coherent, low divergence laser beam elevates the development of optical communication. Owing to atmospheric attenuation, however, laser use is restricted to short distance applications.

Long distance communication employing a laser source became feasible after a breakthrough was reached in 1966, when Kao and Hockham [6] and Werf [7] discovered the use of a glass-based optical waveguide. By trapping light along the central core of the cylindrical waveguide, light confined along the optical fibre could travel a longer distance as compared with atmospheric propagation. Despite the fact that the attenuation of the optical fibre used was so high and with virtually no practical application at that time, this new way to carry an optical signal then received world-wide attention. With improved manufacturing techniques and intensive research, the attenuation of optical fibres continued to drop. A fibre loss of about 4.2 dB/km was reported [8] for wavelengths around 1 μm, while at the same time a low-loss fibre jointing technique became available.

To build an optical communication system based on optical fibres, research in the 1960s started focusing on the development of other optical components, including optical sources and detectors [9–11]. A new family of optical devices based on semiconductor junction diodes were developed. By converting an electrical current directly into a stream of coherent photons, semiconductor lasers are considered to be a reliable optical laser source. On the basis of similar working principles, efficient photo-detectors based on the junction diode were developed. By responding to optical power, rather than

optical electromagnetic fields, optical signals received are converted back into electrical signals. In this early phase of development, the semiconductor lasers used were restricted to pulse operation at very low temperatures. It was not until the 1970s when practical devices, operating in continuous wave at room temperature, became feasible [12].

The availability of both low-loss optical fibres and reliable semiconductor based optical devices laid the cornerstone for modern lightwave communication systems. In the late 1970s, lightwave systems were operated at 0.8 μm [13]. The semiconductor lasers and detectors employed in these system were fabricated using a gallium arsenide alloy (AlGaAs) [14]. The optical fibres used had a large core of diameter between 50 and 400 μm, while the typical attenuation was about 4 dB/km. At the receiver side of the system, direct detection was used in which optical signals were directly converted into baseband optical signals. The overall system performance was limited by the relatively larger attenuation and inter-model dispersion of the optical fibre used.

To reduce the cost associated with the installation and maintainence of the electrical repeaters used in lightwave communication systems, it was clear that the repeater spacing could be improved by extending the operating wavelength to a new region between 1.1 and 1.6 μm where the attenuation of the optical fibre is found to be smaller. Figure 1.1 shows the relationship between the attenuation of a typical SMF and the optical wavelength. For systems operating at longer wavelengths, semiconductor optical devices were

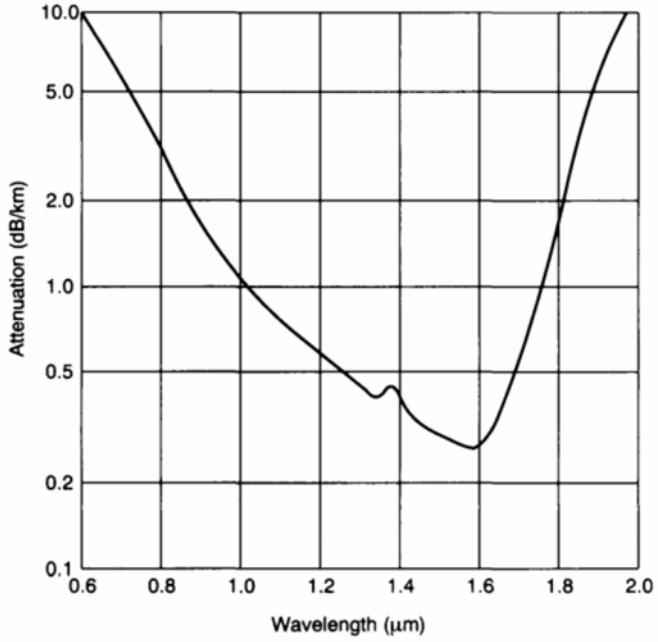

Figure 1.1 Attenuation of silica-based optical fibre with wavelength (after [44]).

fabricated using a quaternary (InGaAsP) alloy. To avoid inter-model competition associated with high order oscillation modes inside the optical fibre, optical fibres having a smaller core diameter of about 8 μm were used. In this way, the oscillation in an optical fibre was reduced to a single mode. For systems operating in such a longer wavelength region, both wavelengths at 1.3 μm and 1.55 μm have received much attention. For wavelengths operating near 1.3 μm, it was found that the SMF has a minimum dispersion, and hence a maximum bandwidth could be achieved. In the early 1980s, many systems were built using an SMF at around the 1.3 μm wavelength. An even lower fibre attenuation of about 0.2 dB/km was found at around 1.55 μm. However, the deployment of a lightwave system in the 1.55 μm region was delayed owing to the intrinsic fibre dispersion which limits the maximum bit rate which the system can support. The problem was later alleviated by adopting a dispersion shifted or dispersion flattened fibre [15,16]. Alternatively, semiconductor lasers oscillating in single longitudinal modes were developed [17,18]. By limiting the spread of the laser spectrum, this type of laser was widely used in upgrading the 1.3 μm lightwave system to the 1.55 μm wavelength in which conventional SMF were used. Since 1988, field trial tests for coherent lightwave communication systems have been carried out [19–21].

To improve the bit rate of the present lightwave system so that the available fibre bandwidth could be utilised in a better way, frequency division multiplexing (FDM) schemes [22] were implemented. Before information is converted into optical signals, electronic multiplexing is often applied to mix the signals. Such a system is normally referred to as coherent optical communication since heterodyne or homodyne detection is used at the receiver end. By mixing the incoming optical signal with an optical local oscillator, coherent detection employed a different technique compared with the direct detection method. In the 1980s, the development of coherent optical communications were hindered owing to poor spectral purity and frequency instability in semiconductor lasers. Owing to the advancement in fabrication techniques, currently, semiconductor lasers show improved performance.

In long-haul optical fibre communication systems, fibre dispersion and intrinsic attenuation are two major obstacles that affect system performance. In the 1990s, optical fibre communication systems that tackle these obstacles continue to develop. To circumvent fibre dispersion, the non-linear optical soliton, which is able to travel extremely long distances, has been proven both theoretically [23,24] and experimentally [25,26]. By using optical amplifiers [27,28] as pre-amplifiers, post-amplifiers and optical repeaters, these wide band amplifiers have been deployed in optical communication networks. In the future, networks employing a densely spaced wavelength division multiplexing (WDM) scheme [29] are expected. As a result, more channels, and hence more information, can be transmitted over a single optical fibre link. There is no doubt that a new paradigm of communication comprising an optically transparent network is already on the way [30].

1.2 OPTICAL FIBRE COMMUNICATION SYSTEMS

By transferring information in the form of light along an optical fibre, a communication system based on optical fibres starts to grow rapidly. This system, like other communication systems, consists of many different components. A simple block diagram, as shown in Figure 1.2, represents the various components required in an optical fibre communication system. At the transmitter side, information is encoded, modulated and is then converted into a stream of optical signals. At the receiver side, the optical signals received are filtered and demodulated into the original information. For long distance applications, repeaters or regenerators have to be used to compensate for the intrinsic attenuation of the optical fibre. To maximise the amount of information that can be transferred over a single optical fibre link, various multiplexing schemes might also be applied.

To ensure the successful implementation of optical fibre communication links, careful planning and system consideration is necessary. Apart from the performance characteristics of every component used within the system, it is also necessary to consider the interactions and compatibility between various components. Depending on the system requirements, the type of transmission (analogue or digital), the transmission bandwidth required, the cost and reliability, may vary from one system to another. According to the type of detection scheme method used at the receiver end, it is common to categorise an optical fibre system into either a direct detection scheme or a coherent detection scheme.

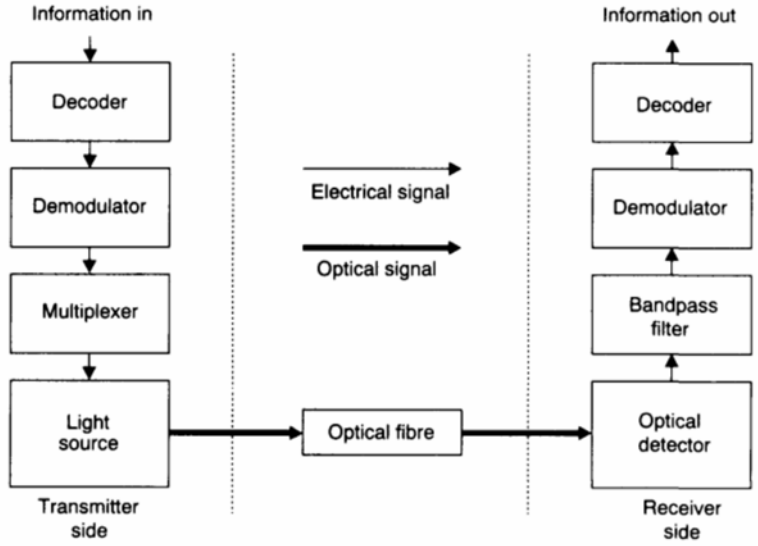

Figure 1.2 Simple block diagram showing the various components of an optical fibre communication system.

1.2.1 Intensity modulation with a direct detection scheme

By simply varying the biasing current injected into a semiconductor laser diode at the transmitter, the so-called *intensity modulation with direct detection* (IM/DD) scheme was widely adopted. The expression "intensity modulation" derives from the fact that the intensity of the light emitted at the transmitter side is linearly modulated with respect to the input signal for either the digital or the analogue system. The expression "direct detection" is used because the optical detector at the receiver end responds to optical power, rather than the electromagnetic field, as compared with radio or microwave links. In other words, all optical signals received at the optical detector are demodulated into baseband electrical signals. Owing to its simplicity and low cost, the IM/DD transmission scheme has had great success, especially in point-to-point transmission systems. To explore the potential of the optical spectrum, however, coherent detection has to be used.

1.2.2 Coherent detection scheme

Compared with the IM/DD transmission scheme, *coherent optical communication* [31-33] is characterised by mixing the incoming optical signal with the local oscillator so that the baseband signal (for homodyne detection) or an intermediate frequency (IF) signal (for heterodyne detection) is generated at the receiver. Since spatial coherence of the carriers and local oscillators are exploited, the expression "coherent" is used to describe such a system configuration. The advantages of coherent detection have long been investigated and were recognised in the 1960s [34], but it was not until in the late 1970s that single mode transmission from an AlGaAs semiconductor laser was demonstrated [35,36]. With a narrower spectral output, fibre-based lightwave systems employing coherent detection became feasible.

Various digital modulation methods have been used in coherent optical communication, including amplitude-shift keying (ASK), frequency-shift keying (FSK) and phase-shift keying (PSK) [37,38]. They differ from one another in the way that digital messages can be transmitted by variations in amplitude, frequency and phase, respectively. For any digital transmission scheme and receiver architecture, a bit error rate (BER) in the region between 10^{-9} and 10^{-10} must be achieved at the receiver side for satisfactory transmission.

A coherent optical communication system using homodyne/heterodyne detection has several advantages over the IM/DD transmission scheme [39,40]. First, coherent detection can improve the receiver sensitivity by about 15-20 dB, which depends on the modulation scheme adopted. As a result, the spacing between repeaters is improved for long distance communication, while the transmission rate can be increased in existing long distance links without reducing the repeater distance. Moreover, by using a modulation like PSK or FSK, which is well known in communication theory, the receiver can

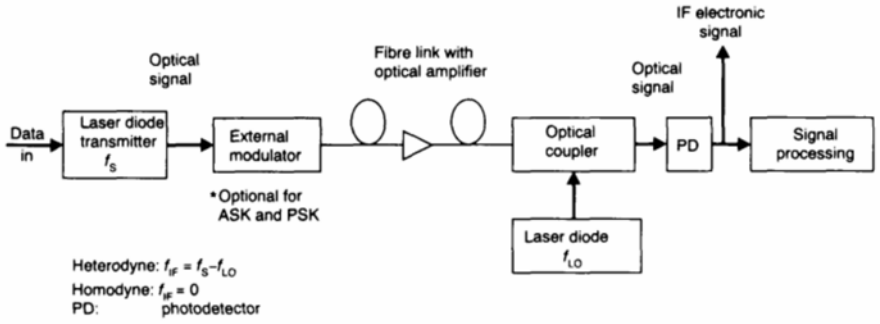

Figure 1.3 Schematic diagram of a coherent optical fibre communication system.

push to reach the ideal quantum noise detection limit. In addition, by adopting densely spaced FDM or WDM, a wider fibre bandwidth can be utilised. In practice, however, the coherent optical system has a stringent requirement in device performance. A general block diagram for the coherent optical communication system is shown in Figure 1.3.

As illustrated in Figure 1.3, two injection lasers are involved in the system. One acts as a transmitter and the other as a local oscillator. The laser transmitter, which acts as an optical frequency oscillator, can be used directly in the FSK transmission. An external modulator is optional for the ASK and the PSK transmission before the optical signals are launched into the SMF. Optical amplifiers like semiconductor amplifiers (SLA) or erbium-doped fibre amplifiers (EDFA) are used in long distance transmission to boost the signal.

Under the heterodyne receiver category with a non-zero IF, two different types of post-detection processes have been adopted. The name *heterodyne receiver with coherent post-detection processing* (HE/CP) is usually given to the one that has an IF carrier recovered at the receiver. Similarly, *heterodyne receiver with incoherent post-detection processing* (HE/IP) describes the system that has no IF carrier recovered. Comparatively, the HE/IP receiver configuration is the simplest, because IF carrier reconstruction is unnecessary. However, it shows the weakest receiver sensitivity among the three receiver designs. Incoherent post-detection processes could be used in conjunction with several modulation schemes such as ASK, FSK and differential phase shift keying (DPSK). In the HE/CP receiver design, IF signals are recovered at the receiver stage for further signal processing. Coherent post-detection processes can improve the receiver performance and so they are applicable to any modulation method. However, they are substantially more complicated than the incoherent method, and stringent device performance is required.

For zero IF, the homodyne receiver has the best receiver sensitivity because data are recovered directly from the optical mixing process at the receiver. A narrower receiver bandwidth and only baseband electronic processing are required. These offer significant advantages over the heterodyne receivers. In

practice, however, the technologies required to achieve these advantages in the homodyne receiver are demanding. An effective synchronous demodulation process is essential in phase-locking the local oscillator and the received optical signal. Phase jitters caused by phase noise and shot noise could easily impair the system performance. It has been evaluated that the phase variance [41] must be limited to within $\sim 10^{\circ}$ to ensure a lower power penalty for a BER $\leq 10^{-9}$. This sets an upper limit on the permissible laser spectral linewidth and other laser performance characteristics. In the following sections, we discuss some fundamental device characteristics and their impact on system performance.

1.3 SYSTEM REQUIREMENTS FOR HIGH-SPEED OPTICAL COHERENT COMMUNICATIONS

1.3.1 Spectral purity requirements

An ideal monochromatic laser source has been needed for some time. As a result, the spectral purity of the laser source has often been the first issue confronting semiconductor lasers used in coherent optical communications. Owing to the dispersive nature of the optical fibres used, digital pulses are broadened as they propagate along the optical fibre. Such pulse spreading causes adjacent pulses to overlap so that errors occur as a result of intersymbolic interference (ISI). Thus, apart from the power limitation due to intrinsic fibre attenuation, the transmission distance is also limited by dispersion.

The use of SMF has eliminated the severe intermodal dispersion of multimode fibres. However, because of the finite spectral width of the optical sources, SMF are limited by chromatic dispersion (or intramodal dispersion). Because the laser sources do not emit a single frequency but rather a band of frequencies, each frequency component of the field propagates with a different time delay in the SMF, causing a broadening of the initial pulse width and hence intramodel dispersion. The delay differences in SMF may be caused by the dispersive properties of the material through a variation in the cladding refractive index (material dispersion) and also the guidance effects within the structure (waveguide dispersion). To minimise the effect of dispersion in SMF and hence improve the transmission distance, there are two different approaches. The first method involves the use of a dispersion shifted or dispersion flattened fibre. With a distinctive refractive index profile, these fibres can significantly reduce the effect of dispersion at the 1.55 μm wavelength. Another possible way involves improvement of the semiconductor laser sources. The ability to lase in single mode and a narrow linewidth can circumvent the effect of dispersion. In the rest of this section, the concept of single mode operation, especially the possibility of a single longitudinal mode, will be discussed, while the impact and the control of spectral linewidth will be left for later sections.

Single mode along the transverse plane

It was shown in the previous section that a coherent optical communication system requires semiconductor lasers that can emit at a monochromatic frequency in order to achieve the required system BER. As a result, it is necessary to achieve a single mode oscillation in each of the orthogonal directions inside the laser cavity.

To understand the transverse waveguiding problem of semiconductor lasers, we start with the time-independent scalar wave equation which can be derived from the Maxwell equations [42]

$$\nabla \times \boldsymbol{E} = -j\omega\mu\boldsymbol{H} \tag{1.3.1}$$

$$\nabla \times \boldsymbol{H} = j\omega\varepsilon\boldsymbol{E} \tag{1.3.2}$$

where ε and μ are the permittivity and permeability of the medium, respectively. The above equations are expressed in time harmonic form (with the time variation term as $e^{j\omega t}$) and is true for source-free and lossless mediums. By using the vector identity and taking the curl on both sides of equation (1.3.1), we arrive at the scalar wave equation for the electric field E such that

$$\begin{aligned} \nabla^2\boldsymbol{E} &= -k^2\boldsymbol{E} = -\omega^2\mu\varepsilon\boldsymbol{E} \\ &= -k_0^2 n^2(x, y)\boldsymbol{E} \end{aligned} \tag{1.3.3}$$

where k is the propagation constant in the medium with the refractive index distribution of $n(x, y)$ and k_0 is the free space propagation constant.

Similarly, by taking the curl on both sides of equation (1.3.2), we end up with the scalar wave equation for the magnetic field H:

$$\nabla^2\boldsymbol{H} + k_0^2 n^2(x, y)\boldsymbol{H} = 0 \tag{1.3.4}$$

Either equations (1.3.3) or (1.3.4) can be used to determine the field components because they are related to one another by the Maxwell equations. Nevertheless, the scalar wave equation for the electric field is often used because electric field is responsible for most physical processes and is the principal field used by photodetectors.

To determine the transverse modal field of the semiconductor laser, we must first find the thickness and the refractive indices of the materials used in the fabrication process. Depending on the specific laser structure, it is quite possible to have three or four epitaxial layers lying on top of and below the active layer of the semiconductor laser. These laser structures may look complicated at first glance. In fact, their waveguiding properties can be explained with the use of a three-layer dielectric slab (or planar) waveguide. As shown in Figure 1.4, the asymmetric waveguide consists of three layers. The active layer, with a refractive index n_1 and thickness d, is sandwiched between the substrate and the cladding of the waveguide.

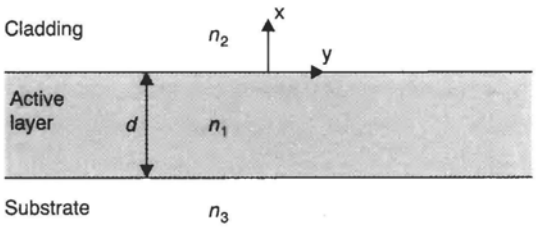

Figure 1.4 Schematic cross-section of a slab dielectric waveguide. The refractive indices for different regions are shown.

Without loss of generality, it is assumed that the refractive indices of the slab waveguide obey the following inequality:

$$n_1 > n_2 \geq n_3 \tag{1.3.5}$$

where the equal sign implies a symmetric waveguiding structure. With such a planar structure, the field variation along the y axis can be ignored and so $\partial/\partial y = 0$. By separating the Maxwell equations into different field components, the following equations are obtained [42]:

$$\frac{\partial E_y}{\partial z} = j\omega\mu H_x \tag{1.3.6a}$$

$$\frac{\partial E_x}{\partial z} - \frac{\partial E_z}{\partial x} = -j\omega\mu H_y \tag{1.3.6b}$$

$$\frac{\partial E_y}{\partial x} = -j\omega\mu H_z \tag{1.3.6c}$$

$$-\frac{\partial H_y}{\partial z} = j\omega\varepsilon E_x \tag{1.3.6d}$$

$$\frac{\partial H_x}{\partial z} - \frac{\partial H_z}{\partial x} = j\omega\varepsilon E_y \tag{1.3.6e}$$

$$\frac{\partial H_y}{\partial x} = j\omega\varepsilon E_z \tag{1.3.6f}$$

The direction of wave propagation has always been assumed to be the longitudinal z direction. By inspecting the above equations carefully, we can separate them into two groups. The first group includes E_y, H_x and H_z from equations (1.3.6a), (1.3.6c) and (1.3.6e). The results generated from these equations are referred to as the transverse electric, *TE, mode* since the electric field is found along the transverse y axis (normal to the propagation direction). The other group includes H_y, E_x and E_z, which generates solutions for the transverse magnetic, *TM, mode*. An inspection of the structure shows that either the TE or the TM mode is supported, but not both simultaneously. Since there is no physical boundary along the y direction, the continuity condition allows only H_z or E_z to exist.

For a travelling wave propagating along the z direction, the electric field takes the form

$$E(\boldsymbol{x}, \boldsymbol{y}, \boldsymbol{z}, t) = E(\boldsymbol{x}, \boldsymbol{y})\mathrm{e}^{j(wt-\beta_z z)} \tag{1.3.7}$$

where the time harmonic term is omitted here for the sake of simplicity. β_z is the propagation constant at a fixed angular frequency ω which can also be written as

$$\beta_z = k_0 n_{\text{eff}} \tag{1.3.8}$$

with n_{eff} being the effective refractive index.

By substituting equation (1.3.7) into the scalar wave equation and putting $\partial/\partial y = 0$, we end up with the following scalar wave equations for different layers found in the slab dielectric waveguide:

$$\frac{\partial^2}{\partial x^2}E_y(x) = -(k_0^2 n_1^2 - \beta_z^2)E_y(x) = -h^2 E_y(x); \quad -d \leq x \leq 0 \tag{1.3.9a}$$

$$\frac{\partial^2}{\partial x^2}E_y(x) = -(k_0^2 n_2^2 - \beta_z^2)E_y(x) = p^2 E_y(x); \quad 0 \leq x \leq \infty \tag{1.3.9b}$$

$$\frac{\partial^2}{\partial x^2}E_y(x) = -(k_0^2 n_3^2 - \beta_z^2)E_y(x) = q^2 E_y(x); \quad -\infty < x \leq -d \tag{1.3.9c}$$

where h, p and q are constants defined as

$$h^2 = k_0^2 n_1^2 - \beta_z^2; \qquad p^2 = \beta_z^2 - k_0^2 n_2^2; \qquad q^2 = \beta_z^2 - k_0^2 n_3^2 \tag{1.3.10}$$

Depending on the relative values of n_1, n_2, n_3, k_0 and β_z, there are different regimes for the propagation constant, as shown in Figure 1.5.

If p^2 and q^2 are negative while h^2 is positive (i.e. $0 < \beta_z < k_0 n_3$), then the propagation is said to be in the continuous radiation regime and the field

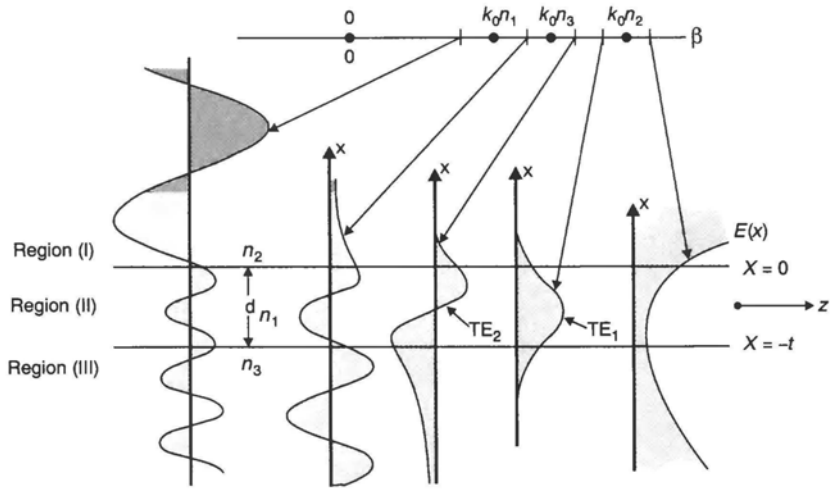

Figure 1.5 Different types of modal solutions determined by the constants p, q and h (after [44]).

solutions show sinusoidal behaviour in all three layers. For a guided mode to occur, the constants p^2, q^2 and h^2 must all be positive. In other words, the inequality $k_0 n_2 < \beta_z < k_0 n_1$ holds so that sinusoidal oscillation is restricted to the central active layer while the electric field is decaying exponentially in the other layers. For the TE mode, a general formulation of $E_y(x)$ takes the form:

$$E_y(x) = \begin{cases} Ae^{-qx}; & 0 \le x < \infty \\ A\cos(hx) + B\sin(hx); & -d \le x \le 0 \\ (A\cos(hx) + B\sin(hx))e^{p(x+d)}; & -\infty < x \le -d \end{cases} \tag{1.3.11}$$

where the constants A and B are two arbitrary constants that are related to the power of the propagating mode. Since the tangential fields must be continuous at the dielectric interface, by rearranging equation (1.3.6c) such that

$$H_z = \frac{j}{\omega\mu}\frac{\partial E_y}{\partial x} \tag{1.3.12}$$

the boundary conditions of the magnetic field H_z at $x = 0$ and $x = -d$ become

$$Aq + Bh = 0 \tag{1.3.13a}$$

$$A[h\sin(hd) - p\cos(hd)] + B[p\sin(hd) + h\cos(hd)] = 0 \tag{1.3.13b}$$

By combining the above equations and eliminating the arbitrary constants A and B, we arrive at the eigenvalue equation for the guided mode [43]:

$$\tan(hd) = \frac{(p+q)h}{h^2 - pq} \tag{1.3.14a}$$

From the above equation it is clear that the active layer thickness d is decisive in determining the guided mode. By replacing n_3 with n_2 (hence $q = p$), the slab waveguide becomes symmetric and the above eigenvalue equation becomes

$$\tan(hd) = \frac{2ph}{h^2 - p^2} = \frac{2p/h}{1 - p^2/h^2} \tag{1.3.14b}$$

By equating the last eigenvalue equation with the half angle trigonometric identity of

$$\tan(x) = \frac{2\tan(x/2)}{1 - \tan^2(x/2)} \tag{1.3.15}$$

we can solve the quadratic equation in terms of $\tan(hd/2)$ such that

$$\tan\left(\frac{hd}{2}\right) = \frac{p}{h} \tag{1.3.16a}$$

and

$$\tan\left(\frac{hd}{2}\right) = -\frac{h}{p} \tag{1.3.16b}$$

Equations (1.3.16a) and (1.3.16b) represent the even and odd TE modes of the slab dielectric waveguide. To solve the eigenvalue equation for the TE mode, an extra equation is necessary. By equating the propagating constants in equations (1.3.10), we obtain [44]

$$\left(\frac{pd}{2}\right)^2 + \left(\frac{hd}{2}\right)^2 = (n_1^2 - n_2^2)k_0^2\left(\frac{d}{2}\right)^2 = D^2 \tag{1.3.17}$$

where D is defined as the normalised waveguide thickness.

Therefore, for a guided mode the constants p and h must satisfy both equations (1.3.14b) and (1.3.17). These equations can be solved using a graphical method. Clearly, equation (1.3.17) represents a circle with radius D on the $(hd/2)$-$(pd/2)$ plane. By putting in the odd and the even TE mode eigenvalue equations in the same $(hd/2)$-$(pd/2)$ plane, we obtain the plot shown in Figure 1.6. Each intersection (or solution) with $p > 0$ and $h > 0$ between the circles and the tangential function corresponds to a guided mode, from which the propagation constant could be determined according to equation (1.3.15).

Owing to the periodicity of the trigonometric function, multiple modes may occur as the frequency and hence the radius of the circle keep increasing. From Figure 1.6 there is only one intersection point between the circle and

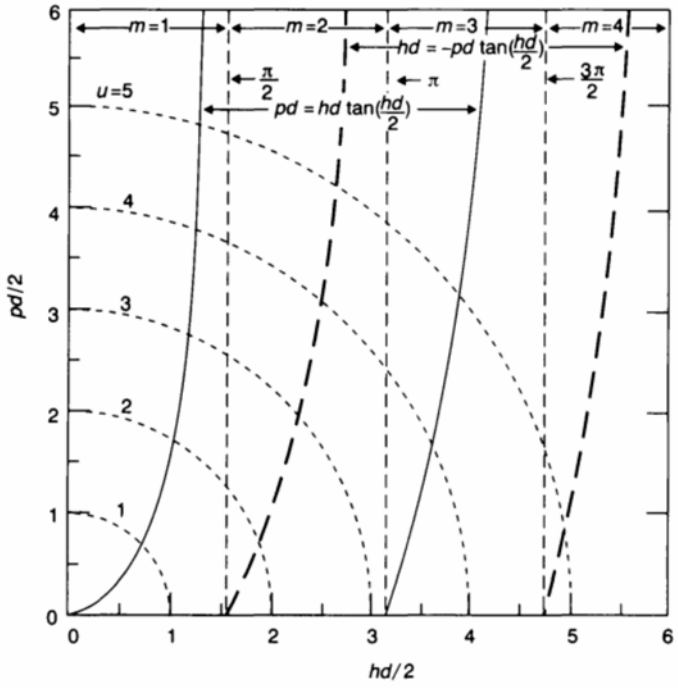

Figure 1.6 Graphical method to solve the eigenequation for a symmetrical three-layer dielectric waveguide (after [44]).

the tangential functions when the normalised waveguide thickness D has the value:

$$0 < D < \frac{\pi}{2} \tag{1.3.18}$$

This mode designated TE_1 is the fundamental mode excited in the slab dielectric waveguide. By expanding D according to equation (1.3.17), the equation shown above becomes:

$$0 < d < \frac{\lambda}{2}(n_1^2 - n_2^2)^{-1/2} \tag{1.3.19}$$

This equation limits the maximum active layer thickness for single transverse mode excitation.

Similarly, by equating the boundary conditions for the TM mode, we end up with the following eigenvalue equations for the asymmetric waveguide:

$$\tan(hd) = \frac{n_1^2 h(n_3^2 p + n_2^2 q)}{n_2^2 n_3^2 h^2 - n_1^4 pq} \tag{1.3.20}$$

and

$$\tan(hd) = \frac{2n_1^2 n_2^2 hp}{n_2^4 h^2 - n_1^4 p^2} \tag{1.3.21}$$

Following the analysis of the TE mode, the even and odd TM eigenvalue equation can be written as:

$$\tan\left(\frac{hd}{2}\right) = \left(\frac{n_1^2}{n_2^2}\right)\frac{p}{h} \tag{1.3.22a}$$

and

$$\tan\left(\frac{hd}{2}\right) = -\left(\frac{n_2^2}{n_1^2}\right)\frac{h}{p} \tag{1.3.22b}$$

Using the same graphical technique, the same limitation for the active layer thickness is obtained for single transverse mode excitation in the TM mode. The only difference between the TE and TM modes is the refractive index correction term added to the TM mode eigenvalue equation for the symmetric slab waveguide.

For most semiconductor lasers that have a lateral confinement, the width of the active layer W is finite. With the width dimension found to be comparable with the active layer thickness, a rectangular waveguide is formed. Nevertheless, we can still follow a similar procedure to that applied to the slab waveguide to solve the field solution of the rectangular waveguide. The schematic cross-section of a rectangular waveguide is shown in Figure 1.7. The central core region, which is surrounded by four cladding regions, has the highest refractive index (n_1). With the propagation mode mainly confined in the central core, the field penetration in the corners (the shaded regions in the figure) of the structure can be ignored [45].

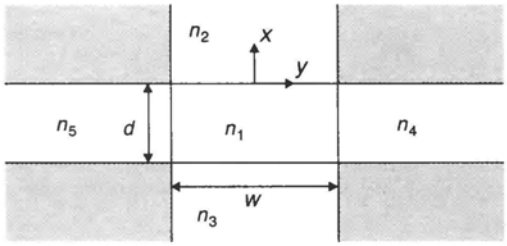

Figure 1.7 Schematic cross-section of a rectangular waveguide. The refractive indices of the different regions are indicated.

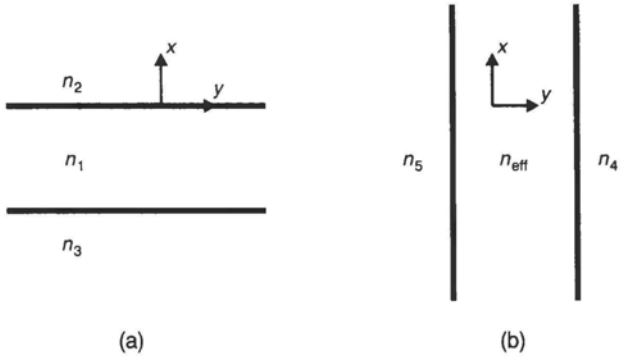

Figure 1.8 Procedures for analysing the rectangular waveguide using EIM. (a) The first slab approximation along the x axis (b) The second slab approximation along the y axis where n_{eff} is used.

An exact analytical solution for the propagation characteristics of the strip waveguide is not possible and a certain degree of approximation is necessary. A convenient technique, known as the effective index method (EIM), can be used to provide an accurate analytical solution for the rectangular waveguide. In this method, the equivalent slab waveguide in one direction is solved first (see Figure 1.8) so that the effective refractive index of the central slab can be generated. This effective refractive index is then used to solve the other slab waveguide which is found perpendicular to the original one. In this way the solutions of the two slab waveguides are coupled. Similar to the slab waveguide analysis, the number of excited transverse modes is determined by both the active thickness (d) and width (w) of the central core region. Therefore, it can be shown that proper controls over the active thickness and width are necessary for single transverse mode operation.

To show how the EIM works, a symmetric rectangular waveguide is used instead. With $n_3 = n_2$ and $n_5 = n_4$, we can solve the central slab first by using the graphical approach as shown earlier in the TE mode of the slab waveguide. For a single transverse mode, along the x axis, we end up with the following inequality [44]:

$$D = k_0 \frac{d}{2}(n_1^2 - n_2^2)^{1/2} < \frac{\pi}{2} \tag{1.3.23a}$$

or

$$d < \frac{\lambda}{2}(n_1^2 - n_2^2)^{-1/2} \tag{1.3.23b}$$

where D is the normalised waveguide thickness, as defined earlier. Then, the second slab waveguide analysis is carried out along the perpendicular y axis. On the basis of the TM mode analysis of the slab waveguide, we end up with [46]

$$W = k_0 \frac{w}{2}(n_{\text{effx}}^2 - n_4^2)^{1/2} < \frac{\pi}{2} \tag{1.3.24a}$$

or

$$w < \frac{\lambda}{2}(n_{\text{effx}}^2 - n_4^2)^{-1/2} \tag{1.3.24b}$$

where W is the normalised waveguide width. In equation (1.3.24), the effective refractive index n_{effx}, which was derived earlier from the first slab approximation, is used instead. So far, a purely index guided structure has been used where all possible gains or losses in the structure have been ignored. Nevertheless, the single mode operating conditions are still feasible since the imaginary part of the refractive index, owing to gains or losses, has a much smaller magnitude when compared with the corresponding real refractive indices. As a result, there is a slight difference between the field solutions of the purely index guided structure and the one that processes the gains/losses [28].

The description of the waveguiding properties in the indexed guided waveguide is now complete. If the active region dimensions are chosen to satisfy both equations (1.3.23b) and (1.3.24b), only a single mode along the transverse plane is supported.

Single longitudinal mode (SLM)

In semiconductor lasers, electron transport occurs between two energy bands that consist of a finite number of discrete energy levels. Rather than a discrete energy transfer like the gaseous laser, semiconductor lasers are characterised by a wider gain spectrum. In an inhomogeneously broadened laser, the gain spectrum may be found to be several times wider than the longitudinal mode spacing. In the simplest type of optical resonator, better described as the Fabry–Perot (FP) cavity, photons escape from a cavity which has two partially reflected mirrors facing each another. Without any frequency discrimination, photons at any frequency could escape the cavity. As a result, it is common that several oscillation modes, as depicted in Figure 1.9, are observed, especially when they are under rapidly pulsed operation.

As will be shown in detail in Chapter 2, the longitudinal mode spacing between each frequency component in the FP semiconductor laser cavity is given as

$$\delta f = \frac{c}{2n_g L} \tag{1.3.25}$$

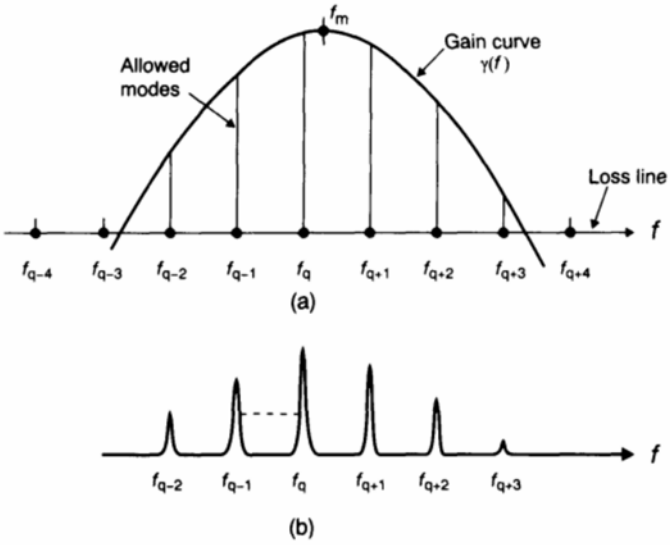

Figure 1.9 (a) Possible gain profile of an inhomogeneously broadened laser. (b) The resulting intensity spectrum (after [44]).

where c is the free space velocity, n_g is the group refractive index and L is the laser cavity length. To have better control over the longitudinal modes in the FP cavity, several methods have been proposed. By using a shorter cavity, we can increase the mode spacing. However, a higher threshold current is expected and several longitudinal modes may occur at severe modulation. Moreover, as we will discuss later, such a shorter cavity will lead to a wider spectral width [17]. A different method involves the injection of an external light from another laser [47]. In this way, an SLM oscillation can be achieved. However, careful tuning is essential so that the lasing modes of the two lasers are matched [48]. By adding a reflecting surface outside the FP cavity, an external coupled cavity has also been used [49]. Owing to the interference with the external cavity, the overall modal loss becomes frequency dependent and hence limits the oscillation mode from the FP laser cavity. However, both the external light injection method and the external coupled cavity laser lack long-term stability. These devices are vulnerable to mechanical vibration, temperature and pressure changes and hence the lasing mode tends to shift from time to time. While they are useful in coherent system experiments, it has becomes evident that they are difficult to realise as commercial products.

To include a wavelength or frequency selective mechanism, one popular technique is to include an etched diffraction grating within the laser waveguide structure. The gratings, based single frequency lasers, are classified into two categories. If the active layer and the grating extend along the whole length of the laser cavity, the device is known as a distributed feedback (DFB) laser. If the grating or feedback sections are passive such that the gain region

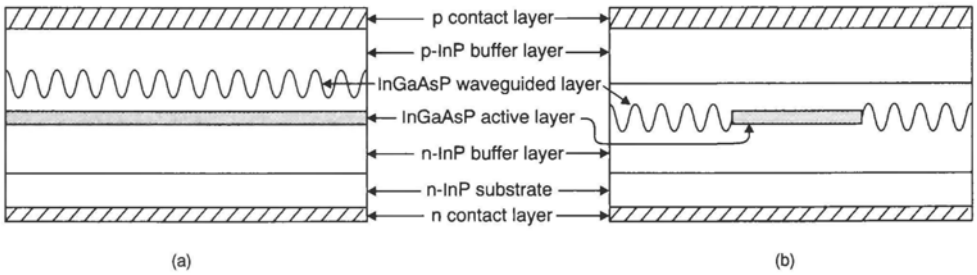

Figure 1.10 Schematic diagrams of a uniform grating (a) DFB laser diode and (b) a DBR laser doide.

is located in a separate planar gain section, a distributed Bragg reflector (DBR) laser structure is formed. Figure 1.10 illustrates the structural differences between the DFB and DBR lasers. One of the most convenient methods of generating gratings is to use the holographic exposure technique [12]. With a two arm interferometer set-up, the interference pattern of two coherent lightwaves cross each other at a predetermined angle, and a periodic grating is formed. Other methods, like electron beam lithography, are also possible. Then, followed by the conventional wet chemical etching or the dry ion-beam etching process, the grating pattern is delineated on the substrate. In general, the grating can be placed below the active layer or in the upper cladding layer.

In DBR lasers, the Bragg grating sections are separated from the active section where major carrier recombination occurs. In other words, the frequency at which the grating section reflects does not depend on the bias current, and so a non-linear influence on the guided refractive index (due to injected carriers) is rare. However, the use of end passive gratings in DBR lasers implies extra etching processes during fabrication. Moreover, the effective length of the planar section, which is crucial in deciding the oscillation frequency of DBR lasers, is difficult to control precisely. Owing to the tolerance inherited in fabrication, the relative grating phases of the two Bragg reflectors become unpredictable. In general, DBR lasers are more complex, and effective measures are needed to tackle the problem of yield and reliability. To suppress any possible FP mode in the grating structures, it is quite usual to have anti-reflective coatings on the laser facets of DFB or DBR lasers.

The working principle of a uniform-grating DFB laser with perfectly anti-reflective facet coatings (sometimes called a conventional DFB laser) was first explained by Kogelnik and Shank in 1971 [50] using coupled wave theory, but it was not until 1974 [51] that the first DFB laser operating at room temperature (300 K) under continuous wave (CW) operation was built. Details of the coupled wave theory will be covered in Chapter 2. Normally, in DFB lasers the grating period Λ must be carefully chosen to satisfy the Bragg condition:

$$\Lambda = \frac{m\lambda_B}{2n_g} \tag{1.3.26}$$

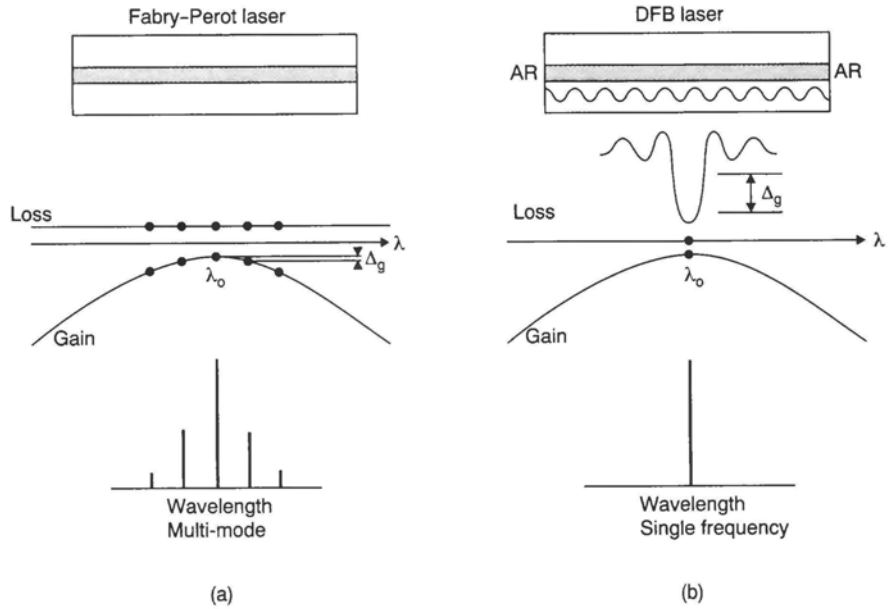

Figure 1.11 The typical gain, loss and spectral profiles of (a) a Fabry–Perot laser diode, and (b) a distributed feedback (DFB) laser diode.

where n_g is the usual group refractive index and λ_B is sometimes called the Bragg wavelength. For a 1.55 μm InGaAsP laser, with a first-order grating ($m = 1$), typical values of n_g are 3.4 and Λ is 0.23 μm. Figure 1.11 shows the difference between the operation of FP and DFB lasers. For DFB lasers, the longitudinal mode, which is found closest to the Bragg wavelength, will lase, while other side modes that have larger losses are severely suppressed as a wavelength/frequency dependent loss is introduced. The net gain difference (or gain margin) between the dominant lasing mode and the most probable side mode is found to be much higher compared with the FP lasers.

1.3.2 Spectral linewidth requirements

Origin of phase noise and the formulation of the spectral linewidth

Owing to the dispersive nature of the optical fibre, laser sources that operate at a single frequency will be necessary for long-haul transmission at speeds higher than a few GHz. However, even the output spectrum of a single frequency semiconductor laser (like DFB semiconductor lasers) is never "pure" but is always contaminated by a finite spectral width. The finite spectral width is mainly due to the random phase of the spontaneous emission that couples into the lasing mode. Consequently, the fluctuation in gain broadens the spectral linewidth as a result of a lasing frequency shift [52]. To measure the spread of the laser spectrum, the spectral linewidth ($\Delta\nu$), which is defined as the full width half maximum (FWHM) of the optical power

spectrum, is used. On the basis of the delayed self-heterodyne technique [53], the spectral linewidth can be measured easily.

To understand the spectral behaviour of the laser light, we can use the classical description [54]. Consider a laser with a spatial mode $\Phi(x)$. The transverse optical field of the laser (which is a real quantity) could be expressed as

$$E(x, t) = B[\beta(t)\Phi(x) + \beta(t)^*\Phi(x)^*] \tag{1.3.27}$$

where $\beta(t)$ is the time-dependent complex wave amplitude and B is a constant. An asterisk indicates a complex conjugate. Usually, the complex amplitude $\beta(t)$ can be expressed in terms of two real quantities: intensity $I(t)$ and phase $\phi(t)$ such that [54,55]

$$\beta(t) = I(t)^{1/2}e^{j\varphi} \tag{1.3.28}$$

where the time harmonic term $\exp(j\omega_0 t)$ is omitted. The real factor B is chosen such that the energy term, which is found to be proportional to the product $\beta\beta^*$, is determined by the expression $\hbar\omega_0 I(t)$. As a result, $I(t)$, as shown in the previous equation, corresponds to the total number of photons found inside the laser cavity.

To understand the origin of phase noise, we must understand the nature of spontaneous emission. There are mainly two mechanisms that lead to a change of phase in a semiconductor laser.

(1) The first contribution of phase noise ($\Delta\phi'$) comes when a spontaneous photon is injected into the lasing mode. Then both the intensity and phase of the optical field in the mode undergo changes. These fluctuations of field due to spontaneous emission will contribute directly to phase noise.

(2) In semiconductor lasers there is a second contribution of phase noise ($\Delta\phi''$) associated with the intensity change, as described in mechanism (1) above. According to the Kramer–Kroenig relation [56], any change of gain inside a semiconductor will alter the refractive index of the semiconductor. Consequently, the optical field experiences an additional phase change, which induces extra linewidth broadening. Note that this is not readily observed in a stable CW gas laser, because the time taken for the intensity to return to its initial steady-state value is shorter than that of the semiconductor laser (of the order of 10^{-9} s). Within such a short period of time, the above processes rarely happen in gas lasers and so the spectral linewidth of the gas laser is narrower than that of the semiconductor laser.

In Figure 1.12, a phasor diagram that follows Henry's works [54,55] is included to show how an arbitrary ith spontaneous emission can produce a change ΔI in the intensity (or photon number) and a phase change of $\Delta\phi_i'$ as described by mechanism (1) above.

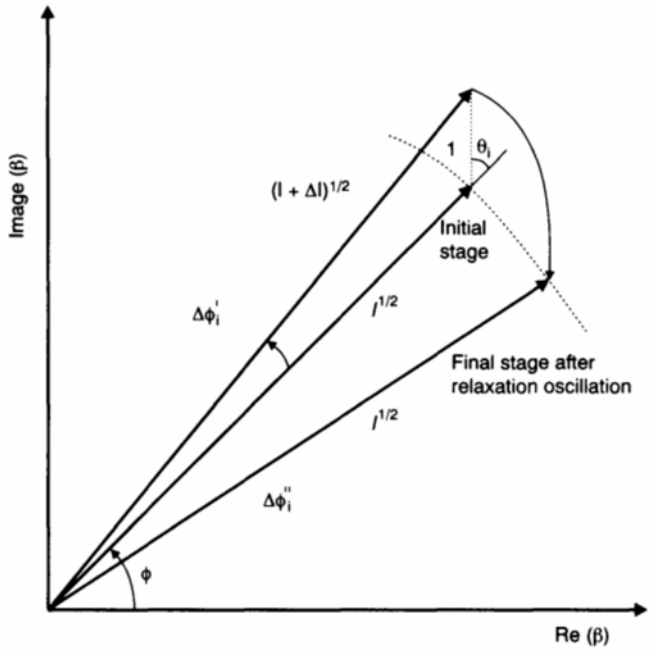

Figure 1.12 The spontaneous change of phase and intensity of the optical field induced by the ith spontaneous event (after [46,47]).

Using simple geometrical considerations, it can be shown that the changes of intensity and phase can be written as

$$\Delta\phi_i = I^{-1/2} \sin\theta_i \tag{1.3.29}$$

$$\Delta I_i = 1 + 2I^{1/2} \cos\theta_i \tag{1.3.30}$$

where the ith spontaneous photon changes the complex wave amplitude $\beta(t)$ by $\Delta\beta(t)$, where $\Delta\beta(t)$ is represented by a unit magnitude and a random phase of θ_i. In this simple analysis it is assumed that a single photon is emitted for each spontaneous emission. Moreover, the average phase change is assumed to be zero over a large number of spontaneous events.

To understand the contribution of phase noise owing to a second contribution of phase noise, $\Delta\phi''$, it is necessary to determine the mutual coupling between the intensity and the phase of the optical mode. From the time-dependent wave equation, we end up with the following rate equation for a complex wave amplitude [54,55]:

$$\frac{d\beta}{dt} = \frac{v_g(\Gamma g - \alpha_0)}{2} \cdot (1 + j\alpha_H)\beta \tag{1.3.31}$$

where v_g is the group velocity, Γ is the optical confinement factor, g is the amplitude gain coefficient due to material gain and α_0 is the cavity

absorption. In the above equation, α_H is the intrinsic linewidth enhancement factor defined as [57–59]

$$\alpha_H = -\frac{d\chi''(N)/dN}{d\chi'(N)/dN} \tag{1.3.32}$$

where χ' and χ'' are the real and imaginary parts of the susceptibility, respectively, while N is the injected carrier concentration. In all practical cases both the carrier-induced refractive index change as well as that induced by the imaginary part of the permittivity are much smaller than the intrinsic refractive index of the semiconductor. As a result, the intrinsic linewidth enhancement factor can also be expressed as

$$\alpha_H = -2k_0 \cdot \frac{dn/dN}{dg/dN} \tag{1.3.33}$$

where the relative change in the refractive index (n) and gain (g) due to variations in the injected carrier concentration (N) are considered. The negative sign included in the above equations is important in keeping α_H positive because the refractive index is found to have a negative change with increasing carrier concentration [58] (i.e. dn/dN is negative). The intrinsic linewidth enhancement factor was first introduced by Henry [54] and used to explain the experimental results of Fleming and Mooradin [60] on AlGaAs semiconductor lasers. In the case of InGaAsP/InP devices, the value of α_H ranges from 4.5 to 7 [58,61].

By examining equation (1.3.32), it is obvious that the intrinsic linewidth enhancement factor depends on several parameters of the medium. The α_H dependence on carrier concentration and photon density was first suggested by Vahala *et al.* [57]. At a fixed carrier concentration, they found that α_H decreases with increasing photon energy, while α_H increases with carrier concentration at a fixed photon energy. On the other hand, α_H remains constant at the peak gain for different values of carrier concentration and photon energies. The results for the quaternary InGaAsP with a bandgap of ~ 0.8 eV (or $\lambda \sim 1.55$ μm) are shown in Figure 1.13. It is interesting to see how α_H will change when the lasing wavelength of a single frequency laser (e.g. a DFB laser) is allowed to shift with respect to the peak gain. It can be seen from Figure 1.13 that α_H would become larger at wavelengths longer than the peak gain, and become smaller on the shorter wavelength side of the spectrum. The detuning effect of the DFB laser was confirmed by Ogita *et al.* [62] and a narrower spectral linewidth was found at the shorter wavelength side of the gain peak.

Besides carrier concentration and photon energies, the intrinsic linewidth enhancement factor also depends on temperature. With decreasing temperature, the change in refractive index with carrier concentration is large, and so is the gain variation. However, the gain variation is faster than that of the refractive index, and consequently α_H decreases as the temperature drops. Since there is no possible way to measure α_H directly, it is still not clear to

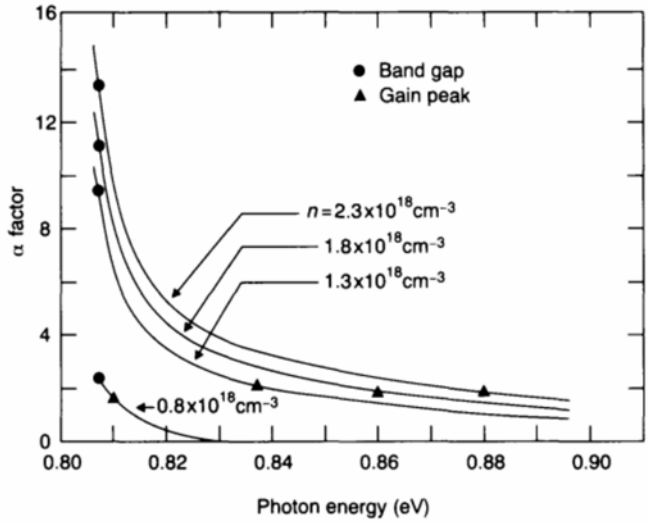

Figure 1.13 Dependence of linewidth enhancement factor α on photon energy for undoped 1.55 μm InGaAsP at various levels of electron concentration, n, indicated in units of 10^{18} cm^{-3} (after [49]).

what extent the linewidth enhancement factor is related to structural change and other experimental uncertainties. Various methods, like the AM/FM noise spectrum measurement [61], and the spectral linewidth measurement [63], have been used to find the value of α_H for DFB semiconductor lasers. However, the relative merits of these methods are still uncertain and so it is difficult to make any direct comparison between these results. On the other hand, it is believed that the intrinsic linewidth enhancement factor α_H is less structurally dependent for a purely index-guided structure as compared with the gain-guided structure. Owing to the lateral guiding characteristics of the gain-guided structure, the variation in the real and imaginary part of the permittivity will not be the same in the lateral direction. In that case, an effective linewidth enhancement factor is used instead [64]. A detailed analysis of the effective linewidth enhancement factor will be given in later chapters.

Similar to equation (1.3.31), the conjugate of the complex wave amplitude also satisfies the following equation:

$$\frac{d\beta^*}{dt} = \frac{v_g(\Gamma_g - \alpha_0)}{2} \cdot (1 - j\alpha_H)\beta^* \tag{1.3.34}$$

From equation (1.3.28) and its complex conjugate, we can express the intensity and phase in terms of the complex wave amplitude such that

$$\begin{aligned} I &= \beta \cdot \beta^* \\ \phi &= \frac{1}{2j} \ln(\beta/\beta^*) \end{aligned} \tag{1.3.35}$$

Therefore, by taking the derivative of equation (1.3.35) and using equations (1.3.31) and (1.3.34), we obtain

$$\frac{dI}{dt} = v_g(\Gamma g - \alpha_0)I \tag{1.3.36a}$$

$$\frac{d\phi}{dt} = \frac{\alpha_H}{2} v_g(\Gamma g - \alpha_0) \tag{1.3.36b}$$

Combining equations (1.3.36a) and (1.3.36b) gives

$$\frac{d\phi}{dt} = \frac{\alpha_H}{2I} \cdot \frac{dI}{dt} \tag{1.3.37}$$

From equation (1.3.37) it is clear that a change in intensity due to spontaneous emission will induce a second phase alternation. If the change in intensity and phase occurs within a short period of time, the second phase change $\Delta\phi''$ could be determined by taking an integral so that equation (1.3.37) becomes

$$\begin{aligned} \Delta\phi_i'' &= -\frac{\alpha_H \Delta I_i}{2I} \\ &= -\frac{\alpha_H}{2I}(1 + 2I^{-1/2}\cos\theta_i) \end{aligned} \tag{1.3.38}$$

For a laser operating at above threshold, the intensity changes instantly from I to $I + \Delta I_i$ and then drops back to a final value of I after the relaxation oscillation has died out. Thus, a minus sign is included in the above equation as the intensity change becomes $-\Delta I_i$. As a result, the total change in phase due to the ith spontaneous emission becomes

$$\begin{aligned} \Delta\phi &= \Delta\phi' + \Delta\phi'' \\ &= -\frac{\alpha_H}{2I} + I^{-1/2}(\sin\theta_i - \alpha_H \cos\theta_i) \end{aligned} \tag{1.3.39}$$

So far, we have considered the total phase change due to a single spontaneous photon. Suppose that the total number of M spontaneous emission events happen within a period of time. Then the total phase fluctuation is obtained by summing equation (1.3.39) over M events such that

$$\Delta\phi = -\frac{\alpha_H M}{2I} + I^{-1/2}\sum_{i=1}^{M}(\sin\theta_i - \alpha_H \cos\theta_i) \tag{1.3.40}$$

Sometimes, instead of using the total number of spontaneous events, it is more convenient to use the spontaneous emission rate R_{sp}. By replacing M with $R_{sp}t$, the first term of the above equation will result in an average phase change of

$$\langle\Delta\phi\rangle = -\frac{\alpha_H R_{sp} t}{2I} \tag{1.3.41}$$

or a frequency shift of

$$\Delta\omega = \frac{\mathrm{d}}{\mathrm{d}t}\langle\Delta\phi\rangle = -\frac{\alpha_{\mathrm{H}}R_{\mathrm{sp}}}{2I} \tag{1.3.42}$$

This frequency shift is caused solely by the spontaneous emission.

From the summation term as shown in equation (1.3.40), the mean square phase variation term can be determined as

$$\langle\Delta\phi^2\rangle = \frac{R_{\mathrm{sp}}(1+\alpha_{\mathrm{H}}^2)t}{2I} \tag{1.3.43}$$

because all phase crossing terms vanish. With a Gaussian probability distribution assumed for the phase change, the power spectrum of the laser becomes Lorentzian in shape [55]. As a result, the spectral linewidth $\Delta\nu$ becomes

$$\Delta\upsilon = \frac{\langle\Delta\phi^2\rangle}{2\pi t} = \frac{R_{\mathrm{sp}}}{4\pi I}(1+\alpha_{\mathrm{H}}^2) \tag{1.3.44}$$

To facilitate experimental measurements on the spectral linewidth of semiconductor lasers, it is better to express the intensity in terms of optical power such that

$$I = \frac{(P_1+P_2)}{v_{\mathrm{g}}\alpha_{\mathrm{m}}} \cdot \frac{\lambda}{hc} \tag{1.3.45}$$

where P_1 and P_2 are the optical power output from the laser facets, while α_{m} is the mirror loss of the laser cavity. For a closed cavity, such as a FP laser with high reflecting ends, the total spontaneous emission rate can be expressed as

$$R_{\mathrm{sp}} = v_{\mathrm{g}}\Gamma g n_{\mathrm{sp}} = v_{\mathrm{g}} g_{\mathrm{th}} n_{\mathrm{sp}} \tag{1.3.46}$$

where g_{th} is the threshold gain and n_{sp} is the population inversion factor defined as

$$1/n_{\mathrm{sp}} = 1 - \exp\left(\frac{\hbar\omega_0 - \mathrm{e}V}{kT}\right) \tag{1.3.47}$$

where $\mathrm{e}V$ is the separation of the quasi-Fermi levels of the conduction band and the valence band of the semiconductor lasers. In the above equation, n_{sp} characterises the incomplete inversion of the laser transition. If there is complete population inversion, then n_{sp} will become unity.

On substituting equations (1.3.44) and (1.3.45) into equation (1.3.43), the spectral linewidth becomes

$$\Delta\upsilon = \frac{v_g^2 n_{\mathrm{sp}} g_{\mathrm{th}} a_{\mathrm{m}}}{4\pi(P_1+P_2)} \cdot \frac{hc}{\lambda}(1+\alpha_{\mathrm{H}}^2) \tag{1.3.48}$$

where the intrinsic linewidth enhancement and the inversion factor n_{sp} are assumed constant and homogeneous' at least over the active region of the laser. Although the spectral linewidth formula above is derived for the FP type

laser, it also holds for the index-guided DFB semiconductor lasers [63,65], provided that the loss term α_m is interpreted as the output loss. In the gain-guided lasers, the maximum gain is found along the centre of the active layer. Rather than having a plane phase front, the phase fronts of gain-guided lasers are curved and so a wider far field spread is expected. Therefore, it is intuitively reasonable to assume that the lasing mode of gain-guided lasers may capture a larger fraction of spontaneous emission than the lasing mode of the index-guided lasers. Such an enhancement in spontaneous emission K_{tr} in a transversely single-mode gain-guided laser was first proposed by Petermann [56] and is given here as

$$K_{tr} = \left| \frac{\iint |\beta_t^2| \, dx dy}{\iint \beta_t^2 \, dx dy} \right|^2 \tag{1.3.49}$$

where β_t is the transverse electric field distribution of the lasing mode. Most often, K_{tr} is defined as the Petermann gain guiding factor. For index-guided semiconductor lasers having plane phase fronts, the transverse electric field is purely real and so K_{tr} becomes unity. Meanwhile, it was also shown that the spontaneous emission coupled to the lasing mode is also enhanced by output coupling, due to the low facet reflectivities in semiconductor lasers. This oscillator loading effect was first noticed by Ujihara [66] and later by Henry [67], but in a different format. According to Wang *et al.* [68], such a longitudinal correction factor K_z is defined as

$$K = \left| \frac{\int_0^L |\beta_z^2| \, dz}{\int_0^L \beta_z^2 \, dz} \right| \tag{1.3.50}$$

where β_z is the longitudinal electric field distribution of the lasing mode and L is the laser cavity length. In defining equations (1.3.49) and (1.3.50), the laser itself must show a constant transverse mode pattern along the longitudinal direction so that the electric field can be separated into the transverse and longitudinal factors. Finally, the corrected spectral linewidth of equation (1.3.48) becomes

$$\Delta\upsilon = \frac{v_g^2 n_{sp} g_{th} a_m}{4\pi(P_1 + P_2)} \cdot \frac{hc}{\lambda}(1 + \alpha_H^2) \cdot K_{tr} \cdot K_z \tag{1.3.51}$$

System requirements

In general, the requirements of a spectral linewidth depend on the modulation scheme, receiver design and transmission bit rate (R_b) of the system. A

Table 1.1 Laser spectral linewidth requirements for a coherent optical communication system. R_b is the transmission bit rate. One dB power penalty is assumed at the receiver (after [60])

Receiver type	IF processing	Modulation	$\Delta v/R_b$ (%)
Heterodyne	incoherent	ASK	9%
Heterodyne	incoherent	FSK	2–9%
Heterodyne	incoherent	DPSK	0.165%
Heterodyne	coherent	PSK	0.226%
Homodyne	coherent	PSK	0.031%

detailed analysis was carried out by Kazovsky [69] in which the maximum permissible laser linewidths for various coherent communication systems were reported. Both heterodyne and homodyne systems were considered. Table 1.1 summarises the results, and different receiver designs are compared.

From Table 1.1 it is clear that the homodyne system, which provides the best receiver sensitivity, requires a laser linewidth of 0.031% R_b. With such a demanding spectral linewidth, it will be more practical to switch to another scheme like the FSK system in which the linewidth requirement is more flexible. Inspection of Table 1.1 also reveals that the HE/IP type receivers are most robust (which permits the largest laser linewidth), followed by the HE/CP type receivers and then by the homodyne receivers.

Limitations of the linewidth formula

According to equation (1.3.51), the spectral linewidth formula for a single mode semiconductor laser is inversely proportional to the total output power. However, experimental results reveal that even in a single frequency laser like a DFB laser, the spectral linewidth tends to saturate or rebroaden at high output power when the laser is severely biased [65,70]. These results were difficult to understand on the basis of Henry's linewidth formula. It was suggested [71,72] that the presence of other non-lasing side modes might contribute to the spectral linewidth for the single mode DFB semiconductor laser. At above threshold bias, a gain depression in the lasing main mode and hopping in the lasing wavelength have also been observed [73,74]. The longitudinal correction term as shown in equation (1.3.51) may not be a constant but may be sensitive to a biasing current and the structural design of laser diodes. For DFB laser diodes operating at a high biasing current, such linewidth saturation or rebroadening phenomena have to be considered since the performance and reliability of a coherent optical fibre communication system depends heavily on the spectral linewidth of the laser source. A more comprehensive approach, which includes the variation due to structural changes, longitudinal variations of both carrier and photon densities will be discussed in a later chapter.

1.4 SUMMARY

The development of optical communications, in particular fibre-based communication systems, have been reviewed from a historical perspective. By trapping light inside the core of a cylindrical fibre as a result of total internal reflection, optical fibres having a low attenuation loss serve as an ideal medium for optical communication. At the transmitter side, information is first converted into a stream of photons before they are launched into the optical fibre. Compact size semiconductor laser diodes served this purpose by generating coherent photons. The availability of both single mode optical fibres and reliable semiconductor optical devices paved the way towards widespread global optical fibre networks.

According to the type of detection method used at the receiver end, an optical fibre system could be categorised into either a direct or a coherent detection scheme. For limited peer to peer application, a direct detection scheme could be very simple. However, with the increased demand in wide bandwidth, long-haul application, the coherent detection scheme is a better alternative. Using the spatial coherence of the optical carriers, a coherent detection scheme shows improved receiver sensitivity, while the available optical spectrum of optical fibre could be utilised in a better way. Using an appropriate multiplexing scheme such as FDM or WDM, more information could be loaded into a single fibre link. In practice, however, optical fibre communication systems using the coherent detection scheme require a more careful design and stringent requirements in device performances.

From the system requirements of coherent optical communication systems, the device characteristics of optical devices, especially semiconductor laser diodes, were briefly reviewed. To minimise the effect caused by the dispersive property of optical fibres, semiconductor laser diodes should have a stable single mode oscillation. By controlling the width and thickness of the active layer, a transverse single mode oscillation could be controlled easily. However, a single longitudinal mode oscillation requires special attention. With the gain spectrum in semiconductors usually found to be broader than the longitudinal mode spacing, multiple mode oscillation in the conventional FP cavity is common. By incorporating a specially designed grating inside the laser cavity, a built-in wavelength selective mechanism is built. This wavelength filtering effect forms the core of the distributed feedback laser diodes. Owing to the characteristics of semiconductors, a laser diode oscillating at a single mode does not generate a pure monochromatic spectrum. The finite spectral spread, formally known as the spectral linewidth, has to be considered in high-speed optical links. The origin and system requirements of spectral linewidths inherent in semiconductor lasers are reviewed at the end of the chapter.

1.5 REFERENCES

[1] Cochrane, P. and Heatley, D.J.T., "Future directions in long-haul optical-fibre systems", *Br. Telecom Technol J.*, **9**, pp. 268–280, 1991.

[2] Microsoft Corporation, *Microsoft Encarta 94*, CD-ROM, 1994.
[3] Ryder, J.D. and Fink, D.G., *Engineer and Electronics*. New York: IEEE Press, 1984.
[4] Bell, A.G., U.S. Patent 174456, 1876.
[5] Maiman, T.H. "Stimulated optical radiation in ruby", *Nature*, **187**, pp. 493-494, 1960.
[6] Kao, C.K. and Hockham, G.A.,"Dielectric fiber surface waveguides for optical frequency", *Proc. IEE*, **113**, no. 7, pp. 1151-1158, 1966.
[7] Werts, A., "Propagation de la lumiere coherente dans les fibres optiques", *L'Onde Electrique*, **46**, pp. 967-980, 1966.
[8] Takahashi, S. and Kawashima, T., "Preparation of low loss multi-component glass fiber", *Tech. Dig. Int. Conf. Integra. Opt. and Opt. Fiber Commu.*, p. 621, 1977.
[9] Kressel, H. and Butler, J.K., *Semiconductor Lasers and Hecterojunction LEDs*. New York: Academic Press, 1977.
[10] Melchior, H., Fisher, M.B. and Arams, F.R., "Photodetectors for optical communication systems", *Proc. IEEE*, **58**, pp. 1446-1486, 1970.
[11] Newman, D.H., Ritchie, S., "Sources and detectors for optical fibre communications application: The first 20 years", *IEE Proc., Pt. J*, **133**, pp. 1213-1229, 1986.
[12] Adams, M.J., Steventon, A.G., Delvin, W.J. and Henning, I.D., *Semiconductor Lasers for Long-wavelength Optical-fibre Communications Systems*, IEE Material and Devices Series, ed. N. Parkman and D.V. Morgan, no. 4. London: Peter Peregrinus, 1987.
[13] Shumate, P.W., Chen, Jr., F.S. and Dorman, P.W., "GaAlAs laser transmitter for lightwave technology", *Bell System J.*, **57**, pp. 1823-1836, 1978.
[14] Alferov, Z.I., Andreev, V.M., Korol'kov, V.I., Portnoi, E.L. and Tret'yakov, D.N., "Injection properties of n-$Al_xGa_{1-x}As$-p-GaAs hecterojunctions", *Soviet Phys. Semicon.*, **2**, no. 10, pp. 3733-3740, 1969.
[15] Neumann, E.G., *Single-mode Fibers: Fundamental*. Spring-Verlag, 1988.
[16] Noda, J., Okamoto, K. and Sasaki, Y., "Polarization-maintaining fibers and their applications", *J. Lightwave Technol.*, **LT-4**, pp. 1071-1089, 1986.
[17] Bell, T.E., "Single-frequency semicondcutor lasers", *IEEE Spectrum*, **20**, p. 38, 1983.
[18] Kobayashi, K. and Mito, I., "Single frequency and tunable laser diodes", *J. Lightwave Technol.*, **LT-6**, no. 11, pp. 1623-1633, 1988.
[19] Creaner, M.J., Steele, R.C., Marshall, I., Walker, G.R., Walker, N.G., Mellis, J., Al-Chalaba, S., Sturgess, I., Rutherford, M., Davidson, J. and Brain, M., "Field demonstration of 565 Mbit/s DPSK coherent transmission system over 176 km of installed fiber", *Electron Lett.*, **24**, pp. 1254-1356, 1988.
[20] Brian, M.C., Creaner, M.J., Steele, R.C., Marshall, I., Walker, G.R., Walker, N.G., Mellis, J., Al-Chalaba, S., Davidson, J., Rutherford, M. and Sturgess, I., "Progress towards the field deployment of coherent optical fiber systems", *J. Lightwave Technol.*, **LT-8**, pp. 423-437, 1990.
[21] Bryan, E.G., Carter, S.F., Wright, J.V., Boggis, J.M. and Cox, J.D., "A 1.2 Gbit/s optical FSK field trial demonstration", *Br. Telecom Technol J.*, **8**, pp. 18-26, 1990.
[22] DeLange, O.E. "Wide band optical communication systems: Part II, frequency-division multiplexing", *Proc. IEEE.*, **58**, pp. 1683-1690, 1970.
[23] Hasegawa, A. and Tappert, F., "Transmission of stationary nonlinear optical pulses in dispersive dielectric fibers. I. Anomalous dispersion", *Appl. Phys. Lett.*, **23**, no. 3, pp. 143-144, 1973.
[24] Ghafouri-Shiraz, H., Shum, P. and Nagata, M., "A novel method for analysis of soliton propagation in optical fibers", *IEEE J. Quantum Electron.*, **QE-31**, no. 1, pp. 190-200, 1995.
[25] Nakazawa, M., Yamada, E., Kubota, H. and Susuki, K., "10 Gbits/s soliton data transmission over one million kilometers", *Electron. Lett.*, **27**, no. 14, pp. 1270-1272, 1991.

[26] Mollenauer, L.F., Neubelt, M.J., Haner, M., Lichtman, E., Evangelides, S.G. and Nyman, B.M., "Demonstration of error-free soliton transmission at 2.5 Gbit/s over more than 14000 km", *Electron Lett.*, **27**, no. 22, pp. 2055-2056, 1991.

[27] Eisenstein, G., "Semiconductor optical amplifiers", *IEEE Circuits Devices Mag.*, pp. 25-30, July 1989.

[28] Ghafouri-Shiraz, H. and Chu, C.Y.J., "Analysis of waveguiding properties of travelling-wave semiconductor laser amplifiers using perturbation technique", *Fiber Int. Opt.*, **11**, pp. 51-70, 1992.

[29] Brackett, C.A., "Dense wavelength division multiplexing networks: Principles and applications", *IEEE J. Select. Areas Commun.*, **SAC-8**, no. 8, pp. 948-965, 1990.

[30] Cochrane, P., Heckingbottom, R. and Heatley, D., "Optical transparency: A new paradigm for telecommunications", *Opt. Phot. News*, **5**, pp. 15-19, 54, 1994.

[31] Linke, R.A., "Optical heterodyne communications systems", *IEEE Commun. Mag.*, pp. 36-41, 1989.

[32] Wagner, R.E. and Linke, R.A., "Heterodyne lightwave systems: Moving towards commercial use", *IEEE LCS Mag.*, **1**, no. 4, pp. 28-35, 1990.

[33] Yamamoto, Y. and Kimura, T., "Coherent optical fiber transmission system", *IEEE J. Quantum Electron.*, **QE- 17**, no. 6, pp. 919-934, 1981.

[34] DeLange, O.E., "Optical heterodyne detection", *IEEE. Spectrum*, pp. 77-85, 1968.

[35] Namizaki, H., "Single mode operation of GaAs-GaAlAs TJS-laser diodes", *Trans. IECE Japan*, **E59**, pp. 8-15, 1978.

[36] Kajimura, M., Aiki, K., Chinone, N., Ito, R. and Umeda, J., "Longitudinal-mode behaviours of mode stabilized AlGaAs injection lasers", *J. Appl. Phys.*, **49**, pp. 4644-4648, 1978.

[37] Stein, S. and Jones, J.J., *Modern Communication Theory*. New York: McGraw-Hill, 1964.

[38] Couch, II,L.W., *Digital and Analog Communication Systems*, 4th edition. New York: Macmillan, 1993.

[39] Yamamoto, Y., "Receiver performance evaluation of various digital optical modulation-demodulation systems in the 0.5-10 μm wavelength region", *IEEE J. Quantum Electron.*, **QE-16**, no. 11, pp. 1251-1259, 1980.

[40] Hodgkinson, T.G., Smith, D.W., Wyatt, R. and Maylon, D.J., "Coherent optical fibre transmission systems", *Br. Telecom Technol. J.*, **3**, pp. 5-18, 1985.

[41] Kazovsky, L.G., "Coherent optical receivers: performance analysis and laser linewidth requirements", *Opt. Eng.*, **24**, no. 4, pp. 575-579, 1986.

[42] Balanis, C.A., *Advanced Engineering Electromagnetics*. New York: John Wiley & Sons, 1989.

[43] Adams, M.J. and Wyatt, R., *An Introduction to Optical Waveguide.*, London: John Wiley & Sons, 1981.

[44] Yariv, A., *Optical Electronics*, 4th edition. Orlando, FL: Saunders College Publishing, 1991.

[45] Marcatilli, E.A.J., "Dielectric rectangular waveguides and directional couplers for integrated optics", *Bell Syst. Technol. J.*, **48**, no. 7, pp. 2071-2102, 1969.

[46] Ghafouri-Shiraz, H., "Single transverse mode condition in long wavelength SCH semiconductor laser diodes", *Trans. IEICE*, **E 70**, no. 2, pp. 130-134, 1987.

[47] Tsang, W.T., Olsson, A., Linke, R.A. and Logan, R.A., "1.5 μm wavelength GaInAsP C^3 lasers: Single-frequency operation and wide-band frequency tuning", *Electron. Lett.*, **19**, pp. 415-416, 1983.

[48] Kobayashi, K. and Mito, I., "Single frequency and tunable laser diodes", *J. Lightwave Technol.*, **LT-6**, no. 11, pp. 1623-1633, 1988.

[49] Wyatt, R. and Devlin, W.J., "10-kHz linewidth 1.5 μm InGaAsP external cavity laser with 55-nm tuning range", *Electron. Lett.*, **19**, pp. 110-112, 1983.

[50] Kogelnik, H. and Shank, C.V., "Coupled-wave theory of distributed feedback lasers", *J. Appl. Phys.*, **43**, no. 5, pp. 2327-2335, 1972.

[51] Nakamura, M., Aiki, K., Umeda, J. and Yariv, A.,"CW operation of distributed feedback GaAs/GaAlAs diode lasers at temperatures up to 300°K", *Appl. Phys. Lett.*, **27**, pp. 403-405, 1975.

[52] Agrawal, G.P. and Dutta, N.K., *Long-wavelength Semiconductor Lasers*. Princeton, NJ: Van Nostrand. 1986.

[53] Okoshi, T., Kikuchi, K. and Nakayama, N., "A novel method for high revolution measurement of laser output spectrum", *Electron. Lett.*, **16**, pp. 630-631, 1980.

[54] Henry, C.H., "Theory of the linewidth of semiconductor laser", *IEEE J. Quantum Electron.*, **QE-18**, no. 2, pp. 259-264, 1982.

[55] Henry, C.H., "Phase noise in semiconductor laser", *J. Lightwave Technol.*, **LT-4**, no. 3, pp. 298-311, 1986.

[56] Petermann, K., *Laser Diode Modulation and Noise*. Tokyo, Japan: KTK Scientific and Kluwer Academic Publishers, 1988.

[57] Vahala, K., Chiu, L.C., Margalit, S. and Yariv, A., "On the linewidth enhancement factor α in semiconductor injection lasers", *Appl. Phys. Lett.*, **42**, pp. 631-633, 1983.

[58] Osinski, M. and Buus, J., "Linewidth broadening factor in semiconductor lasers — an overview", *IEEE J. Quantum Electron.*, **QE-23**, no. 1, pp. 9-28, 1987.

[59] Sugimura, A., Patzak, E. and Meissner, P., "Homogeneous linewidth and linewidth enhancement factor for a GaAs semiconductor laser", *J. Phys. D (Appl. Phys.)*, **19**, pp. 7-16, 1986.

[60] Fleming, M.W. and Mooradian, A., "Fundamental line broadening of single-mode (GaAs) As diode lasers", *Appl. Phys. Lett.*, **38**, no. 7, pp. 511-513, 1981.

[61] Kikuchi, K. and Okoshi, T., "Measurement of FM noise, AM noise and field spectra of 1.3 μm InGaAsP/InP DFB lasers and determination of their linewidth enhancement factor", *IEEE J. Quantum Electron.*, **QE-21**, no. 6, pp. 1814-1818, 1985.

[62] Ogita, S., Yano, M., Ishikawa, H. and Imai, H., "Linewidth reduction in DFB laser by detuning effect", *Electron. Lett.*, **23**, pp. 393-394, 1987.

[63] Fujise, M., "Spectral linewidth estimation of a 1.5 μm range InGaAsP/InP distributed feedback laser", *IEEE J. Quantum Electron.*, **QE-22**, no. 3, pp. 458-462, 1986.

[64] Furuya, K., "Dependence of linewidth enhancement factor α on waveguide structure in semiconductor lasers", *Electron. Lett.*, **21**, pp. 200-201, 1985.

[65] Kojima, K., Kyuma, K. and Nakayama, T., "Analysis of spectral linewidth of distributed feedback laser diodes", *J. Lightwave Technol.*, **LT-3**, no. 5, pp. 1048-1055, 1985.

[66] Ujihara, K., "Phase noise in a laser with output coupling", *IEEE J. Quantum Electron.*, **QE-20**, no. 7, pp. 814-818, 1984.

[67] Henry, C.H., "Theory of spontaneous emission noise in open resonator and its application to lasers and optical amplifiers", *J. Lightwave Technol.*, **LT-4**, no. 3, pp. 288-297, 1986.

[68] Wang, J., Schunk, N. and Petermann, K., "Linewidth enhancement factor for DFB lasers due to longitudinal field dependence in the laser cavity", *Electron. Lett.*, **23**, pp. 715-717, 1987.

[69] Kazovsky, L.G., "Coherent optical receivers: performance analysis and laser linewidth requirements", *Opt. Eng.*, **24**, no. 4, pp. 575-579, 1986.

[70] Kikuchi, K., "Effects of $1/f$-type FM noise on semiconductor laser linewidth residual in high-power limit", *IEEE J. Quantum Electron.*, **QE-25**, pp. 312-315, 1989.

[71] Krüger, U. and Petermann, K., "The semiconductor laser linewidth due to the presence of side modes", *IEEE J. Quantum Electron.*, **QE-24**, no. 12, pp. 2355-2358, 1988.

[72] Miller, S.E., "The influence of power level on injection laser linewidth and intensity fluctuations including side-mode contributions", *IEEE J. Quantum Electron.*, **QE-24**, no. 9, pp. 1837-1876, 1988.

[73] Takano, S., Murata, S., Mito, I. and Kobayashi, K., "Threshold gain difference dependence of the spectral linewidth in DFB DC-PBH LD", *Tech. Dig. 1st Optoelectronics Conf.*, pp. 204-205, 1986.

[74] Ketelsen, L.J.P., Hoshino, I. and Ackerman, D.A., "Experimental and theoretical evaluation of the CW suppression of TE side modes in conventional 1.55 μm InP-InGaAsP distributed feedback lasers", *IEEE J. Quantum Electron.*, **QE-27**, no. 4, pp. 965-975, 1991.

2

PRINCIPLES OF DISTRIBUTED FEEDBACK SEMICONDUCTOR LASERS: COUPLED-WAVE THEORY

2.1 INTRODUCTION

The rapid development of both terrestrial and undersea optical fibre communication networks has paved the way for a global communication network. Highly efficient semiconductor injection lasers have played a leading role in facing the challenges of the information era.

This chapter is organised as follows. Before discussing the operating principle of the semiconductor distributed feedback (DFB) laser diode (LD), general concepts with regard to the principles of lasers will first be presented. In section 2.2.1, the general absorption and emission of radiation will be discussed with the help of a simple two-level system. In order that any travelling wave is amplified along a two-level system, the condition of population inversion has to be satisfied; details are presented in section 2.2.2. Owing to the dispersive nature of the material, any amplification has to be accompanied by a finite change in phase. Such dispersive properties of the atomic transition are discussed in section 2.2.3.

In semiconductor lasers, rather than two discrete energy levels, electrons jump between two energy bands which consist of a finite number of energy levels closely packed together. Following the Fermi–Dirac distribution function, the population inversion in semiconductor lasers will be explained in section 2.3.1. Even though the population inversion condition is satisfied, it is still necessary to form an optical resonator within the laser structure. In section 2.3.2 the simplest Fabry–Perot (FP) etalon, which consists of two partially reflecting mirrors facing one another, is investigated. To reduce

the lasing threshold current of the simplest p–n junction, a brief historical development of semiconductor lasers is reviewed in section 2.3.3. The improvement in both the lateral and transverse carrier confinements will be highlighted. In semiconductor lasers, energy comes in the form of an external current injection. It is important to understand how the injection current can affect the gain spectrum. In section 2.3.4, various aspects affect the material gain of the semiconductor are discussed. In particular, the dependence of the carrier concentration on both the material gain and refractive index will be emphasised. On the basis of the Einstein relation for absorption, spontaneous emission and stimulated emission rates, the carrier recombination rate in semiconductors is presented in section 2.3.5.

The FP etalon, characterised by its wide gain spectrum and multimode oscillation, has limited use in the application of coherent optical communication. On the other hand, a single longitudinal mode (SLM) oscillation becomes feasible by introducing a periodic corrugation along the propagation path. The periodic corrugation, which backscatters all waves propagating along one direction, is the working principle of a DFB semiconductor laser. The periodic Bragg waveguide acts as an optical bandpass filter so that only frequency components close to the Bragg frequency will be coherently reinforced. Other frequency terms are effectively cut off as a result of destructive interference. In section 2.4 this physical phenomena is explained in terms of a pair of coupled wave equations. Based on the nature of the coupling coefficient, DFB semiconductor lasers are classified into purely index-coupled, mixed-coupled as well as purely gain- or loss-coupled structures. The periodic corrugations fabricated along the laser cavity play a crucial role since they strongly affect the coupling coefficient and the strength of the optical feedback. In section 2.5 the impact due to the shape of various corrugations will be discussed. Results based on a five-layer separate confinement structure and a general trapezoidal corrugation function are presented. A summary is given at the end of this chapter.

2.2 BASIC PRINCIPLE OF LASERS

2.2.1 Absorption and emission of radiation

From quantum theory, electrons can only exist in discrete energy states such that the absorption or emission of light is caused by the transition of electrons from one energy state to another. The frequency of the absorbed or emitted radiation, f, is related to the energy difference between the higher energy state, E_2, and the lower energy state, E_1, by Planck's equation such that

$$E = E_2 - E_1 = hf \tag{2.2.1}$$

where $h = 6.63 \times 10^{-34}$ J s is Planck's constant. In an atom, the energy state corresponds to the energy level of an electron with respect to the nucleus, which is usually marked as the ground state. Generally, energy states may

represent the energy of excited atoms, molecules (in gas lasers) or carriers like electrons or holes in semiconductors.

To explain the transitions between energy states, modern quantum mechanics should be used. This gives a probabilistic description in which atoms, molecules or carriers at specific energy levels are most likely to be found. Nevertheless, the concept of stable energy states and electron transitions between two energy states is sufficient in most situations.

Photons have always been used to describe the discrete packets of energy released or absorbed by a system when there is an interaction between light and matter. Suppose a photon of energy $(E_2 - E_1)$ is incident upon an atomic system, as shown in Figure 2.1 with two energy levels along the longitudinal z direction. An electron found at the lower energy state E_1 may be excited to a higher energy state E_2 through absorption of the incident photon. This process is called an *induced absorption*. If the two-level system is considered to be a closed system, then the induced absorption process results in a net energy loss. Alternatively, an electron found initially at the higher energy level E_2 may be induced by the incident photon to jump back to the lower energy state. Such a change of energy will cause the release of a single photon at a frequency f according to Planck's equation. This process is called *stimulated emission*. The emitted photon created by stimulated emission has the same frequency as the incident initiator. Moreover, the output light associated with the incident and stimulated photons shares the same phase and polarisation state. In this way, coherent radiation is achieved. Contrary to the absorption process, there is an energy gain for stimulated emissions.

Apart from induced absorption and stimulated emissions, there is another type of transition within the two-level system. An electron may jump from the higher energy state, E_2, to the lower energy state, E_1 without the presence of

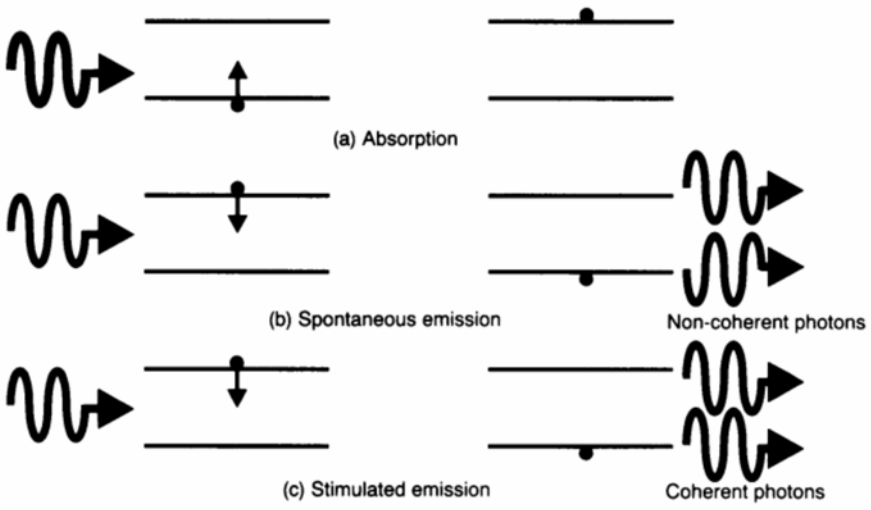

Figure 2.1 Different recombination mechanisms found in a two-energy-level-system.

an incident photon. This type of transition is called a *spontaneous emission*. Just like stimulated emissions, there will be a net energy gain at the system output. However, spontaneous emission is a random process and the output photons show variations in phase and polarisation state. This non-coherent radiation, created by spontaneous emission, is important to the noise characteristics in semiconductor lasers.

2.2.2 The Einstein relations and the concept of population inversion

To create a coherent optical light source, it is necessary to increase the rate of stimulated emission while minimising the rate of absorption and spontaneous emission. By examining the change in field intensity along the longitudinal direction, a necessary condition will be established.

Let N_1 and N_2 be the electron populations found in the lower and higher energy states of the two-level system, respectively. For uniform incident radiation with energy spectral density ρ_f, the total induced upward transition rate R_{12} (the subscript 12 indicates the transition from the lower energy level 1 to the higher energy level 2) can be written as

$$R_{12} = N_1 B_{12} \rho_f = W_{12} N_1 \tag{2.2.2}$$

where B_{12} is the constant of proportionality, known as the Einstein's coefficient of absorption. The product $B_{12}\rho_f$ is commonly known as the induced upward transition rate, W_{12}.

For an excited electron in the higher energy state, it can undergo a downward transition through either spontaneous or stimulated emission. Since the rate of the spontaneous emission is directly proportional to the population N_2, the overall downward transition rate R_{21} becomes

$$\begin{aligned} R_{21} &= A_{21} N_2 + N_2 B_{21} \rho_f \\ &= A_{21} N_2 + W_{21} N_2 \end{aligned} \tag{2.2.3}$$

where the stimulated emission rate is expressed in a similar manner as the rate of absorption. A_{21} is the Einstein coefficient of spontaneous emission and B_{21} is the Einstein coefficient of stimulated emission. The subscript 21 indicates a downward transition from the higher energy state 2 to the lower energy state 1. Correspondingly, $W_{21} = B_{21}\rho_f$ is known as the induced downward transition.

For a system at thermal equilibrium, the total upward transition rate must equal the total downward transition rate, and therefore $R_{12} = R_{21}$, or alternatively

$$N_1 B_{12} \rho_f = A_{21} N_2 + N_2 B_{21} \rho_f \tag{2.2.4}$$

By rearranging the previous equation, it follows that

$$\rho_f = \frac{A_{21}/B_{21}}{\left[\dfrac{B_{12} N_1}{B_{21} N_2} - 1\right]} \tag{2.2.5}$$

At thermal equilibrium, the population distribution in the two-level system is described by the Boltzmann statistics such that

$$\frac{N_2}{N_1} = \mathrm{e}^{-E/kT} \tag{2.2.6}$$

where $k = 1.381 \times 10^{-23}$ J K^{-1} is the Boltzmann constant. Substituting equation (2.2.6) into (2.2.5) gives

$$\rho_\mathrm{f} = \frac{A_{21}/B_{21}}{\left[\dfrac{B_{12}}{B_{21}}\mathrm{e}^{E/kT} - 1\right]} \tag{2.2.7}$$

Since the two-level system is in thermal equilibrium, it is usual to compare the above equations with a blackbody radiation field at temperature T, which is given as [1]

$$\rho_\mathrm{f} = \frac{8\pi n^3 h f^3}{c^3} \frac{1}{\mathrm{e}^{E/kT} - 1} \tag{2.2.8}$$

where n is the refractive index and c is the free space velocity. By equating (2.2.7) with (2.2.8), we can derive the following relations:

$$B_{12} = B_{12} \Rightarrow W_{12} = W_{21} = W \tag{2.2.9}$$

and

$$\frac{A_{21}}{B_{21}} = \frac{8\pi n^3 h f^3}{c^3} \tag{2.2.10}$$

From equation (2.2.7) it is clear that the upward and downward induced transition rates are identical at thermal equilibrium. Then, using equation (2.2.9), the final induced transition rate, W, becomes

$$W = \frac{A_{21} c^3}{8\pi n^3 h f^3} \rho_\mathrm{f} = \frac{A_{21} c^2}{8\pi n^2 h f^3} I \tag{2.2.11}$$

where $I = c\rho_\mathrm{f}/n$ is the intensity (W m^{-2}) of the optical wave.

Since an energy gain is associated with the downward transitions of electrons from a higher energy state to a lower energy state, the net induced downward transition rate of the two-level system becomes $(N_2 - N_1)W$. Therefore, the net power generated per unit volume, V, can be written as

$$\frac{\mathrm{d}P_0}{\mathrm{d}V} = (N_2 - N_1) W \cdot hf \tag{2.2.12}$$

In the absence of a dissipation mechanism, the power change per unit of volume is equivalent to the intensity change per unit of longitudinal length. Substituting equation (2.2.12) into (2.2.11) will generate

$$\frac{\mathrm{d}I}{\mathrm{d}z} = \frac{\mathrm{d}P_0}{\mathrm{d}V} = (N_2 - N_1) \frac{A_{21} c^2}{8\pi n^2 f^2} I(z) \tag{2.2.13}$$

The general solution of the above first-order differential equation is given as

$$I(z) = I_0 e^{\alpha_I(f)z} \tag{2.2.14}$$

where

$$\alpha_I(f) = (N_2 - N_1)\frac{A_{21}c^2}{8\pi n^2 f^2} \tag{2.2.15}$$

In the above equation, $\alpha_I(f)$ is the frequency-dependent intensity gain coefficient. Hence, if $\alpha_I(f)$ is greater than zero, the incident wave will grow exponentially and there will be an amplification. However, recalling the Boltzmann statistics from equation (2.2.6), the electron population N_2 in the higher energy state is always less than N_1 found in the lower energy state at a positive physical temperature. As a result, energy is absorbed at thermal equilibrium for the two-level system. Moreover, according to equations (2.2.8) and (2.2.10), the rate of spontaneous emission (A_{21}) always dominates the rate of stimulated emission ($B_{21}\rho_f$) at thermal equilibrium.

Mathematically, there are two possible ways we can create a stable stream of coherent photons. One method involves a negative temperature, which is physically impossible. The other method is to create a non-equilibrium distribution of electrons so that $N_2 > N_1$. This condition is known as *population inversion*. To fulfil the requirement of the population inversion, it is necessary to excite some electrons to the higher energy state. An external energy source, commonly known as "pumping", is thus required. In a semiconductor injection laser, the external energy source is in the form of an electric current.

2.2.3 Dispersive properties of atomic transitions

Physically, an atom in a dielectric acts like a small oscillating dipole when it is under the influence of an incident oscillating electric field. When the frequency of the incident wave is close to that of the atomic transition, the dipole will oscillate at the same frequency as the incident field. Therefore, the total transmitted field will be the sum of the incident field and the radiated fields from the dipole. However, due to spontaneous emissions, the radiated field may not be in phase with the incident field. As we shall discuss, such a phase difference will alter the propagation constant as well as the amplitude of the incident field. Hence, apart from induced transitions and photonic emissions, dispersive effects should also be considered.

Classically, for a simple two-level system with two discrete energy levels, the problem of dipole moments can be represented by a electron oscillator model [2]. This model is a well-established method and was used long before the advent of quantum mechanics. On the basis of the electron oscillator model, an oscillating dipole in a dielectric is replaced by an electron oscillating in a harmonic potential well.

The effect of dispersion is measured by a change in the relative permittivity with respect to frequency. In the electron oscillator model, any electric

radiation at an angular frequency close to the resonant angular frequency ω_0 is characterised by a frequency-dependent complex electronic susceptibility $\chi(\omega)$ which relates with the polarisation vector $\boldsymbol{P}(\omega)$ such that

$$\boldsymbol{P}(w) = \varepsilon_0 \chi(\omega) \boldsymbol{E} \tag{2.2.16}$$

where

$$\chi(\omega) = \chi'(\omega) - j\chi''(\omega) \tag{2.2.17}$$

in which χ' and χ'' are the real and imaginary components of the electronic susceptibility χ, respectively.

We start by considering a plane electric wave propagating in a medium with a complex permittivity of $\varepsilon'(\omega)$. The wave travelling along the longitudinal z direction can be expressed in phasor form such that

$$E(z) = E_0 e^{j\omega t} e^{-jk'(\omega)z} \tag{2.2.18}$$

where E_0 is the complex amplitude coefficient and $k'(\omega)$, the propagation constant, can be expressed as

$$k'(\omega) = \omega\sqrt{\mu\varepsilon'} \tag{2.2.19}$$

From Maxwell's equations, the complex permittivity of an isotropic medium, ε', is given as

$$\varepsilon'(\omega) = \varepsilon\left(1 + \frac{\varepsilon_0}{\varepsilon}\chi(\omega)\right) \tag{2.2.20}$$

where ε is the relative permittivity of the medium when there is no incident field. χ is the same complex electronic susceptibility mentioned earlier. Using the above equation in (2.2.20) and assuming $(\varepsilon_0/\varepsilon)|\chi| \ll 1$, we obtain

$$k'(\omega) \approx k\left(1 + \frac{\varepsilon_0}{2\varepsilon}\chi(\omega)\right) \tag{2.2.21}$$

where

$$k = \omega\sqrt{\mu\varepsilon} \tag{2.2.22}$$

By expanding $\chi(\omega)$ with equation (2.2.21), the propagation constant k' becomes

$$k'(\omega) \approx k\left(1 + \frac{\chi'(\omega)}{2n^2}\right) - j\left(\frac{k\chi''(\omega)}{2n^2}\right) \tag{2.2.23}$$

where $n = (\varepsilon/\varepsilon_0)^{1/2}$ is the refractive index of the medium at a frequency far from the resonant angular frequency ω_0. Substituting equation (2.2.21) back into (2.2.18), the electric plane wave becomes

$$E(z) = E_0 e^{j\omega t} e^{-j(k+\Delta k)z} e^{(g-\alpha_{\text{int}})z/2} \tag{2.2.24}$$

where α_{int} is introduced to include any internal cavity loss and

$$\Delta k(\omega) = k\frac{\chi'(\omega)}{2n^2} \tag{2.2.25}$$

$$g(\omega) = -k\frac{\chi''(\omega)}{n^2} \tag{2.2.26}$$

In semiconductor lasers it is likely that free carrier absorption and scattering at the heterostructure interface may contribute to the internal losses. In the above equation, Δk corresponds to a shift in the propagation constant, which is frequency dependent. Unless the electric field oscillates at the resonant angular frequency ω_0, there will be a finite phase delay and the new phase velocity of the incident wave will become $\omega/(k + \Delta k)$.

Apart from the phase velocity change, the last exponential term in equation (2.2.24) indicates an amplitude variation with g as the power gain coefficient. When $(g - \alpha_{\text{int}})$ is greater than zero, the electric plane wave will be amplified. Rather than the population inversion condition relating the population density at the two energy levels as in equation (2.2.14), the imaginary part of the electronic susceptibility $\chi''(\omega)$ is used to establish the amplifying condition. Sometimes, the net amplitude gain coefficient, α_{net}, is used to represent the necessary amplifying condition such that

$$\alpha_{\text{net}} = \frac{g - \alpha_{\text{int}}}{2} > 0 \tag{2.2.27}$$

2.3 BASIC PRINCIPLES OF SEMICONDUCTOR LASERS

Before the principles of the semiconductor laser are introduced, some basic concepts of the energy transition between energy states will be discussed. When there is an interaction between light and matter, photons are used to explain discrete packets of energy that may be released or absorbed by the system. Suppose a photon of energy $(E_2 - E_1)$ is incident upon an atomic system with two energy levels, E_1 and E_2 along the longitudinal z direction. An electron at the lower energy state E_1 may be excited to a higher energy state E_2 through the absorption of the incident photon. This process is called *induced absorption*. If the two-level system is considered as a closed system, the induced absorption process results in a net energy loss. Alternatively, an electron found initially at the higher energy level E_2 may be induced by the incident photon to jump back to the lower energy state. Such a change of energy will cause the release of a single photon at a frequency f according to Planck's equation. This process is called *stimulated emission*. The emitted photon created by stimulated emission has the same frequency as the incident initiator. Furthermore, the incident and stimulated photons share the same phase and polarisation state. In this way, coherent radiation is achieved. Contrary to the absorption process, there is an energy gain for stimulated emissions.

Apart from induced absorption and stimulated emissions, an electron may jump from the higher energy state to the lower energy state without the

presence of an incident photon. This type of transition is called a *spontaneous emission* and a net energy gain results at the system output. However, spontaneous emission is a random process and the output photons show variations in phase and polarisation state. This non-coherent radiation created by spontaneous emission is important to noise characteristics in semiconductor lasers.

2.3.1 Population inversion in semiconductor junctions

In gaseous lasers, like CO_2 or He–Ne lasers, an energy transition occurs between two discrete energy levels. In semiconductor lasers these energy levels cluster together to form energy bands. Energy transitions between these bands are separated from one another by an energy barrier known as an *energy gap* (or forbidden gap). With electrons topping up the ground states, the uppermost filled band is called the valence band and the next highest energy band is called the conduction band. The probability of an electronic state at energy E being occupied by an electron is governed by the Fermi–Dirac distribution function, $f(E)$, such that [3]

$$f(E) = 1/\left[e^{(E-E_f)/kT} + 1\right] \tag{2.3.1}$$

where k is the Boltzmann constant, T is the temperature in degrees K and E_f is the Fermi level. The concept of the Fermi level is important in characterising the behaviour of semiconductors. By putting $E = E_f$ in the above equation, the Fermi–Dirac distribution function $f(E_f)$ becomes 1/2. In other words, an energy state at the Fermi level has half the chance of being occupied. The basic properties of an equilibrium p–n junction will not be covered because they can be found in almost any solid state electronics textbook [4]. Only some important characteristics of the p–n junction will be discussed here.

According to Einstein's relationship on the two-level system, the population of electrons in the higher energy state greatly exceeds that of electrons found in the lower energy state before any passing wave can be amplified. Such a condition is known as *population inversion*. At thermal equilibrium, however, this condition cannot be satisfied. To form a population inversion along a semiconductor p–n junction, both the p- and n-type materials must be heavily doped (degenerative doping) so that the doping concentration exceeds the density of states of the band. The doping is so heavy that the Fermi level is forced into the energy band. As a result, the upper part of the valence band of the p-type material (from the Fermi level E_f to the valence band edge E_v) remains empty. Similarly, the lower part of the conduction band is also filled with electrons owing to heavy doping. Figure 2.2(a) shows the energy band diagram for such a heavily doped p–n junction. At thermal equilibrium, any energy transition between the conduction and valence bands is rare.

Using an external energy source, the equilibrium is disturbed. External energy comes in the form of external biasing, which enables more electrons

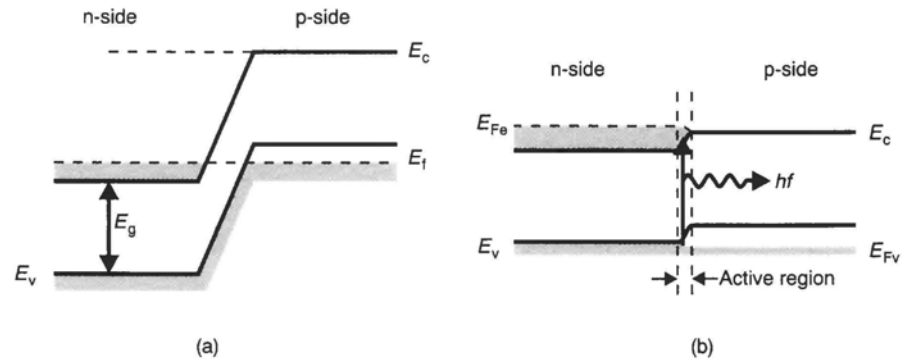

Figure 2.2 Schematic illustration of a degenerate homojunction. (a) Typical energy level diagram at equilibrium with no biasing voltage. (b) The same homojunction under a strong forward bias voltage.

to be pumped into the higher energy state; population inversion is then said to be achieved. When a forward bias voltage close to the bandgap energy is applied across the junction, the depletion layer formed across the p–n junction collapses. As shown in Figure 2.1(b), the quasi-Fermi level in the conduction band, E_{Fc}, and that in the valence band, E_{Fv}, are separated from one another under forward biasing. Quantitatively, E_{Fc} and E_{Fv} could be described in terms of the carrier concentrations such that

$$N = n_i e^{(E_{Fc}-E_i)/kT} \tag{2.3.2}$$

and

$$P = n_i e^{(E_i-E_{Fv})/kT} \tag{2.3.3}$$

where E_i is the intrinsic Fermi level, n_i is the intrinsic carrier concentration, and N and P are the concentration of electrons and holes, respectively. Along the p–n junction, there exists a narrow active region that contains simultaneously the degenerate populations of electrons and holes. Here, population inversion is satisfied and carrier recombination starts to occur.

Since the population distribution in a semiconductor follows the Fermi–Dirac distribution function, the probability of an occupied conduction band at energy E_a can be described by

$$f_c(E_a) = \frac{1}{1 + e^{(E_a-E_{Fc})/kT}} \quad \text{where } E_a > E_{Fc} \tag{2.3.4}$$

Similarly, the probability of an occupied valence band at energy E_b can be written as

$$f_c(E_b) = \frac{1}{1 + e^{(E_b-E_{Fv})/kT}} \quad \text{where } E_b < E_{Fv} \tag{2.3.5}$$

Since any downward transition implies that an electron jumps from the conduction band to the valence band with the release of a single photon, the total downward transition rate, $R_{a\to b}$, is proportional to the probability

that the conduction band is occupied whilst the valence band is vacant. In other words, it can be expressed as

$$R_{a\to b} \propto f_c(E_a)(1 - f_v(E_b)) \tag{2.3.6}$$

Similarly, the total upward transition rate, $R_{b\to a}$ becomes

$$R_{b\to a} \propto f_v(E_b)(1 - f_c(E_a)) \tag{2.3.7}$$

As a result, the net effective downward transition rate becomes

$$\begin{aligned} R_{a\to b}(\text{net}) &= R_{a\to b} - R_{b\to a} \\ &\approx f_c(E_a) - f_v(E_b) \end{aligned} \tag{2.3.8}$$

To satisfy population inversion, the above relationship must remain positive. In other words, it is necessary to have

$$f_c(E_a) > f_v(E_b) \tag{2.3.9}$$

Putting $E_a - E_b = hf$ and using the Fermi–Dirac distribution function, the above equation becomes

$$E_{Fc} - E_{Fv} > hf \tag{2.3.10}$$

which is known as the Bernard–Duraffourg condition [3]. Since the energy of the radiated photon must exceed or equal that of the energy gap, E_g, the final condition for amplification in a semiconductor becomes

$$E_{Fc} - E_{Fv} > hf \geq E_g \tag{2.3.11}$$

From a simple two-level system to the semiconductor p–n junction, a necessary condition for light amplification is established. However, this condition is not sufficient to provide lasing, as we discuss in the next section. To sustain laser oscillation, certain optical feedback mechanisms are necessary.

2.3.2 Principle of the Fabry–Perot etalon

We briefly mentioned the FP laser cavity in Chapter 1. In this section the details of this LD are given. By facing two partially reflected mirrors towards one another, a simple optical resonator is formed. Let L be the separation between the two mirrors. If the spacing between the two mirrors is filled with a medium that possesses gain, a FP etalon is formed. Because an electric field bounces back and forth between the partially reflected mirrors, the wave is amplified as it passes through the laser medium. If the amplification exceeds other cavity losses owing to imperfect reflection from the mirrors or scattering in the laser medium, the field energy inside the cavity will continue to build up. This process will continue until the single pass gain balances the loss. When this occurs, a self-sustained oscillator or a laser

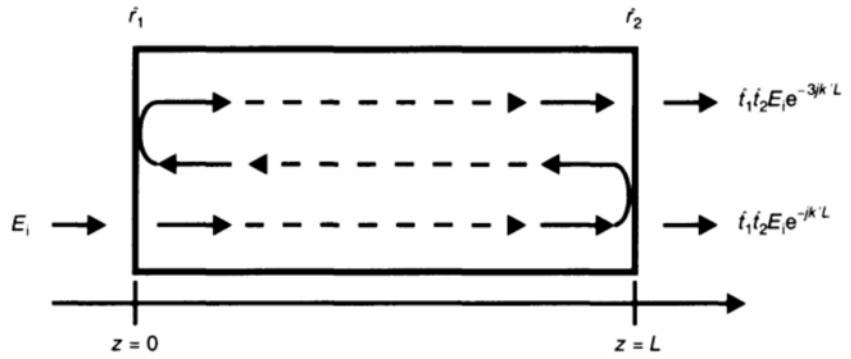

Figure 2.3 A simplified Fabry-Perot cavity.

cavity is formed. Hence, optical feedback is important in building up the internal field energy so that lasing can be achieved. A simplified FP etalon is shown in Figure 2.3.

In Figure 2.3, $\hat{r}_1$ and $\hat{r}_2$ are the amplitude reflection coefficients of the input (left) and output (right) mirrors, respectively. Similarly, $\hat{t}_1$ and $\hat{t}_2$ represent the amplitude transmission coefficients of the mirrors. Suppose an incident wave with complex propagation constant k' enters the etalon from $z = 0$. After a series of parallel reflections, the number of transmitted waves at the output plane ($z = L$) becomes [5]

$$E_0 = E_i\hat{t}_1\hat{t}_2 e^{-jk'L}[1 + \hat{r}_1\hat{r}_2 e^{-2jk'L} + \hat{r}_1^2\hat{r}_2^2 e^{-4jk'L} + \cdots] \tag{2.3.12}$$

Using an infinite sum for a geometric progression (GP) series, the above equation becomes

$$E_0 = \frac{\hat{t}_1\hat{t}_2 e^{-jk'L}}{1 - \hat{r}_1\hat{r}_2 e^{-2jk'L}} E_i \tag{2.3.13}$$

By expanding the propagation constant k' as in equation (2.2.24), equation (2.3.13) can also be expressed as

$$E_0 = E_i \left[\frac{\hat{t}_1\hat{t}_2 e^{-j(k+\Delta k)L} e^{\alpha_{net}L}}{1 - \hat{r}_1\hat{r}_2 e^{-2j(k+\Delta k)L} e^{\alpha_{net}L}} \right] \tag{2.3.14}$$

where α_{net} is the net loss. When $\alpha_{net} > 0$, and the numerator of the above equation becomes very small such that the term in square brackets is larger than unity, amplification will occur.

To obtain the self-sustained oscillation, the denominator of the above equation must be zero, i.e.

$$\hat{r}_1\hat{r}_2 e^{-2jk'L} = 1 \tag{2.3.15}$$

This is the threshold condition of a FP laser as the ratio E_o/E_i becomes infinite. Physically, this corresponds to a finite transmitted wave at the output

with a zero incident wave. With the amplitude and the phase term separated, we obtain

$$\hat{r}_1\hat{r}_2 e^{\alpha_{net}L} = 1 \tag{2.3.16}$$

and

$$2(k + \Delta k)L = 2m\pi \tag{2.3.17}$$

Equation (2.3.16) represents a case in which a wave making a round trip inside the resonator will return with the same amplitude at the same plane. Similarly, the phase change after a roundtrip must be an integer of 2π to maintain a constructive phase interference. By rearranging equations (2.3.16) and (2.2.24), the threshold gain of the FP laser becomes

$$\alpha_{th} = \alpha_0 + \frac{2}{L}\ln\left(\frac{1}{\hat{r}_1\hat{r}_2}\right) \text{ with } g = \alpha_{th} \tag{2.3.18}$$

where

$$\alpha_m = \frac{1}{L}\ln\left(\frac{1}{\hat{r}_1\hat{r}_2}\right) \tag{2.3.19}$$

is the amplitude mirror loss which accounts for the radiation escaping from the FP cavity owing to finite facet reflections. Hence, the threshold gains of FP semiconductor lasers can be determined once the physical structures are known.

From equation (2.3.17), we can determine the lasing frequency. Owing to the dispersive properties, as shown in section 2.2, the frequency-dependent propagation constant $(k + \Delta k)$ is replaced by a group refractive index, n_g, such that

$$\text{Re}(k') = k_0 n_g = k_0 c/v_g \tag{2.3.20}$$

where k_0 is the free space propagation constant. Replacing k_0 with $2\pi f/c$ and rearranging equation (2.3.17), the cavity-resonance frequency f_m becomes

$$f_m = mc/2n_g L \tag{2.3.21}$$

where m is an arbitrary integer. When m increases, it can be seen that there is an infinite number of longitudinal modes. In practice, however, the number of longitudinal modes depends on the width of the material gain spectrum. From the equation shown above, it is also confirmed that the longitudinal mode spacing is the one shown in equation (1.3.25) in Chapter 1. The gain value of all probable modes increases with pumping until the threshold condition is finally attained. The mode with the minimum threshold gain becomes the lasing mode whilst others become non-lasing side modes. After the threshold condition is reached, the laser gain spectrum does not stay at a fixed value like gaseous lasers. Instead, the lasing gain spectrum keeps changing with the biasing current. Such an inhomogeneous broadening effect becomes so complicated that multimode oscillation and mode hopping become common in FP semiconductor lasers.

The lasing spectrum and the spectral properties of the FP laser cavity are important in the field of semiconductor lasers, because other semiconductor lasers resemble its basic design. Simplicity may be an advantage for FP lasers. However, owing to the broad and unstable spectral characteristics, it has limited application in coherent optical communication systems in which a single longitudinal mode is a requirement.

2.3.3 Structural improvements in semiconductor lasers

In section 2.3.1 population inversion in a heavily-doped p–n junction (or diode) was discussed. The so-called homojunction is characterised by having a single type of material found across the p–n junction. When a forward bias voltage is applied across the junction, the contact potential between the p and n junction is lowered. With the energy gap remaining constant throughout the junction, the majority of carriers tend to diffuse easily across the junction. As a result, carrier recombination along the p–n junction becomes less efficient. A typical current density required to achieve lasing in this early diode is of the order of 10^5 A/cm^2 [6]. With such a high current density, continuous wave (CW) operation at room temperature is impossible. Pulse mode operation is allowed at extremely low temperatures only. With such a low efficiency and high threshold current, the homojunction structure was later replaced by more effective structures.

Improvements in transverse carrier confinement

In 1963, it was discovered that the threshold current of semiconductor lasers could be reduced significantly if carriers were confined along the active region. A three-layer structure, which consisted of a thin layer of lower energy gap material sandwiched between two layers of higher energy gap materials, was proposed. However, it was not until 1969 that the liquid phase epitaxy (LPE) growth of AlGaAs on a GaAs homojunction became available. Since two different materials were involved, an additional energy barrier was formed alongside the homogeneous p–n junction. As a result, the chance of carrier diffusion was reduced. The name single heterostructure was given [3] and is shown in Figure 2.4(a). Apart from the difference in energy gaps, the p-GaAs active layer has a higher refractive index than the n-region. Moreover, with the p-AlGaAs cladding having a considerably lower refractive index, an asymmetric three-layer waveguide was formed within the single heterostructure and the highest refractive index was found along the active region. The asymmetric waveguide confined the optical intensity largely to the active region and so the optical loss due to evanescent mode propagation was reduced. However, the best room temperature threshold current density for a single heterostructure device is still too high for CW operation (typical value of 8.6 kA/cm^2). Nevertheless, it is a great improvement on the homostructure.

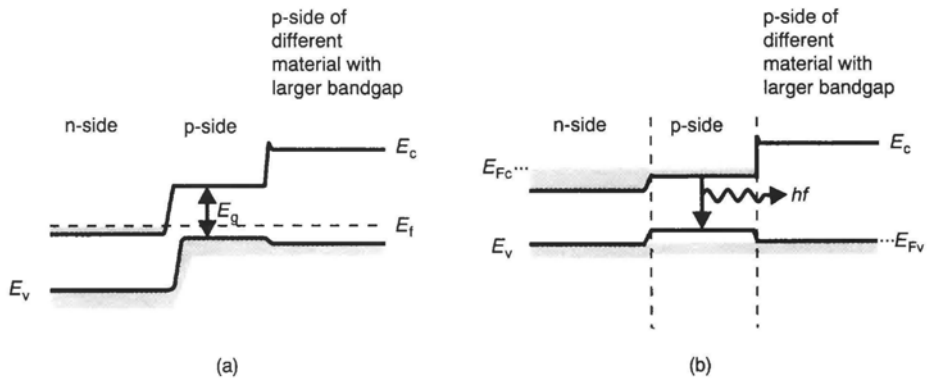

Figure 2.4 Schematic illustration of a single heterojunction [4]. (a) Typical energy level diagram at equilibrium with no biasing voltage. (b) The same heterojunction under a strong forward bias voltage.

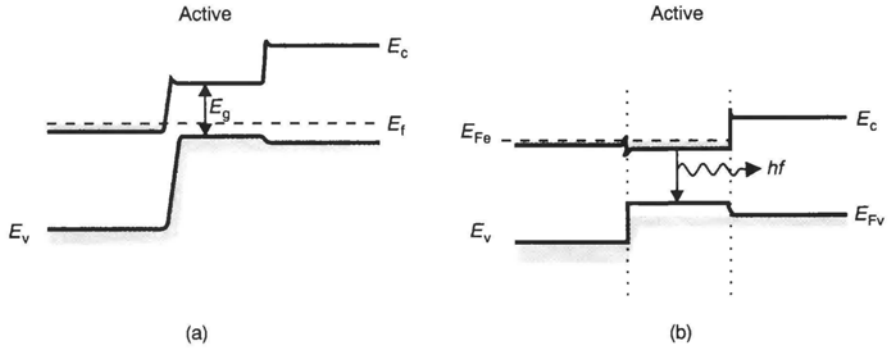

Figure 2.5 Schematic illustration of a double heterojunction [4]. (a) Typical energy level diagram at equilibrium with no bias voltage. (b) Under a strong bias voltage.

The establishment of CW operation at room temperature was finally achieved in the 1970s. As shown in Figure 2.5, the thin active layer is now sandwiched between two layers of a higher energy gap material, and hence a double heterostructure is formed. Along the boundary where two different materials are used, an energy barrier is formed. Carriers find it so difficult to diffuse across the active region that they are trapped. By using a higher refractive index material at the centre, photons are also confined in a similar way. This type of structure is known as the separate confinement heterostructure (SCH). The combined effects of carrier and optical confinement help to bring the threshold current density down to approximately 1.6 kA/cm^2. Operation at CW becomes feasible provided that the laser itself is mounted on a suitable heat sink.

Improvements in lateral carrier confinement

Continuous wave operation at room temperature was a significant achievement and currently the double heterostructure design is more or less standard. So

far, the structures we have discussed belong to the broad-strip laser family since they do not incorporate any mechanism for the lateral (parallel to the junction plane) confinement of the injected current or the optical mode. By adopting a strip geometry, carriers are injected over a narrow central region using a strip contact. With carrier recombination restricted to the narrow strip (a typical width ranging from 1 μm to 10 μm), the threshold current is reduced significantly. Such lasers are also referred to as gain-guided because it is the lateral variation of the optical gain that confines the optical mode to the strip vicinity. On the other hand, lasers in which the optical modes are confined because of lateral variations of refractive index are known as index-guided lasers.

Comparatively, gain-guided lasers are simple to make, but their weak optical confinement limits the beam quality [5]. Moreover, it is difficult to obtain a stable output in an SLM. As a result, the index-guiding mechanism has become the main stream in semiconductor laser development and a large number of index-guided structures have been proposed in the past decade. Basically, a lateral variation of refractive indices is used to confine the optical energy. Various index-guided structures like the buried heterostructure (BH), channelled substrate planar (CSP), buried crescent (BC), ridge waveguide (RW) and dual-channel planar buried heterostructure (DCPBH) have been used. A survey of recent research revealed many other types of lasers, but basically they are alternatives of these basic structural designs. The structural improvement in the development of semiconductor lasers reduces the threshold current density whilst CW single transverse mode operation becomes feasible.

2.3.4 Material gain in semiconductor lasers

Suppose a medium with a complex permittivity ε' is used to build an infinitely long waveguide and an input signal is injected into it. After travelling a distance L, the power gain of the signal can be defined by an amplifying term, G, such that

$$G = \mathrm{e}^{(g-\alpha_{\mathrm{loss}})L} \tag{2.3.22}$$

where g is the material gain (or the power gain coefficient) and α_{loss} is the internal cavity loss. It is important that $(g - \alpha_{\mathrm{loss}}) > 0$ for an amplified signal.

In an index-guided semiconductor laser, the refractive index of the active region (n_1) is higher than the surrounding cladding (n_2) so that a dielectric waveguide is formed. In practice, however, the dielectric waveguide formed is far from ideal. Under the weakly guiding condition where $(n_1 - n_2) \ll n_1$, some energy leaks out into the cladding as a result of the evanescent field. To take into account the power leakage, a weighting factor Γ is introduced in equation (2.3.22) such that

$$G = \mathrm{e}^{[\Gamma(g-\alpha_{\mathrm{a}})-(1-\Gamma)\alpha_{\mathrm{c}}+\alpha_{\mathrm{sca}}]L} \tag{2.3.23}$$

where α_a and α_c are the absorption losses of the active and cladding layers, respectively, and α_{sca} is the scattering loss at the heterostructure interface. The weighting factor Γ, known as the optical confinement factor, defines the ratio of the optical power confined in the active region to the total optical power flowing across the structure.

To determine the optical gain, various approaches have been used. In this section a phenomenological approach [6] will be introduced whilst another approach using Einstein's coefficients [7] will be discussed in the next section. The phenomenological approach is based on experimental observations that the peak material gain varies almost linearly with the injected carrier concentration. Such an observation leads to a linear approximation of [8]:

$$g_{peak} = A_0(N - N_0) \tag{2.3.24}$$

where A_0 is the differential gain and N_0 is the carrier concentration at zero material gain, and is commonly known as the transparency carrier concentration. The above relation gives only a reasonable approximation in a small biasing range when the carrier concentration is comparable with the transparency carrier concentration. The range of accuracy is extended by adopting a parabolic model such that [9]

$$g_{peak} = aN^2 + bN + c \tag{2.3.25}$$

where a, b and c are constants determined by fitting the available exact solutions using the least-squares technique.

Owing to the dispersive properties of the semiconductor, the actual material gain is also affected by the optical frequency f, and hence the wavelength λ. So far, the gain value is assumed to be at the resonant frequency. However, if the optical frequency is tuned away from the resonant peak, the exact value of the gain becomes different from that of g_{peak}.

On the basis of experimental observation, Westbrook [10] extended the linear peak gain model further so that

$$g(N, \lambda) = A_0(N - N_0) - A_1[\lambda - (\lambda_0 - A_2(N - N_0))]^2 \tag{2.3.26}$$

where λ_0 is the wavelength of the peak gain at transparency gain (i.e. $g = 0$) and A_1 governs the base width of the gain spectrum. The wavelength shifting coefficient A_2 takes into account the change in the peak wavelength with respect to the carrier concentration. Notice that the negative sign in front of A_2 indicates a negative wavelength shift in the peak gain wavelength.

In semiconductor lasers, energy enters in the form of an external biasing current. To determine the material gain, we must determine the relationship between the carrier concentration N and the injection current I. This is accomplished through the carrier rate equation, which includes the generation and decay carriers found in the active region. In its general form, the equation is given as [4,11]

$$\frac{\partial N}{\partial t} = \frac{I}{qV} - R(N) - \frac{v_g g(N, \lambda)S}{1 + \varepsilon S} + D(\nabla^2 N) \tag{2.3.27}$$

where q is the electronic charge and $V = dwL$ is the volume of the active layer, with d, w and L being the thickness, the width and the length of the active layer, respectively. I is the injection current, $R(N)$ is the total (i.e. both radiative and non-radiative) carrier recombination process, and the term $v_g g(N, \lambda)S/(1 + \varepsilon S)$, as shown in the above equation, takes into account the carrier loss as a result of stimulated emission. Here, v_g is the group velocity and S is the photon density of the lasing mode. The effect of photon non-linearity is included in the non-linear coefficient ε. In the above equation, the final term, $D(\nabla^2 N)$, represents the carrier diffusion with D representing the diffusion coefficient.

In $R(N)$, shown in the above equation, the non-radiative carrier recombination implies those processes will not generate any photons. For semiconductor lasers operating at a shorter wavelength ($\lambda < 1$ μm), the effects of non-radiative recombination are small. However, non-radiative recombination becomes more important in long-wavelength semiconductor lasers. In quaternary InGaAsP materials operating in the 1.30 μm and 1.55 μm regions, the total carrier recombination rate can be written as

$$R(N) = \frac{N}{\tau} + BN^2 + CN^3 \tag{2.3.28}$$

where τ is the linear recombination lifetime, B is radiative spontaneous emission coefficient and C is the Auger recombination coefficient. The linear recombination lifetime τ includes recombination at defects or surface recombination at the laser facet. With improvements in fabrication techniques, the number of defects and the chances of surface recombination have been reduced significantly. In long-wavelength semiconductor lasers, the cubic term CN^3 takes into account the non-radiative Auger recombination process. Owing to the Coulomb interaction between carriers of the same energy band, each Auger recombination involves four carriers. According to the origins of these carriers, the Auger recombination is classified into band-to-band, photon-assisted and the trap-assisted processes. Details of different types of Auger processes are clearly beyond the scope of the present investigation, though the interested reader may refer to reference [4]. Some typical values of τ, B and C for the quaternary III–V materials at 1.30 μm and 1.55 μm are listed in Table 2.1. On the basis of the simplified carrier rate equation, all these parameters can be measured in a simple way, as explained in a recent paper by Chu and Ghafouri-Shiraz [12].

In an index-guided semiconductor laser where the active layer width and thickness are small compared with the carrier diffusion length of 1–3 μm, the diffusion effect becomes of secondary importance and can be neglected hereafter. At the lasing threshold, the semiconductor laser begins to lase. With $\partial N/\partial t = 0$, the steady-state solution of the carrier rate equation becomes

$$I_{th} = qVR(N_{th})/\eta_i \tag{2.3.29}$$

Table 2.1 Coefficients for the total recombination of quaternary materials at 1.3 μm and 1.55 μm (after reference [4])

$In_{1-x}Ga_xAs_yP_{1-y}$ at $\lambda = 1.30$ μm with $y = 0.61, x = 0.28$ at $T = 300$ K
$\tau = 10.0$ ns
$B = 1.2 \times 10^{-10}$ cm^3/s
$C = 1.5 \times 10^{-9}$ cm^6 s
$In_{1-x}Ga_xAs_yP_{1-y}$ at $\lambda = 1.55$ μm with $y = 0.90, x = 0.42$ at $T = 300$ K
$\tau = 4$ ns
$B = 1.0 \times 10^{-10}$ cm^3/s
$C = 3.0 \times 10^{-29}$ cm^6/s

where I_{th} is the threshold current and N_{th} is the threshold carrier density. The internal quantum efficiency, η_i, gives the ratio of the radiative recombination to the total carrier recombination. In deriving the above equation, S is assumed to be zero at the lasing threshold condition. Sometimes, rather than the threshold current, a nominal threshold current density J_{th} (in A/m^2) is used which relates to the threshold current I_{th} as

$$I_{th}d/V = J_{th} \tag{2.3.30}$$

In semiconductors, any change in the material gain is accompanied by a change in the refractive index as a result of the Kramer–Kroenig relationship [1]. Any change in the carrier density will induce changes in the refractive index [13,14] as

$$n(N) = n_{ini} + \Gamma \frac{dn}{dN} N \tag{2.3.31}$$

where n_{ini} is the refractive index of the semiconductor when no current is injected dn/dN and is the differential index of the semiconductor. It should be noted that the value of dn/dN is usually negative. The refractive index becomes smaller as the injection current increases. As we discuss in a later chapter, any variation in the carrier density will affect the spectral behaviour of the laser because the lasing wavelength is very sensitive to any variation in the refractive index.

Both the Fermi–Dirac distribution and the material gain are found to be sensitive to temperature change. In practice, the operating temperature of the semiconductor lasers is usually stabilised by a temperature control unit. Moreover, it is also known that a change in optical gain due to a variation in the injected carrier is more significant than that due to temperature [15]. As a result, the temperature dependence of the material gain has been neglected in the analysis.

2.3.5 Total radiative recombination rate in semiconductors

The theory for all classes of laser can also be represented by the Einstein relation for absorption, spontaneous emission and stimulated emission rates.

In semiconductors, optical transitions are between energy bands, whilst other laser transitions are between discrete energy levels. Nevertheless, the Einstein relations are still applicable. The major differences between various material systems are contained in the Einstein coefficient (or transition probabilities) which can only be determined by quantum mechanics. Transitions between any pair of discrete energy levels are separated by hf (or E_{21}). The gain coefficient $g(E_{21})$ and emission rates $r_{\text{spon}}(E_{21})$ and $r_{\text{stim}}(E_{21})$ are related to one another by [3,7]

$$g(E_{21}) = \frac{h^3c^2}{8\pi n_g^2 E_{21}^2} r_{\text{stim}}(E_{21}) \tag{2.3.32}$$

$$r_{\text{spon}}(E_{21}) = \frac{8\pi n_g^2 E_{21}^2}{h^3c^2} g_{21}(E_{21}) \frac{f_c(E_2)[1 - f_v(E_1)]}{f_c(E_2) - f_v(E_1)} \tag{2.3.33}$$

and

$$r_{\text{stim}}(E_{21}) = \left(1 - \frac{1}{kT} e^{[E_{21} - (E_{Fc} - E_{Fv})]}\right) r_{\text{spon}}(E_{21}) \tag{2.3.34}$$

where h is the Planck constant, k is the Boltzmann constant, c is the free space velocity, n_g is the group refractive index, and $f_c(E_2)$ and $f_v(E_1)$ are the occupation probabilities of electrons in the conduction and valence bands, respectively. E_{Fc} and E_{Fv} are the quasi-Fermi levels. It should be noted that the unit of the gain coefficient is cm^{-1} whilst the units of the emission rate r_{spon} and r_{stim} are in number of photons per unit volume per second per energy interval.

Equations (2.3.32) to (2.3.34) demonstrate how $g(E_{21})$, $r_{\text{spon}}(E_{21})$ and $r_{\text{stim}}(E_{21})$ are related to one another. To evaluate these expressions, one parameter, such as the spontaneous emission rate, $r_{\text{spon}}(E_{21})$, must be obtained experimentally. Alternatively, they are all related to the Einstein coefficients such that

$$g(E_{21}) = B_{21}[f_c(E_2) - f_v(E_1)]n_g/c \tag{2.3.35}$$

$$r_{\text{spon}}(E_{21}) = A_{21} f_c(E_2)[1 - f_v(E_1)] \tag{2.3.36}$$

$$r_{\text{stim}}(E_{21}) = A_{21}[f_c(E_1) - f_v(E_1)] \tag{2.3.37}$$

with

$$A_{21} = B_{21} \frac{8\pi n_g^3 E_{21}^2}{h^3c^3} \tag{2.3.38}$$

at thermal equilibrium. With a known doping concentration, the unknown parameters g, r_{spon} and r_{stim} in equations (2.3.35) to (2.3.37) can then be fixed after determining either A_{21} or B_{21}.

Without any preference, B_{21} is chosen to be the key parameter. As expected, the coefficient B_{21} takes into account the interaction between electrons and holes in the presence of electromagnetic radiation. To understand the interaction between them, quantum mechanics should be used.

Rather than going through the lengthy analysis, some important results will be shown. Starting with the time-dependent Schrödinger equation, the coefficient B_{21} is given as [3]

$$B_{21} = \frac{q^2 h}{2m_0^2 \varepsilon_0 n_g^2 E_{21}} |\mathbf{M}_{21}| \tag{2.3.39}$$

so that

$$A_{21} = \frac{4\pi n_g q E_{21}}{m_0^2 \varepsilon_0 h^2 c^3} |\mathbf{M}_{21}| \tag{2.3.40}$$

where ε_0 is the free space permittivity, q is the electronic charge, m_0 is the mass of an electron and $\mathbf{M}_{21}$ is the momentum matrix element between the initial (subscript 2) and final (subscript 1) electron state.

With the actual transition involving various energy states between the conduction band and the valence band of the semiconductor, the analysis will not be complete without the inclusion of density of state functions. It is necessary to determine the momentum matrix element as well as the density of states.

The density of state function is not difficult for the parabolic band model. From Yariv [1], it is clear that the density of states in the conduction band is

$$\rho_c(E - E_c) = 4\pi \cdot \left(\frac{2m_n}{h^2}\right)^{3/2} (E - E_c)^{1/2} \tag{2.3.41}$$

where E_c is the conduction band edge and m_n is the effective electron mass. Similarly, the density of states in the valence band can be written as

$$\rho_v(E_v - E) = 4\pi \cdot \left(\frac{2m_p}{h^2}\right)^{3/2} (E_v - E)^{1/2} \tag{2.3.42}$$

where E_v is the valence band edge and m_p is the effective mass of the hole.

The momentum matrix element may be determined empirically from the wave function. For the localised state, the wave function of the band is modified by a slowly varying envelope function which represents the influence of impurities. As a result, the momentum matrix becomes

$$\mathbf{M}_{21} = \mathbf{M} = \mathbf{M}_b \cdot \mathbf{M}_{env} \tag{2.3.43}$$

where $\mathbf{M}_b$ is the average matrix element of the Bloch state for an intrinsic situation and $\mathbf{M}_{env}$ represents the slowly varying envelope function with impurities present. For III–V quaternary semiconductors, $\mathbf{M}_b$ can be expressed as

$$|\mathbf{M}_b|^2 = \frac{m_0^2 E_g (E_g + \Delta)}{12 m_n (E_g + 2/(3\Delta))} \tag{2.3.44}$$

where $E_g = E_c - E_v$ is the energy gap, and Δ is the spin-orbit splitting.

For transition under the k-selection rule, the wave vector difference between the valence and conduction bands must be equal to that of the emitted

photon. In other words, momentum is conserved and the momentum matrix element is given as [3]

$$|\mathbf{M}|^2 \approx \frac{m_0^2 E_g(E_g + \Delta)}{12 m_n (E_g + 2/(3\Delta))} \cdot \frac{(2\pi)^3}{V} \tag{2.3.45}$$

where $(2\pi)^3/V$ is the unit volume in k-space.

However, when the semiconductor is biased with a high injection current, or it is heavily doped, the density of states will be modified. The randomly distributed impurities (from current injection or heavy doping) tend to create an additional continuum of states near the band edge, which is known as the band-tail state. Since momentum will no longer be conserved, one needs to use the relaxed k-selection rule so that the band-tailing effect can be included. Neglecting the band-tailing effect first but including the density of states, the spontaneous emission rate r_{spon} at photon energy E_{21} can be written as

$$r_{spon}(E_{21}) = A_{21} \int_{-\infty}^{\infty} \rho_c(E - E_c) f_c(E) \cdot \rho_v(E_v - E)[1 - f_v(E)]\, dE \tag{2.3.46}$$

The integral shown above takes into account various states in the conduction band and the valence band, which are separated by the photon energy E_{21}. With such a clumsy notation, it is common to shift the valence band edge, E_v, by the photon energy, E_{21}. In this way, E' becomes the energy variable. At the conduction band edge, E' becomes 0 and so we can define $E'' = E' - E_{21}$. As a result, $\rho_c(E - E_c)$ becomes $\rho_c(E')$, while $\rho_v(E_v - E)$ is shifted to become $\rho_v(E'')$. By substituting A_{21} into the above equation, the spontaneous emission becomes

$$r_{spon}(E_{21}) = \frac{4\pi n_g q^2 E_{21}}{m_0^2 \varepsilon_0 h^2 c^3} \int_{-\infty}^{\infty} \rho_c(E') f(E') \cdot \rho_v(E'')[1 - f(E'')]|\mathbf{M}|^2\, dE' \tag{2.3.47}$$

Under the relaxed k-selection rule, the momentum matrix $\mathbf{M}$ can be considered as energy independent and so it is taken out of the integration. What remains in the integration is the density of holes (P) and electrons (N). Therefore, equation (2.3.47) is simplified to give

$$r_{spon}(E_{21}) = \frac{4\pi n_g q^2 E_{21}}{m_0^2 \varepsilon_0 h^2 c^3} |\mathbf{M}|^2 PN \tag{2.3.48}$$

Within a narrow range of photon energy, $E_{21} \approx E_0$ is fairly constant. As a result, the total spontaneous emission rate (R_{sp}) can be written as

$$\begin{aligned} R_{sp} &\equiv \int r_{spon}(E)\, dE \\ &= \frac{4\pi n_g q^2 E_0}{m^2 \varepsilon_0 h^2 c^3} |\mathbf{M}|^2 PN \\ &= B \cdot NP \end{aligned} \tag{2.3.49}$$

Here, B is commonly known as the radiative recombination coefficient. In most cases the density of electrons and holes are the same and hence equation (2.3.49) can be written as

$$R_{sp} = BN^2 \tag{2.3.50}$$

2.4 COUPLED-WAVE EQUATIONS IN DISTRIBUTED FEEDBACK (DFB) SEMICONDUCTOR LASER DIODES

To understand the operational characteristics of a DFB semiconductor laser, it is necessary to consider wave propagation in periodic structures. Grating or corrugation-induced dielectric perturbation leads to coupling between the forward and backward propagating waves. Historically, various approaches like coupled-wave theory [16,17] and Bloch wave analysis [18] have been adopted. Although these methods were proven to be equivalent [19], researchers have been keen on the coupled-wave theory because of its ease of understanding, and numerical algorithms could be implemented to solve the equations [20].

In a homogeneous, source-free and lossless medium, any time harmonic electric field must satisfy the vector wave equation [21]

$$\nabla^2 \boldsymbol{E} + k_0^2 n^2 \boldsymbol{E} = 0 \tag{2.4.1}$$

where the time dependence of the electric field is assumed to be $e^{j\omega t}$, n is the refractive index and k_0 is the free space propagation constant.

In a semiconductor laser which has a transversely and laterally confined structure, the electric field must satisfy the one-dimensional homogeneous wave equation such that

$$\left[\frac{d^2}{dz^2} + k^2(z)\right] E(z) = 0 \tag{2.4.2}$$

We consider a multi-dielectric stack in which periodic corrugations are formed along one boundary, as illustrated in Figure 2.6.

The material complex permittivity in each layer is denoted ε_j, while g and Λ are the height and the period of corrugation, respectively. With corrugations extending along the longitudinal direction, the wave propagation constant, $k(z)$, can be written as

$$k^2(z) = \omega^2 \mu \varepsilon' \tag{2.4.3}$$

where ω is the angular frequency and ε' is the complex permittivity. When the radiation frequency is sufficiently close to the resonance frequency, equation (2.4.3) becomes [1]

$$k^2 = k_0^2 n^2(z) \left(1 + j\frac{2\alpha(z)}{k_0 n(z)}\right) \tag{2.4.4}$$

where $n(z)$ and $\alpha(z)$ are the refractive index and the amplitude gain coefficient, respectively. Within the grating region ($d_x \leq x \leq d_x + g$), a perturbation is

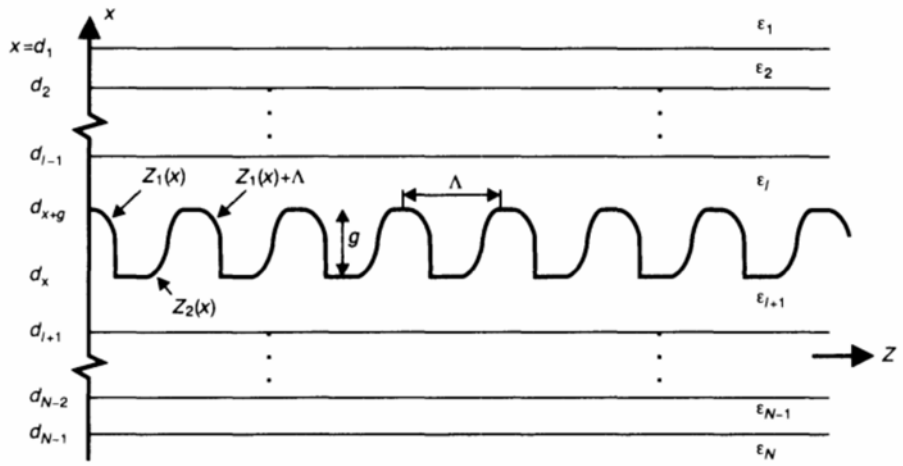

Figure 2.6 General multi-dielectric layers used to show the perturbation of the refractive index and amplitude gain. $Z_1(x)$ and $Z_2(x)$ are two corrugation functions.

introduced so that the refractive index and the amplitude gain coefficient become [16,20]

$$n(z) = n_0 + \Delta n \cos(2\beta_0 z + \Omega) \tag{2.4.5a}$$

and

$$\alpha(z) = \alpha_0 + \Delta\alpha \cos(2\beta_0 z + \Omega + \theta) \tag{2.4.5b}$$

Here, n_0 and α_0 are the steady-state values of the refractive index and amplitude gain, respectively, Δn and $\Delta\alpha$ are the amplitude modulation terms, Ω is the non-zero residue phase at the z-axis origin and β_0 is the propagation constant. In the above equation, θ takes into account the relative phase difference between perturbations of the refractive index and the amplitude gain.

Suppose there is an incident plane wave entering the periodic, lossless waveguide at an angle Φ, as shown in Figure 2.7. The propagation constant of the wave is assumed to be β_0. At every periodic interval Λ, the incident wave will experience the same degree of refractive index change so that the incident wave will be reflected in the same direction. For a waveguide that consists of N periodic corrugations, there will be N reflected wavelets. In order that any two reflected wavelets add up in phase or interfere constructively, the phase difference between the reflected wavelets must be an integer of 2π. In other words,

$$\beta_0(AB + BC) = \beta_0(2\Lambda \sin\Phi) = 2m\pi \tag{2.4.6}$$

where m is an integer. If the incident wave now approaches more or less at a right angle to the wavefront (i.e. $\Phi \approx \pi/2$), equation (2.4.6) becomes

$$2\beta_0\Lambda = 2m\pi \tag{2.4.7}$$

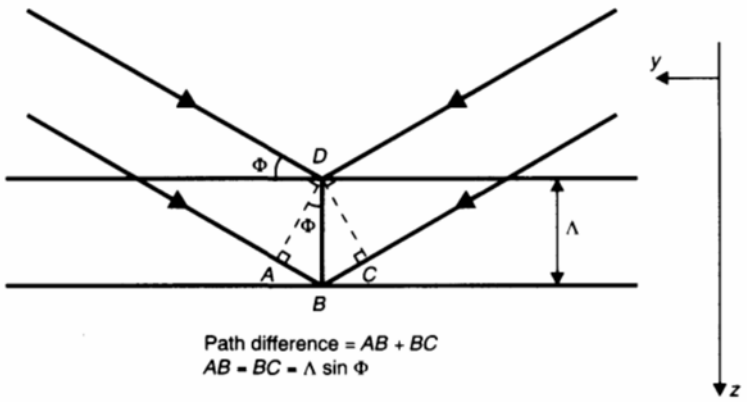

Figure 2.7 The simple model used to explain Bragg conditions in a periodic waveguide.

This is known as the Bragg condition and β_0 becomes the Bragg propagation constant. The integer m shown in the above equation defines the order of the Bragg diffraction. Unless otherwise stated, first-order Bragg resonance ($m = 1$) is assumed. Since a laser forms a self-sustained resonant cavity, the Bragg condition must be satisfied [16]. Rearranging equation (2.4.7) gives

$$\beta_0 \equiv \frac{2\pi n_0}{\lambda_B} \equiv \frac{n_0 \omega_B}{c} = \frac{\pi}{\Lambda} \tag{2.4.8}$$

where λ_B and ω_B are the Bragg wavelength and the Bragg frequency, respectively. From equation (2.4.8), it is clear that the Bragg propagation constant is related to the period of the physical grating, Λ . By altering the grating period Λ, the Bragg wavelength can be shifted according to the specific application.

Using the small signal analysis, the perturbations of the refractive index and gain are always smaller than their average values, i.e.

$$\Delta n \ll n_0, \qquad \Delta\alpha \ll \alpha_0 \tag{2.4.9}$$

Using the above assumption and substituting equation (2.4.5) into (2.4.4), will generate

$$\begin{aligned} k^2(z) = k_0^2 n_0^2 + j2k_0 n_0 \alpha_0 + 2k_0[k_0 n_0 + j\alpha_0]\Delta n \cos(2\beta_0 z + \Omega) \\ + 2jk_0 n_0 \Delta\alpha \cos(2\beta_0 z + \Omega + \theta) \end{aligned} \tag{2.4.10}$$

With $k_0 n_0$ replaced by β and $\alpha_0 < \beta$, the above equation becomes

$$\begin{aligned} k^2(z) \approx \beta^2 + 2j\beta\alpha_0 + 2\beta\left[\frac{\pi\Delta n}{\lambda} + j\frac{\Delta\alpha}{2}e^{j\theta}\right]e^{j(2\beta_0 z+\Omega)} \\ + 2\beta\left[\frac{\pi\Delta n}{\lambda} + j\frac{\Delta\alpha}{2}e^{-j\theta}\right]e^{-j(2\beta_0 z+\Omega)} \end{aligned} \tag{2.4.11}$$

For the case when $\theta = 0$, we can simplify equation (2.4.10) to [20]

$$k^2 \approx \beta^2 + 2j\beta\alpha_0 + 4\beta\left[\frac{\pi\Delta n}{\lambda} + j\frac{\Delta\alpha}{2}\right]\cos(2\beta_0 z + \Omega) \tag{2.4.12}$$

By collecting all the perturbed terms, we can define a parameter κ such that [16,22,23]

$$\kappa = \frac{\pi\Delta n}{\lambda} + j\frac{\Delta\alpha}{2} = \kappa_i + j\kappa_g \tag{2.4.13}$$

Here κ_i includes all contributions from the refractive index perturbation whilst κ_g covers all contributions from the gain perturbation. The parameter κ introduced in the above equation is known as the coupling coefficient. After a series of simplifications, equation (2.4.12) becomes

$$k^2 \approx \beta^2 + 2j\beta\alpha_0 + 4\kappa\beta\cos(2\beta_0 z + \Omega) \tag{2.4.14}$$

On substituting the above equation back into the wave equation, we end up with

$$\frac{d^2E}{dz^2} + \{\beta^2 + 2j\beta\alpha_0 + 2\kappa\beta e^{j(2\beta_0 z+\Omega)} + 2\kappa\beta e^{-j(2\beta_0 z+\Omega)}\}E = 0 \tag{2.4.15}$$

where the cosine function shown in equation (2.4.14) has been expressed in phasor form. A trial solution of the scalar wave equation could be a linear superimposition of two opposing travelling waves such that

$$E(z) = A(z)e^{-jk_{un}z} + B(z)e^{jk_{un}z} \tag{2.4.16}$$

with

$$\begin{aligned} k_{un}^2 &= \beta^2 + 2j\beta\alpha_0 \\ &\approx (\beta + j\alpha_0)^2 \quad (\because\ \alpha_0 \ll \beta) \end{aligned} \tag{2.4.17}$$

In the above equation, $A(z)$ and $B(z)$ are complex amplitudes of the forward and backward propagating waves [20]. κ_{un} is the complex propagation constant for the unperturbed structure with $\Delta n = \Delta\alpha = 0$ (i.e. $\kappa = 0$). Since $k_{un} \approx \beta + j\alpha_0$, the trial solution of the scalar wave equation can also be expressed in terms of the real propagation constant, β, such that

$$\begin{aligned} E(z) &= A(z)e^{\alpha_0 z}e^{-j\beta z} + B(z)e^{-\alpha_0 z}e^{j\beta z} \\ &= C(z)e^{-j\beta z} + D(z)e^{j\beta z} \end{aligned} \tag{2.4.18}$$

To satisfy the Bragg condition, as shown earlier in equation (2.4.7), the actual propagation constant, β, should be sufficiently close to the Bragg propagation constant, β_0, so that the absolute difference between them should be much smaller than the Bragg propagation constant. In other words,

$$|\beta - \beta_0| \ll \beta_0 \tag{2.4.19}$$

Such a difference between the two propagation constants is commonly known as the detuning factor or detuning coefficient, δ, which is defined as

$$\delta = \beta - \beta_0 \tag{2.4.20}$$

In other words, the trial solution can also be expressed in terms of the Bragg propagation constant, i.e.

$$\begin{aligned} E(z) &= C(z)\mathrm{e}^{-\delta z}\mathrm{e}^{-j\beta_0 z} + D(z)\mathrm{e}^{\delta z}\mathrm{e}^{j\beta_0 z} \\ &= R(z)\mathrm{e}^{-j\beta_0 z} + S(z)\mathrm{e}^{j\beta_0 z} \end{aligned} \tag{2.4.21}$$

where $R(z)$ and $S(z)$ are complex amplitude terms. Since the grating period, Λ, in a DFB semiconductor laser is usually fixed, and so is the Bragg propagation constant, it is more convenient to consider equation (2.4.21) as the trial solution of the scalar wave equation. By substituting equation (2.4.21) into (2.4.15), we end up with the following equation:

$$\begin{aligned} &(R'' - 2j\beta_0 R' - \beta_0^2 R + \beta^2 R + 2j\beta\alpha_0 R)\mathrm{e}^{-j\beta_0 z} \\ &\quad + (S'' + 2j\beta_0 S' - \beta_0^2 S + \beta^2 S + 2j\beta\alpha_0 S)\mathrm{e}^{j\beta_0 z} \\ &\quad + 2\kappa\beta(\mathrm{e}^{2j\beta_0 z}\mathrm{e}^{j\Omega} + \mathrm{e}^{-2j\beta_0 z}\mathrm{e}^{-j\Omega}) \cdot (R\mathrm{e}^{-j\beta_0 z} + S\mathrm{e}^{j\beta_0 z}) = 0 \end{aligned} \tag{2.4.22}$$

where R' and R'' are the first- and second-order derivatives of R, respectively. Similarly, S' and S'' represent the first- and second-order derivatives of S, respectively. With a "slow" amplitude approximation, high order derivatives like R'' and S'' become negligible when compared with their first-order terms. By separating the above equation into two groups, each having similar exponential dependence, we obtain the following pair of coupled wave equations:

$$-\frac{\mathrm{d}R}{\mathrm{d}z} + (\alpha_0 - j\delta)R = j\kappa S\mathrm{e}^{-j\Omega} \tag{2.4.23}$$

$$\frac{\mathrm{d}S}{\mathrm{d}z} + (\alpha_0 - j\delta)S = j\kappa R\mathrm{e}^{j\Omega} \tag{2.4.24}$$

Equation (2.4.23) collects all the $\exp(-j\beta_0 z)$ phase terms propagating along the positive z direction, whilst equation (2.4.24) gathers all the $\exp(j\beta_0 z)$ phase terms propagating along the negative direction. Since $|\delta| \ll \beta$, other rapid changing phase terms such as $\exp(\pm j3\beta_0 z)$ have been dropped. In deriving the above equations, the following approximation has been assumed

$$\frac{\beta^2 - \beta_0^2}{2\beta_0} \approx \beta - \beta_0 = \delta \tag{2.4.25}$$

Following the above procedures, we end up with a similar pair of coupled wave equations for a non-zero relative phase difference between the refractive index and the gain perturbation (i.e. $\theta \neq 0$) such that

$$-\frac{\mathrm{d}R}{\mathrm{d}z} + (\alpha_0 - j\delta)R = j\kappa_{\mathrm{RS}} S\mathrm{e}^{-j\Omega} \tag{2.4.26}$$

$$\frac{dS}{dz} + (\alpha_0 - j\delta)S = j\kappa_{SR}Re^{j\Omega} \tag{2.4.27}$$

where

$$\kappa_{RS} = \kappa_i + j\kappa_g e^{-j\theta} \tag{2.4.28}$$

is the general form [24] known as the forward coupling coefficient and

$$\kappa_{SR} = \kappa_i + j\kappa_g e^{j\theta} \tag{2.4.29}$$

is the backward coupling coefficient.

From the scalar wave equation, a pair of coupled wave equations have been established. The forward coupling coefficient κ_{RS} in equation (2.4.26) induces the negative travelling electric field $S(z)$ to couple in the counter propagating one $R(z)$, and vice versa for equation (2.4.27). Contrary to FP lasers, where optical feedback is originated from the laser facets, optical feedback in DFB semiconductor lasers occurs continuously along the active layer where corrugations are fabricated. On the basis of the nature of the coupling coefficient, DFB semiconductor lasers are classified into three different groups: (a) purely index-coupled DFB semiconductor lasers; (b) mixed-coupled DFB semiconductor lasers; and (c) purely gain- or loss-coupled DFB semiconductor lasers.

2.4.1 A purely index-coupled DFB laser diode (LD)

Most practical DFB semiconductor lasers belong to this type, where coupling is solely generated by the refractive index perturbation. A single layer of corrugation is fabricated above (or below) the active layer, as shown in Figure 2.8.

Since most carrier recombinations are confined along the active layer, the amplitude gain of the DFB laser will not be affected. Therefore, with $\kappa_g = 0$, the index coupling coefficient κ_i (which is purely real) is related to κ_{RS} and κ_{SR} by the expression [20]

$$\kappa_{RS} = \kappa_{SR} = \kappa_i \tag{2.4.30}$$

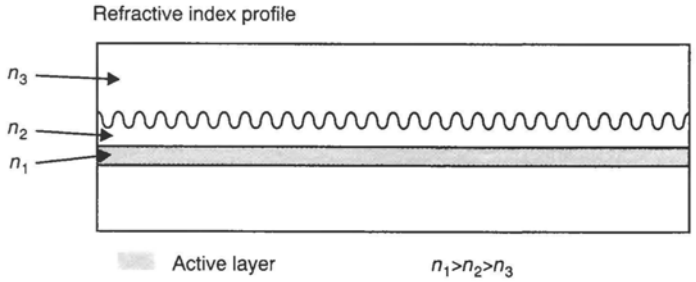

Figure 2.8 A simplified schematic diagram for a purely index-coupled DFB semiconductor laser.

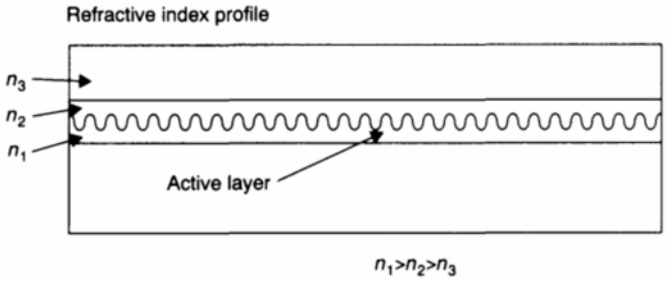

Figure 2.9 A simplified schematic diagram showing a mixed-coupled DFB semiconductor laser diode.

2.4.2 A mixed-coupled DFB LD

If the corrugation layer is fabricated on the upper part of the active layer, as shown in Figure 2.9, the DFB semiconductor laser will show a mixed coupling characteristic [24–26].

Owing to the variation in the refractive index along the corrugation layer, index-coupling is induced. However, the occurrence of gain-coupling needs further explanation. As illustrated in Figure 2.9, the active layer thickness becomes a periodic function along the longitudinal direction and thus is the optical confinement factor. Such a periodic modulation of the optical confinement factor modifies the amplitude gain along the longitudinal direction and so gain-coupling is induced [27]. Since both refractive index and gain-coupling are induced by the same corrugation, the corresponding phases of the κ_i and κ_g are assumed to be equal. For a zero relative phase difference ($\theta = 0$), we end up with the following identity:

$$\kappa_{RS} = \kappa_{SR} = \kappa_i + j\kappa_g \tag{2.4.31}$$

2.4.3 A gain-coupled or loss-coupled DFB LD

With only one single layer of grating, it is difficult to achieve a purely gain-coupled DFB device. However, by fabricating a second layer of grating on top of the original one, as shown earlier in the mixed-coupled DFB laser, the effect of index-coupling can be cancelled out.

As illustrated in Figure 2.10, the second corrugation demonstrates an inverse corrugation phase with respect to the first layer of grating. Utilising the metal–organic chemical vapour deposition (MOCVD) technique, the first purely gained DFB laser based on this double grating structure was made in 1989 by Luo *et al.* [28]. GaAs was used as the active layer of the laser and the lasing wavelength was about 877 nm. Owing to the direct modulation of the active layer thickness, the actual gain-coupling coefficient of this structure may fluctuate according to the strength of the injection current. For such a purely gain-coupled structure having $\kappa_i = 0$, both the forward and backward coupling coefficients become purely imaginary and so

$$\kappa_{RS} = \kappa_{SR} = j\kappa_g \tag{2.4.32}$$

The relative phase difference between the index and gain-coupling becomes insignificant as the index-coupling is cancelled.

Apart from the possibility shown in Figure 2.10, a second way to realise purely gain-coupled characteristics is to fabricate a periodic variation of loss, as sketched in Figure 2.11. The optical confinement factor remains constant whilst the cavity loss becomes a periodic function of z. With such a loss-coupling structure, the strength of the gain-coupling will not be affected by any change in the injection current. However, owing to the additional loss, the loss-coupling structure results in a higher threshold current.

Comparatively, the design of purely index-coupled DFB semiconductor lasers has received significant attention in the past decade. There are reasons why the development of mixed- or gain-coupled DFB lasers were hindered. In a mixed-coupled DFB laser, a large number of non-radiative recombination centres were introduced during the fabrication of the corrugation layer. Since the corrugation layer has direct contact with the active layer, such an increase in non-radiative recombination centres implies an enormous increase in the threshold current. The performance of the laser also deteriorates rapidly as the temperature increases. Moreover, the change in amplitude gain becomes complicated since the gain always depends on the injection current. Even though the loss-coupling structure proposed [29] may ease the problem, it is

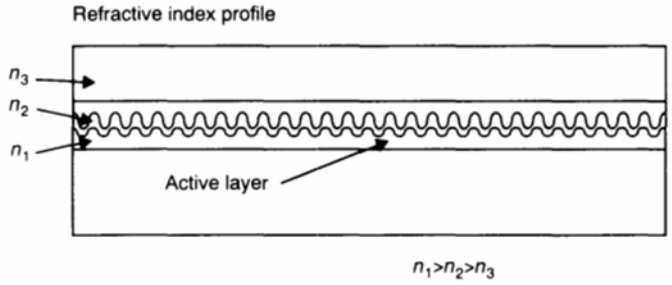

Figure 2.10 A simplified schematic diagram showing a purely gain-coupled DFB semiconductor laser diode.

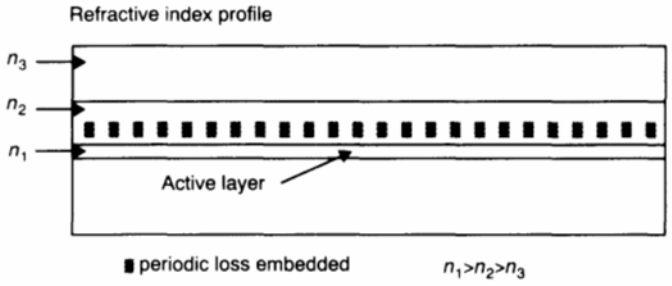

Figure 2.11 A simplified schematic diagram showing a purely loss-coupled DFB semiconductor laser diode.

limited by a higher threshold current. In the manufacture of the double grating structure the alignment between the first and the second corrugations must be considered because this is crucial in the cancellation of the index-coupling effect.

From the pair of coupled wave equations shown earlier, i.e. equations (2.4.26) and (2.4.27), we can also obtain the net power change experienced by both counter-running waves travelling along the laser cavity. By considering the conjugate pairs of equations (2.4.26) and (2.4.27), the rate of total power change is found [30]:

$$\frac{\mathrm{d}}{\mathrm{d}z}[RR^* - SS^*] = 2\alpha_0[RR^* + SS^*] + P_{\mathrm{mut}} \tag{2.4.33}$$

where an asterisk is used to represent the complex conjugate and

$$\begin{aligned} P_{\mathrm{mut}} &= j(\kappa^*_{\mathrm{RS}} - \kappa_{\mathrm{SR}})RS^*\mathrm{e}^{j\Omega} - j(\kappa_{\mathrm{RS}} - \kappa^*{}_{\mathrm{SR}})R^*S\mathrm{e}^{-j\Omega} \\ &= -2\left\{\mathrm{Im}\,(\kappa_{\mathrm{RS}} - \kappa^*_{\mathrm{RS}})R^*S\mathrm{e}^{-j\Omega}\right\} \\ &= -2\left\{\mathrm{Im}\,(\kappa^*_{\mathrm{RS}} - \kappa_{\mathrm{SR}})RS^*\mathrm{e}^{j\Omega}\right\} \end{aligned} \tag{2.4.34}$$

The first term on the right-hand side of equation (2.4.33) describes the total power change experienced by each individual coupled wave, while the second term, P_{mut}, describes the mutual interaction between the coupled waves. For a purely index-coupled DFB laser, both the forward and backward coupling coefficients are real and equal. As a result, the mutual interaction term becomes negligible. However, we must take into account the mutual interaction term when purely gain-coupled, purely loss-coupled or mixed-coupled DFB lasers are used.

The pair of coupled-wave equations that characterise the interaction of electric fields are general. With modification, the pair can be used in other applications which may involve wave or mode interaction. The complex permittivity, i.e. the refractive index and amplitude gain, may change in a different way according to various applications. On the basis of the coupled wave analysis, equations that describe other physical processes like the electro-optic modulation, the magneto-optic modulation or the non-linear interaction can be found in other references like Yariv [2].

2.5 THE COUPLING COEFFICIENT

2.5.1 A structural definition of the coupling coefficient for DFB semiconductor lasers

Depending on the position of the corrugation relative to the active layer, both the refractive index and/or gain vary along the longitudinal direction, z. By solving the coupled-wave equations, we can solve the threshold conditions of the conventional DFB semiconductor lasers. The coupling coefficients κ_{RS} and κ_{SR} play an important role because they measure the wave feedback

capability due to the presence of the corrugation. So far, the coupling coefficient has been defined with respect to the changes in the refractive index and gain such that

$$\kappa = \frac{\pi \Delta n}{\lambda} + j\frac{\Delta \alpha}{2} \tag{2.5.1}$$

In this section, on the basis of a general perturbation of the relative permittivity, the coupling coefficient is found to be related to the shape, depth and period of the corrugation. To build such a structural definition for the coupling coefficient, we start again with the time harmonic vector wave equation:

$$\nabla^2 \boldsymbol{E} + k^2 \boldsymbol{E} = 0 \tag{2.5.2}$$

By expanding the propagation constant to include the relative permittivity, the above wave equation becomes

$$\nabla^2 \boldsymbol{E} + \varepsilon(x, y, z) k_0^2 \boldsymbol{E} = 0 \tag{2.5.3}$$

where ε is the relative permittivity and $k_0 = \omega/c$ is the free space propagation constant. There is a major difference between a normal dielectric planar waveguide and a corrugated waveguide. Provided that the corrugation is extended in the longitudinal direction, we can express the relative permittivity of the corrugated region of the laser as

$$\varepsilon(x, y, z) = \varepsilon_{\text{ini}}(x, y) + \Delta\varepsilon(x, y, z) \tag{2.5.4}$$

where $\varepsilon_{\text{ini}}(x, y)$ is the average relative permittivity of the transverse x-y plane, and $\Delta\varepsilon$ is a perturbation term which is zero everywhere except for the corrugated region, the thickness of which is equivalent to the corrugation depth. Assuming TE mode excitation only and following equation (2.4.18), a general solution of the vector wave solution may take the form

$$\boldsymbol{E} = U(x, y)[C\mathrm{e}^{-j\beta z} + D\mathrm{e}^{j\beta z}]\hat{j} = E_y \hat{j} \tag{2.5.5}$$

where $\hat{j}$ is the unit vector along the junction plane for the TE mode, β is the mode propagating constant and $U(x, y)$ is the field solution along the transverse x-y plane. The trial solution shown above is slightly different from the one we used in the previous section. For a specific waveguiding structure, the field distribution can be obtained by solving

$$\frac{\partial^2 U}{\partial x^2} + \frac{\partial^2 V}{\partial y^2} + [\varepsilon_{\text{ini}}(x, y) k_0^2 - \beta^2]U = 0 \tag{2.5.6}$$

with appropriate boundary conditions.

With careful control over the active layer width and the active layer thickness, a single mode oscillation along the transverse plane is assumed. Under the influence of the perturbation term $\Delta\varepsilon$, the amplitude coefficients C and D become z-dependent. Assuming only a small perturbation, i.e.

$\Delta\varepsilon \ll \varepsilon_{\text{ini}}$, it is unlikely that the field distribution $U(x, y)$ will be affected and so it is made separable from the longitudinal component of the field solution. We then substitute equation (2.5.5) into (2.5.3) and allow a "slow" variation of C and D. By multiplying the resulting equation by $U(x, y)$ and integrating over the transverse $x-y$ plane, we end up with

$$\frac{dC}{dz}e^{-j\beta z} - \frac{dD}{dz}e^{j\beta z} = \frac{-jk_0^2}{2\beta V}\iint \Delta\varepsilon(x, y, z)U^2(x, y) [Ce^{-j\beta z} + De^{j\beta z}]\,dx\,dy \tag{2.5.7}$$

where

$$V = \iint U^2(x, y)\,dx\,dy \tag{2.5.8}$$

is the mode intensity for the unperturbed planar waveguide. For simplicity, only index coupling is assumed so that $\Delta\varepsilon$ is real. Since the perturbed term $\Delta\varepsilon$ is a periodic function of z, it could be expanded in Fourier series such that [31,32]

$$\Delta\varepsilon(x, y, z) = \sum_{q=-\infty}^{\infty} A_{q\neq 0}(x, y)\exp\left(\frac{2jq\pi z}{\Lambda}\right) \tag{2.5.9}$$

where $A_{q\neq 0}(x, y)$ is the qth harmonic Fourier coefficient that depends on the shape, depth and period of the corrugation. When $q = 0$, a z-independent function is formed which equals the average relative permittivity term, ε_{ini}. Now, by substituting the above equation into equation (2.5.7) and equating coefficients with exponential terms $e^{\pm j\beta z}$, we obtain:

$$\frac{dC}{dz} = -j\kappa^* De^{j2\delta z} \tag{2.5.10}$$

$$\frac{dD}{dz} = j\kappa Ce^{-j2\delta z} \tag{2.5.11}$$

where

$$\begin{aligned}\delta &= \beta - \beta_0 \\ &= \beta - m\pi/\Lambda\end{aligned} \tag{2.5.12}$$

in which δ is the same detuning factor and m is the order of the Bragg diffraction. Usually, the smallest detuning factor is found by allowing $q = m$ in equation (2.5.9). In the analysis, other higher order phase terms have been neglected. κ and κ^* are complex conjugate pairs that can be written as

$$\kappa = \frac{k_0^2}{2\beta}\frac{\iint A_{q\neq 0}(x, y)U^2(x, y)\,dx\,dy}{\iint U^2(x, y)\,dx\,dy} \tag{2.5.13}$$

When the corrugation is removed or the grating depth is diminished to become zero, a planar waveguide is formed. With the coupling coefficient κ

vanished, the coupled-wave equations could be satisfied by any z-independent function. However, owing to the material gain characteristics inside the laser cavity, an additional term is added to equations (2.5.10) and (2.5.11). As a result, the independent solutions C and D correspond respectively to the exponentially growing waves along the $+z$ and $-z$ directions when $\kappa = 0$. To fulfil the physical requirement, equations (2.5.10) and (2.5.11) become

$$\frac{dC}{dz} = -j\kappa^* D e^{j2\delta z} + \alpha_s C \tag{2.5.14}$$

$$\frac{dD}{dz} = j\kappa C e^{-j2\delta z} - \alpha_s D \tag{2.5.15}$$

where the amplitude gain coefficient, α_s, is appended.

Unsurprisingly, a similar pair of coupled-wave equations have been derived. Compared with equations (2.4.23) and (2.4.24), the pair of equations shown above look distinctive because a different trial solution has been used in solving the wave equation. By replacing β with $\beta_0 + \delta$ in the above equations, the original coupled-wave equations can be recovered. The parameter κ, as shown in equation (2.5.13), is the coupling coefficient as defined earlier for the purely index-coupled DFB lasers.

2.5.2 The effect of corrugation shape on the coupling coefficient

Since the coupling coefficient is associated with the perturbed relative permittivity, the numerical value of κ depends on the shape, depth and period of the corrugation. Moreover, the composition and thickness of the active and cladding layers will also affect the coupling coefficient because κ involves calculating the transverse mode energy. Evaluation of the coupling coefficient and the impact on the corrugation shape of the three-layer GaAs DFB lasers have been discussed extensively [31,32]. However, little work [33] has been done on the five-layer InGaAsP DFB semiconductor lasers.

In a BH, where the active layer thickness is much narrower than its width, we assume that the corrugation is laterally uniform so that the relative permittivity term $\Delta\varepsilon$ is independent of y. As a result, equation (2.5.4) is simplified to

$$\varepsilon(x, y) = \varepsilon_{ini}(x) + \Delta\varepsilon(x, y) \tag{2.5.16}$$

and the coupling coefficient for the purely index-coupled DFB laser becomes

$$\kappa = \frac{k_0^2}{2\beta} \frac{\int_{\text{corrugation}} A_{q\neq 0} E_y^2(x)\,dx}{\int E_y^2(x)\,dx} \tag{2.5.17}$$

where $E_y(x)$ is the transverse field component of the TE mode which satisfies the wave equation (2.5.3). The integral in the numerator is restricted to the

corrugated layer only because the perturbed relative permittivity $\Delta\varepsilon$ (or the Fourier coefficient $A_{q\neq 0}$) is not defined in any other layer.

To investigate the effect of different periodic grating shapes, a general multi-layer model, as illustrated in Figure 2.12 is used. Similar to the one shown in Figure 2.6, the cosinusoidal corrugation is now replaced by two discontinuous arbitrary functions $Z_1(x) + p\Lambda$ and $Z_2(x) + p\Lambda$, where p is any integer. For any periodic corrugation shape, it is important that the sum of the corrugation functions $Z_1(x) + p\Lambda$ and $Z_2(x) + p\Lambda$ will span a longitudinal distance of Λ, the period of the corrugation. For simplicity, the integer p is set to zero for the first corrugation function found on the positive x–z plane as the corrugation is extended along the positive z direction. Then, we can express the relative permittivity $\varepsilon(x, z)$ analytically as

$$\begin{aligned}
\varepsilon(x, z) &= n_1^2; \quad x > d_1 \\
&= n_2^2; \quad d_1 > x > d_2 \\
&\vdots \\
&= n_l^2; \quad d_{l-1} > x > d_x + g \\
&= n_{l+1}^2; \quad d_x > x > d_{l+1} \\
&\vdots \\
&= n_{N-1}^2; \quad d_{N-2} > x > d_{N-1} \\
&= n_N^2; \quad d_{N-1} > x
\end{aligned} \tag{2.5.18}$$

for layers found outside the corrugated layer. For the relative permittivity of the corrugated layer, we can write [31]

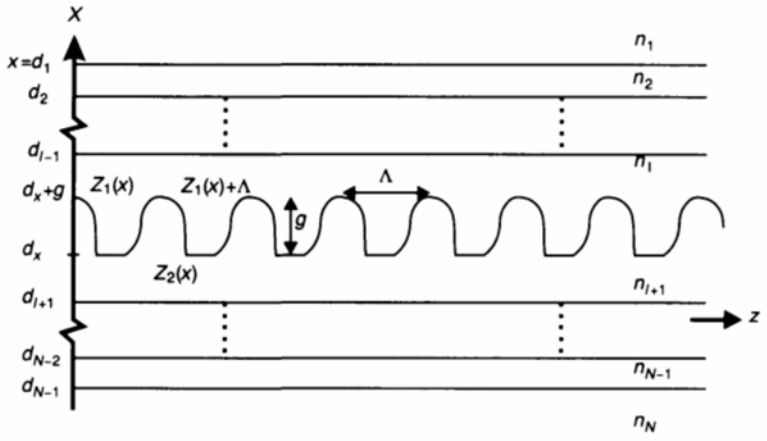

Figure 2.12 A general multi-dielectric stack used to evaluate the coupling coefficient of DFB semiconductor laser diodes.

$$\varepsilon(x, z) = \sum_{p=-\infty}^{\infty} n_l^2\{u[z - Z_1(z) - p\Lambda] - u[z - Z_2(z) - p\Lambda]\} + n_{l+1}^2\{u[z - Z_2(z) - p\Lambda] - u[z - Z_1(z) - (p+1)\Lambda]\} \tag{2.5.19}$$

where

$$u(\xi) = \begin{cases} 1, & \xi > 0 \\ 0, & \xi < 0 \end{cases} \tag{2.5.20}$$

is the unit step function in ξ. By equating equation (2.5.9) with (2.5.19) and setting $p = 0$, we can express the harmonic Fourier coefficient as

$$A_{q=0} = A_0 = n_{l+1}^2 + \frac{1}{L}[Z_2(x) - Z_1(x)]n_l^2 - n_{l+1}^2 \tag{2.5.21}$$

for $q = 0$ and

$$\begin{aligned} A_{q\neq 0} &= \frac{1}{\Lambda}\int_{Z_1(z)}^{Z_1(z)+\Lambda} n^2(x, z)\mathrm{e}^{\frac{-j2\pi qz}{\Lambda}}\,\mathrm{d}z \\ &= \frac{n_{l+1}^2 - n_l^2}{2j\pi q} \cdot \left[\mathrm{e}^{\frac{-j2\pi qZ_2(x)}{\Lambda}} - \mathrm{e}^{\frac{-j2\pi qZ_1(x)}{\Lambda}}\right] \end{aligned} \tag{2.5.22}$$

for $q \neq 0$. The last equation is justified because the integral can be separated into

$$\int_{Z_1(x)}^{Z_1(x)+\Lambda} = \int_{Z_1(x)}^{Z_2(x)} + \int_{Z_2(x)}^{Z_1(x)+\Lambda} \tag{2.5.23}$$

The relative permittivities at different integral ranges can be expressed as

$$n^2(x, z) = \begin{cases} n_l^2, & Z_2(x) > z > Z_1(x) \\ n_{l+1}^2, & Z_1(x) + \Lambda > z > Z_2(x) \end{cases} \tag{2.5.24}$$

Since $Z_1(x) + Z_2(x) = \Lambda$, equation (2.5.22) is simplified to become [33]

$$A_{q\neq 0} = \frac{n_{l+1}^2 - n_l^2}{m\pi} \cdot \sin\left[\frac{2m\pi}{\Lambda}Z_1(z)\right]; \quad d_x < x < d_x + g \tag{2.5.25}$$

where $q = m$ is assumed for the smallest detuning factor. The corrugation functions $Z_1(x)$ for trapezoidal, rectangular, triangular and sinusoidal corrugations are listed in Table 2.2. For the trapezoidal shape, W_T and W_B denoted the top width and the bottom width of the corrugation. For simplicity, the rising edge and the dropping edge are assumed to occupy the same widths of W. Finally, on combining equation (2.5.25) with (2.5.17), we end up with the following expression for the coupling coefficients of the purely indexed-coupled DFB LDs [34]:

$$\kappa = \frac{k_0^2(n_{l+1}^2 - n_l^2)}{2m\pi\beta\int E_y^2(x)\,\mathrm{d}x} \cdot \left|\int_{\text{corrugation}} \sin\left[\frac{2m\pi Z_1(x)}{\Lambda}\right] E_y^2(x)\,\mathrm{d}x\right| \tag{2.5.26}$$

Table 2.2 Various grating shapes and the corresponding corrugation fuctions $Z_1(x)$

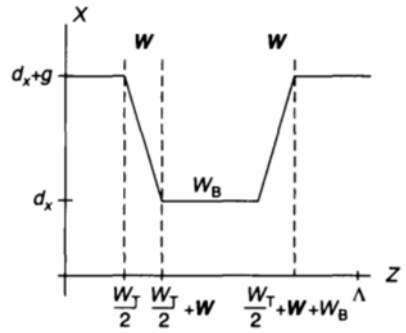

normal trapezoidal shape

$$Z_1(x) = \frac{W_T}{2} + \frac{W}{g}(d_x + g - x)$$

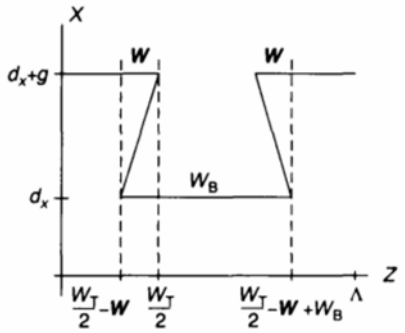

inverted trapezoidal shape

$$Z_1(x) = \frac{W_T}{2} - \frac{W}{g}(d_x + g - x)$$

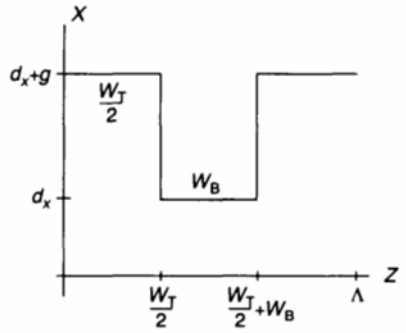

rectangular shape

$$Z_1(x) = \frac{W_T}{2}$$

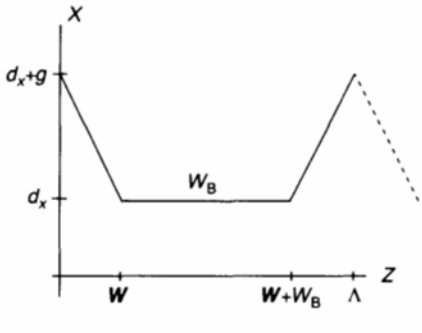

triangular shape

$$Z_1(x) = \frac{W}{g}(d_x + g - x)$$

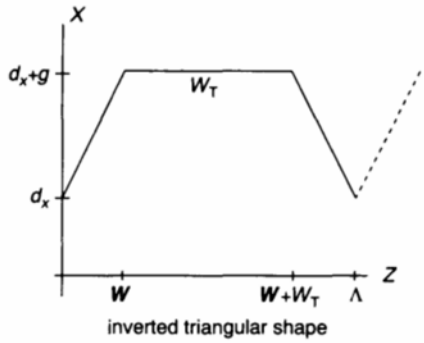

inverted triangular shape

$$Z_1(x) = \frac{W}{g}(x - d_x)$$

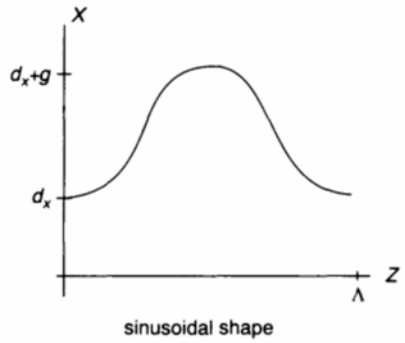

sinusoidal shape

$$Z_1(x) = \frac{\Lambda}{2\pi}\cos^{-1}\left[1 - \frac{2}{g}(x - d_x)\right]$$

where an absolute sign is used to make sure a positive value for the coupling coefficient.

2.5.3 Transverse field distribution in an unperturbed waveguide

From equation (2.5.26) in the previous section, the coupling coefficients of the purely index-coupled DFB LDs were expressed. With a specific corrugation function and a given refractive index distribution, we still need to determine the propagation constant β and the mode energy of the unperturbed waveguide before the value of the coupling coefficient can be evaluated.

Figure 2.13 shows the structure of the five-layer SCH DFB LD used in the analysis. It consists of a thin optical confinement region, itself divided into three parts that include the active layer and two waveguiding layers. III–V InGaAsP compounds are used to fabricate the optical confinement region. The refractive indices of the waveguiding layers (n_2 and n_4) are slightly smaller than that of the active layer (n_3) so that photons are confined in the active layer. Optical feedback provided by a layer of trapezoidal corrugation is fabricated within the upper waveguiding layer. The optical confinement region is bounded by two thick cladding layers with a higher bandgap material used, the cladding layers act as optical barriers. Since the active layer thickness remains constant along the longitudinal direction, any gain- or loss-coupling can be neglected and only pure index-coupling is allowed.

To compute the unperturbed transverse electric field $E_y(x)$ in the five-layer SCH, the effect due to the presence of corrugations cannot be ignored. One method, which was proposed by Handa *et al.* [35], is to replace the

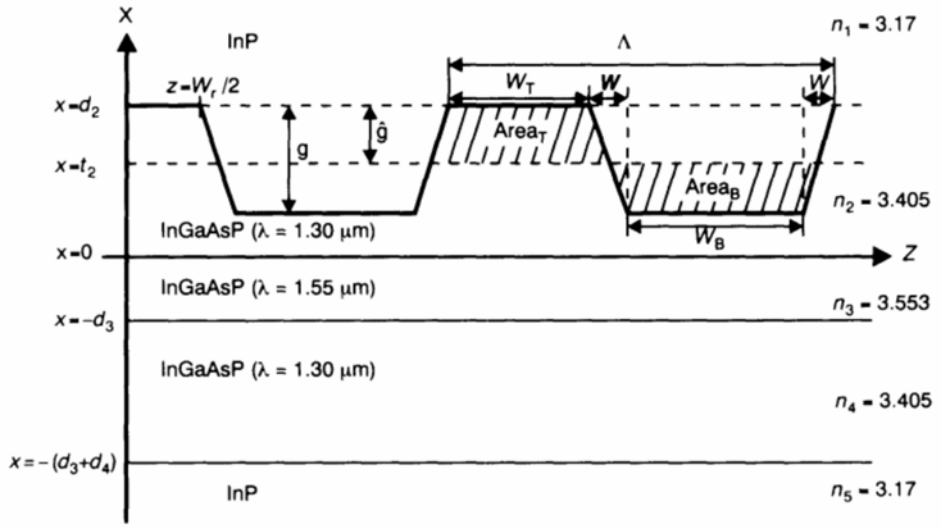

Figure 2.13 A simplified five-layer DFB structure with trapezoidal corrugation.

corrugation layer that has an additional layer with an intermediate refractive index. However, the waveguiding properties become more complicated as one extra layer is added. Another method [31,32] that enables us to obtain adequate accuracy without excessive complexity is to choose the unperturbed waveguide boundary at $x = d_2' < d_2$ as shown in Figure 2.13. Since the corrugation depth g is found to be much smaller than the actual lasing wavelength, the unperturbed waveguide boundary at d_2' is chosen such that the volume of the n_2 material extending into the upper cladding layer equals the volume of n_1 extending into the upper waveguiding layer. As a result, the contribution due to the refractive index changes above the unperturbed waveguide boundary will be the same as the one below. Since the active layer thickness, d_3, is usually smaller than the active layer width, the transverse field along the y direction becomes negligible. As a result, the corresponding boundary is determined by equating the area bounded by the upper part of the corrugation (Area_T) to that of the area (Area_B) bounded below. This method, that involves a dynamic shifting of one of the waveguide boundaries, is simpler and more effective than the one proposed by Handa *et al.* [35]. On the other hand, we must take care when choosing the unperturbed waveguide boundary because it is sensitive to a change of corrugation shape. Mathematically, the boundary of the corresponding unperturbed waveguide can be expressed as

$$\hat{g} = d_2 - t_2 = \frac{1}{\Lambda} \int_{d_2 - g}^{d_2} [Z_2(x) - Z_1(x)]\, \mathrm{d}x \tag{2.5.27}$$

where g is the depth of the corrugation and $\hat{g} = d_2 - t_2$ is the boundary shift measured from the top of the corrugation to the new boundary of the corresponding unperturbed waveguide. The upper surface of the active layer is fixed at $x = 0$. Then, Maxwell's wave equations in each of the five layers may be written as [36]

$$\frac{\mathrm{d}^2 E_y}{\mathrm{d}x^2} + h_j E_y = 0; \quad j = 1, \ldots, 5 \tag{2.5.28}$$

where j is an integer used to represent different layers and h_j is the propagation constant of the jth layer. For the structure shown, it is assumed that the unperturbed transverse electric field is exponentially decaying in the cladding layers while it is sinusoidal in the other. Then, the propagation constant h_j can be written as [6,21]

$$h_j = \begin{cases} \beta_{\text{eff}}^2 - k_0^2 n_j^2; & j = 1 \text{ and } 5 \\ k_0^2 n_j^2 - \beta_{\text{eff}}^2; & j = 2, 3 \text{ and } 4 \end{cases} \tag{2.5.29}$$

where $\beta_{\text{eff}} = k_0 n_{\text{eff}} = \beta$ in equation (2.5.26) and n_{eff} is denoted the *effective refractive index*. Because the transverse electric field is propagating along the waveguiding layers as well as the active layer, the refractive index distribution must satisfy the following relation [37]:

$$n_5 \leq n_1 < n_{\text{eff}} < n_4 \leq n_2 < n_3 \tag{2.5.30}$$

For the TE mode excitation in the five-layer SCH laser structure, the transverse electric field in each layer can be written as [36]

$$E_y = \begin{cases} A_1 \exp[h_1(t_2 - x)], & \text{for } x \geq t_2 \\ A_2 \cos(h_2 x - \alpha_2), & 0 \leq x \leq t_2 \\ A_3 \cos(h_3 x - \alpha_3), & -d_3 \leq x \leq 0 \\ A_4 \cos(h_4 x - \alpha_4), & -(d_3 + d_4) \leq x \leq -d_3 \\ A_5 \exp[h_5(d_3 + d_4 + x)], & x \leq -(d_3 + d_4) \end{cases} \tag{2.5.31}$$

where A_1 to A_5 are the leading coefficients of the transverse electric field in various layers, t_2 is the boundary separation for the corresponding unperturbed waveguide and α_2, α_3 and α_4 are three constants. Because the field components E_y and $\partial E_y/\partial x$ must be continuous at various boundaries for TE mode excitation, we end up with the following equations for the TE mode:

At $x = t_2$

$$h_2 \tan(h_2 t_2 - \alpha_2) = h_1 \tag{2.5.32a}$$

At $x = 0$

$$h_3 \tan(\alpha_3) = h_2 \tan(\alpha_2) \tag{2.5.32b}$$

At $x = -d_3$

$$h_3 \tan(h_3 d_3 + \alpha_3) = h_4 \tan(h_4 d_3 + \alpha_4) \tag{2.5.32c}$$

At $x = -(d_3 + d_4)$

$$h_4 \tan[h_4(d_3 + d_4) + \alpha_4] = h_5 \tag{2.5.32d}$$

where the constants α_2, α_3 and α_4 can then be determined as

$$\alpha_2 = h_2 t_2 - \tan^{-1}\left(\frac{h_1}{h_2}\right) \tag{2.5.33a}$$

$$\alpha_3 = \tan^{-1}\left[\frac{h_2}{h_3}\tan(\alpha_2)\right] \tag{2.5.33b}$$

and

$$\alpha_4 = -h_4(d_3 + d_4) + \tan^{-1}\left(\frac{h_5}{h_4}\right) \tag{2.5.33c}$$

To reduce the number of variables used, it is easier to select one of them as a common variable so that others can then be written in terms of it. From the boundary conditions for the E_y field component, we can express the leading coefficients of the electric field in terms of the common coefficient A_1 such that

$$A_2 = \frac{A_1}{\cos(h_2 t_2 - \alpha_2)} \tag{2.5.34a}$$

$$A_3 = \frac{A_1 \cos(\alpha_2)}{\cos(h_2 t_2 - \alpha_2)\cos(\alpha_3)} \tag{2.5.34b}$$

$$A_4 = \frac{A_1 \cos(\alpha_2)\cos(h_3 d_3 + \alpha_3)}{\cos(h_4 d_3 + \alpha_4)\cos(h_2 t_2 - \alpha_2)\cos(\alpha_3)} \tag{2.5.34c}$$

$$A_5 = \frac{A_1 \cos(\alpha_2)\cos(h_3 d_3 + \alpha_3)\cos[h_4(d_3 + d_4) + \alpha_4]}{\cos(h_4 d_3 + \alpha_4)\cos(h_2 t_2 - \alpha_2)\cos(\alpha_3)} \tag{2.5.34d}$$

where the constants α_2, α_3 and α_4 have been fixed in equation (2.5.33). By joining all the equations in (2.5.32), an eigenvalue equation for the even TE mode is found which [36] can be expressed as

$$\tan(h_3 d_3/2) = \frac{-(1 + AB) + [(1 + A^2)(1 + B^2)]^{1/2}}{A - B} \tag{2.5.35a}$$

where

$$A = h_4 \tan(h_4 d_3 + \alpha_4)/h_3 \tag{2.5.35b}$$

$$B = \tan(\alpha_2) = h_2 \tan(\alpha_2)/h_3 \tag{2.5.35c}$$

In finding the effective refractive index, the method of bisection is employed to solve the above eigenequation. The total number of iteration steps used is usually smaller than 10 and an error of less than 10^{-9} may be achieved. After fixing the effective refractive index, the propagation constants h_j in each layer can readily be found using equation (2.5.29). Then, following equations (2.5.33), α_2, α_3 and α_4 are determined.

The transverse electric field in the five-layer laser structure can be obtained after solving the eigenequation. However, in evaluating the coupling coefficient, we must determine the total mode energy confined in the five-layer structure. From the proposed transverse electric field distribution, we end up with [34]

$$I = \int_{-\infty}^{\infty} E_y^2(x)\,dx = \int_{-\infty}^{-(d_3+d_4)} E_y^2(x)\,dx + \int_{-(d_3+d_4)}^{-d_3} E_y^2(x)\,dx + \int_{-d_3}^{0} E_y^2(x)\,dx + \int_{0}^{t_2} E_y^2(x)\,dx + \int_{t_2}^{\infty} E_y^2(x)\,dx = I_5 + I_4 + I_3 + I_2 + I_1 \tag{2.5.36}$$

where

$$I_1 = A_1^2/2h_1 \tag{2.5.37a}$$

$$I_2 = \frac{A_2^2}{2}\left[t_2 + \frac{1}{2h_2}\sin(2h_2 t_2 - 2\alpha_2) + \frac{1}{2h_3}\sin(2\alpha_2)\right] \tag{2.5.37b}$$

$$I_3 = \frac{A_3^2}{2}\left[d_3 + \frac{1}{2h_3}\sin(2h_3 d_3 + 2\alpha_3) - \frac{1}{2h_3}\sin(2\alpha_3)\right] \tag{2.5.37c}$$

$$I_4 = \frac{A_4^2}{2}\left[d_4 + \frac{1}{2h_4}\sin[2h_4(d_3 + d_4) + 2\alpha_4] - \frac{1}{2h_4}\sin(2h_4 d_3 + 2\alpha_3)\right] \tag{2.5.37d}$$

$$I_5 = A_5^2/2h_5 \tag{2.5.37e}$$

By choosing A_1 as the common variable, the total mode energy confined in the five-layer waveguide is finalised after the effective refractive index, the propagation constants h_1 to h_5 as well as the constants α_1, α_2 and α_3 have been confirmed from the eigenequation for a particular corrugation function. The integral I_2, which is a function of t_2, depends on the shape of the corrugation.

2.5.4 Results based upon the trapezoidal corrugation

In this section the coupling coefficient values based on the five-layer DFB lasers are evaluated for the trapezoidal corrugation. From the previous section, the total mode energy found inside the five-layer waveguide is expressed in terms of the leading coefficient A_1. Before the Fourier coefficient A_q, and hence the coupling coefficients, are determined, the corrugation functions $Z_1(x)$ and $Z_2(x)$ of the trapezoidal corrugation must be defined. According to Figure 2.13, we end up with

$$Z_1(x) = \frac{W_T}{2} + \frac{\boldsymbol{W}}{g}(d_2 - x) \tag{2.5.38a}$$

$$Z_2(x) = \frac{W_T}{2} + 2\boldsymbol{W} + W_B + \frac{\boldsymbol{W}}{g}(x - d_2) \tag{2.5.38b}$$

Therefore, the unperturbed boundary t_2 for the equivalent unperturbed planar waveguide can be determined after following equation (2.5.27) since

$$\begin{aligned} \hat{g} = d_2 - t_2 &= \frac{1}{\Lambda}\int_{d_2-g}^{d_2} [Z_2(x) - Z_1(x)]\,\mathrm{d}x \\ &= \frac{W_B + \boldsymbol{W}}{\Lambda} \cdot g \end{aligned} \tag{2.5.39}$$

where W_T and W_B are the top width and the bottom width of the trapezoidal corrugation, respectively. The variable $\boldsymbol{W}$ denotes the longitudinal distance spanned by the rise and fall of the corrugation. As a result, the coupling coefficient of the trapezoidal corrugation becomes

$$\kappa = \frac{k_0^2(n_2^2 - n_1^2)}{2m\pi\beta \int E_y^2(x)\,\mathrm{d}x} \cdot \left| \int_{d_2-g}^{d_2} \sin[a + b(d_2 - x)]\, E_y^2(x)\,\mathrm{d}x \right| \tag{2.5.40}$$

where m is the order of the Bragg diffraction, β is the propagation constant determined from the effective refractive index and

$$a = \frac{m\pi W_T}{\Lambda} \tag{2.5.41a}$$

$$b = \frac{2m\pi}{\Lambda} \cdot \frac{\boldsymbol{W}}{g} \tag{2.5.41b}$$

Extracting from equation (2.5.31), the proposed transverse electric field found along the corrugated layer ($d_2 \geq x \geq d_2 - g$) can be written as

$$E_y(x) = \begin{cases} A_1 e^{h_1(t_2 - x)}; & d_2 \geq x \geq t_2 \\ A_2 \cos[h_2 x - \alpha_2]; & t_2 \geq x \geq d_2 - g \end{cases} \tag{2.5.42}$$

Then, by joining equations (2.5.40), (2.5.41) and (2.5.42), and after substantial simplification, the coupling coefficient of the trapezoidal corrugation becomes [33]

$$\kappa = \frac{k_0^2(n_2^2 - n_1^2)}{4\pi\beta N^2} g \left\{ Q_1 + \left[1 + \left(\frac{h_2}{h_1}\right)^2\right] \frac{Q_2}{2} + \left[1 - \left(\frac{h_1}{h_2}\right)^2\right] \frac{Q_3}{2} + \frac{h_1}{h_2} Q_4 \right\} \tag{2.5.43}$$

where

$$Q_1 = \frac{(h_1 g \sin \bar{c} - b) - \exp(-2h\hat{g}) \cdot (h_1 g \sin a - b \cos a)}{(h_1 g)^2 + b^2} \tag{2.5.44a}$$

$$Q_2 = \frac{\cos \bar{c} - \cos c}{b} \tag{2.5.44b}$$

$$Q_3 = \frac{b(\cos \bar{c} - \cos c \cos v) - h_2 g(\sin c \sin v)}{b^2 - (h_2 g)^2} \tag{2.5.44c}$$

$$Q_4 = \frac{h_2 g(\sin c \cos v - \sin \bar{c}) - b(\cos c \sin v)}{b^2 - (h_2 g)^2} \tag{2.5.44d}$$

and

$$c = a + bg; \qquad \bar{c} = a + b\hat{g}; \qquad v = 2h_2(g - \hat{g}) \tag{2.5.45}$$

Trapezoidal corrugation for first-order Bragg diffraction (m = 1)

In our calculations, we have considered only the TE_0 mode. The structural parameters used are given in Table 2.3. By setting $m = 1$ in equation (2.5.41), the coupling coefficient of the first-order trapezoidal corrugation can be

Table 2.3 Structural parameters used in determining the coupling coefficient of the first-order trapezoidal corrugation

$m = 1$
$d_2 = d_4 = 200$ μm
$d_3 = 100$ μm
$n_1 = n_5 = 3.17$
$n_2 = n_4 = 3.405$
$n_3 = 3.553$
$g = 75$ nm

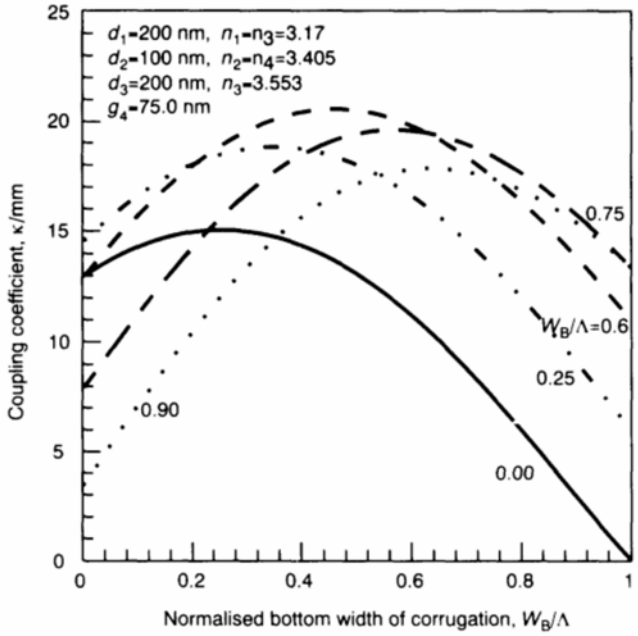

Figure 2.14 The change in the first-order coupling coefficient with W_B/Λ for different values of W_T/Λ.

determined. The effects of different corrugation shapes are illustrated in Figure 2.14, where the coupling coefficient is plotted against the bottom width of the corrugation, W_B, while different values of W_T (the top width of the corrugation) are used for comparison. Both W_T and W_B are normalised with respect to the corrugation period Λ. As observed in Figure 2.14, for each selected value of W_T/Λ there exists a peak coupling coefficient where the largest possible optical feedback can be achieved. For instance, the triangular corrugation (with $W_T/\Lambda = 0$) tends to show a peak coupling coefficient of about 15/mm when the normalised bottom width $W_B/\Lambda = 0.25$. With the normalised top width W_T/Λ increasing from 0.0 to 0.9, the associated W_B/Λ values of the peak coupling coefficients also increase. The largest coupling coefficient found near $W_B/\Lambda = W_T/\Lambda = 0.5$ has a value of 20.9/mm. This is the place where the symmetric rectangular corrugation is found.

So far, discrete values of W_T/Λ have been used. By expanding the results into a contour map, as shown in Figure 2.15, the structural impact due to variations in the corrugation shapes can be examined comprehensively. In fact, the trapezoidal corrugation we examined is so general that other shapes like the triangular and rectangular corrugations, are included. At the origin, where $W_T/\Lambda = W_B/\Lambda = 0$, the symmetric triangular corrugation is located. With a corrugation depth $g = 75$ nm, the coupling coefficient is found to be about 13.0/mm. Other asymmetric triangular corrugations are included along the W_B/Λ axis when W_T/Λ is forced to become zero. Similarly, the inverted

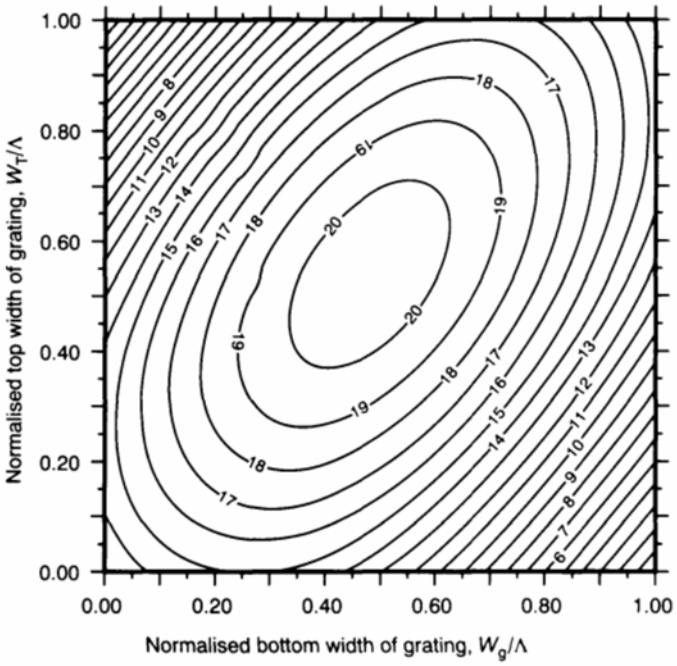

Figure 2.15 Contour map showing the coupling coefficient κ for the first-order trapezoidal corrugation.

triangular corrugation (see Table 2.2 for the exact corrugation shapes) is found along the W_T/Λ axis as W_B/Λ drops to zero. For the rectangular corrugation, $W/\Lambda = 0$ and $W_T + W_B = \Lambda$. Therefore, by joining the point $W_T/\Lambda = 0$, $W_B/\Lambda = 1$ to the opposite diagonal of the contour (i.e. $W_T/\Lambda = 1$, $W_B/\Lambda = 0$), we can evaluate the coupling coefficients for the rectangular corrugation. The symmetric rectangular corrugation, which is included as a special case, is located at the centre of the contour with $W_T/\Lambda = W_B/\Lambda = 0.5$. Similarly, by joining the origin with the other extreme end where $W_T/\Lambda = W_T/\Lambda = 1$, the coupling coefficient of the symmetric trapezoidal corrugation can be determined.

Owing to the presence of the corrugation and the use of the boundary shifting method, the calculated boundary at $x = t_2$ for the corresponding unperturbed waveguiding structure is expected to be smaller than the actual thickness of the upper waveguiding layer d_2. As a result, the DFB waveguiding structure is no longer symmetric. The thickness of the upper cladding layer, that depends on the corrugation shape, is found to be thinner than the lower waveguiding layer. Thus, the maximum coupling coefficient is found to be slightly displaced from the centre of the contour where the symmetric rectangular corrugation is located. The maximum coupling coefficient found is about 20.5/mm.

Trapezoidal corrugation for second-order Bragg diffraction (m = 2)

To compare the coupling coefficients of the DFB LDs having different orders of Bragg diffraction, the effective refractive index and thus the boundary shift g of the DFB structures must be identical. For the mth order Bragg diffraction, the Bragg propagation constant is defined as

$$\beta_0 = \frac{m\pi}{L} \tag{2.5.46}$$

To maintain the Bragg propagation constant at the second-order corrugation ($m = 2$), the second-order grating period must be doubled. Meanwhile, the corrugation depth g is also increased to twice that of the first-order value so that the boundary of the unperturbed waveguide g of equation (2.5.39) is maintained.

The parameters used to determine the coupling coefficient of the second-order trapezoidal corrugation can be found in Table 2.4.

By inserting the above parameters into equations (2.5.43), (2.5.44) and (2.5.45), the effect of the corrugation shapes on the second-order coupling coefficient is investigated, and illustrated in Figure 2.16. Just like the first-order plot shown in Figure 2.14, the coupling coefficient is shown as a function of W_B for various values of W_T. Both W_B and W_T are normalised with respect to the second-order corrugation period, Λ. As observed in Figure 2.16, there exist two peak values of coupling coefficients along the W_B/Λ axis for each selected value of W_T/Λ chosen. In between the peaks there are places where the coupling coefficient drops to zero value. It is believed that the electric field diffracted by the second-order corrugation is completely out of phase with the incident wave. Therefore, zero coupling coefficients follow at that particular corrugation shape. The maximum coupling coefficient value of about 26.9/mm is located near the point when $W_B/\Lambda = 0.25$ and $W_T/\Lambda = 0.75$. Compared with the results from the first-order coupling coefficient, we can see significant changes in the magnitude of the maximum coupling coefficient as well as the normalised corrugation width associated with it.

Table 2.4 Structural parameters used in determining the coupling coefficient of the second-order trapezoidal corrugation

$m = 2$
$d_2 = d_4 = 200\ \mu m$
$d_3 = 100\ \mu m$
$n_1 = n_5 = 3.17$
$n_2 = n_4 = 3.405$
$n_3 = 3.553$
$g = 150\ nm$

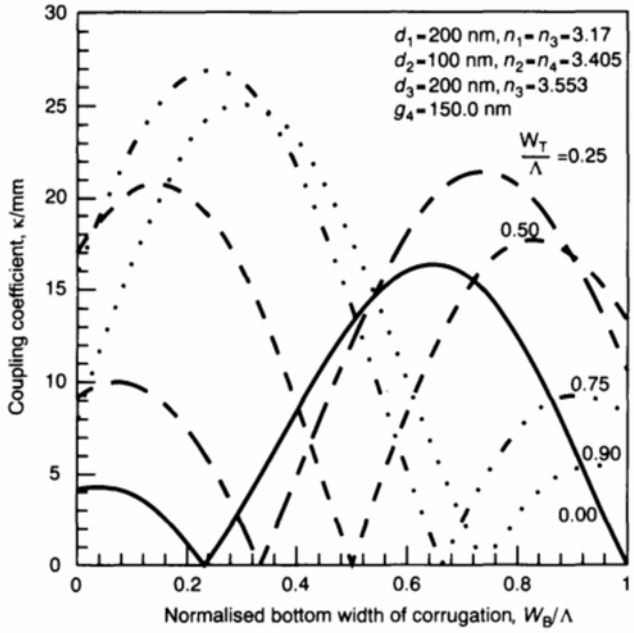

Figure 2.16 The change in the second-order coupling coefficient with W_B/Λ for different values of W_T/Λ.

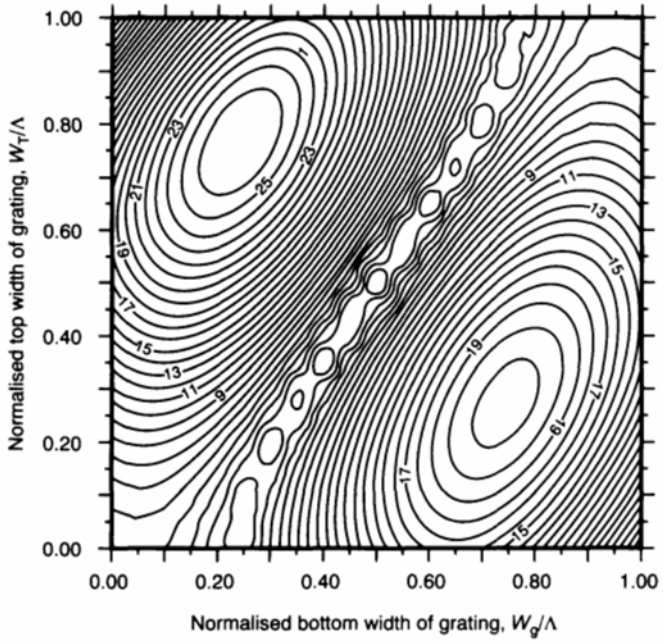

Figure 2.17 Contour map showing the coupling coefficient κ for the second-order trapezoidal corrugation.

From the contour map as shown in Figure 2.17, we can obtain a better understanding of the change in the coupling coefficient with a continuous change of corrugation shapes. Rather than a single peak, as seen earlier in the first-order contour map, two outstanding peaks can be observed. For an effective optical feedback in DFB lasers, a device engineer must be aware of the specific corrugation shapes in second-order corrugation design that may lead to extremely low values of the coupling coefficient. The FP effect due to non-zero facet reflection has to be considered in DFB lasers when the value of the coupling coefficient becomes small.

The corrugation of both the first- and second-order gratings has been computed for the fundamental TE mode in a five-layer slab waveguide structure. It has been found that a larger value of the coupling coefficient can be obtained when second-order corrugation is used. However, the design of the second-order grating requires precise control of the grating parameters. It is shown in the contour that certain corrugation shapes may lead to very low values of the coupling coefficient. Impacts due to variations in the lateral electric field [31,38], any misalignment or curvature [39], and any deformation [40] of corrugations which may form during the fabrication process, have been explored in other references and will not be discussed further.

2.6 SUMMARY

In this chapter, the operational principles of lasers, in particular the semiconductor laser, are presented. To build a self-sustained oscillator like a laser, it is important that the condition of population inversion is satisfied and an optical resonator is formed. The FP semiconductor laser, which forms the simplest optical resonant cavity, has limited applications owing to its broad gain spectrum. Multimode oscillations and unstable mode hopping are common in this type of laser. In optical coherent communication systems it is important that the optical source generates a single stable longitudinal mode output. With built-in periodic corrugations along the direction of propagation, an SLM operation becomes feasible in the DFB semiconductor laser. The built-in corrugation acts as an optical bandpass filter so that only frequencies with components near the Bragg frequency are allowed to pass. The operational principles of DFB LDs was explained with the help of coupled-wave equations. From the nature of the coupling coefficient, DFB semiconductor lasers can be classified into purely index-coupled, mixed-coupled and purely gain- or loss-coupled structures. The magnitude of the coupling coefficient, and hence the optical feedback, depends on the corrugation. Using the Fourier series technique, the coupling coefficient of a five-layer SCH structure was computed. Contours showing the relationship between the coupling coefficient and the physical dimensions of the corrugation were shown for both first- and second-order Bragg diffraction.

2.7 REFERENCES

[1] Yariv, A., *Quantum Electronics*, 3rd edition. New York: Wiley, 1989.

[2] Yariv, A., *Optical Electronics*, 4th edition. Orlando, FL: Saunders College Publishing, 1991.

[3] Casey, Jr., H.C. and Panish, M.B., *Heterostucture Lasers Part A: Fundamental Principles*. New York: Academic Press, 1978.

[4] Agrawal, G.P. and Dutta, N.K., *Long-wavelength Semiconductor Lasers*. Princeton, NJ: Van Nostrand, 1986.

[5] Petermann, K., *Laser Diode Modulation and Noise*. Tokyo, Japan: KTK Scientific and Kluwer Academic Publishers, 1988.

[6] Adams, M.J., Steventon, A.G., Delvin, W.J. and Henning, I.D., *Semiconductor Lasers for Long-wavelength Optical-fibre Communications Systems*, IEE Material and Devices Series, ed. N. Parkman and D.V. Morgan, no. 4. London: Peter Peregrinus, 1987.

[7] Lasher, G. and Stern, F., "Spontaneous and stimulated recombination radiation in semiconductor", *Phys. Rev.*, **133**, no. 2A, pp. 553-563, 1964.

[8] Osinski, M. and Adams, M.J., "Gain spectra of quaternary semiconductor", *IEE Proc.*, **129**, pt. I, no. 3, pp. 229-236, 1982.

[9] Ghafouri-Shiraz, H., "Temperature, bandgap-wavelength, and doping dependence of peak-gain coefficient parabolic model parameters for InGaAsP/InP semiconductor laser", *J. Lightwave Technol.*, **LT-6**, no. 4, pp. 500-506, 1988.

[10] Westbrook, L.D., "Measurement of dg/dN and dn/dN and their dependence on photon energy in $\lambda = 1.5$ μm InGaAsP laser diodes", *IEE Proc. Pt. J*, **133**, no. 2, pp. 135-143, 1985.

[11] Bissessur, H., "Effects of hole burning, carrier-induced losses and the carrier-dependent differential gain on the static characteristics of DFB lasers", *J. Lightwave Technol.*, **LT-10**, no. 11, pp. 1617-1630, 1992.

[12] Chu, C.Y.J. and Ghafouri-Shiraz, H., "A simple method to determine carrier recombinations in a semiconductor laser optical amplifier", *IEEE Photon. Tech. Lett.*, **5**, no. 10, pp. 1182-1185, 1994.

[13] Manning, J., Olshansky, R. and Su, C.B., "The carrier-induced index change in AlGaAS and 1.30 μm InGaAsP diode lasers", *IEEE J. Quantum Electron.*, **QE-19**, no. 10, pp. 1525-1530, 1983.

[14] Bennett, B.R., Soref, R.A. and Alamo, A. D., "Carrier-induced change in refractive index in InP, GaAs and InGaAsP", *IEEE J. Quantum Electron.*, **QE-26**, no. 1, pp. 113-122, 1990.

[15] Kotaki, Y. and Ishikawa, H., "Wavelength tunable of DFB and DBR lasers for coherent optical fibre communications", *IEE Proc. Pt. J*, **138**, no. 2, pp. 171-177, 1991.

[16] Kogelnik, H. and Shank, C.V., "Coupled-wave theory of distributed feedback lasers", *J. Appl. Phys.*, **43**, no. 5, pp. 2327-2335, 1972.

[17] Kogelnik, H., "Coupled wave theory for thick hologram grating", *Bell System Tech. J.*, **48**, pp. 2909-2947, 1969.

[18] Wang, S., "Principles of distributed feedback and distributed Bragg reflector lasers", *IEEE J. Quantum Electron.*, **QE-10**, no. 4, pp. 413-427, 1974.

[19] Yariv, A. and Gower, A., "Equivalent of the coupled mode and Floquet-Bloch formalism in periodic optical waveguide", *Appl. Phys. Lett.*, **26**, pp. 537-539, 1975.

[20] Streifer, W., Burnham, R.D. and Scifres, D.R., "Effect of external reflectors on longitudinal modes of distributed feedback laser", *IEEE J. Quantum Electron.*, **QE-11**, no. 4, pp. 154-161, 1975.

[21] Balanis, C.A., *Advances in Engineering Electromagnetics*. New York: John Wiley & Sons, 1989.

[22] David, K., Morthier, G., Vankvikelberge, P., Baets, R., Wolf, T. and Borchert, B., "Gain-coupled DFB lasers versus index-coupled and phase-shifted DFB lasers: A comparison based on spatial hole burning corrected yield", *IEEE J. Quantum Electron.*, **27**, no. 6, pp. 1714-1724, 1991.

[23] David, K., Buus, J., Morthier, G., and Baets, R., "Coupling coefficient in gain-coupled DFB lasers: Inherent compromise between strength and loss", *Photon. Technol. Lett.*, **3**, no. 5, pp. 439-441, 1991.

[24] David, K., Buus, J. and Baets, R., "Basic analysis of AR-coated. partly gain-coupled DFB lasers: The standing wave effect", *IEEE J. Quantum Electron.*, **28**, no. 2, pp. 427-433, 1992.

[25] Luo, Y., Nakano, Y., Tada, K., Inoue, T., Homsomatsu, H. and Iwaoka, H., "Fabrication and characteristics of gain-coupled distributed feedback semiconductor lasers with a corrugated active layer", *IEEE. J. Quantum Electron.*, **QE-27**, no. 6, pp. 1724-1732, 1991.

[26] Nakano, Y., Luo, Y. and Tada, K., "Facet reflection independent, single longitudinal mode oscillation in a GaAlAs/GaAs distributed feedback laser equipped with a gain-coupling mechanism", *Appl. Phys. Lett.*, **55**, no. 16, pp. 1606-1608, 1989.

[27] David, K., Morthier, G., Vankvikelberge, P. and Baets, R., "Yield analysis of non-AR-coated DFB lasers with combined index and gain coupling", *Electron. Lett.*, **26**, no. 4, pp. 238-239, 1990.

[28] Luo, Y., Nakano, Y. and, Tada, K., "Purely gain-coupled distributed feedback semiconductor lasers", *Appl. Phys. Lett.*, **56**, no. 17, pp. 1620-1622, 1990.

[29] Morthier, G., Vankwikelberge, P., David, K. and Baets, R., "Improved performance of AR-coated DFB lasers by the introduction of gain coupling", *IEEE Photon. Technol. Lett.*, **2**, no. 3, pp. 170-172, 1990.

[30] Kapon, E., Hardy, A. and Katzir, A., "The effect of complex coupling coefficients on distributed feedback lasers", *IEEE J. Quantum Electron.*, **QE-18**, no. 1, pp. 66-71, 1982.

[31] Streifer, W., Scifres, D.R. and Burnham, R.D., "Analysis of grating-coupled radiation in GaAs:GaAlAs lasers and waveguides", *IEEE J. Quantum Electron.*, **QE-12** no. 7, pp. 422-428, 1976.

[32] Streifer, W., Scifres, D.R. and Burnham, R.D., "Coupling coefficient for distributed feedback single- and double-heterostructure diode laser", *IEEE J. Quantum Electron.*, **QE-11**, no. 11, pp. 867-873, 1975.

[33] Correc, P., "Coupling coefficient for trapezoidal grating", *IEEE J. Quantum Electron.*, **QE-24**, no. 1, pp. 8-10, 1988.

[34] Ghafouri-Shiraz, H. and Lo, B., "Computation of coupling coefficient for a five-layer trapezoidal grating structure", *Opt. Laser Technol.*, **27**, no. 1, pp. 45-48, 1994.

[35] Handa, K., Peng, S.T. and Tamir, T., " Improved perturbation analysis of dielectric gratings", *Appl. Phys.*, **5**, pp. 325-328, 1975.

[36] Ghafouri-Shiraz, H., "Single transverse mode condition in long wavelength SCH semiconductor laser diodes", *Trans. IEICE*, **E 70**, no. 2, pp. 130-134, 1987.

[37] Adams, M.J. and Wyatt, R., *An Introduction to Optical Waveguides*. London: John Wiley & Sons, 1981.

[38] Kazarinov, R.F. and Henry, C.H., "Second-order distributed feedback lasers with mode selection provided by first-order radiation losses", *IEEE J. Quantum Electron.*, **QE-21**, no. 2, pp. 144-150 ,1985.

[39] Streifer W. and Hardy A., "Analysis of two dimensional waveguides with misaligned or curved gratings", *IEEE J. Quantum Electron.*, **QE-14**, no. 12, pp. 935-943, 1978.

[40] Correc P., "Coupling coefficients for partially meltback trapezoidal gratings", *IEEE J. Quantum Electron.*, **QE-24**, no. 10, pp. 1963-1965, 1988.

3

STRUCTURAL IMPACTS ON THE SOLUTIONS OF COUPLED-WAVE EQUATIONS: AN OVERVIEW

3.1 INTRODUCTION

The introduction of semiconductor lasers has boosted the development of coherent optical communication systems. With the built-in wavelength selection mechanism, distributed feedback (DFB) semiconductor laser diodes (LDs) having a higher gain margin are superior to the Fabry–Perot (FP) laser in such a way that a single longitudinal mode (SLM) of lasing can be achieved.

In this chapter, results obtained from the threshold analysis of the conventional and single-phase shifted DFB lasers will be discussed. In particular, structural impacts on the threshold characteristic will be discussed in a systematic way. In section 3.4, the lasing characteristic of the conventional DFB LD will be presented, whilst the effects of the residue corrugation phase at the laser facets will be discussed in section 3.5. By introducing a phase shift along the corrugations of DFB LDs, the degenerate oscillating characteristic of the conventional DFB LD can be removed. In section 3.6, structural impacts due to the phase shift and the corresponding phase shift position (PSP) will be considered.

As mentioned in Chapter 2, the introduction of the coupling coefficient κ in the coupled wave equations plays a vital role because it measures the strength of feedback provided by the corrugation. In section 3.7 the effect of corrugation shape on the magnitude of κ will be presented. With a $\pi/2$ phase shift fabricated at the centre of the DFB cavity, the quarterly wavelength shifted (QWS) DFB LD oscillates at the Bragg wavelength. However, the

deterioration of the gain margin limits its use as the current injection increases. This phenomenon, induced by the spatial hole burning effect, which is the major drawback of the QWS laser structure, will be examined at the end of the chapter. The limited application of the eigenvalue equation in solving the coupled-wave equations will also be considered.

3.2 SOLUTIONS OF THE COUPLED-WAVE EQUATIONS

From Chapter 2 we know that the characteristics of DFB LDs can be described by a pair of coupled-wave equations. The strength of the feedback induced by the perturbed refractive index or gain is measured by the coupling coefficient. Relationships between the forward and the backward coupling coefficients, κ_{RS} and κ_{SR}, were derived for the purely index-coupled, mixed-coupled and the purely gain-coupled structures. By assuming a zero phase difference between the index and the gain term, the complex coupling coefficient could be expressed as

$$\kappa_{RS} = \kappa_{SR} = \kappa_i + j\kappa_g = \kappa \tag{3.2.1}$$

where κ becomes a complex coupling coefficient. According to equation (2.4.21) in Chapter 2, a trial solution of the coupled-wave equation can be expressed in terms of the Bragg propagation constant such that

$$E(z) = R(z)e^{-j\beta_0 z} + S(z)e^{j\beta_0 z} \tag{3.2.2}$$

where the leading coefficients, $R(z)$ and $S(z)$ are reported as [1]

$$R(z) = R_1 e^{(\gamma L)} + R_2 e^{(-\gamma L)} \tag{3.2.3a}$$

and

$$S(z) = S_1 e^{(\gamma L)} + S_2 e^{(-\gamma L)} \tag{3.2.3b}$$

In the above equations, R_1, R_2, S_1 and S_2 are complex coefficients and γ is the complex propagation constant to be determined from the boundary conditions at the laser facets. Without loss of generality, we can assume $\mathrm{Re}(\gamma) > 0$. As a result, those terms with leading coefficients R_1 and S_2 become amplified as the waves propagate along the cavity. On the contrary, those terms with R_2 and S_1 as leading coefficients are attenuated. By combining the above equations with (3.2.2), we can easily show that the propagation constant of the amplified waves becomes $\beta_0 - \mathrm{Im}(\gamma)$, whilst the decaying waves propagate at $\beta_0 + \mathrm{Im}(\gamma)$.

By substituting equations (3.2.3a) and (3.2.3b) into the coupled-waves equations, the following relations are obtained by collecting identical exponential terms [2]:

$$\hat{\Gamma} R_1 = j\kappa e^{-j\Omega} S_1 \tag{3.2.4a}$$

$$\Gamma R_2 = j\kappa e^{-j\Omega} S_2 \tag{3.2.4b}$$

$$\Gamma S_1 = j\kappa e^{j\Omega} R_1 \tag{3.2.4c}$$

$$\hat{\Gamma} S_2 = j\kappa e^{j\Omega} R_2 \tag{3.2.4d}$$

where

$$\hat{\Gamma} = \alpha_s - j\delta - \gamma \tag{3.2.5a}$$

$$\Gamma = \alpha_s - j\delta + \gamma \tag{3.2.5b}$$

By comparing the equations (3.2.4a) and (3.2.4c), a non-trivial solution exists if the following equation is satisfied:

$$\rho = \frac{\hat{\Gamma}}{j\kappa} = \frac{j\kappa}{\Gamma} \tag{3.2.6}$$

On the basis of the equation shown above, equation (3.2.4) is simplified to become:

$$R_1 = \frac{1}{\rho} e^{-j\Omega} S_1 \tag{3.2.7a}$$

$$R_2 = \rho e^{-j\Omega} S_2 \tag{3.2.7b}$$

Similarly, by equating equations (3.2.4a) with (3.2.4c), we obtain:

$$\gamma^2 = (\alpha_s - j\delta)^2 + \kappa^2 \tag{3.2.8}$$

It is important that the dispersion equation shown above is independent of the residue corrugation phase, Ω.

With a finite laser cavity length of L extending from $z = z_1$ to $z = z_2$ (where both z_1 and z_2 are assumed to be greater than zero), the boundary conditions at the terminating facets become

$$R(z_1) e^{-j\beta_0 z_1} = \hat{r}_1 S(z_1) e^{j\beta_0 z_1} \tag{3.2.9a}$$

$$S(z_2) e^{j\beta_0 z_2} = \hat{r}_2 R(z_2) e^{-j\beta_0 z_2} \tag{3.2.9b}$$

where $\hat{r}_1$ and $\hat{r}_2$ are amplitude reflection coefficients at the laser facets z_1 and z_2, respectively. According to equations (3.2.3) and (3.2.4), the above equations could be expanded in such a way that

$$R_2 = \frac{(1 - \rho r_1) e^{2\gamma z_1}}{r_1/\rho - 1} \cdot R_1 \tag{3.2.10a}$$

$$R_2 = \frac{(r_2 - \rho) e^{2\gamma z_2}}{1/\rho - r_2} \cdot R_1 \tag{3.2.10b}$$

In the above equation, all the $R(z)$ and $S(z)$ terms are expressed in terms of R_1 and R_2, whilst r_1 and r_2 are the complex field reflectivity of the left and the right facets, respectively, such that

$$r_1 = \hat{r}_1 e^{2j\beta_0 z_1} e^{j\Omega} = \hat{r}_1 e^{j\Psi_1} \tag{3.2.11a}$$

$$r_2 = \hat{r}_2 e^{-2j\beta_0 z_2} e^{-j\Omega} = \hat{r}_2 e^{j\Psi_2} \tag{3.2.11b}$$

where ψ_1 and ψ_2 are the corresponding corrugation phase at the facets. Equations (3.2.10a) and (3.2.10b) are homogeneous in R_1 and R_2. To obtain a non-trivial solution, the following solution must be satisfied:

$$\frac{(1-\rho r_1)e^{2\gamma z_1}}{r_1-\rho} = \frac{(r_2-\rho)e^{2\gamma z_2}}{1-\rho r_2} \tag{3.2.12}$$

Then, the above equation can be solved for ρ and $1/\rho$ whilst employing the relation

$$\gamma = \frac{-j\kappa}{2}\left(\rho - \frac{1}{\rho}\right) \tag{3.2.13}$$

derived from equations (3.2.5a) and (3.2.5b). After some lengthy manipulation [2], we end up with an eigenvalue equation:

$$\gamma L = \frac{-j\kappa \sinh(\gamma L)}{D} \cdot \left\{(r_1+r_2)(1-r_1r_2)\cosh(\gamma L) \pm (1+r_1r_2)\Delta^{1/2}\right\} \tag{3.2.14}$$

where

$$\Delta = (r_1-r_2)^2\sinh^2(\gamma L) + (1-r_1r_2)^2 \tag{3.2.15a}$$

$$D = (1+r_1r_2)^2 - 4r_1r_2\cosh^2(\gamma L) \tag{3.2.15b}$$

$$r_1 = \hat{r}_1 e^{2j\beta_0 z_1} e^{j\Omega} = \hat{r}_1 e^{j\psi_1} \tag{3.2.15c}$$

$$r_2 = \hat{r}_2 e^{-2j\beta_0 z_2} e^{-j\Omega} = \hat{r}_2 e^{j\psi_2} \tag{3.2.15d}$$

By squaring equation (3.2.1) and after some simplification, we end up with a transcendental function:

$$\begin{aligned}(\gamma L)^2 + (\kappa L)^2\sinh^2(\gamma L)(1-r_1^2)(1-r_2^2) \\ + 2j\kappa L(r_1+r_2)^2(1-r_1r_2)\gamma L\sinh(\gamma L)\cosh(\gamma L) = 0\end{aligned} \tag{3.2.16}$$

In the above equation there are four parameters which govern the threshold characteristics of DFB laser structures. These include the coupling coefficient κ, the laser cavity length L and the complex facet reflectivities r_1 and r_2. Owing to the complex nature of the above equation, numerical methods like the Newton–Raphson iteration technique can be used provided that the Cauchy–Riemann condition on complex analytical functions is satisfied.

Before stating the Newton–Raphson iteration, an initial value of $(\alpha, \delta)_{\text{ini}}$ is chosen from a selected range of (α, δ) values. Usually, the first selected guess will not be a solution of the threshold equation and hence the iteration continues. At the end of the first iteration, a new pair of (α', δ') will be generated and checked to see if they satisfy the threshold equation. The iteration will continue until the newly generated (α', δ') pair satisfy the threshold equation within a reasonable range of error. Starting with different initial guesses of $(\alpha, \delta)_{\text{ini}}$, other oscillating modes can also be determined in a similar way. By collecting all (α', δ') pairs that satisfy the threshold equation, the one that shows the smallest amplitude gain will then become the lasing

mode. The final value $(\alpha, \delta)_{\text{final}}$ is then stored up for later use, in which the threshold current and the lasing wavelength of the LD are to be decided. In general, equation (3.2.16) characterises all conventional DFB semiconductor LDs with continuous corrugations fabricated along the laser cavity.

3.3 SOLUTIONS OF COMPLEX TRANSCENDENTAL EQUATIONS USING THE NEWTON–RAPHSON APPROXIMATION

All complex transcendental equations can be expressed in a general form such that

$$W(z) = U(z) + jV(z) = 0 \tag{3.3.1}$$

where $z = x + jy$ is a complex number and $U(z)$ and $V(z)$ are, respectively, the real and imaginary parts of the complex function. From the above equation, we can deduce the following equality easily such that

$$U(z) = V(z) = 0 \tag{3.3.2}$$

By taking the first-order derivative of equation (3.3.1) with respect to z, we obtain

$$\frac{\partial W}{\partial z} = \frac{\partial U}{\partial z} + j\frac{\partial V}{\partial Z} = \frac{\partial U}{\partial x} + j\frac{\partial V}{\partial x} \tag{3.3.3}$$

The second equality sign can be obtained using the chain rule. Using the Taylor series, the functions $U(z)$ and $V(z)$ can be approximated about the exact solution $(x_{\text{req}}, y_{\text{req}})$ such that

$$U(x_{\text{req}}, y_{\text{req}}) = U(x, y) + \frac{\partial U}{\partial x}(x_{\text{req}} - x) + \frac{\partial U}{\partial y}(y_{\text{req}} - y) \tag{3.3.4}$$

$$V(x_{\text{req}}, y_{\text{req}}) = V(x, y) + \frac{\partial V}{\partial x}(x_{\text{req}} - x) + \frac{\partial V}{\partial y}(y_{\text{req}} - y) \tag{3.3.5}$$

where the (x, y) chosen are sufficiently closed to the exact solutions. Other higher derivative terms from the Taylor series have been ignored. We can obtain the following equations from the above simultaneous equations for x_{req} and y_{req} such that [2]

$$x_{\text{req}} = x + \frac{V(x, y)\dfrac{\partial U}{\partial y} - U(x, y)\dfrac{\partial V}{\partial y}}{\text{Det}} \tag{3.3.6}$$

$$y_{\text{req}} = y + \frac{U(x, y)\dfrac{\partial V}{\partial x} - V(x, y)\dfrac{\partial U}{\partial x}}{\text{Det}} \tag{3.3.7}$$

where

$$\text{Det} = \left(\frac{\partial U}{\partial x}\right)^2 + \left(\frac{\partial V}{\partial y}\right)^2 \tag{3.3.8}$$

Terms like $\partial U/\partial x$, $\partial V/\partial x$, $\partial U/\partial y$ and $\partial V/\partial y$ are the first derivatives of the functions $U(z)$ and $V(z)$.

For an analytical complex function $W(z)$, the Cauchy–Riemann condition must be satisfied, which states that [3]

$$\frac{\partial U}{\partial x} = \frac{\partial V}{\partial y}, \quad \frac{\partial U}{\partial y} = -\frac{\partial V}{\partial x} \tag{3.3.9}$$

On replacing all the $\partial/\partial y$ terms with $\partial/\partial x$ using the above Cauchy–Riemann condition, equations (3.3.6) and (3.3.8) can be simplified such that

$$\text{Det} = 2\left(\frac{\partial U}{\partial x}\right)^2 \tag{3.3.10}$$

$$x_{\text{req}} = x - \frac{V(x, y)\dfrac{\partial V}{\partial x} + U(x, y)\dfrac{\partial U}{\partial x}}{\text{Det}} \tag{3.3.11}$$

Here, only the first-order derivatives $\partial U/\partial x$ and $\partial V/\partial x$ are used where they can be determined from the complex function of equation (3.3.3).

Given an initial guess of (x, y), the numerical iteration process will then start. A new guess is generated after following equations (3.3.7), (3.3.10) and (3.3.11). Unless the new guess is sufficiently close to the exact solution (within 10^{-9}, say), the new guess solutions formed will become the initial guess for the next iteration. The iteration process continues until the approximated solutions of $(x_{\text{req}}, y_{\text{req}})$ appear.

The advantages of this method are its speed and flexibility. The derivative term $\partial W/\partial z$ is found analytically first before any numerical iteration is started. Using this method, we can avoid any errors associated with other numerical methods such as numerical differentiation.

3.4 CONCEPTS OF MODE DISCRIMINATION AND GAIN MARGIN

At a fixed value of κ, the pair $(\delta, \alpha)_{\text{final}}$ can be determined following the method as shown in the previous section. Each $(\delta, \alpha)_{\text{final}}$ pair, which represents an oscillation mode, is plotted on the δ–α plane. Similarly, $(\delta, \alpha)_{\text{final}}$ values can be obtained by changing the values of κ. By plotting all $(\delta, \alpha)_{\text{final}}$ points on the δ–α plane, the mode spectrum of the DFB LD is formed. A simplified δ–α plot is shown in Figure 3.1. Different symbols shown represent various longitudinal modes obtained for various coupling coefficient while the solid curve shows how longitudinal modes join to form an oscillating mode.

As the biasing current increases, the longitudinal mode showing the smallest amplitude gain will reach the threshold condition first and begin to lase. Other modes that fail to reach the threshold condition will then be suppressed and become non-lasing side modes. On the δ–α plane, the $\delta = 0$ line, or the Bragg wavelength, splits the δ–α plane into two halves. As we move along the positive δ-axis, any oscillation modes encountered will be

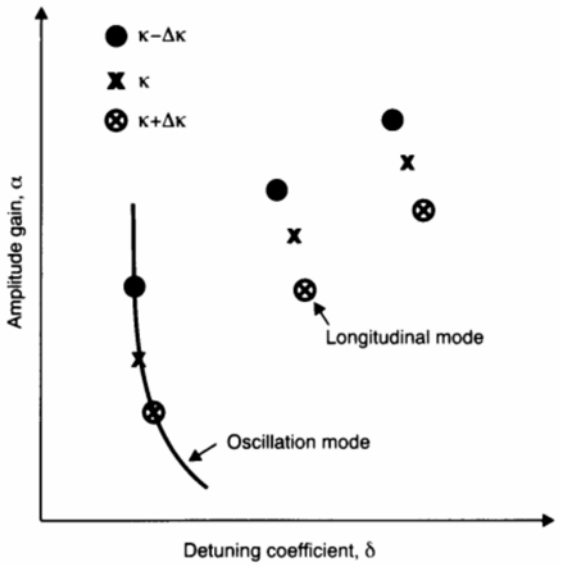

Figure 3.1 A simplified $\delta - \alpha$ plot showing the mode spectrum and the oscillating mode of a DFB LD. Different symbols are used to show longitudinal modes obtained from various κ values.

denoted as the +1, +2 modes, and so on. Similarly, negative modes such as −1, −2 are used for those found on the negative δ-axis.

The importance of the SLM in coherent optical communications was discussed in Chapter 1. To measure the stability of the lasing spectrum, we need to determine the amplitude gain difference between the lasing mode and the most probable side mode of the DFB laser [4,5]. A larger amplitude gain difference, better known as the gain margin ($\Delta\alpha$), implies a better mode discrimination. In other words, the SLM oscillation in the DFB LD involved is said to be more stable. In practice, the actual requirement of $\Delta\alpha$ may vary from one system to another depending on the encoding format (return to zero, RZ, or non-return to zero, NRZ), transmission rate, the biasing condition of the laser sources, and the length and the characteristics of the single mode fibre (SMF) used. A simulation based on a 20 km dispersive SMF [6] indicated that a $\Delta\alpha$ of 5/cm is required for a 2.4 Gb/s in order that a bit error rate, BER $< 10^{-9}$ can be achieved. A detailed analysis on the requirement of $\Delta\alpha$ under different system configurations is clearly beyond the scope of the present analysis. However, we get some idea of the typical value of gain margins required in a coherent optical communication system.

The value of the gain margin, however, is difficult to measure directly from an experiment. An alternative method is to measure the spontaneous emission spectrum. For a stable SLM source, a minimum of 25 dB side mode suppression ratio (SMSR) [7] between the power of the lasing mode and the most probable side mode is necessary.

3.5 THRESHOLD ANALYSIS OF A CONVENTIONAL DFB LASER DIODE

For a conventional DFB laser with a zero facet reflection, the threshold equation (3.2.16) becomes

$$j\gamma L = \pm\kappa L \sinh(\gamma L) \tag{3.5.1}$$

Using the Newton–Raphson iteration approach, the eigenvalue equation can be solved as a fixed coupling coefficient. Results obtained for the above equation are shown in Figure 3.2. All parameters used have been normalised with respect to the overall cavity length L. Discrete values of κL have been selected between 0.25 and 10.0. As shown in the inset of Figure 3.2, solutions obtained from various κL products are shown using different symbols. Oscillation modes are then formed by joining the appropriate solutions together. Solid lines have been used to represent the -4 to $+4$ modes. From the figure, it is clear that oscillating modes distribute symmetrically with respect to the Bragg wavelength whilst no oscillation is found at the Bragg wavelength. Furthermore, it can be seen that the $+1$ and -1 modes with different lasing wavelengths will share the same amplitude gain. As a result, degenerate oscillation occurs and these modes will have the same chance to lase once the lasing condition is reached. Figure 3.2 also reveals that the amplitude threshold gain decreases with increasing values of κL. Since a larger value of κ implies a stronger optical feedback, a smaller threshold gain results. Similarly, lasers with a long cavity length help to reduce the amplitude gain because a larger single pass gain can be achieved.

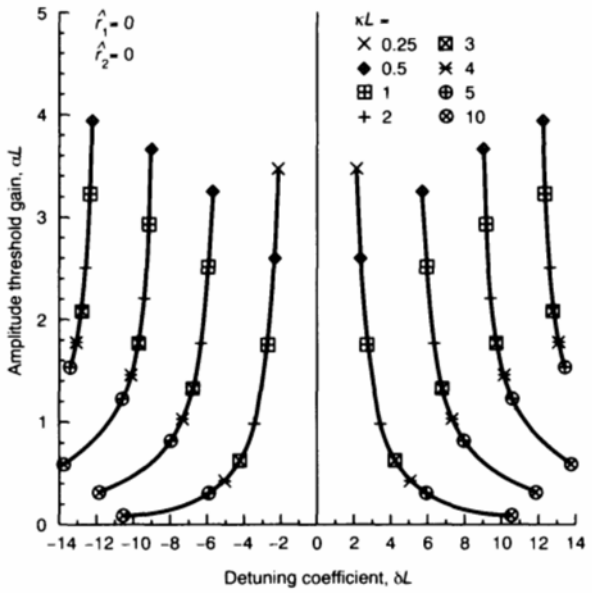

Figure 3.2 Relationship between the amplitude threshold gain and the detuning coefficient of a mirrorless index-coupled DFB LD.

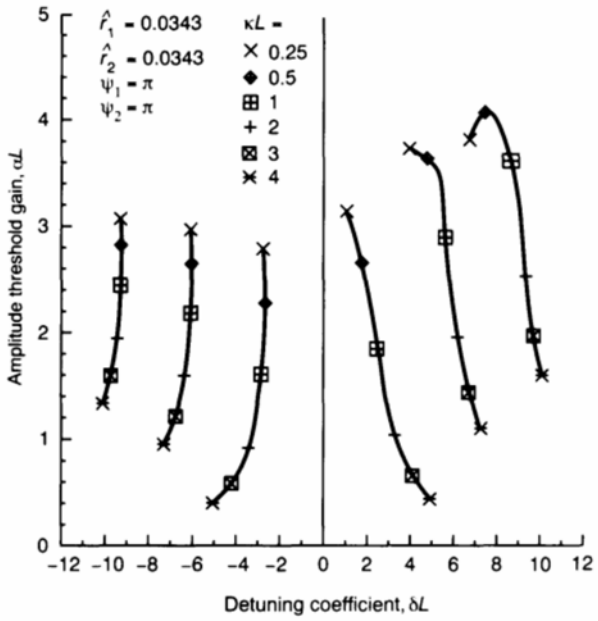

Figure 3.3 Relationship between the amplitude threshold gain and the detuning coefficient of a DFB LD with finite reflectivities.

With no oscillation found at the Bragg wavelength, a stopband region is formed between the $+1$ and -1 modes of the conventional mirrorless DFB LD. From Figure 3.2, we conclude that the normalised stopband width is a function of κL. Although the change in stopband width becomes less noticeable at lower values of κL, the measurement of the stopband width has been used to determine the coupling coefficient of DFB LDs [8]. Figure 3.3 shows the characteristic of a DFB LD with finite facet reflections. It is shown in the figure that the mode distribution is no longer symmetric and no oscillation is found at the Bragg wavelength. The -1 mode with the smallest amplitude gain becomes the lasing mode.

3.6 IMPACT OF THE CORRUGATION PHASE AT LASER FACETS

So far, symmetric laser cavities that share identical facet reflectivities have been used. To understand the effects of the residue phases at the facets [2, 9], asymmetric cavities are considered. The threshold characteristic of one of these asymmetric DFB LDs is shown in Figure 3.4. The amplitude reflectivity $\hat{r}_1 = 0.0343$ is assumed, whilst the other facet is assumed to be naturally cleaved such that $\hat{r}_2 = 0.535$. Discrete values of κL have been chosen. In the figure, the corrugation phase ψ_1 is fixed at π whilst ψ_2 changes in steps of $\pi/2$. Different symbol markers have been used to represent different ψ_2. Solutions obtained from the same κL product are joined together as usual to form the oscillation mode. Let us consider $\kappa L = 1.0$ as an example. It can be

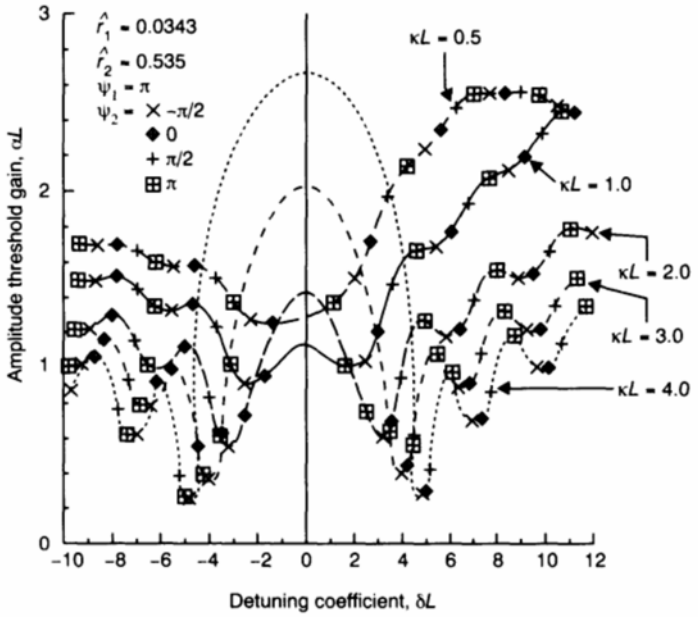

Figure 3.4 The lasing characteristic of a DFB LD having asymmetric facet reflection. The corrugation phase ψ_1 is fixed while ψ_2 is allowed to change. Results obtained for various κL products are compared.

seen that the lasing mode changes from the negative to the positive mode as the facet phase ψ_2 changes from $-\pi/2$ to π. For $\kappa L > 1.0$, the amplitude gain at the Bragg wavelength remains so high that it never reaches the threshold condition. The -1 mode showing the smallest amplitude gain becomes the dominant lasing mode.

By replacing the natural cleaved facet with a highly reflective surface such that $\hat{r}_2 = 1.0$, the lasing characteristic of the new structure is shown in Figure 3.5. Various values of κL have been used for comparison. Similar to the one shown in Figure 3.4, the oscillation mode shifts from the -1 to the $+1$ mode when ψ_2 changes from $-\pi/2$ to $\pi 4$. From both Figures 3.4 and 3.5 it is clear that SLM operation depends on both the facet reflectivity and the associated phase. However, due to tolerances inherent during the fabrication process, it is difficult to control accurately the corrugation phase at the laser facets [10].

Various methods have been proposed for adjusting the corrugation phase. One such method is to use the ion beam etching technique [11,12]. A continuous flux of neutralised argon gas, which acts as an abrasive tool, is targeted at one laser facet. By abrading the facet slowly across the beam at a constant rate, a 20–50 nm depth can be etched away at the laser facet in a single process. An annealing process is usually applied afterwards. Experimental results [11,12] also show that the annealing process has no significant variation in the threshold and the external quantum efficiency in

$$\Gamma S_1 = j\kappa e^{j\Omega} R_1 \tag{3.2.4c}$$

$$\hat{\Gamma} S_2 = j\kappa e^{j\Omega} R_2 \tag{3.2.4d}$$

where

$$\hat{\Gamma} = \alpha_s - j\delta - \gamma \tag{3.2.5a}$$

$$\Gamma = \alpha_s - j\delta + \gamma \tag{3.2.5b}$$

By comparing the equations (3.2.4a) and (3.2.4c), a non-trivial solution exists if the following equation is satisfied:

$$\rho = \frac{\hat{\Gamma}}{j\kappa} = \frac{j\kappa}{\Gamma} \tag{3.2.6}$$

On the basis of the equation shown above, equation (3.2.4) is simplified to become:

$$R_1 = \frac{1}{\rho} e^{-j\Omega} S_1 \tag{3.2.7a}$$

$$R_2 = \rho e^{-j\Omega} S_2 \tag{3.2.7b}$$

Similarly, by equating equations (3.2.4a) with (3.2.4c), we obtain:

$$\gamma^2 = (\alpha_s - j\delta)^2 + \kappa^2 \tag{3.2.8}$$

It is important that the dispersion equation shown above is independent of the residue corrugation phase, Ω.

With a finite laser cavity length of L extending from $z = z_1$ to $z = z_2$ (where both z_1 and z_2 are assumed to be greater than zero), the boundary conditions at the terminating facets become

$$R(z_1) e^{-j\beta_0 z_1} = \hat{r}_1 S(z_1) e^{j\beta_0 z_1} \tag{3.2.9a}$$

$$S(z_2) e^{j\beta_0 z_2} = \hat{r}_2 R(z_2) e^{-j\beta_0 z_2} \tag{3.2.9b}$$

where $\hat{r}_1$ and $\hat{r}_2$ are amplitude reflection coefficients at the laser facets z_1 and z_2, respectively. According to equations (3.2.3) and (3.2.4), the above equations could be expanded in such a way that

$$R_2 = \frac{(1 - \rho r_1) e^{2\gamma z_1}}{r_1/\rho - 1} \cdot R_1 \tag{3.2.10a}$$

$$R_2 = \frac{(r_2 - \rho) e^{2\gamma z_2}}{1/\rho - r_2} \cdot R_1 \tag{3.2.10b}$$

In the above equation, all the $R(z)$ and $S(z)$ terms are expressed in terms of R_1 and R_2, whilst r_1 and r_2 are the complex field reflectivity of the left and the right facets, respectively, such that

$$r_1 = \hat{r}_1 e^{2j\beta_0 z_1} e^{j\Omega} = \hat{r}_1 e^{j\Psi_1} \tag{3.2.11a}$$

$$r_2 = \hat{r}_2 e^{-2j\beta_0 z_2} e^{-j\Omega} = \hat{r}_2 e^{j\Psi_2} \tag{3.2.11b}$$

where ψ_1 and ψ_2 are the corresponding corrugation phase at the facets. Equations (3.2.10a) and (3.2.10b) are homogeneous in R_1 and R_2. To obtain a non-trivial solution, the following solution must be satisfied:

$$\frac{(1-\rho r_1)e^{2\gamma z_1}}{r_1-\rho} = \frac{(r_2-\rho)e^{2\gamma z_2}}{1-\rho r_2} \tag{3.2.12}$$

Then, the above equation can be solved for ρ and $1/\rho$ whilst employing the relation

$$\gamma = \frac{-j\kappa}{2}\left(\rho - \frac{1}{\rho}\right) \tag{3.2.13}$$

derived from equations (3.2.5a) and (3.2.5b). After some lengthy manipulation [2], we end up with an eigenvalue equation:

$$\gamma L = \frac{-j\kappa \sinh(\gamma L)}{D} \cdot \left\{(r_1+r_2)(1-r_1r_2)\cosh(\gamma L) \pm (1+r_1r_2)\Delta^{1/2}\right\} \tag{3.2.14}$$

where

$$\Delta = (r_1-r_2)^2\sinh^2(\gamma L) + (1-r_1r_2)^2 \tag{3.2.15a}$$

$$D = (1+r_1r_2)^2 - 4r_1r_2\cosh^2(\gamma L) \tag{3.2.15b}$$

$$r_1 = \hat{r}_1 e^{2j\beta_0 z_1} e^{j\Omega} = \hat{r}_1 e^{j\psi_1} \tag{3.2.15c}$$

$$r_2 = \hat{r}_2 e^{-2j\beta_0 z_2} e^{-j\Omega} = \hat{r}_2 e^{j\psi_2} \tag{3.2.15d}$$

By squaring equation (3.2.1) and after some simplification, we end up with a transcendental function:

$$\begin{aligned}(\gamma L)^2 + (\kappa L)^2\sinh^2(\gamma L)(1-r_1^2)(1-r_2^2) \\ + 2j\kappa L(r_1+r_2)^2(1-r_1r_2)\gamma L\sinh(\gamma L)\cosh(\gamma L) = 0\end{aligned} \tag{3.2.16}$$

In the above equation there are four parameters which govern the threshold characteristics of DFB laser structures. These include the coupling coefficient κ, the laser cavity length L and the complex facet reflectivities r_1 and r_2. Owing to the complex nature of the above equation, numerical methods like the Newton–Raphson iteration technique can be used provided that the Cauchy–Riemann condition on complex analytical functions is satisfied.

Before stating the Newton–Raphson iteration, an initial value of $(\alpha, \delta)_{\text{ini}}$ is chosen from a selected range of (α, δ) values. Usually, the first selected guess will not be a solution of the threshold equation and hence the iteration continues. At the end of the first iteration, a new pair of (α', δ') will be generated and checked to see if they satisfy the threshold equation. The iteration will continue until the newly generated (α', δ') pair satisfy the threshold equation within a reasonable range of error. Starting with different initial guesses of $(\alpha, \delta)_{\text{ini}}$, other oscillating modes can also be determined in a similar way. By collecting all (α', δ') pairs that satisfy the threshold equation, the one that shows the smallest amplitude gain will then become the lasing

mode. The final value $(\alpha, \delta)_{\text{final}}$ is then stored up for later use, in which the threshold current and the lasing wavelength of the LD are to be decided. In general, equation (3.2.16) characterises all conventional DFB semiconductor LDs with continuous corrugations fabricated along the laser cavity.

3.3 SOLUTIONS OF COMPLEX TRANSCENDENTAL EQUATIONS USING THE NEWTON–RAPHSON APPROXIMATION

All complex transcendental equations can be expressed in a general form such that

$$W(z) = U(z) + jV(z) = 0 \tag{3.3.1}$$

where $z = x + jy$ is a complex number and $U(z)$ and $V(z)$ are, respectively, the real and imaginary parts of the complex function. From the above equation, we can deduce the following equality easily such that

$$U(z) = V(z) = 0 \tag{3.3.2}$$

By taking the first-order derivative of equation (3.3.1) with respect to z, we obtain

$$\frac{\partial W}{\partial z} = \frac{\partial U}{\partial z} + j\frac{\partial V}{\partial Z} = \frac{\partial U}{\partial x} + j\frac{\partial V}{\partial x} \tag{3.3.3}$$

The second equality sign can be obtained using the chain rule. Using the Taylor series, the functions $U(z)$ and $V(z)$ can be approximated about the exact solution $(x_{\text{req}}, y_{\text{req}})$ such that

$$U(x_{\text{req}}, y_{\text{req}}) = U(x, y) + \frac{\partial U}{\partial x}(x_{\text{req}} - x) + \frac{\partial U}{\partial y}(y_{\text{req}} - y) \tag{3.3.4}$$

$$V(x_{\text{req}}, y_{\text{req}}) = V(x, y) + \frac{\partial V}{\partial x}(x_{\text{req}} - x) + \frac{\partial V}{\partial y}(y_{\text{req}} - y) \tag{3.3.5}$$

where the (x, y) chosen are sufficiently closed to the exact solutions. Other higher derivative terms from the Taylor series have been ignored. We can obtain the following equations from the above simultaneous equations for x_{req} and y_{req} such that [2]

$$x_{\text{req}} = x + \frac{V(x, y)\dfrac{\partial U}{\partial y} - U(x, y)\dfrac{\partial V}{\partial y}}{\text{Det}} \tag{3.3.6}$$

$$y_{\text{req}} = y + \frac{U(x, y)\dfrac{\partial V}{\partial x} - V(x, y)\dfrac{\partial U}{\partial x}}{\text{Det}} \tag{3.3.7}$$

where

$$\text{Det} = \left(\frac{\partial U}{\partial x}\right)^2 + \left(\frac{\partial V}{\partial y}\right)^2 \tag{3.3.8}$$

Terms like $\partial U/\partial x$, $\partial V/\partial x$, $\partial U/\partial y$ and $\partial V/\partial y$ are the first derivatives of the functions $U(z)$ and $V(z)$.

For an analytical complex function $W(z)$, the Cauchy–Riemann condition must be satisfied, which states that [3]

$$\frac{\partial U}{\partial x} = \frac{\partial V}{\partial y}, \quad \frac{\partial U}{\partial y} = -\frac{\partial V}{\partial x} \tag{3.3.9}$$

On replacing all the $\partial/\partial y$ terms with $\partial/\partial x$ using the above Cauchy–Riemann condition, equations (3.3.6) and (3.3.8) can be simplified such that

$$\text{Det} = 2\left(\frac{\partial U}{\partial x}\right)^2 \tag{3.3.10}$$

$$x_{\text{req}} = x - \frac{V(x, y)\dfrac{\partial V}{\partial x} + U(x, y)\dfrac{\partial U}{\partial x}}{\text{Det}} \tag{3.3.11}$$

Here, only the first-order derivatives $\partial U/\partial x$ and $\partial V/\partial x$ are used where they can be determined from the complex function of equation (3.3.3).

Given an initial guess of (x, y), the numerical iteration process will then start. A new guess is generated after following equations (3.3.7), (3.3.10) and (3.3.11). Unless the new guess is sufficiently close to the exact solution (within 10^{-9}, say), the new guess solutions formed will become the initial guess for the next iteration. The iteration process continues until the approximated solutions of $(x_{\text{req}}, y_{\text{req}})$ appear.

The advantages of this method are its speed and flexibility. The derivative term $\partial W/\partial z$ is found analytically first before any numerical iteration is started. Using this method, we can avoid any errors associated with other numerical methods such as numerical differentiation.

3.4 CONCEPTS OF MODE DISCRIMINATION AND GAIN MARGIN

At a fixed value of κ, the pair $(\delta, \alpha)_{\text{final}}$ can be determined following the method as shown in the previous section. Each $(\delta, \alpha)_{\text{final}}$ pair, which represents an oscillation mode, is plotted on the δ–α plane. Similarly, $(\delta, \alpha)_{\text{final}}$ values can be obtained by changing the values of κ. By plotting all $(\delta, \alpha)_{\text{final}}$ points on the δ–α plane, the mode spectrum of the DFB LD is formed. A simplified δ–α plot is shown in Figure 3.1. Different symbols shown represent various longitudinal modes obtained for various coupling coefficient while the solid curve shows how longitudinal modes join to form an oscillating mode.

As the biasing current increases, the longitudinal mode showing the smallest amplitude gain will reach the threshold condition first and begin to lase. Other modes that fail to reach the threshold condition will then be suppressed and become non-lasing side modes. On the δ–α plane, the $\delta = 0$ line, or the Bragg wavelength, splits the δ–α plane into two halves. As we move along the positive δ-axis, any oscillation modes encountered will be

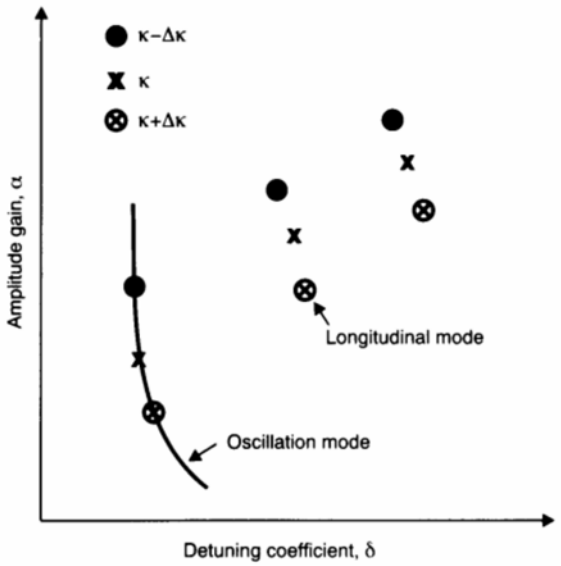

Figure 3.1 A simplified $\delta - \alpha$ plot showing the mode spectrum and the oscillating mode of a DFB LD. Different symbols are used to show longitudinal modes obtained from various κ values.

denoted as the +1, +2 modes, and so on. Similarly, negative modes such as −1, −2 are used for those found on the negative δ-axis.

The importance of the SLM in coherent optical communications was discussed in Chapter 1. To measure the stability of the lasing spectrum, we need to determine the amplitude gain difference between the lasing mode and the most probable side mode of the DFB laser [4,5]. A larger amplitude gain difference, better known as the gain margin ($\Delta\alpha$), implies a better mode discrimination. In other words, the SLM oscillation in the DFB LD involved is said to be more stable. In practice, the actual requirement of $\Delta\alpha$ may vary from one system to another depending on the encoding format (return to zero, RZ, or non-return to zero, NRZ), transmission rate, the biasing condition of the laser sources, and the length and the characteristics of the single mode fibre (SMF) used. A simulation based on a 20 km dispersive SMF [6] indicated that a $\Delta\alpha$ of 5/cm is required for a 2.4 Gb/s in order that a bit error rate, BER $< 10^{-9}$ can be achieved. A detailed analysis on the requirement of $\Delta\alpha$ under different system configurations is clearly beyond the scope of the present analysis. However, we get some idea of the typical value of gain margins required in a coherent optical communication system.

The value of the gain margin, however, is difficult to measure directly from an experiment. An alternative method is to measure the spontaneous emission spectrum. For a stable SLM source, a minimum of 25 dB side mode suppression ratio (SMSR) [7] between the power of the lasing mode and the most probable side mode is necessary.

3.5 THRESHOLD ANALYSIS OF A CONVENTIONAL DFB LASER DIODE

For a conventional DFB laser with a zero facet reflection, the threshold equation (3.2.16) becomes

$$j\gamma L = \pm\kappa L \sinh(\gamma L) \tag{3.5.1}$$

Using the Newton–Raphson iteration approach, the eigenvalue equation can be solved as a fixed coupling coefficient. Results obtained for the above equation are shown in Figure 3.2. All parameters used have been normalised with respect to the overall cavity length L. Discrete values of κL have been selected between 0.25 and 10.0. As shown in the inset of Figure 3.2, solutions obtained from various κL products are shown using different symbols. Oscillation modes are then formed by joining the appropriate solutions together. Solid lines have been used to represent the -4 to $+4$ modes. From the figure, it is clear that oscillating modes distribute symmetrically with respect to the Bragg wavelength whilst no oscillation is found at the Bragg wavelength. Furthermore, it can be seen that the $+1$ and -1 modes with different lasing wavelengths will share the same amplitude gain. As a result, degenerate oscillation occurs and these modes will have the same chance to lase once the lasing condition is reached. Figure 3.2 also reveals that the amplitude threshold gain decreases with increasing values of κL. Since a larger value of κ implies a stronger optical feedback, a smaller threshold gain results. Similarly, lasers with a long cavity length help to reduce the amplitude gain because a larger single pass gain can be achieved.

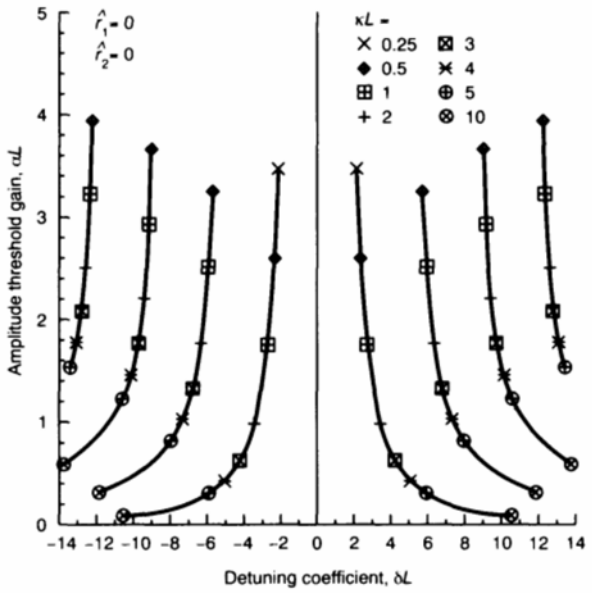

Figure 3.2 Relationship between the amplitude threshold gain and the detuning coefficient of a mirrorless index-coupled DFB LD.

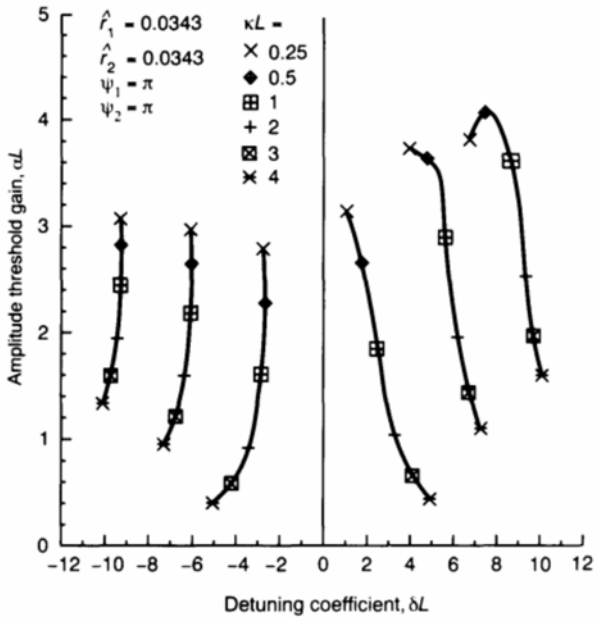

Figure 3.3 Relationship between the amplitude threshold gain and the detuning coefficient of a DFB LD with finite reflectivities.

With no oscillation found at the Bragg wavelength, a stopband region is formed between the $+1$ and -1 modes of the conventional mirrorless DFB LD. From Figure 3.2, we conclude that the normalised stopband width is a function of κL. Although the change in stopband width becomes less noticeable at lower values of κL, the measurement of the stopband width has been used to determine the coupling coefficient of DFB LDs [8]. Figure 3.3 shows the characteristic of a DFB LD with finite facet reflections. It is shown in the figure that the mode distribution is no longer symmetric and no oscillation is found at the Bragg wavelength. The -1 mode with the smallest amplitude gain becomes the lasing mode.

3.6 IMPACT OF THE CORRUGATION PHASE AT LASER FACETS

So far, symmetric laser cavities that share identical facet reflectivities have been used. To understand the effects of the residue phases at the facets [2, 9], asymmetric cavities are considered. The threshold characteristic of one of these asymmetric DFB LDs is shown in Figure 3.4. The amplitude reflectivity $\hat{r}_1 = 0.0343$ is assumed, whilst the other facet is assumed to be naturally cleaved such that $\hat{r}_2 = 0.535$. Discrete values of κL have been chosen. In the figure, the corrugation phase ψ_1 is fixed at π whilst ψ_2 changes in steps of $\pi/2$. Different symbol markers have been used to represent different ψ_2. Solutions obtained from the same κL product are joined together as usual to form the oscillation mode. Let us consider $\kappa L = 1.0$ as an example. It can be

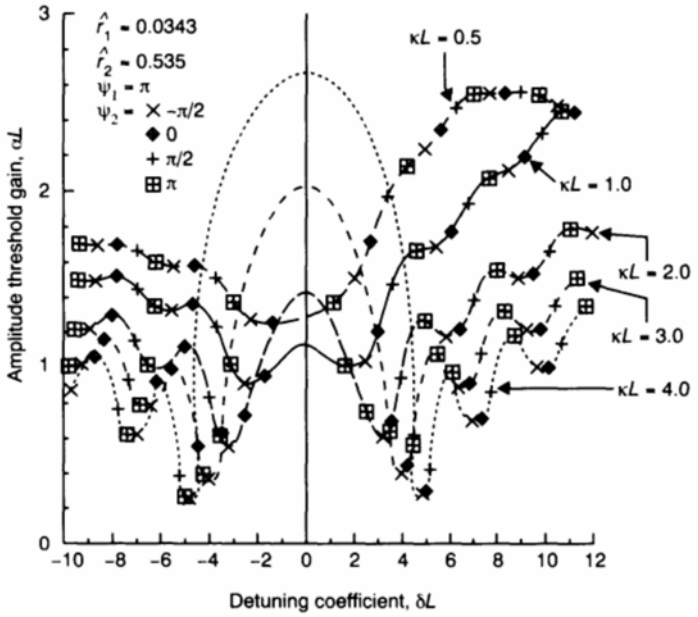

Figure 3.4 The lasing characteristic of a DFB LD having asymmetric facet reflection. The corrugation phase ψ_1 is fixed while ψ_2 is allowed to change. Results obtained for various κL products are compared.

seen that the lasing mode changes from the negative to the positive mode as the facet phase ψ_2 changes from $-\pi/2$ to π. For $\kappa L > 1.0$, the amplitude gain at the Bragg wavelength remains so high that it never reaches the threshold condition. The -1 mode showing the smallest amplitude gain becomes the dominant lasing mode.

By replacing the natural cleaved facet with a highly reflective surface such that $\hat{r}_2 = 1.0$, the lasing characteristic of the new structure is shown in Figure 3.5. Various values of κL have been used for comparison. Similar to the one shown in Figure 3.4, the oscillation mode shifts from the -1 to the $+1$ mode when ψ_2 changes from $-\pi/2$ to $\pi 4$. From both Figures 3.4 and 3.5 it is clear that SLM operation depends on both the facet reflectivity and the associated phase. However, due to tolerances inherent during the fabrication process, it is difficult to control accurately the corrugation phase at the laser facets [10].

Various methods have been proposed for adjusting the corrugation phase. One such method is to use the ion beam etching technique [11,12]. A continuous flux of neutralised argon gas, which acts as an abrasive tool, is targeted at one laser facet. By abrading the facet slowly across the beam at a constant rate, a 20–50 nm depth can be etched away at the laser facet in a single process. An annealing process is usually applied afterwards. Experimental results [11,12] also show that the annealing process has no significant variation in the threshold and the external quantum efficiency in

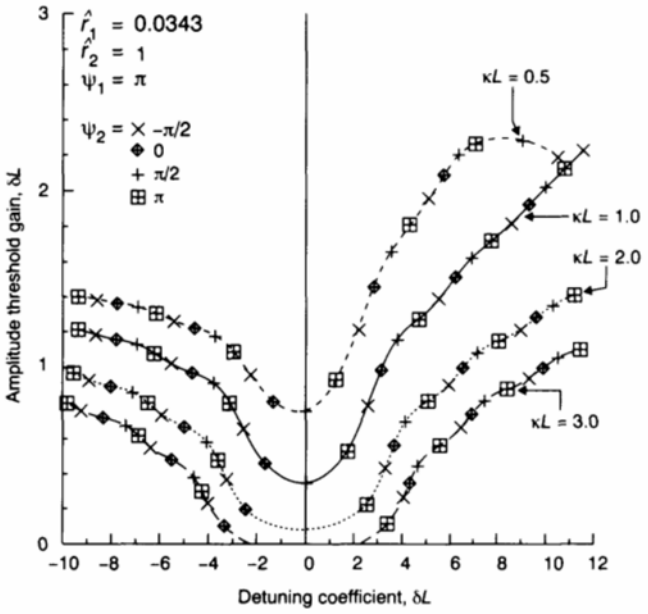

Figure 3.5 The lasing characteristic of a DFB LD having asymmetric facet reflection. The corrugation phase ψ_1 is fixed whilst ψ_2 is allowed to change. Results obtained from various κL products are compared.

DFB lasers. Apart from the extra annealing process required, the ion beam etching technique is effective in adjusting the position of the facets and thus the associated corrugation phases.

Since the etching depth required may vary from one DFB laser to another, the ion beam etching technique is classified as a chip-by-chip optimisation method. To improve the efficiency, other methods like the phase control technique [13] can be used. Basically, a multi-layer coating with precise refractive indices and thicknesses is applied to the laser facets so that the overall facet phase and the amplitude reflection can be controlled and determined easily.

3.7 THE EFFECTS OF PHASE DISCONTINUITY ALONG THE DFB LASER CAVITY

In the previous section the threshold analysis of conventional DFB lasers comprising uniform corrugations was presented. The SLM operation can be achieved when different values of the facet reflectivity are employed. However, owing to the randomness of the corrugation phase at the laser facet, stable SLM oscillation is not guaranteed. To improve the single mode performance of DFB lasers, phase discontinuity or phase shift is introduced [14] along the corrugation. As shown in Figure 3.6, phase shifts along the corrugation can be introduced by two methods. As shown in Figure 3.6(a), the

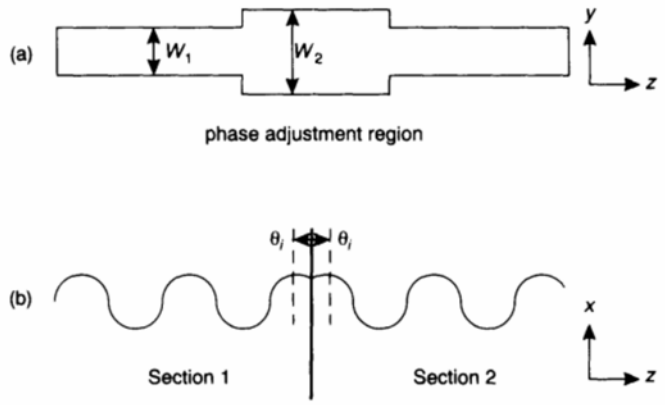

Figure 3.6 Phase discontinuity that may be introduced along a DFB laser cavity. (a) Phase shift with uniform corrugation but non-uniform active layer dimension. (b) Phase shift with uniform active layer dimension but discontinuous corrugation.

width of the active layer is not uniform while the shape and the dimension of the corrugation remain constant [15,16]. In Figure 3.6(b), on the other hand, the corrugation shows a phase slip whilst the active layer dimensions remain uniform [17,18]. Using method (a), the actual phase shift depends on the length of the phase-adjustment region and the difference in strip width $(W_2 - W_1)$. Precise control over the active layer width is required. Using method (b), phase discontinuity is introduced during fabrication in which the slip is written directly along the corrugation. In our analysis, we adopted the latter method in preparing phase shifts in a DFB laser.

We consider a single phase-shifted (1PS) DFB laser as shown in Figure 3.7. A phase slip of 2θ is fabricated along the corrugation at the z origin so that the cavity is subdivided into two sections. As can be seen, these sections may have a different length and each resembles a conventional DFB laser cavity with uniform corrugation. In the analysis, zero facet reflectivity is assumed. Following the argument presented in Chapter 2, the refractive index of each section can be written as

$$n^{(1)}(z) = n_0 + \Delta n \cos(2\beta_0 z + \phi) \tag{3.7.1a}$$

$$n^{(2)}(z) = n_0 + \Delta n \cos(2\beta_0 z - \phi) \tag{3.7.1b}$$

where the superscripts (1) and (2) correspond to sections 1 and 2, respectively. In the above equations it is assumed that the phase shift is equally split between sections 1 and 2.

On the basis of the coupled wave theory, counter-running waves are built up in each section such that the following equations can be derived for each section of the laser:

$$-\frac{dR^{(1)}}{dz} + (\alpha - j\delta)R^{(1)} = j\kappa S^{(1)} e^{-j\phi} \tag{3.7.2a}$$

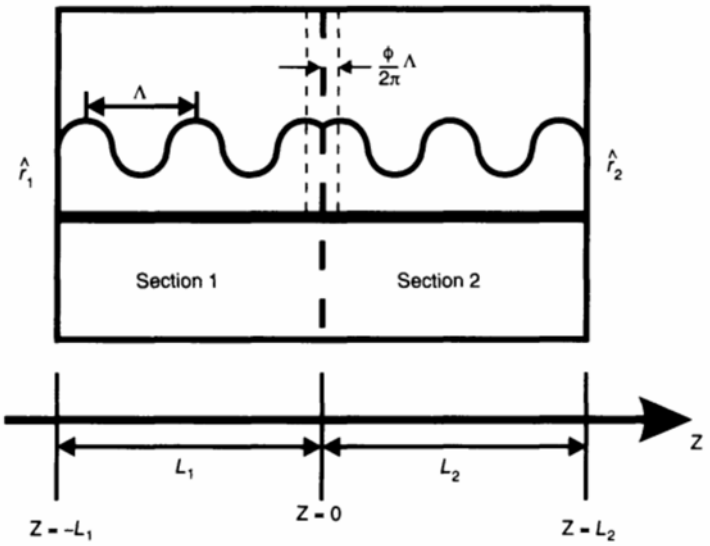

Figure 3.7 Schematic representation of a single phase-shifted (1PS) DFB LD. The phase shift is represented by ϕ.

$$\frac{dS^{(1)}}{dz} + (\alpha - j\delta)S^{(1)} = j\kappa R^{(1)}e^{j\phi} \tag{3.7.2b}$$

$$-\frac{dR^{(2)}}{dz} + (\alpha - j\delta)R^{(2)} = j\kappa S^{(2)}e^{j\phi} \tag{3.7.2c}$$

$$\frac{dS^{(2)}}{dz} + (\alpha - j\delta)S^{(2)} = j\kappa R^{(2)}e^{-j\phi} \tag{3.7.2d}$$

where $R^{(1)}$, $S^{(1)}$ and $R^{(2)}$, $S^{(2)}$ are the counter-running waves propagating in sections (1) and (2), respectively. In both sections, the corrugation shape and grating depth are assumed to be equal. As a result, the coupling coefficient remains constant throughout. Following equation (2.4.21), the solution of the coupled wave equations can be written as

$$E^{(k)}(z) = R^{(k)}(z)e^{-j\beta_0 z} + S^{(k)}(z)e^{j\beta_0 z} \tag{3.7.3}$$

where

$$R^{(k)}(z) = R_1^{(k)}e^{\gamma z} + R_2^{(k)}e^{-\gamma z} \tag{3.7.4a}$$

$$S^{(k)}(z) = S_1^{(k)}e^{\gamma z} + S_2^{(k)}e^{-\gamma z} \tag{3.7.4b}$$

and $k = 1$ and 2 for sections (1) and (2), respectively. Here, $R_1^{(k)}$, $R_2^{(k)}$, $S_1^{(k)}$ and $S_2^{(k)}$ are the complex leading coefficients associated with the particular section. Since the discontinuity caused by the phase slip is assumed to be very small, the waves in the two sections can be considered to be continuous

at $z = 0$. In other words,

$$R^{(1)}(z = 0) = R^{(2)}(z = 0) \tag{3.7.5a}$$

$$S^{(1)}(z = 0) = S^{(2)}(z = 0) \tag{3.7.5b}$$

By allowing both $\hat{r}_1$ and $\hat{r}_2$ to be the respective amplitude facet reflection coefficients at the left and right laser facets, the boundary conditions of the 1PS DFB laser become

$$R^{(1)}(-L_1)e^{j\beta_0 L_1} = \hat{r}_1 S^{(1)}(-L_1)e^{-j\beta_0 L_1} \tag{3.7.5c}$$

$$S^{(2)}(L_2)e^{j\beta_0 L_2} = \hat{r}_2 R^{(2)}(L_2)e^{-j\beta_0 L_2} \tag{3.7.5d}$$

By matching all the boundary conditions, non-trivial solutions exist if and only if the following eigenvalue equation is satisfied [17]:

$$\frac{j\Psi^{(1)}r_1 + \Theta^{(1)}}{j\Theta^{(1)}r_1 + T^{(1)}} \cdot \frac{j\Psi^{(2)}r_2 + \Theta^{(2)}}{j\Theta^{(2)}r_2 + T^{(2)}} = -e^{j2\phi} \tag{3.7.6}$$

where

$$\begin{aligned} \Psi^{(k)} &= \hat{\Gamma}^2 + \kappa^2 e^{2\gamma L_{(k)}} \\ \Theta^{(k)} &= \kappa\hat{\Gamma}(1 - e^{2\gamma L_{(k)}}) \\ T^{(k)} &= \kappa^2 + \hat{\Gamma}^2 e^{2\gamma L_{(k)}} \end{aligned} \tag{3.7.7}$$

with $k = 1$ and 2, and

$$L_{(1)} = L_1, \qquad L_{(2)} = L_2 \tag{3.7.8}$$

In the above equation, r_1 and r_2 are the complex field reflectivities and $\hat{\Gamma}$ are defined as

$$\begin{aligned} r_1 &= \hat{r}_1 e^{-j(2\beta_0 L_1 - \phi)} \\ r_2 &= \hat{r}_2 e^{-j(2\beta_0 L_2 - \phi)} \\ \hat{\Gamma} &= \alpha - j\delta - \gamma \end{aligned} \tag{3.7.9}$$

Compared with the conventional DFB laser, the boundary conditions at the phase shift have to be matched for the mirrorless 1PS DFB laser structure. Nevertheless, it was pointed out by Utaka *et al.* [17] that the use of non-zero facet reflection may not be desirable. This is because the random corrugation phases at the laser facets will cause extra difficulty in controlling the lasing characteristic. Therefore, it is best to have AR coatings applied to both facets of the 1PS DFB laser. For a mirrorless, symmetric 1PS DFB laser cavity with $L_1 = L_2 = L/2$, the phase shift is located at the centre of the cavity. As a result, equation (3.7.6) can be simplified further such that [19]:

$$\left[\frac{\kappa\hat{\Gamma}(1 - e^{\gamma L})}{(\kappa^2 + \hat{\Gamma}e^{\gamma L})}\right]^2 = e^{2j\phi} \tag{3.7.10}$$

3.7.1 Effects of phase shifts on the lasing characteristics of a 1PS DFB LD

To investigate the effects of phase shifts on the lasing characteristic of 1PS DFB lasers, a symmetric laser cavity is assumed with a single phase shift fabricated at the centre of the DFB laser. Using a numerical method such as the Newton–Raphson method, the eigenvalue equation (3.7.10) can be solved numerically for the normalised amplitude threshold gain $\alpha_{th}L$ (amplitude gain of the lasing mode) and the lasing wavelength at specific values of κ and phase shift.

Figure 3.8 illustrates how the variation of phase shift value affects $\alpha_{th}L$ for the mirrorless 1PS DFB LD. All parameters used are normalised with respect to the overall cavity length L. Three different κL values are plotted in the figure for comparison. All curves in Figure 3.8 are symmetric and have a minimum amplitude threshold gain at $\phi = 90^\circ$ (or $\pi/2$ in radians) as can be seen. This phase change corresponds to a quarter wavelength shift and so the name single $\lambda/4$-shifted DFB or quarterly wavelength shifted (QWS) DFB laser is usually used to represent this laser structure. When the phase shift approaches zero or π, the phase-shifted structure is reduced to the conventional, mirrorless DFB laser in which degenerate oscillation results.

Figure 3.9 shows the variation of the lasing wavelength with respect to the phase shift. As in Figure 3.8, the results of three sets of κL products are shown and compared. In this case, the Bragg wavelength λ_B is assumed to be 1330 nm and the actual wavelength is shown on the left y-axis. The

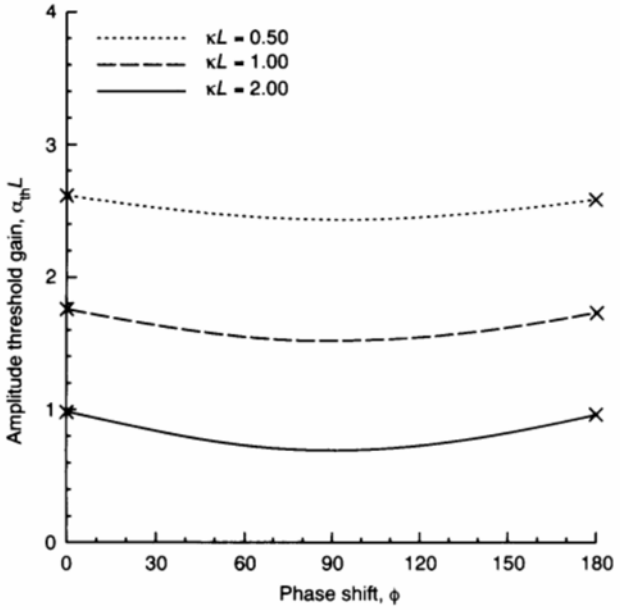

Figure 3.8 The variation of the amplitude threshold gain with the phase shift of a 1PS DFB LD.

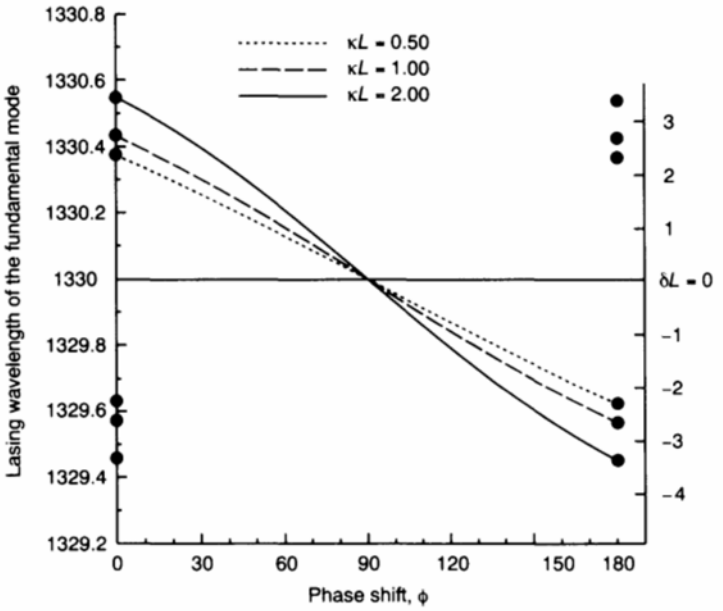

Figure 3.9 The variation of the lasing wavelength with the phase shift of a 1PS DFB LD.

corresponding normalised detuning coefficient $\delta_{th}L$ is shown on the right-hand side. At $\phi = \pi/2$, the lasing wavelength of all three κL values coincide at the Bragg wavelength. This reveals an important characteristic of the symmetric 1PS DFB laser. A QWS DFB LD always oscillates at the Bragg wavelength irrespective of the κL chosen. When κL increases, the range of the lasing wavelength also increases with varying phase shift. At $\kappa L = 2.0$, the wavelength range is found to be 10.8 nm whilst it is about 7.4 nm for $\kappa L = 0.50$. So far, the phase shift is assumed to be at the centre of the laser cavity. In the next section, the effects of the PSP on the lasing characteristics of 1PS DFB lasers will be discussed.

3.7.2 Effects of PSP on the lasing characteristics of a 1PS DFB LD

To investigate the effect of the location of the phase shift [20], a parameter known as the PSP is introduced along the asymmetric laser cavity such that

$$\text{PSP} = L_1/L \tag{3.7.11}$$

The variations of the amplitude gain and gain margin obtained from a 500 μm long DFB laser cavity with $\kappa = 2/\text{mm}$ (i.e. $\kappa L = 1$) are shown in Figures 3.10 and 3.11, respectively. In the analysis, the Bragg wavelength is assumed to be at 1330 nm and the phase shift is fixed at $\pi/2$. Both Figures 3.10 and 3.11 show a symmetric distribution of curves at PSP = 0.5, where the phase shift is found. When the phase shift moves from the centre towards the laser facets, the effect of the phase shift becomes less influential. Solutions obtained from

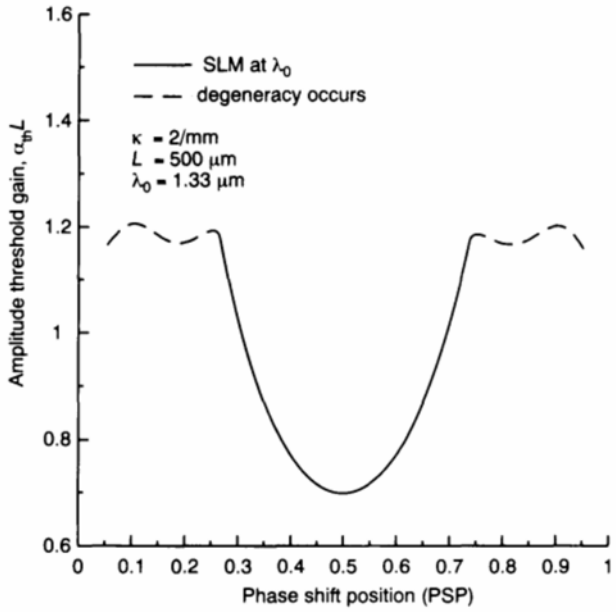

Figure 3.10 The variation of the amplitude threshold gain with the PSP of a 1PS DFB LD. The phase shift is fixed at $\pi/2$.

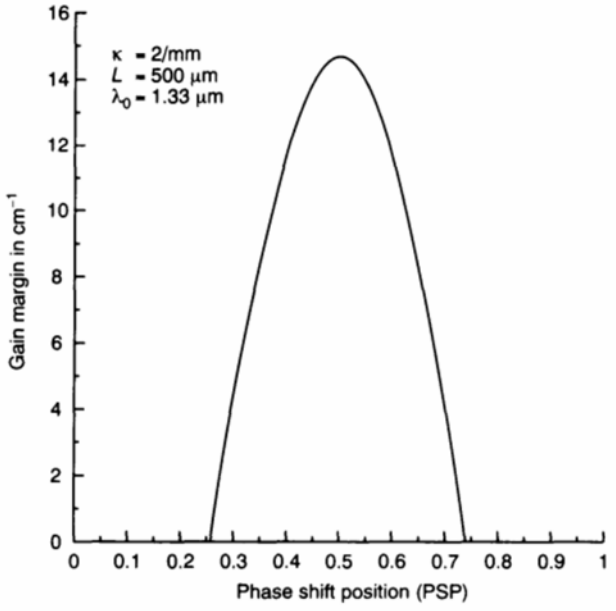

Figure 3.11 The variation of the gain margin with the PSP of a 1PS DFB LD. The phase shift is fixed at $\pi/2$.

the threshold equation indicate that degenerate oscillation begins to occur at PSP = 0.26 and PSP = 0.74. In this situation, the QWS DFB laser is reduced to a conventional one. The dramatic fall in the gain margin shown in Figure 3.11 confirms the above argument. When the position of the phase shift moves from the centre (PSP = 0.5) to the laser facets, the gain margin drops from a peak value of 14.7/cm to zero value at PSP = 0.26 and PSP = 0.74. Provided the phase shift is fabricated near the centre of the cavity, a QWS DFB laser can operate at the Bragg wavelength.

3.8 ADVANTAGES AND DISADVANTAGES OF A QUARTERLY WAVELENGTH SHIFTED (QWS) DFB LD

By introducing a QWS at the centre of the DFB laser cavity, SLM operation at the Bragg wavelength can be achieved. However, it was first discussed by Soda *et al.* [16] that for a high κL QWS DFB LD, the gain margin drops drastically with increasing biasing current. Multimode oscillation at two distant wavelengths is observed when the optical output power increases. Such a reduction in gain margin is thought to be induced by the longitudinal spatial hole burning effect [21]. When DFB LDs are biased below the threshold current, where spontaneous emission is still dominant, the longitudinal carrier and the field intensity distributions are relatively uniform. However, when the bias current exceeds that of the threshold value, the optical field inside the laser cavity becomes intensified at places where corrugation reflections occur [22]. For a QWS DFB LD, the field intensity is so intense at the PSP that the rate of spontaneous recombination increases near the phase shift. To maintain a unity round-trip gain, carriers located near to the phase shift will move to fill the carrier depletion. From Chapter 2, we know that the refractive index of the semiconductor depends on the carrier injection. Such a local variation of carrier concentration will result in a non-uniform distribution of refractive indices along the laser cavity. The situation is made worse by the fact that the gain and refractive index are related to one another as a result of the Kramer–Kroenig relationship [23]. When the biasing current changes, the gain in the lasing mode and other non-lasing side modes will change in such a way that the gain margin reduces and consequently, multimode oscillation occurs.

Owing to the deterioration of single mode stability, the longitudinal spatial hole burning effect limits the QWS DFB LD to a lower power of operation. Although laser structures with a smaller κL value are found to be less vulnerable to the longitudinal spatial hole burning effect, these structures are characterised by larger amplitude gain values and relatively large threshold currents. To suppress the spatial hole burning whilst improving the maximum single mode output power available, it was proposed that a laser structure with a flatter field intensity may be used [24]. To optimise the structure with respect to the intensity distribution, a parameter known as the flatness (F) is

defined as

$$F = \frac{1}{L}\int_{\text{cavity}} (I(z) - I_{\text{avg}})^2 \, dz \tag{3.8.1}$$

where $I(z)$ is the local field intensity and I_{avg} is the average field intensity. In the QWS DFB laser, an optimum value of flatness is found when $\kappa L = 1.25$ [16].

In flattening the field intensity whilst improving the optimum κL value that can be used in QWS DFB lasers, a three-electrode QWS DFB laser structure, as shown in Figure 3.12 was proposed [25]. By passing a larger biasing current into the central electrode, carriers lost due to the spatial hole burning are compensated for [26]. An alternative approach that retains the uniform current injection is also used. By introducing more phase shifts along the DFB laser cavity, a multiple phase shift (MPS) structure can flatten the field distribution [27]. Figure 3.13 shows a three-phase-shift (3PS) DFB LD.

Longitudinal spatial hole burning must be considered when the LD operates in the above threshold condition. To decide the above threshold characteristics, we must take into account the local carrier concentration. Using the perturbation method [27] or the quasi-uniform gain assumption [16], the characteristics of QWS DFB LDs operating slightly above the threshold current are predicted. However, these methods may not be appropriate when the injection current becomes high and other non-linear effects such as the gain saturation [28] must be considered.

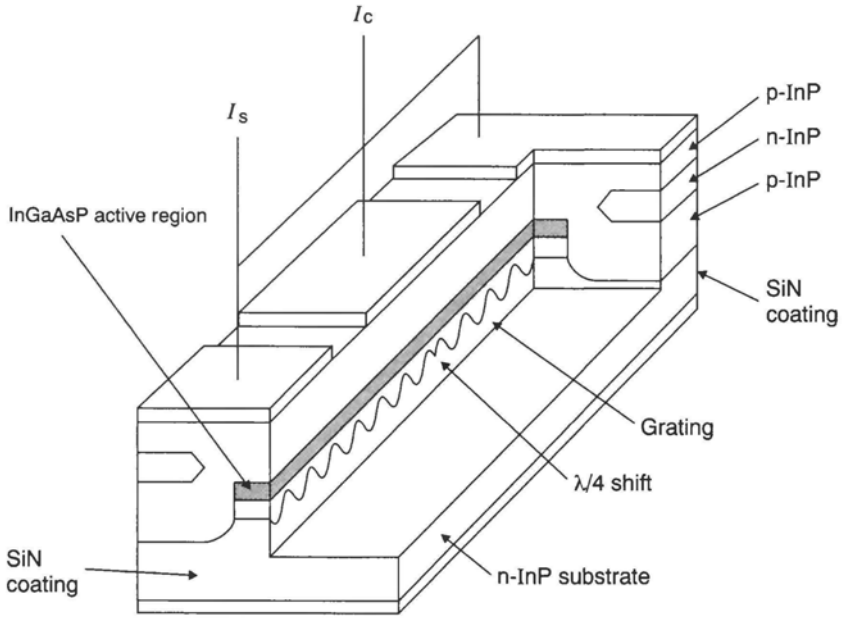

Figure 3.12 A three-electrode QWS DFB LD (after [29]).

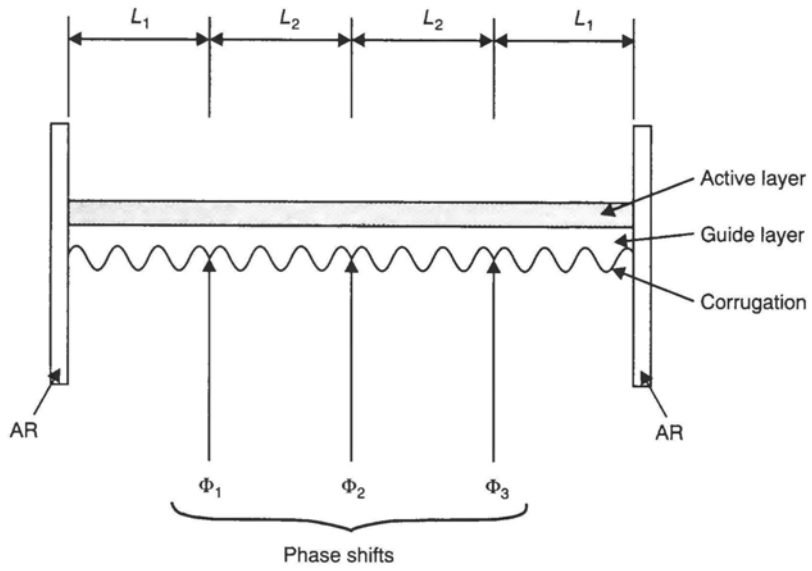

Figure 3.13 Schematic representation of a three phase shift (3PS) DFB LD (after [30]).

Throughout the analysis, the derivation of the eigenvalue equation becomes tedious as the laser structure becomes more and more complex. The use of a numerical analysis like the Newton–Raphson method becomes impracticable since a first-order derivative is required. A new model that can cope with various designs of DFB LDs such as the three-electrode (QWS) [29] and/or the 3PS DFB LD structures [30] while maintaining a wider range of injection current is necessary. With increasing output power, any local variation and the gain saturation effect can be considered.

3.9 SUMMARY

In this chapter the coupled-wave equations are solved under various structural configurations. By matching all boundary conditions, eigenvalue equations were derived. From the solutions of the eigenvalue equations, the threshold current and the lasing wavelength are determined. Impacts due to the coupling coefficient, the laser cavity length, the facet reflectivities, the residue corrugation phases and phase discontinuities are discussed in a systematic way on behalf of the lasing threshold characteristics. With a single QWS fabricated at the centre of the DFB cavity, the QWS DFB LD oscillates at the Bragg wavelength. Owing to a non-uniform field distribution, however, the single mode stability is threatened by the spatial hole burning effect. To extend the analysis to the above threshold operation, a new model is required such that all localised effects and other non-linear effects can be included in the analysis.

3.10 REFERENCES

[1] Kogelnik, H. and Shank C.V., "Coupled-wave theory of distributed feedback lasers," *J. Appl. Phys.*, **43**, no. 5, pp. 2327-2335, 1972.

[2] Streifer, W., Burnham, R.D. and Scifres, D.R., "Effect of external reflectors on longitudinal modes of distributed feedback laser," *IEEE J. Quantum Electron.*, **QE-11**, no. 4, pp. 154-161, 1975

[3] Arfken, G., *Mathematical Methods for Physicists*, 3rd edition. New York: Academic Press, 1985.

[4] Ketelsen, L.J.P., Hoshino, I. and Ackerman, D.A., "The role of axially nonuniform carrier density in altering the TE-TE gain margin in InGaAsP-InP DFB lasers", *IEEE J. Quantum Electron.*, **QE-27**, no. 4, pp. 957-964, 1991.

[5] Itaya, Y., Matsuoka, T., Kuroiwa, K., and Ikegami, T., "Longitudinal mode behaviours of 1.5 μm range InGaAsP/InP distributed feedback lasers", *IEEE J. Quantum Electron.*, **QE-20**, no. 3, pp. 230-235, 1984.

[6] Cartledge, J.C. and Elrefaie, A.F., "Threshold gain difference requirements for nearly single-longitudinal-mode lasers", *J. Lightwave Technol.*, **LT-8**, no. 5, pp. 704-715, 1990.

[7] Agrawal, G.P. and Dutta, N.K., *Long-wavelength Semiconductor Lasers*. Princeton, NJ: Van Nostrand, 1986.

[8] Kinoshita, J., "Validity of κL evaluation by stopband method for $\lambda/4$ DFB lasers with low reflecting facets", *IEEE J. Quantum Electron.*, **QE-23**, no. 5, pp. 499-501, 1987.

[9] Chinn, S.R., "Effects of mirror reflectivity in a distributed-feedback laser", *IEEE J. Quantum Electron.*, **QE-9**, no. 6, pp. 574-580, 1973.

[10] Buus, J., "Mode selectivity in DFB lasers with cleaved facets", *Electron. Lett.*, **21**, pp. 179-180, 1985.

[11] Itaya, Y., Wakita, K., Motosugi, G. and Ikegami, T., "Phase control by coating in 1.5 μm distributed feedback lasers", *IEEE J. Quantum Electron.*, **QE-21**, no. 6, pp. 527-532, 1985.

[12] Matsuoka, T., Yoshikuni, Y. and Nagai, H., "Verification of the light phase effect at the facet on DFB laser properties", *IEEE J. Quantum Electron.*, **QE-21**, no. 12, pp. 1880-1886, 1985.

[13] Mols, P.P.G., Kuindersma, P.I., Es-spiekman, W.V. and Baele, I.A.G., "Yield and device characteristics of DFB lasers: Statistics and novel coating design in theory and experiment", *IEEE J. Quantum Electron.*, **QE-25**, no. 6, pp. 1303-1312, 1989.

[14] Hau, H. and Shank, C., "Asymmetric tapers of distributed feedback lasers," *IEEE J. Quantum Electron.*, **QE-12**, pp. 532-539, 1976.

[15] Nakano, Y., Luo, Y. and Tada, K., "Facet reflection independent, single longitudinal mode oscillation in a GaAlAs/GaAs distributed feedback laser equipped with a gain-coupling mechanism", *Appl. Phys. Lett.*, **55**, no. 16, pp. 1606-1608, 1989.

[16] Soda, H., Kotaki, Y., Sudo, H., Ishikawa, H., Yamakoshi, S. and Imai, H., "Stability in single longitudinal mode operation in GaInAsP/InP phase-adjusted DFB lasers", *IEEE J. Quantum Electron.*, **QE-23**, no. 6, pp. 804-814, 1987.

[17] Utaka, K., Akiba, S., Sakai, K. and Matsushima, Y., "$\lambda/4$-shifted InGaAsP DFB lasers", *IEEE J. Quantum Electron.*, **QE-22**, no. 3, pp. 1042-1051, 1986.

[18] McCall, S.L. and Platzman, P.M., "An optimized $\pi/2$ distributed feedback laser", *IEEE J. Quantum Electron.*, **QE-21**, no. 12, pp. 1899-1904, 1985.

[19] Ghafouri-Shiraz, H. and Chu, C., "Effect of phase shift position on spectral linewidth of the $\pi/2$ distributed feedback laser diode", *J. Lightwave Technol.*, **LT-8**, no. 7, pp. 1033-1037, 1990.

[20] Usami, M., Akiba, S. and Utaka, K., "Asymmetric λ/4-shifted InGaAsP/InP DFB lasers", *IEEE J. Quantum Electron.*, **QE-23**, no. 6, pp. 815-821, 1987.

[21] Rabinovich, W.S. and Feldman, B.J., "Spatial hole burning effects in distributed feedback lasers", *IEEE J. Quantum Electron.*, **QE-25**, no. 1, pp. 20-30, 1989.

[22] Kinoshita, K. and Matsumoto, K., "Transient chirping in distributed feedback lasers: Effect of spatial hole-burning along the laser axis", *IEEE J. Quantum Electron.*, **QE-24**, no. 11, pp. 2160-2169, 1988.

[23] Yariv, A., *Quantum Electronics*, 3rd edition. New York: Wiley, 1989.

[24] Kimura, T. and Sugimura, A., "Coupled phase-shift distributed-feedback lasers for narrow linewidth operation", *IEEE J. Quantum Electron.*, **QE-25**, no. 4, pp. 678-683, 1989.

[25] Usami, M. and Akiba, S., "Suppression of longitudinal spatial hole-burning effect in λ/4-shifted DFB lasers by nonuniform current distribution", *IEEE J. Quantum Electron.*, **QE-25**, no. 6, pp. 1245-1253, 1989.

[26] Kikuchi, K. and Tomofuji, H., "Performance analysis of separated-electrode DFB laser diode", *Electron. Lett.*, **25**, no. 2, pp. 162-163, 1989.

[27] Kimura, T., and Sugimura, A., "Narrow linewidth asymmetric coupled phase-shift DFB lasers", *Trans IEICE.*, **E 79**, no. 1, pp. 71-76, 1990.

[28] Huang, J. and Casperson, L.W., "Gain and saturation in semiconductor lasers", *Optical Quantum Electron.*, **QE-27**, pp. 369-390, 1993.

[29] Kotaki, Y. and Ishikawa, H., "Wavelength tunable of DFB and DBR lasers for coherent optical fibre communications", *IEE Proc. Pt. J*, **138**, no. 2, pp. 171-177, 1991.

[30] Ogita, S., Kotaki, Y., Hatsuda, M., Kuwahara, Y. and Ishikawa, H., "Long cavity multiple-phase shift distributed feedback laser diode for linewidth narrowing", *J. Lightwave Technol.*, **LT-8**, no. 10, pp. 1596-1603, 1990.

4

TRANSFER MATRIX MODELLING IN DFB SEMICONDUCTOR LASERS

4.1 INTRODUCTION

In Chapter 3 we derived eigenvalue equations by matching boundary conditions inside distributed feedback (DFB) laser cavities. From the eigenvalue problem, the lasing threshold characteristic of DFB lasers is determined. The single $\pi/2$ phase-shifted (PS) DFB laser is fabricated with a phase discontinuity of $\pi/2$ at or near the centre of the laser cavity. It is characterised by the Bragg oscillation and the high gain margin value. On the other hand, the single longitudinal mode (SLM) deteriorates quickly when the optical power of the laser diode (LD) increases. This phenomenon, known as the spatial hole burning, limits the maximum single mode optical power and, consequently, the spectral linewidth. Using a multiple-phase-shift (MPS) DFB laser structure, the electric field distribution is flattened and hence the spatial hole burning is suppressed.

In dealing with such a complicated DFB laser structure, it is tedious to match all the boundary conditions. A more flexible method capable of handling different types of DFB laser structures is necessary. In section 4.2 the transfer matrix method (TMM) [1–4] will be introduced and explored comprehensively. From the coupled wave equations, it is found that the field propagation inside a corrugated waveguide (e.g. the DFB laser cavity) can be represented by a transfer matrix. Provided that the electric fields at the input plane are known, the matrix acts as a transfer function so that electric fields at the output plane can be determined. Similarly, other structures like the active planar Fabry–Perot (FP) section, the passive corrugated distributed Bragg reflector (DBR) section and the passive planar waveguide (WG) section can also be expressed using the idea of a transfer matrix. By joining these transfer matrices as a building block, a general N-section laser cavity model will be

presented. Since the outputs from a transfer matrix automatically become the inputs of the following matrix, all boundary conditions inside the composite cavity are matched. The unsolved boundary conditions are those at the left and right facets. In section 4.3 the threshold equation for the N-section laser cavity model will be determined and the use of TMM in other semiconductor laser devices will be discussed.

An adequate treatment of the amplified spontaneous emission spectrum (P_N) is very important in the analysis of semiconductor lasers [5], optical amplifiers [6–8] and optical filters [9,10]. In semiconductor lasers, P_N is important for both the estimation of linewidth [11] and the estimation of single mode stability in DFB LDs [12]. In optical amplifiers and filters, P_N has also been used to simulate the bandwidth, tunability and the signal gain characteristic. In section 4.3 the TMM formulation will be extended to include the below-threshold spontaneous emission spectrum of the N-section DFB laser structure. Numerical results based on 3PS DFB LDs will be presented.

4.2 BRIEF REVIEW OF MATRIX METHODS

By matching boundary conditions at the facets and the phase shift position, the threshold condition of the single PS DFB LD can be determined from the eigenvalue equations. However, this approach lacks the flexibility required in the structural design of DFB LDs. Whenever a new structural design is involved, a new eigenvalue equation has to be derived by matching all boundary conditions. For lasers with the MPS DFB structure, the formation of the eigenvalue equation becomes tedious since it may involve a large number of boundary conditions.

One possible approach to simplifying the analysis, whilst improving the flexibility and robustness, is to employ matrix methods. Matrices have been used extensively in engineering problems which are highly numerical in nature. In microwave engineering [13], matrices are used to find the electric and magnetic fields inside various microwave waveguides and devices. One major advantage of the matrix method is its flexibility. Instead of repeatedly finding complicated analytical eigenvalue equations for each laser structure, a general matrix equation is derived. A threshold analysis of various laser structures, including planar sections, corrugated sections or a combination of them, can be carried out in a systematic way. Since the laser structures can be represented by the same general matrix equation, the algorithm derived can be applied to various laser structures. However, because of the numerical nature of the matrix method, it cannot be used to verify the existence of analytical expressions in a particular problem.

In all matrix methods the structures involved will first be divided into a number of smaller sections. In each section, all physical parameters, like the injection current and material gain, are assumed to be homogeneous. As a result, the total number of smaller sections used varies and mostly depends

on the type of problem. For a problem like the analysis of transient responses in LDs [14], a fairly large number of sections are needed since a highly non-uniform process is involved. On the other hand, only a few sections are required for the threshold analysis of DFB lasers since a fairly uniform process is concerned.

For an arbitrary one-dimensional laser structure as shown in Figure 4.1, the wave propagation is modelled by a 2×2 matrix **A** such that any electric field leaving (i.e. $E_R(z_{i+1})$ and $E_S(z_i)$) and those entering (i.e. $E_R(z_i)$ and $E_S(z_{i+1})$) that section are related to one another as

$$\mathbf{U} = \mathbf{AV} \tag{4.2.1}$$

where **U** and **V** are two column matrices each containing two electric wave components. Depending on the type of matrix method, the contents of **U** and **V** may vary.

In the scattering matrix method, the matrix **U** includes all electric waves leaving the arbitrary section whilst the matrix **V** contains those entering the section. In both the transmission line matrix (TLM) and the TMM, the matrix **U** represents the electric wave components from one side of the section whilst wave components from the other side are included in the matrix **V**. For the analysis of semiconductor laser devices, both TLM and TMM have been used. The difference between TLM and TMM lies in the domain of analysis. TLM is performed in the time domain, whereas TMM works extremely well in the frequency domain. Table 4.1 summarises the characteristics of the matrix methods.

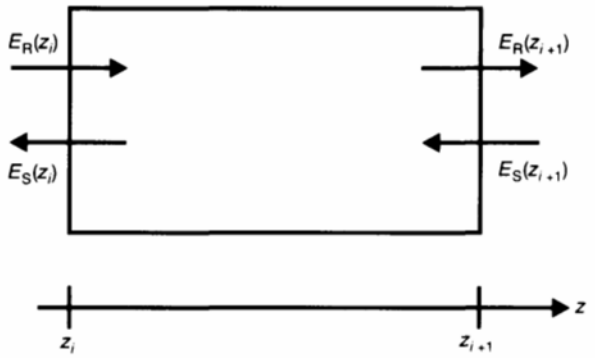

Figure 4.1 Wave propagation in a general one-dimensional laser diode structure.

Table 4.1 Different types of matrix methods

Name	U	V	Domain
Scattering matrix	$E_R(z_{i+1})$ and $E_S(z_i)$	$E_R(z_i)$ and $E_S(z_{i+1})$	frequency
TLM	$E_R(z_{i+1})$ and $E_S(z_{i+1})$	$E_R(z_i)$ and $E_S(z_i)$	time
TMM	$E_R(z_{i+1})$ and $E_S(z_{i+1})$	$E_R(z_i)$ and $E_S(z_i)$	frequency

Using the time-domain-based TLM, transient responses like switching in semiconductor laser devices can be analysed. Steady-state values may then be determined from the asymptotic approximation. However, it is difficult to use TLM to determine noise characteristics and hence the spectral linewidth of semiconductor lasers. Owing to the fact that most noise-related phenomena are time-averaged stochastic processes, a long sampling time will be necessary if TLM is used. In general, TLM is not suitable for the analysis of noise characteristics in semiconductor laser devices.

The TMM was first proposed in 1987 by Yamada and Suematsu to analyse the transmission and reflection gains of laser amplifiers with corrugated structures. This frequency-domain-based method works extremely well for both steady-state and noise analysis [6,9]. In the present study, we are interested in the steady-state and noise characteristics of DFB lasers. Hence, the use of TMM will be more appropriate.

4.2.1 Formulation of transfer matrices

On the basis of the coupled wave equations, we can derive the transfer matrix for a corrugated DFB laser section. From the solution of the coupled wave equations, we can write

$$\begin{aligned} E(z) &= E_R(z) + E_S(z) \\ &= R(z)e^{-j\beta_0 z} + S(z)e^{j\beta_0 z} \end{aligned} \tag{4.2.2}$$

where $E_R(z)$ and $E_S(z)$ are the complex electric fields of the wave solutions, $R(z)$ and $S(z)$ are two slow varying complex amplitude terms and β_0 is the Bragg propagation constant. From equation (3.2.3), $R(z)$ and $S(z)$ have proposed solutions of the form

$$R(z) = R_1 e^{\gamma z} + R_2 e^{-\gamma z} \tag{4.2.3a}$$

$$S(z) = S_1 e^{\gamma z} + S_2 e^{-\gamma z} \tag{4.2.3b}$$

where R_1, R_2, S_1 and S_2 are complex coefficients which are found to be related to one another as [15]

$$S_1 = \rho e^{j\Omega} R_1 \tag{4.2.4a}$$

$$R_2 = \rho e^{-j\Omega} S_2 \tag{4.2.4b}$$

where and $\rho = j\kappa/(\alpha - j\delta + \gamma)$ and Ω is the residue corrugation phase at the origin. By substituting equation (4.2.4) into (4.2.3), we obtain

$$R(z) = R_1 e^{\gamma z} + \rho S_2 e^{-j\Omega} e^{-\gamma z} \tag{4.2.5a}$$

$$S(z) = \rho R_1 e^{j\Omega} e^{\gamma z} + S_2 e^{-\gamma z} \tag{4.2.5b}$$

Instead of four variables, the solution of the coupled wave equations is simplified to functions of two coefficients, R_1 and S_2. Suppose the corrugation

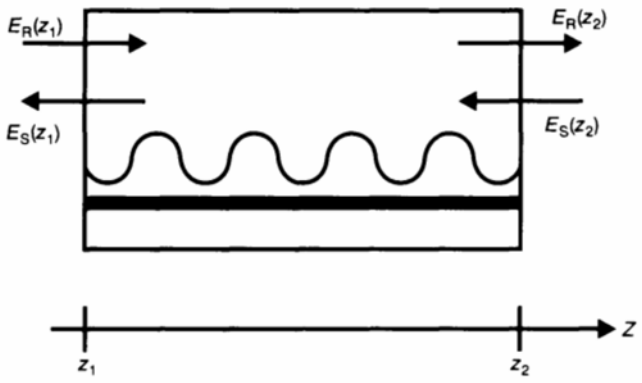

Figure 4.2 A simplified schematic diagram for a one-dimensional corrugated DFB laser diode section.

inside the DFB laser extends from $z = z_1$ to $z = z_2$, as shown in Figure 4.2, the amplitude coefficients at the left and right facets can then be written as

$$R(z_1) = R_1 e^{\gamma z_1} + \rho S_2 e^{-j\Omega} e^{-\gamma z_1} \tag{4.2.6a}$$

$$S(z_1) = \rho R_1 e^{j\Omega} e^{\gamma z_1} + S_2 e^{-\gamma z_1} \tag{4.2.6b}$$

$$R(z_2) = R_1 e^{\gamma z_2} + \rho S_2 e^{-j\Omega} e^{-\gamma z_2} \tag{4.2.6c}$$

$$S(z_2) = \rho R_1 e^{j\Omega} e^{\gamma z_2} + S_2 e^{-\gamma z_2} \tag{4.2.6d}$$

From equations (4.2.6a) and (4.2.6b) we can express R_1 and S_2 such that

$$R_1 = \frac{\rho S(z_1) e^{-j\Omega} - R(z_1)}{(\rho^2 - 1) e^{\gamma z_1}} \tag{4.2.7a}$$

and

$$S_2 = \frac{\rho R(z_1) e^{j\Omega} - S(z_1)}{(\rho^2 - 1) e^{-\gamma z_1}} \tag{4.2.7b}$$

By substituting the above equations back into equations (4.2.6c) and (4.2.6d), we obtain

$$R(z_2) = \frac{E - \rho^2 E^{-1}}{1 - \rho^2} R(z_1) - \frac{\rho(E - E^{-1}) e^{-j\Omega}}{1 - \rho^2} S(z_1) \tag{4.2.8a}$$

and

$$S(z_2) = \frac{\rho(E - E^{-1}) e^{j\Omega}}{1 - \rho^2} R(z_1) - \frac{\rho^2 E - E^{-1}}{1 - \rho^2} S(z_1) \tag{4.2.8b}$$

where

$$E = e^{\gamma(z_2 - z_1)}, \quad E^{-1} = e^{-\gamma(z_2 - z_1)} \tag{4.2.8c}$$

From the above equations it is clear that the electric fields at the output plane z_2 can be expressed in terms of the electric waves at the input plane.

By combining the above equations with equation (4.2.2) we can relate the output and input electric fields through the following matrix equation [6]:

$$\begin{bmatrix} E_R(z_2) \\ E_S(z_2) \end{bmatrix} = \mathbf{T}(z_2|z_1) \cdot \begin{bmatrix} E_R(z_1) \\ E_S(z_1) \end{bmatrix} = \begin{bmatrix} t_{11} & t_{12} \\ t_{21} & t_{22} \end{bmatrix} \cdot \begin{bmatrix} E_R(z_1) \\ E_S(z_1) \end{bmatrix} \tag{4.2.9}$$

where the matrix $\mathbf{T}(z_2|z_1)$ represents any wave propagation from $z = z_1$ to $z = z_2$ and its elements $t_{ij}(i, j = 1, 2)$ are given as

$$t_{11} = (E - \rho^2 E^{-1}) \cdot e^{-j\beta_0(z_2 - z_1)}/(1 - \rho^2) \tag{4.2.10a}$$

$$t_{12} = -\rho(E - E^{-1}) \cdot e^{-j\Omega} e^{-j\beta_0(z_2 + z_1)}/(1 - \rho^2) \tag{4.2.10b}$$

$$t_{21} = \rho(E - E^{-1}) \cdot e^{j\Omega} e^{j\beta_0(z_2 + z_1)}/(1 - \rho^2) \tag{4.2.10c}$$

$$t_{22} = -(\rho^2 E - E^{-1}) \cdot e^{j\beta_0(z_2 - z_1)}/(1 - \rho^2) \tag{4.2.10d}$$

For convenience, the matrix written in this way is called the forward transfer matrix because the output plane at $z = z_2$ is located farther away from the origin. Similarly, waves propagating inside the corrugated structure can also be expressed as the backward transfer matrix such that [16]

$$\begin{bmatrix} E_R(z_1) \\ E_S(z_1) \end{bmatrix} = \mathbf{U}(z_1|z_2) \cdot \begin{bmatrix} E_R(z_2) \\ E_S(z_2) \end{bmatrix} = \begin{bmatrix} u_{11} & u_{12} \\ u_{21} & u_{22} \end{bmatrix} \cdot \begin{bmatrix} E_R(z_2) \\ E_S(z_2) \end{bmatrix} \tag{4.2.11}$$

where the matrix $\mathbf{U}(z_1|z_2)$ represents any field propagation inside the section from $z = z_2$ to $z = z_1$. By comparing equation (4.2.9) with equation (4.2.11), it is obvious that

$$\mathbf{U}(z_1|z_2) = [\mathbf{T}(z_2|z_1)]^{-1} \tag{4.2.12}$$

where the superscript -1 shown denotes the inverse of the matrix. Owing to the conservation of energy, both matrices $\mathbf{T}(z_2|z_1)$ and $\mathbf{U}(z_1|z_2)$ must satisfy the reciprocity rule such that their determinants always give unity value [4]. In other words,

$$\begin{aligned} |\mathbf{T}| &= t_{11}t_{22} - t_{12}t_{21} = 1 \\ |\mathbf{U}| &= u_{11}u_{22} - u_{12}u_{21} = 1 \end{aligned} \tag{4.2.13}$$

4.2.2 Introduction of the phase shift (or phase discontinuity)

For a single PS DFB laser cavity, as shown in Figure 4.3, the PS at $z = z_2$ divides the laser cavity into two sections.

The field discontinuity is usually small along the plane of phase shift and any wave travelling across the PS is assumed to be continuous. As a result, the transfer matrices are linked at the PS position (PSP) as

$$\begin{bmatrix} E_R(z_2^+) \\ E_S(z_2^+) \end{bmatrix} = \mathbf{P}^{(2)} \cdot \begin{bmatrix} E_R(z_2^-) \\ E_S(z_2^-) \end{bmatrix} = \begin{bmatrix} e^{j\theta_2} & 0 \\ 0 & e^{-j\theta_2} \end{bmatrix} \cdot \begin{bmatrix} E_R(z_2^-) \\ E_S(z_2^-) \end{bmatrix} \tag{4.2.14}$$

where $\mathbf{P}^{(2)}$ is the PS matrix at $z = z_2$; z_2^+ and z_2^- are the greater and the lesser values of z_2, respectively, and θ_2 corresponds to the phase change experienced

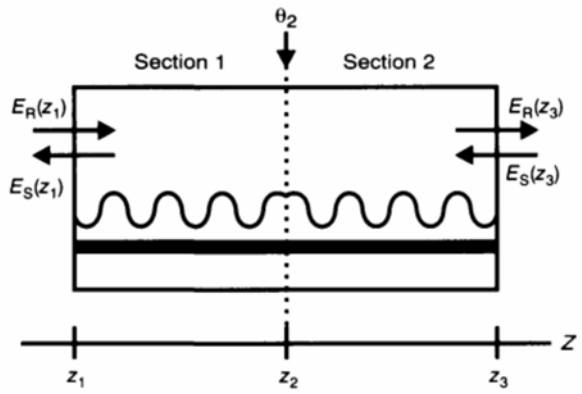

Figure 4.3 Schematic diagram showing a 1PS DFB laser diode section.

by the electric waves $E_R(z)$ and $E_S(z)$. Alternatively, the physical phase shift of the corrugation may be used [9]. To avoid any confusion, in what follows we will use the phase shift of the electric wave.

On combining equation (4.2.14) with the transfer matrix as shown earlier in equation (4.2.9), the overall transfer matrix chain of a single PS DFB laser becomes

$$\begin{bmatrix} E_R(z_3) \\ E_S(z_3) \end{bmatrix} = \begin{bmatrix} t_{11}^{(2)} & t_{12}^{(2)} \\ t_{21}^{(2)} & t_{22}^{(2)} \end{bmatrix} \cdot \begin{bmatrix} e^{j\phi_2} & 0 \\ 0 & e^{-j\phi_2} \end{bmatrix} \cdot \begin{bmatrix} t_{11}^{(1)} & t_{12}^{(1)} \\ t_{21}^{(1)} & t_{22}^{(1)} \end{bmatrix} \cdot \begin{bmatrix} E_R(z_1) \\ E_S(z_1) \end{bmatrix}$$

$$= \mathbf{T}^{(2)} \cdot \mathbf{P}^{(2)} \cdot \mathbf{T}^{(1)} \cdot \begin{bmatrix} E_R(z_1) \\ E_S(z_1) \end{bmatrix} \tag{4.2.15}$$

Without affecting the results of the above equations, we can multiply the matrix $\mathbf{T}^{(1)}$ by the unity matrix $\mathbf{I}$. The matrix $\mathbf{I}$ behaves as if an imaginary PS of zero or a multiple of 2π has been introduced. As a result, the above matrix equation can be simplified such that

$$\begin{bmatrix} E_R(z_3) \\ E_S(z_3) \end{bmatrix} = \mathbf{Y}(z_3|z_1) \cdot \begin{bmatrix} E_R(z_1) \\ E_S(z_1) \end{bmatrix} \tag{4.2.16}$$

where

$$\mathbf{Y}(z_3|z_1) = \prod_{m=2}^{1} \mathbf{F}^{(m)} = \begin{bmatrix} y_{11}(z_3|z_1) & y_{12}(z_3|z_1) \\ y_{21}(z_3|z_1) & y_{22}(z_3|z_1) \end{bmatrix} \tag{4.2.17a}$$

$$\mathbf{F}^{(m)} = \mathbf{T}^{(m)} \cdot \mathbf{P}^{(m)} = \begin{bmatrix} f_{11}^{(m)} & f_{12}^{(m)} \\ f_{21}^{(m)} & f_{22}^{(m)} \end{bmatrix} = \begin{bmatrix} t_{11}^{(m)} e^{j\theta_m} & t_{12}^{(m)} e^{-j\theta_m} \\ t_{21}^{(m)} e^{j\theta_m} & t_{22}^{(m)} e^{-j\theta_m} \end{bmatrix} \tag{4.2.17b}$$

$$\mathbf{P}^{(1)} = \mathbf{I} = \begin{bmatrix} 1 & 0 \\ 0 & 1 \end{bmatrix} \tag{4.2.17c}$$

In the above equation the overall matrix $\mathbf{Y}(z_3|z_1)$ comprises the characteristics of the field propagation inside the DFB laser cavity, whilst the corrugated

matrix $\mathbf{T}^{(m)}$ and the PS matrix $\mathbf{P}^{(m)}(m = 1, 2)$ are combined to form the matrix $\mathbf{F}^{(m)}$.

The use of the TMM is not restricted to the corrugated DFB laser structure. By modifying the values of κ and α in the elements of the transfer matrix, other structures like the planar FP structure, the planar WG structure and the corrugated DBR structure can also be represented using the transfer matrix. A DBR structure is different from the DFB structure because DBR structures have no underlying active region. The corrugated DBR structure simply acts as a partially reflecting mirror that depends on the wavelength. The maximum reflection occurs near the central Bragg wavelength. Table 4.2 summarises all laser structures that can be represented by transfer matrices. The differences between them are also listed.

When the grating height g reduces to zero and the grating period Λ approaches infinity, the feedback caused by the presence of corrugations becomes less important. At $g = 0$, κ becomes zero as does the variable ρ. When Λ becomes infinite, the detuning coefficient δ is reduced to the propagation constant $2\pi n/\lambda$. In this case, the DFB corrugated structure becomes a planar structure. Following equations (4.2.9) and (4.2.10), the transfer matrix equation of the planar structure becomes

$$\begin{bmatrix} E_R(z_2) \\ E_S(z_2) \end{bmatrix} = \mathbf{T}^{(1)} \cdot \begin{bmatrix} E_R(z_1) \\ E_S(z_1) \end{bmatrix} = \begin{bmatrix} t_{11}^{(1)} & t_{12}^{(1)} \\ t_{21}^{(1)} & t_{22}^{(1)} \end{bmatrix} \cdot \begin{bmatrix} E_R(z_1) \\ E_S(z_1) \end{bmatrix} \tag{4.2.18}$$

where

$$\begin{aligned} t_{11}^{(1)} &= e^{\alpha(z_2 - z_1)} e^{-j\beta(z_2 - z_1)} \\ t_{12}^{(1)} &= t_{21}^{(1)} = 0 \\ t_{22}^{(1)} &= e^{-\alpha(z_2 - z_1)} e^{j\beta(z_2 - z_1)} \end{aligned} \tag{4.2.19}$$

In the above equation the amplitude gain term α decides the characteristics of the planar structure. For $\alpha > 0$, the amplitude of the electric wave passing through will be amplified and the structure will behave as if it is a laser amplifier. For $\alpha \leq 0$, the amplitude of the electric wave will either remain constant or be attenuated because the planar structure becomes a passive WG. Similarly, the sign of α will decide whether a corrugated structure belongs to the DFB or DBR structure. By joining these matrices together as building

Table 4.2 Laser structures that can be represented using the TMM

Structure	Active layer	Corrugation	Comments
FP	√	×	$\kappa = 0$ and $\alpha > 0$
WG	×	×	$\kappa = 0$ and $\alpha \leq 0$
DFB	√	√	finite κ and $\alpha > 0$
DBR	×	√	finite κ and $\alpha \leq 0$

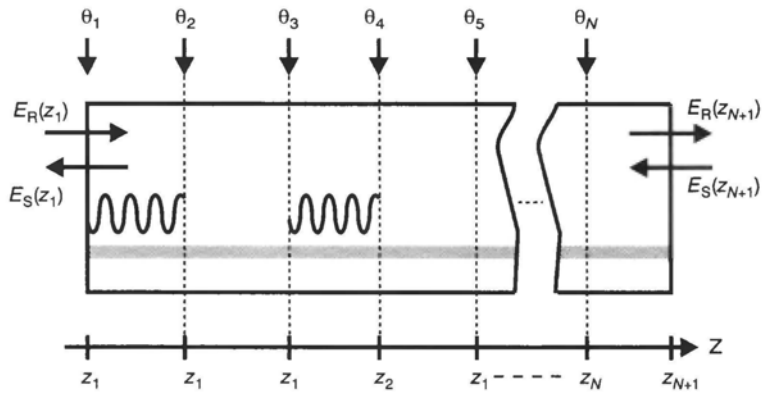

Figure 4.4 Schematic diagram of a general N-section laser cavity. The phase shifts $\{\theta_1, \theta_2, \ldots, \theta_n\}$ are shown. The active regions along the laser cavity are shaded.

blocks, we can extend the idea further to form a general N-section composite laser cavity, as shown in Figure 4.4.

Laser structures that comprise different combinations of the sections shown in Table 4.2 can be modelled. By joining these matrices together appropriately, we end up with

$$\begin{bmatrix} E_R(z_{N+1}) \\ E_S(z_{N+1}) \end{bmatrix} = \mathbf{F}^{(N)} \cdot \mathbf{F}^{(N-1)} \cdots \mathbf{F}^{(2)} \cdot \mathbf{F}^{(1)} \begin{bmatrix} E_R(z_1) \\ E_S(z_1) \end{bmatrix}$$

$$= \mathbf{Y}(z_{N+1}|z_1) \cdot \begin{bmatrix} E_R(z_1) \\ E_S(z_1) \end{bmatrix} \tag{4.2.20}$$

where the matrix $\mathbf{Y}(z_{N+1}|z_1)$ becomes the overall transfer matrix for the N-section laser cavity. Using the backward transfer matrix together with equations (4.2.11) and (4.2.14), we obtain

$$\begin{bmatrix} E_R(z_1) \\ E_S(z_1) \end{bmatrix} = \prod_{m=1}^{N} \mathbf{G}^{(m)} \cdot \begin{bmatrix} E_R(z_{N+1}) \\ E_S(z_{N+1}) \end{bmatrix} = \mathbf{Z}(z_1|z_{N+1}) \begin{bmatrix} E_R(z_{N+1}) \\ E_S(z_{N+1}) \end{bmatrix} \tag{4.2.21}$$

where

$$\mathbf{G}^{(m)} = \left[\mathbf{P}^{(m)}\right]^{-1} \cdot \mathbf{U}^{(m)} = \begin{bmatrix} g_{11}^{(m)} & g_{12}^{(m)} \\ g_{21}^{(m)} & g_{22}^{(m)} \end{bmatrix} = \begin{bmatrix} u_{11}^{(m)} e^{-j\theta_m} & u_{12}^{(m)} e^{-j\theta_m} \\ u_{21}^{(m)} e^{j\theta_m} & u_{22}^{(m)} e^{j\theta_m} \end{bmatrix} \tag{4.2.22a}$$

$$\mathbf{Z}(z_1|z_{N+1}) = \begin{bmatrix} z_{11}(z_1|z_{N+1}) & z_{12}(z_1|z_{N+1}) \\ z_{21}(z_1|z_{N+1}) & z_{22}(z_1|z_{N+1}) \end{bmatrix} \tag{4.2.22b}$$

In the above equation, $[\mathbf{P}^{(m)}]^{-1}$ is the inverse of the PS matrix $\mathbf{P}^{(m)}$ and $\mathbf{Z}(z_1|z_{N+1})$ is the overall backward transfer matrix. Comparing equations (4.2.20) with (4.2.21), it is clear that the matrices $\mathbf{Y}(z_{N+1}|z_1)$ and

$\mathbf{Z}(z_1|z_{N+1})$ are inverse to one another such that

$$\mathbf{Z}(z_1|z_{N+1}) = [\mathbf{Y}(z_{N+1}|z_1)]^{-1} \tag{4.2.23}$$

where the superscript -1 indicates the inverse of the matrix. From the property of the inverse of matrix products, the individual transfer matrices $\mathbf{G}^{(m)}$ and $\mathbf{F}^{(m)}$ are related to one another. That is

$$\mathbf{G}^{(m)} = [\mathbf{F}^{(m)}]^{-1} \quad \text{for } m = 1 \text{ to } N \tag{4.2.24}$$

The above equation shows the equivalence between the forward and the backward transfer matrices in the general N-section laser cavity. Unless stated otherwise, the forward transfer matrix is assumed hereafter.

4.2.3 Effects of finite facet reflectivities

In Chapter 3 we stated that the lasing characteristic of the DFB laser depend on the facet reflectivity. In this section the facet reflectivity will be implemented using the TMM. In Figure 4.5 we show a simplified schematic diagram for the reflections at the facets of the N-section laser cavity.

In Figure 4.5, $\hat{r}_1$ and $\hat{r}_2$ are the amplitude reflections at the left and right facets, respectively, and medium 1 is the active region of the LD. In most practical cases, medium 2 is air. Owing to the finite thickness of the coating on the laser facets, any electric field passing through may suffer a phase change of $\phi_i (i = 1, 2)$. Depending on the direction of propagation, all the outgoing electric fields at the left facet (i.e. $E_R(z_1^+)$ and $E_S(z_1^-)$ can be expressed in terms of the incoming waves as

$$E_R(z_1^+) = \sqrt{1 - \hat{r}_1^2}\, e^{-j\phi_1} E_R(z_1^-) + \hat{r}_1 E_S(z_1^+) \tag{4.2.25a}$$

$$E_S(z_1^-) = \hat{r}_1 E_R(z_1^-) + \sqrt{1 - \hat{r}_1^2}\, e^{j\phi_1} E_S(z_1^+) \tag{4.2.26b}$$

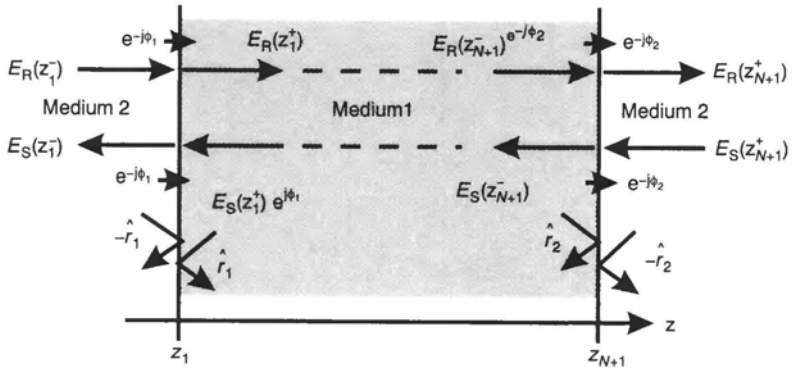

Figure 4.5 Schematic diagram showing reflections at the facets of a DFB LD.

Rearranging the above equations for the electric fields at $z = z_1^+$, we obtain

$$E_R(z_1^+) = \frac{e^{-j\phi_1}}{\sqrt{1-\hat{r}_1^2}} E_R(z_1^-) + \frac{\hat{r}_1 e^{-j\phi_1}}{\sqrt{1-\hat{r}_1^2}} E_S(z_1^-) \tag{4.2.27}$$

$$E_S(z_1^+) = \frac{\hat{r}_1 e^{-j\phi_1}}{\sqrt{1-\hat{r}_1^2}} E_R(z_1^-) + \frac{e^{-j\phi_1}}{\sqrt{1-\hat{r}_1^2}} E_S(z_1^-) \tag{4.2.28}$$

In matrix form, the above equations shown can be written as:

$$\begin{bmatrix} E_R(z_1^+) \\ E_S(z_1^+) \end{bmatrix} = \frac{1}{e^{j\phi_1}\sqrt{1-\hat{r}_1^2}} \cdot \begin{bmatrix} 1 & \hat{r}_1 \\ \hat{r}_1 & 1 \end{bmatrix} \cdot \begin{bmatrix} E_R(z_1^-) \\ E_S(z_1^-) \end{bmatrix} \tag{4.2.29a}$$

Similarly, the reflection at the right facet can be written as

$$\begin{bmatrix} E_R(z_{N+1}^+) \\ E_S(z_{N+1}^+) \end{bmatrix} = \frac{1}{e^{j\phi_2}\sqrt{1-\hat{r}_2^2}} \cdot \begin{bmatrix} 1 & -\hat{r}_2 \\ -\hat{r}_2 & 1 \end{bmatrix} \cdot \begin{bmatrix} E_R(z_{N+1}^-) \\ E_S(z_{N+1}^-) \end{bmatrix} \tag{4.2.29b}$$

On combining the propagation matrix $\mathbf{Y}(z_{N+1}|z_1)$ with the reflections at the laser facets, the overall transfer function of the N-section DFB laser structure becomes

$$\begin{bmatrix} E_R(z_{N+1}^+) \\ E_S(z_{N+1}^+) \end{bmatrix} = \frac{1}{e^{j\phi_2}\sqrt{1-\hat{r}_2^2}} \cdot \begin{bmatrix} 1 & -\hat{r}_2 \\ -\hat{r}_2 & 1 \end{bmatrix} \cdot \mathbf{Y}(z_{N+1}|z_1) \cdot \frac{1}{e^{j\phi_1}\sqrt{1-\hat{r}_1^2}} \begin{bmatrix} 1 & \hat{r}_1 \\ \hat{r}_1 & 1 \end{bmatrix} \begin{bmatrix} E_R(z_1^-) \\ E_S(z_1^-) \end{bmatrix} \tag{4.2.30}$$

It will be easier to simplify the above matrix equation by an overall transfer matrix $\mathbf{H}$ such that

$$\begin{bmatrix} E_R(z_{N+1}^+) \\ E_S(z_{N+1}^+) \end{bmatrix} = \mathbf{H} \cdot \begin{bmatrix} E_R(z_1^-) \\ E_S(z_1^-) \end{bmatrix} = \begin{bmatrix} h_{11} & h_{12} \\ h_{21} & h_{22} \end{bmatrix} \cdot \begin{bmatrix} E_R(z_1^-) \\ E_S(z_1^-) \end{bmatrix} \tag{4.2.31}$$

where $h_{i,j}(i, j = 1, 2)$ are the elements of the overall transfer matrix H.

4.3 THRESHOLD CONDITION FOR THE N-SECTION LASER CAVITY

Since the laser itself is an oscillatory device, the output waves $E_R(z_{N+1}^+)$ and $E_S(z_1^-)$ denoted in the N-section laser cavity should have finite values even though there are no incoming waves [9]. Suppose one of the incoming waves, $E_R(z_1^-)$, becomes zero, then equation (4.2.31) is simplified to become

$$E_R(z_{N+1}^+) = h_{12} E_S(z_1^-) \tag{4.3.1}$$

$$E_S(z_{N+1}^+) = h_{22} E_S(z_1^-) \tag{4.3.2}$$

The transmission gain A_t of the backward travelling wave can then be expressed as [2]

$$A_t = \frac{E_S(z_1^-)}{E_S(z_{N+1}^+)} = \frac{1}{h_{22}} \tag{4.3.3}$$

When the matrix element h_{22} approaches zero, the transmission gain becomes infinite and a resonant cavity is formed. Physically, a laser that operates in this condition is said to have the threshold condition satisfied. After substantial manipulation of equation (4.2.30), the threshold condition becomes

$$y_{22}(z_{N+1}|z_1) + \hat{r}_1 y_{21}(z_{N+1}|z_1) - \hat{r}_2 y_{12}(z_{N+1}|z_1) - \hat{r}_1 \hat{r}_2 y_{11}(z_{N+1}|z_1) = 0 \tag{4.3.4}$$

For DFB semiconductor lasers with finite facet reflections, we need to find all the elements of the propagation matrix $\mathbf{Y}(z_{N+1}|z_1)$. For a mirrorless DFB laser cavity where $\hat{r}_1 = \hat{r}_2 = 0$, the above-threshold equation is simplified such that

$$y_{22}(z_{N+1}|z_1) = 0 \tag{4.3.5}$$

Table 4.3 Semiconductor laser diode structures that can be analysed using the TMM (after [27])

Laser structures	Number of transfer matrices	Phase shifts	Remarks
FP lasers	1	—	$\kappa = 0$, $\Lambda \to \infty$
Conventional DFB LD	1	—	$\hat{r}_1 = \hat{r}_2 = 0$ for a mirrorless cavity
Single PS DFB	2	θ_2	θ_1 is always zero
Multiple PS DFB	$N+1$	$\theta_2 \ldots \theta_{N+1}$	θ_1 is always zero
Multiple electrodes DFB — non-uniform current injection	N	—	laser medium is homogeneous within a single section only
Corrugation-pitch-modulated DFB — different corrugation period in each section	3	—	β_0 changes in each section
Linear chirped corrugation — continuous change in corrugation period	large number	—	β_0 varies along the laser cavity
Tapered corrugation — continuous change in corrugation depth g	large number	—	κ varies along the laser cavity
N-layer surface emitting laser	N	—	—

In fact, equation (4.3.4) is a general expression that can be used to determine the lasing threshold characteristics of semiconductor laser devices. These include FP lasers, conventional DFB lasers (both mirrorless and those with finite facet reflections), single PS DFB laser structures, multiple PS DFB laser structures [17–19] as well as multiple electrode DFB laser structures [16,20–23]. By increasing the number of sections, TMM is also used to represent a tapered or chirped DFB laser structure [3,4,24]. Similarly, a transfer matrix has also been used in the surface-emitting devices [25,26] which have received worldwide attention in recent years. Table 4.3 summarises the minimum number of transfer matrices and PS required in the threshold analysis of some popular semiconductor laser structures [27].

4.4 FORMULATION OF THE AMPLIFIED SPONTANEOUS EMISSION SPECTRUM USING THE TRANSFER MATRIX METHOD (TMM)

In the previous section the threshold equation for the N-section laser cavity was defined using the transfer matrix. In fact, the TMM can also be applied to the below-threshold analysis. In semiconductor-based optical amplifiers and filters, the spontaneous emission spectrum has been used to determine the bandwidth, tunability and signal gain characteristics. On the basis of the use of Green's function [28] for the noise calculation of the open resonator, the transfer matrix formulation will be extended to include the output spontaneous emission spectrum taken from the right laser facet.

4.4.1 *Green's function method based on the transfer matrix formulation*

In this section we refer once again to the general N-section laser cavity as shown earlier in Figure 4.4. The amplitude reflections at the left and right laser facets are $\hat{r}_1$ and $\hat{r}_2$, respectively, and perfect index-coupling is assumed. Following Henry [28], the one-dimensional inhomogeneous wave equation of a transversely and laterally confined laser mode in the composite longitudinal structure can be expressed as

$$\left[\frac{\mathrm{d}^2}{\mathrm{d}z^2} + \beta(z)^2\right] E_\omega(z) = F_\omega(z) \tag{4.4.1}$$

where $\beta(z)$ is the propagation constant, $E_\omega(z)$ is the complex Fourier component of the electric wave and $F_\omega(z)$ is the Langevin force term which accounts for the distributed spontaneous emission noise inside the semiconductor laser [28,29]. In the above equation, $\beta(z)$ includes any spatial variation in the physical systems that may affect the propagation constant. The electric field $E(z)$ in the time domain is determined from the inverse Fourier transform such that

$$E(z) = \int_0^\infty E_\omega(z)\mathrm{e}^{j\omega t}\,\mathrm{d}\omega + \text{c.c.} \tag{4.4.2}$$

where c.c. is the complex conjugate. Using Green's function [30,31], the general solution of equation (4.4.1) can be written as

$$E_\omega = \int_{z_1}^{z} G(z, z')F_\omega(z')\mathrm{d}z' \tag{4.4.3}$$

where z' locates the spontaneous noise source and $G(z, z')$ is Green's function. In the above equation the integral sums up the impulse responses of the spontaneous emission noise source that originates from the left facet at $z = z_1$ to that at the observation point, z. The function $G(z, z')$ is given as [32]

$$G(z, z') = \begin{cases} Z_1(z)Z_2(z')/W, & \text{for } z < z' \\ Z_1(z')Z_2(z)/W, & \text{for } z > z' \end{cases} \tag{4.4.4}$$

where $Z_1(z)$ and $Z_2(z)$ are two independent solutions of the homogeneous wave equation (with $F_\omega(z) = 0$) that satisfy the boundary conditions at $z = z_1$ and $z = z_{N+1}$, respectively. The Wronskian term W is defined as

$$W = Z_1(z)\frac{\mathrm{d}Z_2(z)}{\mathrm{d}z} - Z_2(z)\frac{\mathrm{d}Z_1(z)}{\mathrm{d}z} \tag{4.4.5}$$

From the above equation it is obvious that W is finite if and only if $Z_1(z)$ and $Z_2(z)$ are two independent functions. According to the solution of the coupled-wave equations, the normalised electric field at an arbitrary point $z_1 \le z' \le z_{N+1}$ inside a general N-section DFB laser cavity can be expressed as

$$\begin{aligned} E(z') &= E_{\mathrm{R}}(z') + E_{\mathrm{S}}(z') \\ &= R(z')\mathrm{e}^{-j\beta_0 z'} + S(z')\mathrm{e}^{j\beta_0 z'} \end{aligned} \tag{4.4.6}$$

where z' is an arbitrary point lying within the transfer matrix section $\mathbf{F}^{(k)}$ such that $z_k \le z' \le z_{k+1}$. Using the forward transfer matrix as shown in the previous section, the complex electric fields $E_{\mathrm{R}}(z')$ and $E_{\mathrm{S}}(z')$ become

$$\begin{aligned} \begin{bmatrix} E_{\mathrm{R}}(z') \\ E_{\mathrm{S}}(z') \end{bmatrix} = \begin{bmatrix} E_{\mathrm{R}}(z'|z_1) \\ E_{\mathrm{S}}(z'|z_1) \end{bmatrix} &= \mathbf{F}^{(k)}(z'|z_k) \cdot \prod_{j=k-1}^{1} \mathbf{F}^{(j)} \cdot \begin{bmatrix} E_{\mathrm{R}}(z_1) \\ E_{\mathrm{S}}(z_1) \end{bmatrix} \\ &= \mathbf{Y}(z'|z_1) \cdot \begin{bmatrix} E_{\mathrm{R}}(z_1) \\ E_{\mathrm{S}}(z_1) \end{bmatrix} \end{aligned} \tag{4.4.7}$$

where the transfer matrix $\mathbf{F}^{(k)}(z'|z_k)$ has taken into account any wave propagation between $z = z_k$ and $z = z'$ in section k. In simplifying the matrix representation, a matrix is used to represent any wave change between the input plane at $z = z_1$ and the output at $z = z'$. Similarly, the complex electric fields at $z = z_{N+1}$ can be expressed in terms of the complex electric field at $z = z'$ such that

$$\begin{bmatrix} E_{\mathrm{R}}(z_{N+1}) \\ E_{\mathrm{S}}(z_{N+1}) \end{bmatrix} = \prod_{j=N}^{k+1} \mathbf{F}^{(j)} \cdot \mathbf{F}^{(k)}(z_{k+1}|z') \begin{bmatrix} E_{\mathrm{R}}(z') \\ E_{\mathrm{S}}(z') \end{bmatrix} = \mathbf{Y}(z_{N+1}|z') \cdot \begin{bmatrix} E_{\mathrm{R}}(z') \\ E_{\mathrm{S}}(z') \end{bmatrix} \tag{4.4.8}$$

where the same forward transfer matrix technique has been used. Similar to equation (4.4.7), the matrix representation is simplified by the matrix $\mathbf{Y}(z_{N+1}|z')$ which corresponds to any wave change between $z = z'$ and $z = z_{N+1}$. By multiplying both sides of equation (4.4.8) by the the inverse matrix $[\mathbf{Y}(z_{N+1}|z')]^{-1}$, we obtain

$$[\mathbf{Y}^{(k)}(z_{N+1}|z')]^{-1} \cdot \begin{bmatrix} E_R(z_{N+1}) \\ E_S(z_{N+1}) \end{bmatrix} = [\mathbf{Y}^{(k)}(z_{N+1}|z')]^{-1} \cdot \mathbf{Y}^{(k)}(z_{N+1}|z') \cdot \begin{bmatrix} E_R(z') \\ E_S(z') \end{bmatrix}$$

$$\prod_{j=N}^{k+1} \mathbf{F}^{(j)}[\mathbf{F}^{(k)}(z_{N+1}|z')]^{-1} \cdot \begin{bmatrix} E_R(z_{N+1}) \\ E_S(z_{N+1}) \end{bmatrix} = \begin{bmatrix} E_R(z') \\ E_S(z') \end{bmatrix}$$

$$\left[\mathbf{G}^{(k)}(z'|z_{N+1}) \prod_{j=k+1}^{N} \mathbf{G}^{(j)}\right] \cdot \begin{bmatrix} E_R(z_{N+1}) \\ E_S(z_{N+1}) \end{bmatrix} = \begin{bmatrix} E_R(z') \\ E_S(z') \end{bmatrix} \tag{4.4.9}$$

$$\mathbf{Z}(z'|z_{N+1}) \cdot \begin{bmatrix} E_R(z_{N+1}) \\ E_S(z_{N+1}) \end{bmatrix} = \begin{bmatrix} E_R(z') \\ E_S(z') \end{bmatrix} = \begin{bmatrix} E_R(z'|z_{N+1}) \\ E_S(z'|z_{N+1}) \end{bmatrix}$$

where equation (4.2.24) has been used to establish the last equality. In the above equation, backward transfer matrices have been used in which the complex electric fields at the right laser facets are used as inputs. Following the matrix equations (4.4.7) and (4.4.9), $Z_1(z)$ and $Z_2(z)$ can be written in term of the elements of the transfer matrix as

$$\begin{aligned} Z_1(z) &= E_R(z|z_1) + E_S(z|z_1) \\ &= [\hat{r}_1 y_{11}(z|z_1) + y_{12}(z|z_1)] + [\hat{r}_1 y_{21}(z|z_1) + y_{22}(z|z_1)] \end{aligned} \tag{4.4.10a}$$

$$\begin{aligned} Z_2(z) &= E_R(z_{N+1}|z_1) \cdot [E_R(z|z_{N+1}) + E_S(z|z_{N+1})] \\ &= E_R(z_{N+1}|z_1) \cdot \{[z_{11}(z|z_{N+1}) + \hat{r}_2 z_{12}(z|z_{N+1})] \\ &\quad + [z_{21}(z|z_{N+1}) + \hat{r}_2 z_{22}(z|z_{N+1})]\} \end{aligned} \tag{4.4.10b}$$

In equation (4.4.10b), the elements of the backward transfer matrix have been used. Since $y_{ij}(z_1|z_1) = z_{ij}(z_{N+1}|z_{N+1}) = \delta_{ij}(i, j = 1, 2)$, the Kronecker delta function [30], it is straightforward to verify that $Z_1(z)$ and $Z_2(z)$ satisfy the boundary conditions at the left and the right laser facets, respectively, such that

$$\frac{E_R(z_1)}{E_S(z_1)} = \frac{E_R(z_1|z_1)}{E_S(z_1|z_1)} = \hat{r}_1 \tag{4.4.11}$$

$$\frac{E_S(z_{N+1})}{E_R(z_{N+1})} = \frac{E_S(z_{N+1}|z_{N+1})}{E_R(z_{N+1}|z_{N+1})} = \hat{r}_2 \tag{4.4.12}$$

Finally, by substituting equations (4.4.10a) and (4.4.10b) into equation (4.4.5), the Wronskian term becomes

$$W = 2j\beta_0 E_R(z_{N+1}|z_1) \cdot \{E_R(z|z_1)E_S(z|z_{N+1}) - E_S(z|z_1)E_R(z|z_{N+1})\} \tag{4.4.13}$$

where the leading coefficient, $j\beta_0$, is obtained from the exponential expression, as shown in equation (4.4.6). By expanding the above equation with the matrix equations (4.4.7) and (4.4.9), we end up with

$$\begin{aligned} W = 2j\beta_0 E_R(z_{N+1}|z_1) \cdot \{ & z_{21}(z|z_{N+1}) y_{12}(z|z_1) - z_{11}(z|z_{N+1}) y_{22}(z|z_1) \\ & + \hat{r}_1 [z_{21}(z|z_{N+1}) y_{11}(z|z_1) - z_{11}(z|z_{N+1}) y_{12}(z|z_1)] \\ & + \hat{r}_2 [z_{22}(z|z_{N+1}) y_{12}(z|z_1) - z_{12}(z|z_{N+1}) y_{22}(z|z_1)] \\ & + \hat{r}_1 \hat{r}_2 [z_{22}(z|z_{N+1}) y_{11}(z|z_1) - z_{12}(z|z_{N+1}) y_{12}(z|z_1)] \} \end{aligned} \tag{4.4.14}$$

On the other hand, the elements of the matrix $\mathbf{Y}(z|z_1)$ and those of the matrix $\mathbf{Z}(z|z_{N+1})$ obey the following quality after equation (4.4.9) such that

$$\begin{aligned} [\mathbf{Z}(z|z_{N+1})]^{-1} &= \begin{bmatrix} z_{11}(z|z_{N+1}) & z_{12}(z|z_{N+1}) \\ z_{21}(z|z_{N+1}) & z_{22}(z|z_{N+1}) \end{bmatrix}^{-1} = \begin{bmatrix} z_{22}(z|z_{N+1}) & -z_{12}(z|z_{N+1}) \\ -z_{21}(z|z_{N+1}) & z_{11}(z|z_{N+1}) \end{bmatrix} \\ &= \begin{bmatrix} y_{11}(z_{N+1}|z) & y_{12}(z_{N+1}|z) \\ y_{21}(z_{N+1}|z) & y_{22}(z_{N+1}|z) \end{bmatrix} = \mathbf{Y}(z_{N+1}|z) \end{aligned} \tag{4.4.15}$$

As a result, the Wronskian term is simplified to become

$$W = -2j\beta_0 E_R(z_{N+1}|z_1)[y_{22} + \hat{r}_1 y_{21} - \hat{r}_2 y_{12} - \hat{r}_1 \hat{r}_2 y_{11}] \tag{4.4.16}$$

where the term in brackets in the above equation is the threshold equation of the N-section laser cavity, as shown in equation (4.3.4). In deriving the above equation, the following identities were used:

$$\begin{aligned} y_{22} &= y_{22}(z_{N+1}|z_1) = y_{21}(z_{N+1}|z) y_{12}(z|z_1) + y_{22}(z_{N+1}|z) y_{22}(z|z_1) \\ y_{21} &= y_{21}(z_{N+1}|z_1) = y_{21}(z_{N+1}|z) y_{11}(z|z_1) + y_{22}(z_{N+1}|z) y_{21}(z|z_1) \\ y_{12} &= y_{12}(z_{N+1}|z_1) = y_{11}(z_{N+1}|z) y_{12}(z|z_1) + y_{12}(z_{N+1}|z) y_{22}(z|z_1) \\ y_{11} &= y_{11}(z_{N+1}|z_1) = y_{11}(z_{N+1}|z) y_{11}(z|z_1) + y_{12}(z_{N+1}|z) y_{21}(z|z_1) \end{aligned} \tag{4.4.17}$$

When the threshold condition is reached, the term in brackets in (4.4.16) becomes zero and, hence, so does the Wronskian term. In other words, the proposed solutions $Z_1(z)$ and $Z_2(z)$ of the wave equation become dependent upon one another. In fact, it was shown by Makino [2] that they are identical at threshold.

4.4.2 Determination of below-threshold spontaneous emission power

When a LD is biased in the below-threshold regime, there is finite optical power output due to spontaneous emission. From the Poynting vector of the propagating field, the spontaneous emission power $P_N(z)$ within an angular frequency bandwidth $\Delta\omega$ can be written as [28]

$$P_N(z) = \frac{c\Delta\omega}{4\pi} \cdot \int_0^{\infty} dw' \int_{z_1}^{z} (E_\omega(z) H^*_{\omega'}(z) \cdot e^{j(\omega-\omega')t} + \text{c.c.}) dz \tag{4.4.18}$$

where c.c. is the complex conjugate of the integrand. For a laterally confined structure, the magnetic field H_ω be expressed as

$$H_\omega = \frac{j}{\omega\mu} \cdot \frac{\partial E_\omega(z)}{\partial z} \tag{4.4.19}$$

At the below-threshold biasing condition, there is no stimulated emission. Variables such as the optical gain (g) and the refractive index (n) remain homogeneous along the laser cavity. As a result, by replacing E_ω with Green's function and the Wronskian, equation (4.4.18) becomes

$$P_N(z) = \frac{c^2\Delta\omega}{4\pi\omega} \cdot \frac{2D_{FF^*}}{|W|^2} \cdot \left(-jZ_2(z)\frac{\mathrm{d}Z_2^*(z)}{\mathrm{d}z} + \text{c.c.}\right) \int_{z_1}^{z} |Z_1(z)|^2 \mathrm{d}z \tag{4.4.20}$$

where D_{FF^*} is the diffusion coefficient given as [28]

$$D_{FF^*} = 2\omega^3 \hbar n g n_{\text{sp}}/c^3 \tag{4.4.21}$$

where $\hbar = h/2\pi$ is the angular Planck constant and n_{sp} is the population inversion factor defined as [33]

$$n_{\text{sp}} = [1 - \mathrm{e}^{(\hbar\omega - \Delta E)/kT}]^{-1} \tag{4.4.22}$$

In the above equation, ΔE is the energy separation of the quasi-Fermi level between the conduction band and the valence band, k is Boltzmann's constant and T is the temperature in degrees Kelvin.

By replacing the Wronskian term and D_{FF^*} with the appropriate transfer matrix elements in the N-section laser cavity, equation (4.4.11) finally becomes [6]

$$P_N(z_{N+1}) = \frac{hc\Delta\omega}{\lambda} \cdot \frac{(1 - \hat{r}_2^2)n_{\text{sp}}g}{|y_{22} + \hat{r}_1 y_{21} - \hat{r}_2 y_{12} - \hat{r}_1\hat{r}_2 y_{11}|^2} \int_{z_1}^{z_{N+1}} |Z_1(z)|^2 \mathrm{d}z \tag{4.4.23}$$

where $Z_1(z)$ is the solution of the homogeneous wave equation as defined in equation (4.4.10a). Using the transfer matrix, the above equation agrees with the one obtained using the multiple reflection inside the DFB laser cavity [7]. To evaluate the integral shown above, a numerical technique such as the trapezoidal rule can be applied. For below-threshold and threshold analyses when g is assumed to be independent of z, an analytical expression was proposed [2]. Basically, the integral is broken up first and the contribution from each transfer matrix is then found. In other words, we obtain

$$\int_{z_1}^{z_{N+1}} |Z_1(z)|^2 \mathrm{d}z = \sum_{k=1}^{N} \int_{z_k}^{z_{k+1}} |Z_1(z')|^2 \mathrm{d}z' \tag{4.4.24}$$

where

$$\int_{z_k}^{z_{k+1}} |Z_1(z')|^2 \mathrm{d}z' = (1 + |\rho|^2)\left\{|a_k|^2 \cdot \left(\frac{\mathrm{e}^{2\gamma_r L_k} - 1}{2\gamma_r}\right) + |b_k|^2 \cdot \left(\frac{1 - \mathrm{e}^{-2\gamma_r L_k}}{2\gamma_r}\right)\right\}$$
$$+ 2\mathrm{Re}\left\{(\rho + \rho^*)a_k b_k^* \left(\frac{\mathrm{e}^{2j\gamma_i L_k} - 1}{2j\gamma_i}\right)\right\} \tag{4.4.25}$$

where an asterisk indicates the complex conjugate and

$$a_k = \frac{E_R(z_k|z_1)e^{j\beta_0 z_k}e^{j\Omega} - \rho E_S(z_k|z_1)e^{-j\beta_0 z_k}}{1-\rho^2} \tag{4.4.26a}$$

$$b_k = \frac{E_S(z_k|z_1)e^{-j\beta_0 z_k} - \rho E_R(z_k|z_1)e^{j\beta_0 z_k}e^{j\Omega}}{1-\rho^2} \tag{4.4.26b}$$

In the above equations, $L_k = z_{k+1} - z_k$ is the length of the section k; γ_r and γ_i are the real and imaginary parts of the complex propagation constant γ, respectively, and $\rho = j\kappa/(\alpha - j\delta + \gamma)$. In the above threshold operation, when the spatial hole-burning effect becomes dominant, the carrier distribution along the laser cavity becomes non-uniform. As a result, the refractive index and, consequently, the propagation constant, become spatially dependent. These variations violate the assumption of the analytical expression in which g is homogeneous along the z direction. Hence, it can be shown that the analytical expression is restricted to the below-threshold condition, when uniformity can still be maintained along the laser cavity. A different technique is required in the above-threshold since variables become longitudinally (i.e. z) dependent.

4.4.3 Numerical results from various DFB LDs

In this section the below-threshold P_N of various DFB LDs will be presented. Results obtained from a conventional, a quarterly wavelength shifted (QWS) and a 3PS DFB LD will be compared. In all these lasers a laser cavity length of 500 μm and zero facet reflection are assumed. Therefore, any difference between P_N in these lasers is caused solely by the structural variation between them. From the threshold equation of the N-section laser cavity, the normalised amplitude gains $\alpha_{th}L$ of these lasers are determined first. Under the below-threshold condition, the refractive index and hence the propagation constant are assumed to be constant along the cavity.

Figure 4.6 shows a schematic diagram of the 3PS used in the analysis. The PS θ_3 shown in the figure has been fixed at the centre of the structure, whilst the positions of the PS θ_2 and θ_4 are allowed to move along the cavity. Their relative position is defined by a position parameter, ψ, as

$$\Psi = 2L_1/L \tag{4.4.27}$$

It should be noticed that when $\psi = 0$ or 1, the structure becomes a single PS laser.

Figure 4.7 shows the variation of the normalised intensity P_N/hfn_{sp} as a function of the detuning coefficient δL for three DFB LDs. These include conventional, QWS and 3PS DFB LDs. Degenerate oscillation is observed for the conventional case. Compared with the QWS LD, the lasing mode of the 3PS LD is characterised by a detuned oscillation from the Bragg wavelength.

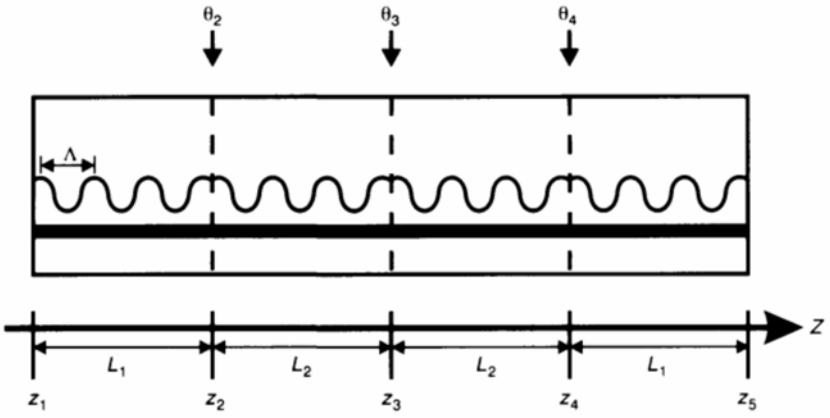

Figure 4.6 A simplified schematic diagram showing a 3PS DFB laser diode structure.

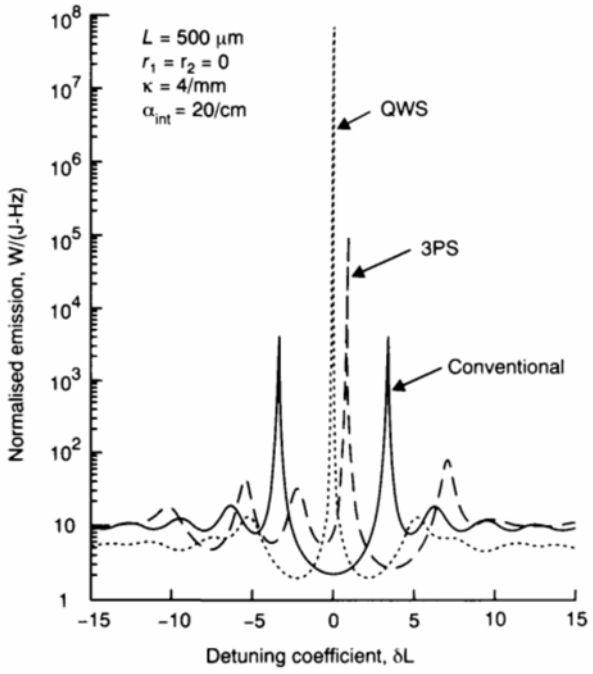

Figure 4.7 Below-threshold spectra of various DFB semiconductor laser diodes (after [32]).

Figures 4.8 and 4.9 show results obtained from 3PS DFB LDs under different values of the amplitude threshold gain $\alpha_{th}L$. Other parameters used in the analysis are listed in the figures. The values of the PS used in the calculations are fixed at $\pi/3$ whilst ψ is assumed to be 0.50 and 0.75, respectively. By increasing the amplitude gain from $0.5\alpha_{th}L$ to $\alpha_{th}L$, the normalised intensity shows a substantial increase across the spectrum. The peak showing the largest intensity will become the lasing mode when the

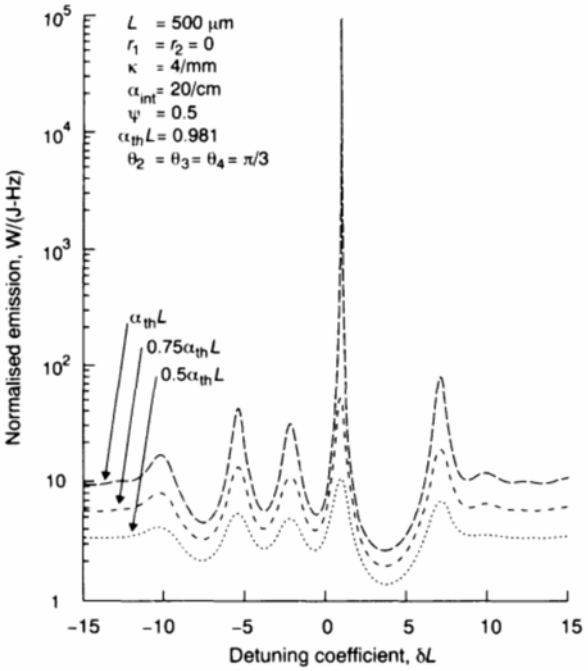

Figure 4.8 Below-threshold spectra of 3PS DFB laser diodes with $\psi = 0.5$ (after [32]).

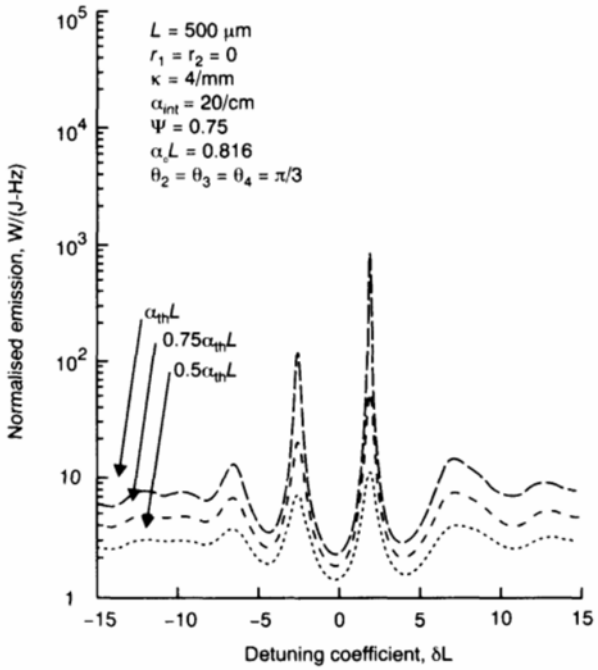

Figure 4.9 Below-threshold spectra of 3PS DFB laser diodes with $\psi = 0.75$ (after [32]).

threshold condition is reached. Other smaller peaks shown become the non-lasing side modes. From Figures 4.8 and 4.9, it can be seen that both spectra shown are asymmetric with respect to the Bragg wavelength ($\delta = 0$). Such an uneven mode distribution is a well-known characteristic of a 3PS DFB laser [19]. By measuring the intensity difference between the major lasing mode and the next highest potential side mode in the spontaneous emission spectrum, a side mode suppression ratio (SMSR) is used to measure the single mode stability [5]. At the lasing threshold, an SMSR of 30 dB is achieved in the structure, as shown in Figure 4.8, while a 20 dB SMSR is observed in Figure 4.9. Comparing these figures, our results reveal that the below-threshold output spectrum is very sensitive to the PSP. Fewer modes are excited in the structure shown in Figure 4.9 as compared with the one shown in Figure 4.8, where ψ has changed from 0.5 to 0.75. Other structural variations and impacts induced by variations in the PS and PSP can be found in a recent paper by Ghafouri-Shiraz and Lo [34]. From the spectral measurement of the P_N, information such as the coupling coefficient, the reflection at laser facets and the PS may also be evaluated [7]. By testing various samples obtained from a wafer, the measurement of P_N plays an important role in the quality control of the fabrication process.

4.5 SUMMARY

In this chapter the idea of the transfer matrix is introduced and explored. Compared with the boundary matching approach, the TMM is more robust and flexible. By converting the coupled-wave equations into a matrix equation, the wave-propagating characteristics of the corrugated DFB section can be represented using a transfer matrix. The transfer matrix approach has been extended to include phase discontinuity and the residue reflection at the facets. By modifying the elements of the transfer matrix, it can be used to represent other planar and corrugated structures, including passive WGs, passive DBRs and planar FP sections. By joining these transfer matrices as building blocks, a general N-section laser cavity model was constructed and the threshold equation associated with this laser mode was determined.

The use of the transfer matrix is not restricted to threshold analysis. Combining the Poynting vector with Green's function method, the TMM can also be implemented to evaluate the below-threshold spontaneous emission power spectrum, P_N. Results obtained from conventional, QWS and 3PS DFB LDs are presented and compared. From the results of 3PS DFB LDs, it is shown that P_N is sensitive to any structural variation. As a result, by comparing P_N measured from a batch of LDs, PN can be used for quality control over the fabrication process. In the next chapter the use of the TMM in both the threshold and the below-threshold applications will be explored further. In particular, the structural design and optimisation of DFB LDs will be discussed.

4.6 REFERENCES

[1] Makino, T., "Transfer-matrix analysis of the intensity and phase noise of multi-section DFB semiconductor lasers", *IEEE J. Quantum Electron.*, **QE-27**, no. 11, pp. 2404-2415, 1991.

[2] Makino, T., "Transfer-matrix formulation of spontaneous emission noise of DFB semiconductor lasers", *J. Lightwave Technol.*, **LT-9**, no. 1, pp. 84-91, 1991.

[3] Yamada, M. and Sakuda, K., "Analysis of almost-periodic distributed feedback slab waveguides via a fundamental matrix approach", *Appl. Opt.*, **26**, no. 16, pp. 3474-3478, 1987.

[4] Yamada, M. and Sakuda, K., "Adjustable gain and bandwidth of light amplifiers in terms of distributed-feedback structures", *J. Opt. Soc. Am A.*, **4**, no. 1, pp. 69-76, 1987.

[5] Whiteaway, J.E.A. Thompson, G.H.B., Collar, A.J. and Armistead, C.J., "The design and assessment of $\lambda/4$ phase-shifted DFB laser structure", *IEEE J. Quantum Electron.*, **QE-25**, no. 6, pp. 1261-1279, 1989.

[6] Makino, T. and Glinski, J., "Transfer matrix analysis of the amplified spontaneous emission of DFB semiconductor laser amplifier", *IEEE J. Quantum Electron.*, **QE-24**, no. 8, pp. 1507-1518, 1988.

[7] Soda, H. and Imai, H., "Analysis of the spectrum behaviour below the threshold in DFB lasers," *IEEE J. Quantum Electron.*, **QE-22**, no. 5, pp. 637-641, 1986.

[8] Chu, C.Y.J. and Ghafouri-Shiraz, H., "Analysis of gain and saturation characteristics of a semiconductor laser optical amplifier using transfer matrix", *J. Lightwave Technol.*, **LT-12**, no. 8, pp. 1378-1386, 1994.

[9] Numai, T., "1.5-μm wavelength tunable phase-shift-controlled distributed feedback laser", *J. Lightwave Technol.*, **LT-10**, no. 2, pp. 199-205, 1992.

[10] Tan, P.W., Ghafouri-Shiraz, H. and Lo, B.S.K., "Theoretical analysis of multiple-phase-shift controlled DFB wavelength tunable optical filters", *Microwave Opt. Tech. Lett.*, **8**, no. 2, pp. 72-75, 1995.

[11] Björk, G. and Nilsson, O., "A new exact and efficient numerical matrix theory of complicated laser structures: properties of asymmetric phase-shifted DFB lasers", *J. Lightwave Technol.*, **LT-5**, no. 1, pp. 140-146, 1987.

[12] Okai, M., Tsuji, T. and Chinone, N., "Stability of the longitudinal mode in $\lambda/4$-shifted InGaAsP/InP DFB lasers", *IEEE J. Quantum Electron.*, **QE-25**, no. 6, pp. 1314-1319, 1989.

[13] Ramo, S, Whinnery, J.R. and Van Duzer, T., *Fields and Waves in Communication Electronics*. New York: John Wiley & Sons, 1984.

[14] Lowery, A.J., "Amplified spontaneous emission in semicondcutor laser amplifiers: validity of the transmission line model", *IEE Proc. Pt. J*, **137**, no. 4, pp. 241-247, 1990.

[15] Streifer, W., Burnham, R.D. and Scifres, D.R., "Effect of external reflectors on longitudinal modes of distributed feedback laser", *IEEE J. Quantum Electron.*, **QE-11**, no. 4, pp. 154-161 ,1975.

[16] Agrawal, G.P. and Bobeck, A.H., "Modelling of distributed feedback semiconductor lasers with axially-varying parameters", *IEEE J. Quantum Electron.*, **QE-24**, no. 12, pp. 2407-2414. 1988.

[17] Kimura, T. and Sugimura, A., "Narrow linewidth asymmetric coupled phase-shift DFB lasers", *Trans IEICE.*, **E 79**, no. 1, pp. 71-76, 1990 .

[18] Ogita, S., Kotaki, Y., Hatsuda, M., Kuwahara, Y. and Ishikawa, H., "Long cavity multiple-phase shift distributed feedback laser diode for linewidth narrowing", *J. Lightwave Technol.*, **LT-8**, no. 10, pp. 1596-1603, 1990.

[19] Yoshikuni, Y. and Motosugi, G., "Multielectrode distributed feedback laser for pure frequency modulation and chirping suppressed amplitude modulation", *J. Lightwave Technol.*, **LT-5**, pp. 516-522, 1987.

[20] Davis, M.G. and O'Dowd, R.F., "A transfer matrix-based analysis of multielectrode DFB lasers", *Photon. Technol. Lett.*, **3**, no. 7, pp. 603-605, 1991.

[21] Kawaguchi, H., Magari, K., Yasaka, H., Fukuda, M. and Oe, K., "Tunable optical-wavelength conversion using triggerable multielectrode distributed feedback laser diode", *IEEE J. Quantum Electron.*, **QE-24**, no. 11, pp. 2153-2159, 1988.

[22] Kikuchi, K. and Tomofuji, H., "Analysis of oscillation characteristics of separated-electrode DFB laser diodes", *IEEE J. Quantum Electron.*, **QE-26**, no. 10, pp. 1717-1727, 1990.

[23] Kuznetsov, M., "Theory of wavelength tuning in two-segment distributed feedback lasers", *IEEE J. Quantum Electron.*, **QE-24**, no. 9, pp. 1837-1844, 1988.

[24] Zhou, P. and Lee, G.S., "Chirped grating $\lambda/4$-shifted distributed feedback laser with uniform longitudinal field distribution", *Electron Lett.*, **26**, pp. 1660-1661, 1990.

[25] Makino, T., "Theoretical analysis of the spectral linewidth of a surface-emitting DFB semiconductor laser", *Optics Comm.*, **81**, no. 2, pp. 71-74, 1991.

[26] Makino, T., "Transfer-matrix formulation of spontaneous emission noise of DFB semiconductor lasers", *J. Lightwave Technol.*, **LT-9**, no. 1, pp. 84-91, 1991.

[27] Ghafouri-Shiraz, H. and Lo, B., "Structural dependence of three-phase-shift distributed feedback semiconductor laser diodes at threshold using the transfer-matrix method (TMM)", *Semi. Sci. Technol.*, **8**, no. 5, pp. 1126-1132, 1994.

[28] Henry, C.H., "Theory of spontaneous emission noise in open resonator and its application to lasers and optical amplifiers", *J. Lightwave Technol.*, **LT-4**, no. 3, pp. 288-297, 1986.

[29] Yamamoto, Y., *Coherence, Amplification, and Quantum Effects in Semiconductor Lasers*. New York: Wiley, 1991.

[30] Arfken, G., *Mathematical Methods for Physicists*, 3rd edition. New York: Academic Press, 1985.

[31] Trombrog, B., Olesen, H. and Pan, X., "Theory of linewidth for multielectrode laser diode with spatially distributed noise sources", *IEEE J. Quantum Electron.*, **QE-27**, no. 2, pp. 178-192, 1991.

[32] Morse, P.M. and Feshbach, H., *Methods of Theoretical Physics*, vol. 1, International Series in Pure and Applied Physics. New York: McGraw-Hill, 1953.

[33] Agrawal, G.P. and Dutta, N.K., *Long-wavelength Semiconductor Lasers*. Princeton, NJ: Van Nostrand, 1986.

[34] Ghafouri-Shiraz, H. and Lo, B., "Structural impact on the below threshold spectral behavior of three phase shift (3PS) distributed feedback (DFB) lasers", *Microwave Opt. Tech. Lett.*, **7**, no. 6, pp. 296-299, 1994.

5

THRESHOLD ANALYSIS AND OPTIMISATION OF VARIOUS DFB LDs USING THE TRANSFER MATRIX METHOD

5.1 INTRODUCTION

In the previous chapter the transfer matrix method (TMM) was introduced to solve the coupled-wave equations in distributed feedback (DFB) laser structures. The method's efficiency and flexibility in aiding the analysis of DFB semiconductor laser diodes (LDs) has been explored theoretically. A general N-section DFB laser model was built comprised of active/passive and corrugated/planar sections. In this chapter the N-section laser model will be used in the practical design of the DFB laser.

The spatial hole-burning effect (SHB) [1] has been known to limit the performance of DFB LDs. As the biasing current of a single quarterly wavelength shifted (QWS) DFB LD increases, the gain margin reduces. Therefore, the maximum single mode output power of the QWS DFB LD is restricted to a relatively low power operation. The SHB phenomena caused by the intense electric field leads to a local carrier depletion at the centre of the cavity. Such a change in carrier distribution alters the refractive index along the laser cavity and ultimately affects the lasing characteristics. By changing the structural parameters inside the DFB LD, an attempt will be made to reduce the effect of the SHB. As a result, a larger single mode power, and consequently a narrower spectral linewidth, may be achieved. A full structural optimisation will often involve the examination of all possible structural combinations in the above-threshold regime. On the other hand, the analysis of the structural design may be simplified, in terms of time and effort, by optimising the threshold gain margin and the field uniformity.

The structural changes and their impact on the characteristics of DFB LDs will now be presented. By introducing more phase shifts along the laser cavity, a three-phase shift (3PS) DFB LD will be investigated in section 5.2. In particular, impacts due to the variation of both phase shifts and their positions on the lasing characteristics of the 3PS DFB LD will be discussed. To reduce the SHB effect, it is necessary to obtain a more uniform field distribution, while maintaining a large gain margin ($\Delta\alpha L$). On the basis of the values of $\Delta\alpha L$ and the flatness (F) of the field distribution, the optimised structural design for the 3PS DFB laser will be discussed in section 5.3 [2].

By changing the height of the corrugation and thus the coupling coefficient along a DFB laser cavity, a distributed coupling coefficient (DCC) DFB laser is built. In section 5.4 the threshold characteristics of this structure will be shown. In particular, the effects due to the variation of the coupling ratio and the position of the corrugation change will be investigated. To maintain a single mode oscillation, a single phase shift has been introduced at the centre of the cavity. By changing the value of the phase shift, the combined effect with the non-uniform coupling coefficient will be presented. Optimised structural combinations that satisfy both a high gain margin and a low value of flatness will be selected for later use in the above-threshold analysis.

In section 5.5 the combined effect of both multiple phase shifts (MPS) and non-uniform coupling coefficients will be investigated using a DCC + 3PS DFB laser structure. Finally, a summary will be presented at the end of the chapter.

5.2 THRESHOLD ANALYSIS OF THE THREE-PHASE-SHIFT (3PS) DFB LASER

By introducing more phase shifts along the laser cavity, it has been shown [3–5] that the SHB effect can be reduced in a 3PS DFB LD which is characterised by a more uniform internal field distribution. Experimental measurements have been carried out [5] using a fixed value of the phase shift. However, independent changes over the value of the phase shift have not been fully explored. Using the TMM, it was shown in Table 4.1 of the previous chapter that four transfer matrices are necessary to determine the threshold condition of 3PS DFB lasers. In Figure 5.1 a schematic diagram of the 3PS DFB laser structure is shown. In the figure, θ_2, θ_3 and θ_4 represent phase shifts, whereas the length of each smaller section is labelled as L_j ($j = 1, 2$). In the analysis, zero facet reflection at the laser facets is assumed. Following the formulation of the TMM, the overall transfer matrix of the 3PS DFB laser becomes

$$\mathbf{Y}(z_5|z_1) = \mathbf{F}^{(4)}\mathbf{F}^{(3)}\mathbf{F}^{(2)}\mathbf{F}^{(1)} = \begin{bmatrix} y_{11}(z_5|z_1) & y_{12}(z_5|z_1) \\ y_{21}(z_5|z_1) & y_{22}(z_5|z_1) \end{bmatrix} \tag{5.2.1}$$

where $F(j)$ ($j = 1$ to 4) corresponds to the transfer matrix of each smaller section. For a mirrorless cavity, the threshold condition can be found by

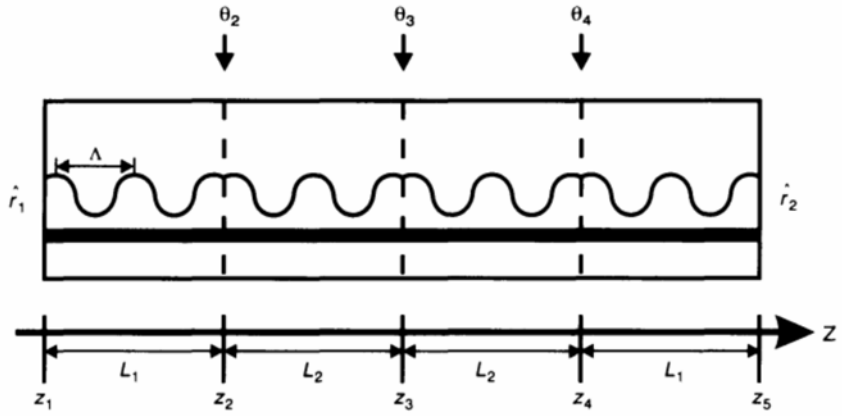

Figure 5.1 Schematic diagram showing a 3PS DFB LD.

solving the following equation:

$$y_{22}(z_5|z_1) = 0 \tag{5.2.2}$$

Using a numerical approach such as the Newton–Raphson method [6] for analytical complex equations, the above-threshold equation may be solved. Figure 5.2 shows the resonance modes obtained from a symmetric 3PS DFB laser where $\theta_2 = \theta_3 = \theta_4 = \pi/2$ and $L_1 = L_2$ are assumed. For comparison

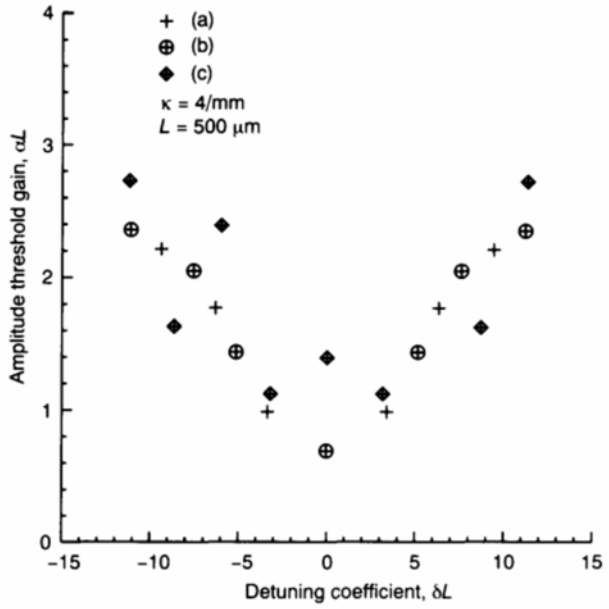

Figure 5.2 Resonance modes of various DFBs that include: (a) a conventional DFB laser diode; (b) a single QWS DFB laser diode; and (c) a three $\pi/2$ phase-shifted DFB laser diode.

purposes, results obtained from a mirrorless conventional DFB laser and a single $\pi/2$ phase-shifted DFB laser are also included. In all three cases the coupling coefficient and the overall laser cavity length L are fixed at 4/mm and 500 μm, respectively. Oscillation modes at the Bragg wavelength are found for both the single $\pi/2$ and a 3PS DFB structure. However, the Bragg resonance mode of the 3PS DFB laser does not show the smallest amplitude threshold gain. Instead, degenerate oscillation occurs since it is shown that both the -1 and $+1$ modes share the same value of the amplitude threshold gain. It is interesting to see how a single $\pi/2$ phase shift enables single longitudinal mode (SLM) operation whilst multi-mode oscillation occurs in the case where there are three phase shifts, i.e. $\{\pi/2, \pi/2, \pi/2\}$. In what follows the braces will indicate a phase combination in the 3PS structure, i.e. $\{\theta_2, \theta_3, \theta_4\}$.

5.2.1 Effects of a phase shift on the lasing characteristics

In order that stable SLM operation can be achieved in the 3PS DFB laser, we must change the value or the position of the phase shift. Figure 5.3 shows the oscillation modes of various 3PS DFB laser structures. In the analysis, the value of the three phase shifts are assumed to be equal and the phase shift positions are the same as in Figure 5.2. A shift of resonance mode can be seen when all phase shifts change from $\pi/2$ to $2\pi/5$. The $+1$ mode, which demonstrates the smallest amplitude threshold gain, will become the lasing

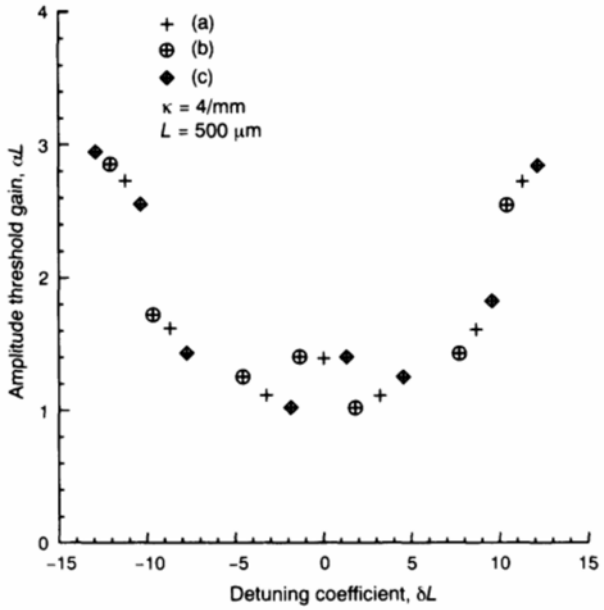

Figure 5.3 Resonance modes in various 3PS DFBs that include: (a) $a\{\pi/2, \pi/2, \pi/2\}$ 3PS DFB laser diode; (b) $a\{2\pi/5, 2\pi/5, 2\pi/5\}$ 3PS DFB laser diode; (c) $a\{3\pi/5, 3\pi/5, 3\pi/5, \}$ laser diode.

mode after the lasing threshold is reached. On the other hand, the -1 mode will become the lasing mode when the three phase shifts change from $\pi/2$ to $3\pi/5$. With all three phase shifts displaced from the usual $\pi/2$ values, SLM can be achieved in the 3PS DFB LD.

5.2.2 Effects of the phase shift position (PSP) on the lasing characteristics

The 3PS DFB laser structure we have discussed so far is said to be symmetric. For a cavity length of L, the position of the phase shifts is assumed in such a way that $L_1 = L_2 = L/4$. To investigate the effect of the phase shift position (PSP) on the threshold characteristics, a position factor ψ is introduced such that

$$\psi = \frac{L_1}{L_1 + L_2} = \frac{2L_1}{L} \tag{5.2.3}$$

where θ_3 is assumed to be located at the centre of the cavity. Using the above equation, it should be noted that both $\psi = 0$ or 1 corresponds to a single phase-shifted DFB laser structure.

In Figure 5.4 the variation in the amplitude threshold gain is shown with the position factor ψ for different values of the normalised coupling coefficient κL. All the phase shifts are fixed at $\theta_2 = \theta_3 = \theta_4 = \pi/3$. At a fixed value of ψ, the figure shows a decrease in the amplitude threshold gain

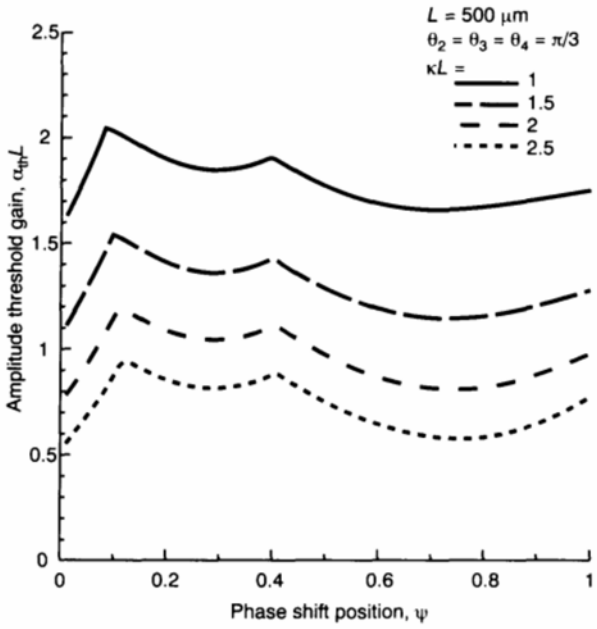

Figure 5.4 The change of amplitude threshold gain with respect to the phase shift position for different values of the coupling coefficient κ.

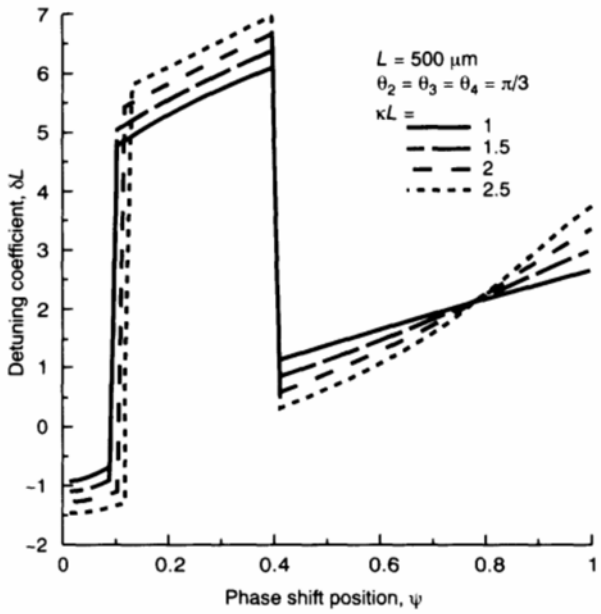

Figure 5.5 The variation of detuning coefficient with respect to the phase shift position for the coupling coefficient κ.

as κL increases. Along the curve $\kappa L = 1.0$, discontinuities at $\psi = 0.12$ and $\psi = 0.41$ indicate a possible change in the oscillation mode.

Such a change in oscillation is confirmed when the relationship between the detuning coefficient and the position factor is as shown in Figure 5.5. Along $\kappa L = 1.0$ it is shown that the -1 mode remains as the oscillation mode when ψ increases from zero. When $\psi = 0.12$ is reached, however, a sudden change in the oscillation mode is observed. Similar mode jumping occurs at $\psi = 0.41$. When the PSP shifts, there is a continuous change in the resonant cavity formed by the DFB laser such that the actual lasing mode may alter. At $\psi = 0.77$ it is interesting to see how all κL values converge to the same lasing wavelength. It appears that at this particular PSP the effect due to the variation in κL is irrelevant and the lasing characteristic depends on the presence of the $\pi/3$ phase shifts.

5.3 OPTIMUM DESIGN OF A 3PS DFB LASER STRUCTURE

A complete structural optimisation of 3PS DFB lasers cannot be achieved without analysing the above threshold performances. This involves solving the carrier rate equation, which is a fairly complex process and needs intensive computation. However, it is believed that the complexity of the structural design in the 3PS DFB laser can be reduced by optimising the threshold amplitude gain difference and the flatness of the field distribution. Hence, we can then simply concentrate on those structures that satisfy these design

criteria. For a high performance DFB LD, both a stable single mode oscillation and a uniform field distribution are important to prevent LDs from being affected by the SHB effect. In our analysis, DFB laser structures with a high gain margin ($\Delta\alpha L$) are considered while the SHB effect is included by analysing the corresponding effects on field uniformity. Reports by Kimura and Sugimura [3,4] as well as Ogita *et al.* [5] suggest that the lasing characteristics are strongly influenced by both ψ and θ. To maintain a stable SLM oscillation, and consequently improve the performance of the spectral linewidth, these structural parameters need to be optimised.

5.3.1 Structural impacts on the gain margin

To achieve a stable laser source that oscillates at an SLM, it is important that there is a gain margin of $\Delta\alpha L > 0.25$ [1]. In the analysis we assumed the length of the laser L to be 500 μm. For a 3PS DFB LD, Figure 5.6 shows the relationship between the gain margin and the phase shift θ in a symmetric structure for different values of κL ranging from 1 to 3. The position factor $\psi = 0.5$ corresponds to the case where $L_1 = L_2 = L/4$. In all cases the degenerate oscillations occur at $\theta = 0$, $\pi/2$ and π, and the distributions of the gain margins are symmetric with respect to $\theta = \pi/2$. It is also shown that the variation in κL has little effect on the gain margin of the 3PS laser structure. Along the $\kappa L = 1$ line it is found that a stable laser

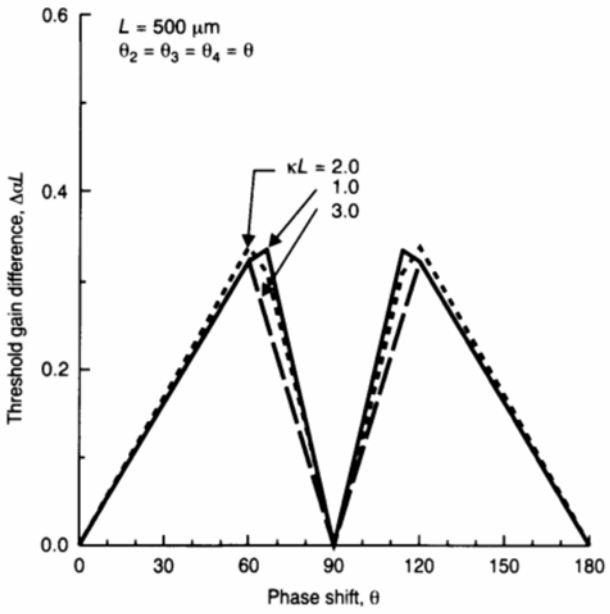

Figure 5.6 Variation in the threshold gain difference versus the phase shift for different coupling coefficients.

with $\Delta\alpha L > 0.25$ can be obtained provided that $47^\circ < \theta < 73^\circ$ or $107^\circ < \theta < 133^\circ$.

In Figure 5.7 a contour map is shown which relates the gain margin to the values of the phase shifts in the 3PS $\{\theta_2, \theta_3, \theta_4\}$ DFB LDs. In the calculations, $\kappa L = 2$ and $\psi = 0.5$ are assumed. The phase shift θ_3 introduced at the centre of the cavity is separated from the rest so that its value can be selected independently. Other phase shifts are assumed to be equal as $\theta_2 = \theta_4 = \theta_{side}$. As stated earlier, to satisfy the requirement of $\Delta\alpha L > 0.25$, it is shown that θ_{side} must either be greater than 105° or less than 80° if θ_3 can be varied freely between 0 and π. A maximum value of $\Delta\alpha L = 0.73$ is obtained at $\{0, \pi/2, 0\}$ and $\{\pi, \pi/2, \pi\}$, which corresponds to a single $\pi/2$ phase-shifted DFB laser.

The variation in $\Delta\alpha L$ with respect to the position factor ψ is shown in Figure 5.8. In this figure the values of the phase shifts are equal (i.e. $\theta_2 = \theta_3 = \theta_4 = \theta$) and three different sets of results are calculated with $\theta = \pi/2$, $2\pi/5$ and $\pi/3$. By changing the values of the phase shifts, $\Delta\alpha L$ also changes for each particular value of ψ. At a fixed phase shift $\theta = \pi/2$ (solid line), it is shown that a non-zero value of the gain margin is observed where $\psi < 0.13$ and $\psi > 0.725$. As ψ approaches zero, the phase shifts θ_2 and θ_4 move towards the laser facets and their contributions become less influential. Also, as ψ approaches unity, both θ_2 and θ_4 move towards the central phase shift, θ_3. In this case the 3PS laser structure is reduced to a single phase-shifted

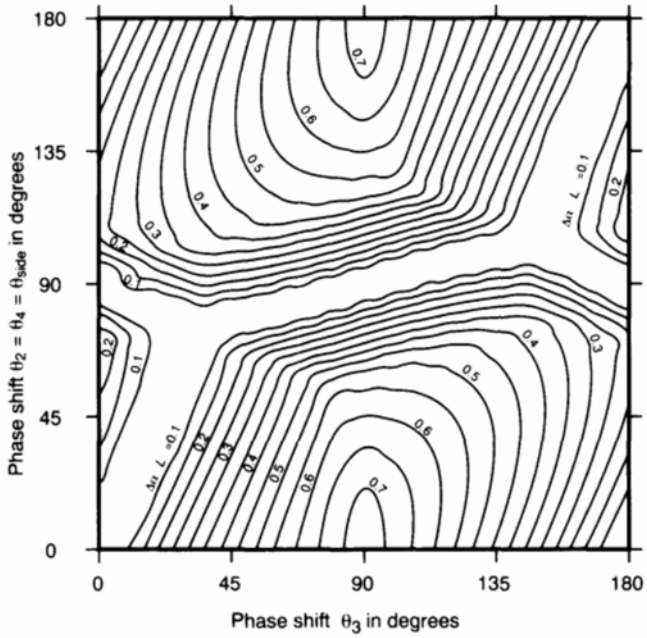

Figure 5.7 Relationship between the gain margin ($\Delta\alpha L$) and phase shifts for a 3PS DFB laser diode.

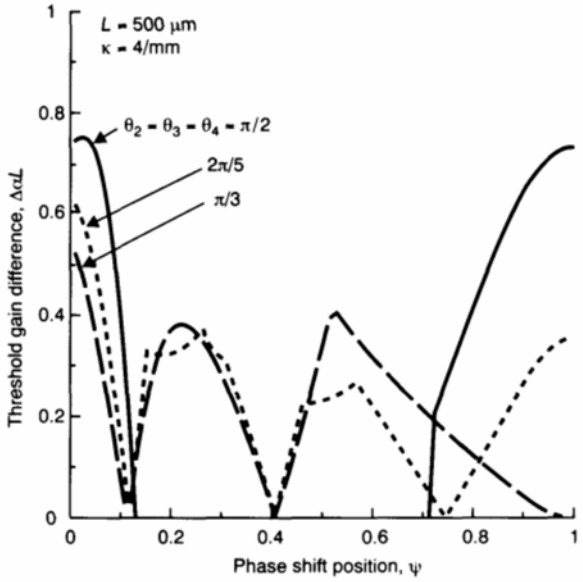

Figure 5.8 Variations in the threshold gain difference versus ψ for various 3PS DFB laser diode structures.

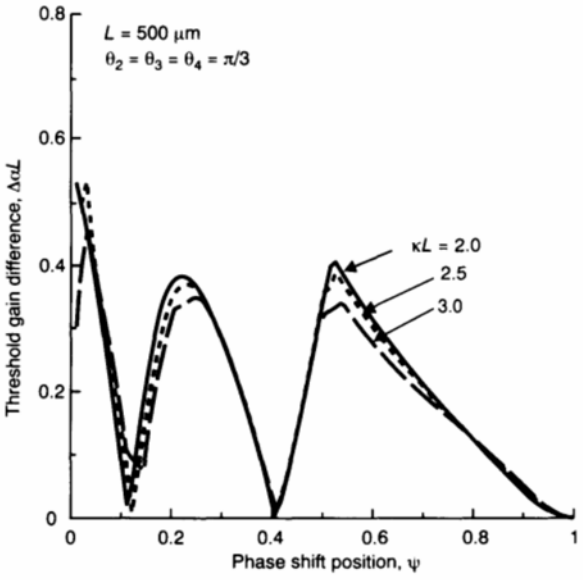

Figure 5.9 Variations in the threshold gain difference versus ψ for different coupling coefficients.

structure and the lasing characteristic is described by an effective phase shift of $\theta_\varepsilon \approx \theta_2 + \theta_3 + \theta_4$.

Figure 5.9 shows the dependence of $\Delta\alpha L$ upon ψ for different values of κL. In the analysis, all phase shifts are assumed to be identical (i.e. $\theta = \pi/3$). From this figure it is clear that κL has little effect on $\Delta\alpha L$ in 3PS DFB lasers.

5.3.2 Structural impacts on the uniformity of the internal field distribution

In this section we discuss the structural impact on the internal field distribution. To quantify the uniformity of the field distribution, we showed in Chapter 3 that the flatness (F) of the internal field of a general N-section DFB laser cavity is defined as

$$F = \frac{1}{L}\int_{z_1}^{z_{N+1}} (I(z) - I_{\text{avg}})^2 \, \mathrm{d}z \tag{5.3.1}$$

where $I(z)$ is the electric field intensity along the longitudinal axis and I_{avg} is its average value. In the above equation, a zero value of F corresponds to a complete uniform field.

To minimize the effects of longitudinal SHB, it has been shown experimentally [1,7] that a DFB laser cavity with $F < 0.05$ is necessary for stable SLM oscillation. To optimise the structural design of 3PS DFB lasers, $F < 0.05$ will be used as one of the design criteria. To evaluate the flatness of the internal field distribution, the threshold equation of the 3PS DFB laser will be solved first. The normalised amplitude threshold gain $\alpha_{\text{th}}L$ and the normalised detuning coefficient $\delta_{\text{th}}L$ of the lasing mode are then used to determine the field distribution. In our analysis, a 500 μm long DFB laser is subdivided into a substantial number of small sections with equal length. From the output of each transfer matrix, both the forward and the backward propagating electric fields can be determined, and the electric field intensity at an arbitrary position z' is found as

$$I(z') = |E_{\text{R}}(z')|^2 + |E_{\text{S}}(z')|^2 \tag{5.3.2}$$

In Figure 5.10 the internal field distributions of three different structures are shown. These structures include a conventional mirrorless, a single $\pi/2$ phase-shifted and a 3PS $\{\pi/3, \pi/3, \pi/3\}$ DFB laser. All the electric field distributions have been normalised so that the intensity at the laser facets is unity. It is shown that the single $\pi/2$ phase-shifted DFB laser has a flatness value of $F = 0.301$. Such a high value of F (which means that the field is highly non-uniform) induces a local carrier escalation near the centre of the cavity after the laser threshold is reached, consequently affecting the single mode stability of the laser device. With three phase shifts incorporated into the cavity, the intensity distribution spreads out and the overall distribution becomes more uniform (see the solid line with $F = 0.012$). By optimising the values and the positions of the phase shifts with respect to the flatness, a 3PS DFB laser can maintain a uniform field distribution even at a high value of κL, which is necessary to reduce the spectral linewidth of the laser.

The effect of ψ on F is shown in Figure 5.11 for different combinations of κL. When small values of κL (< 1.5) are used, the field intensity distribution becomes less uniform when the phase shifts θ_2 and θ_4 shift towards the laser facets (i.e. as ψ tends to 0). As the optical feedback becomes stronger with

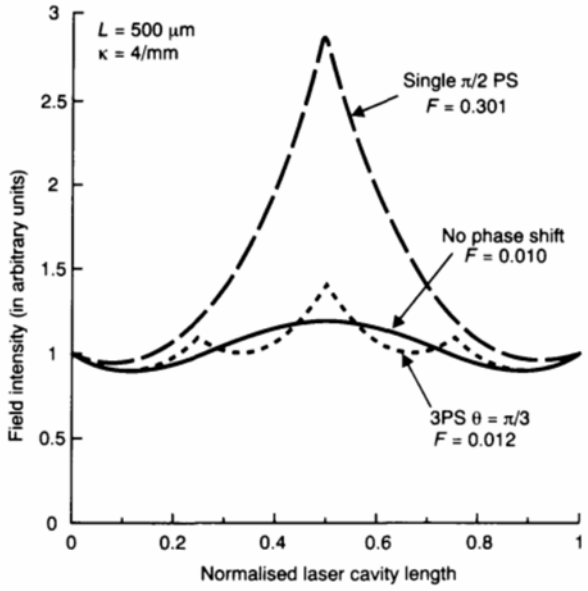

Figure 5.10 Field distribution in various DFB laser diode structures.

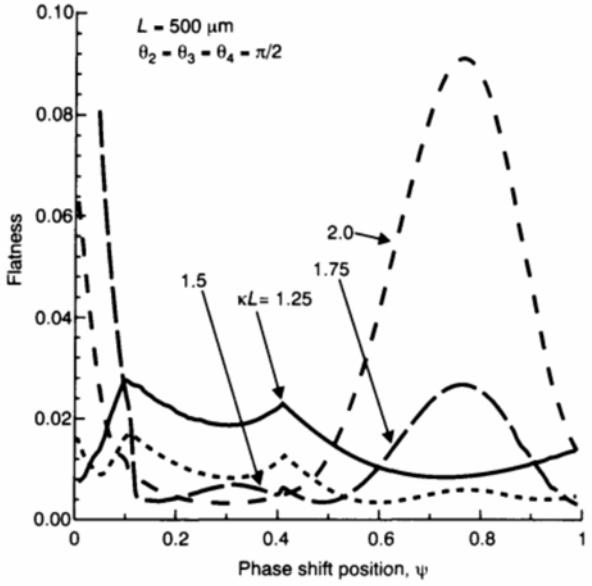

Figure 5.11 Variations in flatness versus ψ for different coupling coefficients κ.

increasing κL, the field intensity distribution becomes more intense near the centre of the laser cavity where ψ is found to be about 0.77.

The contour map shown in Figure 5.12 can be used to optimise the value of the phase shifts with respect to F. Similar to Figure 5.7, the central phase shift θ_3 is used as the x-axis where other phase shifts are represented on the

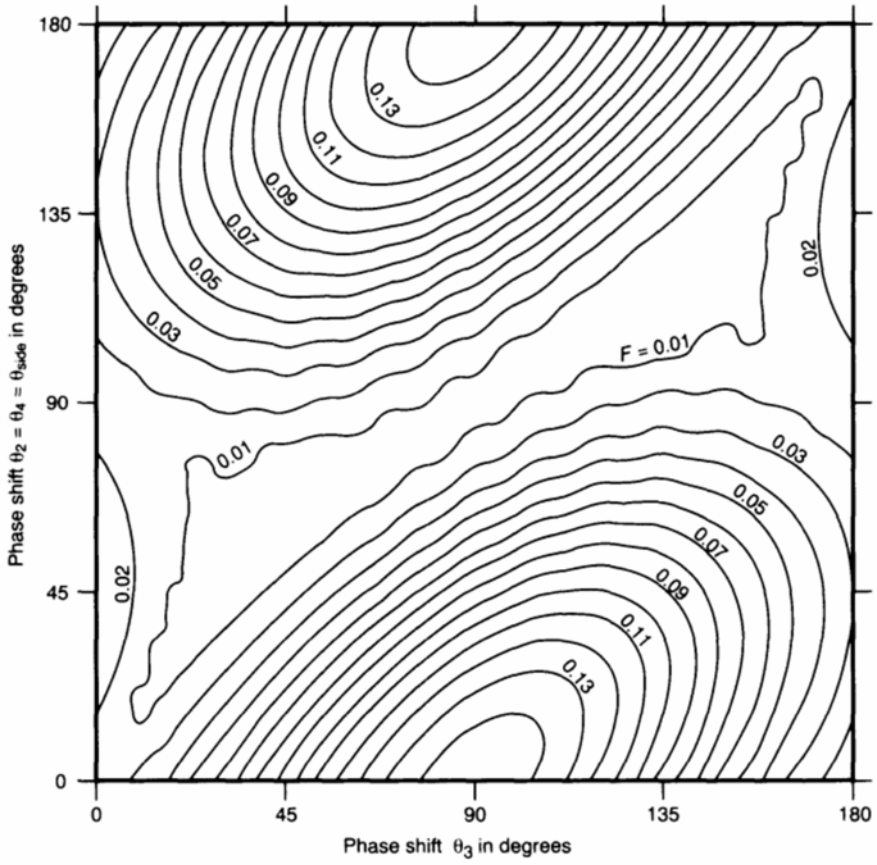

Figure 5.12 Relationship between the flatness and the phase shift for a 3PS DFB LD.

y-axis. In this figure, all phase combinations with $F < 0.05$ form a ribbon shape stretching from the lower left-hand corner to the upper right-hand corner of the contour. The worst case, which leads to the largest value of F, can be found at phase combinations of $\{0, \pi/2, 0\}$ and $\{\pi, \pi/2, \pi\}$. For $F < 0.05$, θ_{side} must lie in the range of $67.5^\circ < \theta_{\text{side}} < 112.5^\circ$ for unrestricted values of θ_3. By comparing Figure 5.12 with Figure 5.7, it can be seen that a trade-off exists in selecting the appropriate phase shift value for the optimum values of $\Delta\alpha L$ and F. On the one hand, phases should be chosen such that the gain margin is large enough to avoid mode hopping. On the other hand, the corresponding combination of phase shifts will result in a relatively large value of F. Owing to the SHB effect, the associated single mode stability deteriorates with increasing output power. As a result, a compromise has to be made in selecting the phase shifts in 3PS DFB lasers such that high performance LDs with high $\Delta\alpha$ (> 0.05 cm) values and small F (< 0.05) can be obtained. Figure 5.13 is a combination of the region $\Delta\alpha L \geq 0.25$ in Figure 5.8 and the region $F \leq 0.05$ from Figure 5.12. In the shaded area of

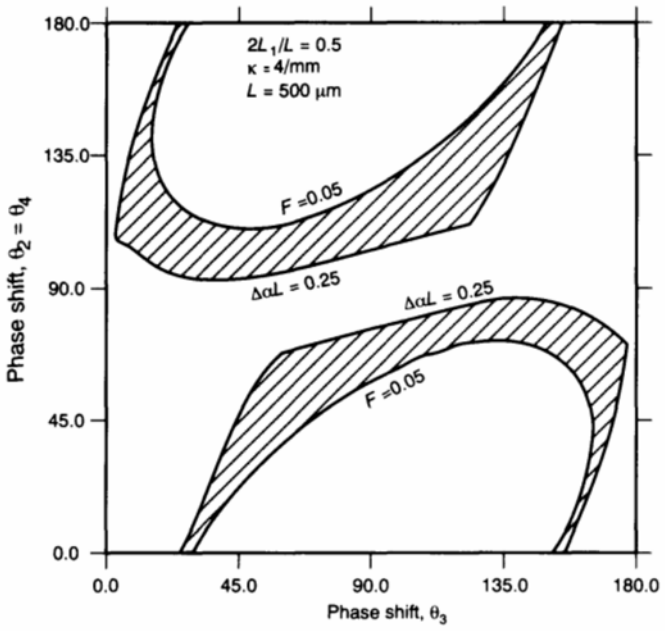

Figure 5.13 Variations in the gain margin and flatness with respect to phase shifts. The hatched area covers all phase combinations that satisfy both $\Delta\alpha L > 0.25$ and $F < 0.05$ selection criteria for stable single mode operation.

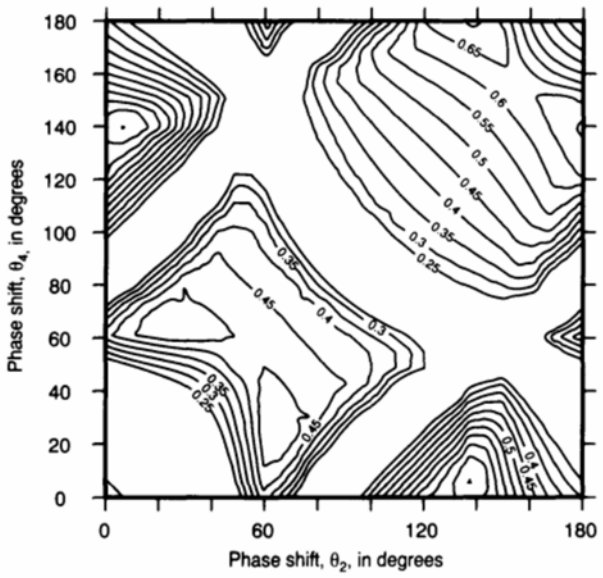

Figure 5.14 Relationship between the gain margin and the phase shift for a 3PS DFB laser diode. $\theta_3 = 20°$ and $\psi = 0.3$ are assumed.

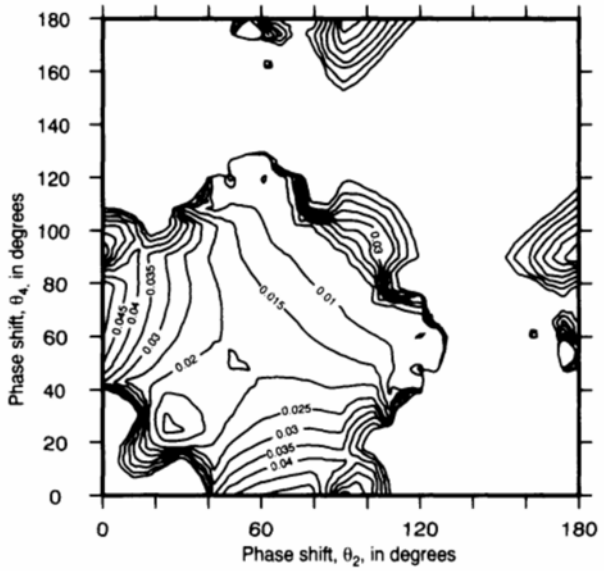

Figure 5.15 Relationship between the flatness and the phase shift for a 3PS DFB laser diode. $\theta_3 = 20°$ and $\psi = 0.3$ are assumed.

this figure it can be seen that a phase combination of $\{\pi/3, \pi/3, \pi/3\}$ will satisfy the design criteria of both the gain margin and flatness.

So far, the values of the phase shifts θ_2 and θ_4 are assumed to be identical. By varying θ_2 and θ_4 from 0° to 180°, the contour map of both the gain margin and the flatness of the 3PS DFB LD can be plotted, as shown in Figures 5.14 and 5.15, respectively [8]. In the analysis, the PSP is fixed at 0.3 and θ_3 is fixed at $\pi/9$ (or 20°). Contours shown are for $\Delta\alpha L > 0.25$ and $F < 0.05$. As expected, both contours show a symmetric distribution along the line where $\theta_2 = \theta_4$. From Figures 5.14 and 5.15 it can be seen that most of the region that satisfies $\Delta\alpha L > 0.25$ does not match with the region for $F < 0.05$. The only area that matches both selection criteria is found when $40° < \theta_2 < 90°$ and $40° < \theta_4 < 80°$.

5.4 THRESHOLD ANALYSIS OF THE DISTRIBUTED COUPLING COEFFICIENT (DCC) DFB LD

By incorporating more phase shifts along the DFB laser cavity, 3PS DFB LDs show an improved performance in maintaining the single mode stability. With a flatter internal field distribution, the SHB effect is suppressed. The gain margin of the 3PS DFB laser diode, however, is reduced as compared with the QWS DFB laser diode, while oscillation at the Bragg wavelength cannot be maintained. To improve the lasing characteristics of the QWS DFB laser diode, a novel structure with a non-uniform coupling coefficient has been proposed [9]. Basically, a corrugation having a non-uniform depth

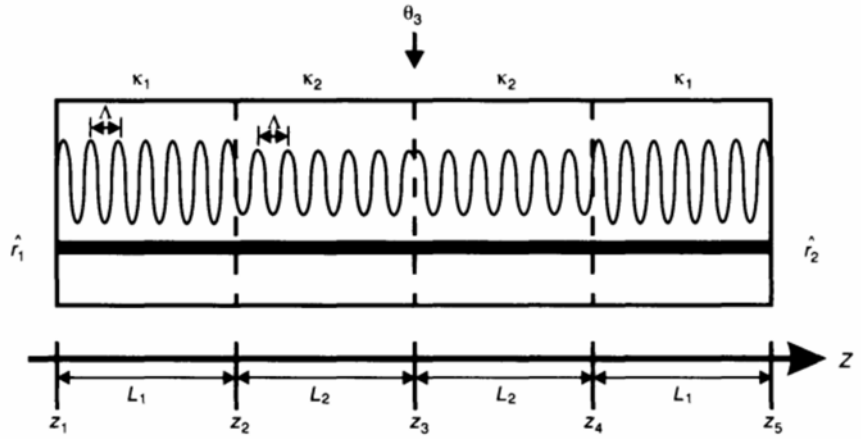

Figure 5.16 Schematic diagram of a single phase-shifted distributed coupling coefficient (DCC) DFB LD.

is fabricated along the laser cavity. Since the coupling coefficient depends on the height of the corrugation, lasers employing this structural configuration are better known as DCC DFB LDs.

Figure 5.16 shows the schematic diagram of a DCC DFB LD. The height of the corrugations fabricated near the centre of the cavity are different from those located near the laser facets. As a result, a laser cavity with a longitudinal variation of κ is achieved. With a $\pi/2$ phase shift fabricated at the centre of the cavity, oscillation at the Bragg wavelength is ensured. In the analysis, a constant corrugation period of Λ and hence a fixed Bragg wavelength λ_B are assumed. The DCC laser structure used is different from the continuous-pitch-modulated (CPM) DFB laser [10] in which Λ varies along the laser cavity. In a DCC DFB laser, it is important that the corrugations change smoothly from one height to another, and that there is no change in the corrugation phase along with the position of the corrugation change. To obtain the best performance from the DCC DFB structure, it is necessary to investigate the structural impact of DCC LDs on the threshold characteristics. In the following sections the structural design, and in particular, the effects of the coupling ratio and the position of the corrugation change, will be discussed. Both the gain margin and the field uniformity reduce the complexity of the structural design. Optimised structures that satisfy the selection criteria will be presented.

5.4.1 Effects of the coupling ratio on the threshold characteristics

In the structural design of DCC DFB lasers both the coupling ratio (κ_1/κ_2) and the position of the corrugation play a crucial role in the threshold characteristics. To determine the position of the corrugation change, a parameter known as the corrugation position (CP) is defined such that [11]

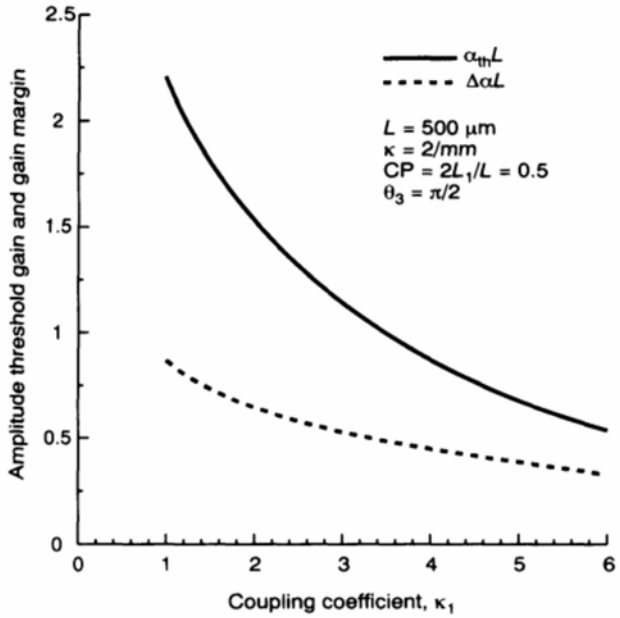

Figure 5.17 Variations in both the amplitude threshold gain and the gain margin are shown with respect to coupling coefficient κ_1.

$$CP = 2L_1/L \tag{5.4.1}$$

In Figure 5.17 the variations in both the amplitude threshold gain ($\alpha_{th}L$) and the gain margin ($\Delta\alpha L$) are shown with respect to the coupling coefficient κ_1. In the analysis, $\kappa_2 = 2/\text{mm}$, $\theta_3 = \pi/2$ and $CP = 0.5$ are assumed. When κ_1 increases, both $\alpha_{th}L$ and $\Delta\alpha L$ show a monotonic decrease in values. The reduction in $\alpha_{th}L$ is obvious since a larger κ_1 implies a stronger optical feedback and consequently a smaller amplitude threshold gain. At $\kappa_1 = 2.0/\text{mm}$, the corrugation becomes uniform and the DCC laser is reduced to a uniform QWS DFB laser.

5.4.2 Effects of the position of the corrugation

At a fixed coupling ratio, the effects due to a variation in the corrugation position (CP) will be investigated in this section. In Figure 5.18 the variation of the field uniformity (F) as well as the gain margin are shown for different values of CP. In the analysis, a fixed value of $\kappa_2 = 2.0/\text{mm}$ and $\theta_3 = \pi/2$ are assumed. Results obtained from various coupling ratios are compared. The other parameters used are listed in the inset of the figure. When CP increases, with the ratio κ_1/κ_2 having the value of 2, we see a substantial increase in flatness. Structures showing such a high flatness value are undesirable since they are vulnerable to SHB. Near to a CP value of 0.78, results from the gain margin revealed that all DCC structures show characteristics similar to

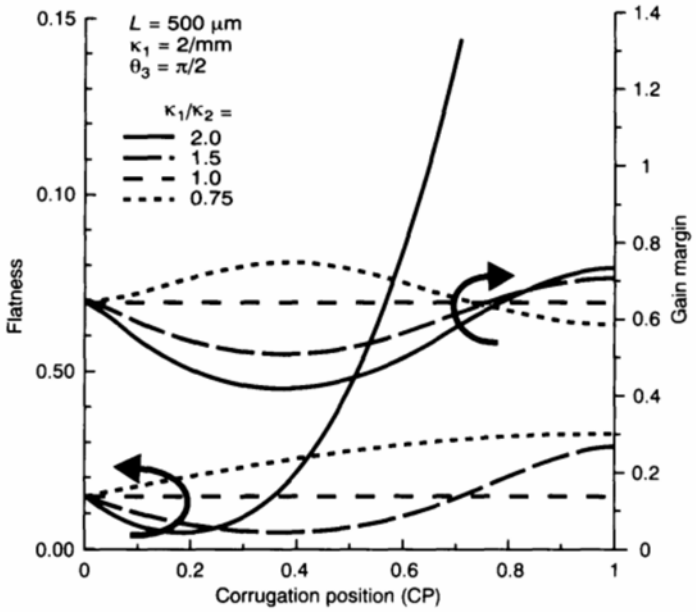

Figure 5.18 Variations in the flatness and the gain margin with respect to the corrugation position for various DCC laser diode structures.

those of the uniform QWS structure. It is believed that at this particular corrugation position (CP) value, the characteristics of the non-uniform corrugations become irrelevant and the effect of using the DCC becomes less efficient. As far as single mode stability is concerned, trade-offs exist in selecting the optimum position of the corrugation change and the coupling ratio.

5.4.3 Optimisation of the DCC DFB laser structure

On the basis of the threshold characteristic, we attempt to optimise the DCC DFB laser structure. In order that the results obtained can be compared with QWS and 3PS DFB LDs, a parameter known as the averaged coupling coefficient, κ_{avg}, is introduced in the DCC laser structure such that

$$\kappa_{avg} = \kappa_1(CP) + \kappa_2(1 - (CP)) \tag{5.4.2}$$

where κ_1 and κ_2 are the coupling coefficients inside the DCC laser cavity and CP is the position of the corrugation change. For a 500 μm long laser cavity, κ_{avg} is assumed to be 4.0/mm so that the value $\kappa_{avg}L = 2.0$ can be maintained. At a fixed value of κ_{avg}, other variables like κ_1, κ_2 and CP are allowed to change. At a fixed value of $\kappa_1/\kappa_2 = r$, the above equation becomes

$$\kappa_1 = r \cdot \kappa_{avg}/[1 + (r - 1)CP] \tag{5.4.3}$$

where κ_1 can be determined.

Figure 5.19 demonstrates the variation in the gain margin with the position factor CP. Results obtained from various coupling ratios, κ_1/κ_2, are compared. At $CP = 0$ and $CP = 1$ it can be seen that a uniform QWS DFB laser is formed. For a DCC laser structure with a coupling ratio $\kappa_1/\kappa_2 > 1$, the gain margin reduces as CP increases from zero. On the other hand, results obtained from $\kappa_1/\kappa_2 < 1$ indicate a significant improvement in the gain margin. At $\kappa_1/\kappa_2 = 1/3$, a normalised gain margin value of 1.69 is found at $CP = 0.46$.

Figure 5.20 shows the dependence of the flatness on the variation in CP. Among the various κ_1/κ_2 ratios used, those with $\kappa_1/\kappa_2 < 1$ show an improvement in the field uniformity. At low values of κ_1/κ_2, however, the differences in F due to the variation in κ_1/κ_2 becomes less obvious. Such a phenomenon can be explained by the presence of the $\pi/2$ phase shift. Owing to the intense electrical field associated with the phase shift, the change in the distribution of flatness becomes less prominent.

From the results obtained in Figures 5.19 and 5.20, a DCC DFB with $\kappa_1/\kappa_2 < 1$ seems desirable since a high gain margin and a relatively flat field distribution can be achieved. Owing to the intense electrical field at the centre of the DCC DFB LD, it is difficult to achieve a very low flatness value (i.e. $F < 0.05$). On the other hand, the significant improvement in the gain margin should relax the constraints on flatness. Along the line at $\kappa_1/\kappa_2 = 1/3$, the optimised design is located at $CP = 0.46$, where the gain margin and the flatness are found to be 1.69 and 0.17, respectively.

Throughout the analysis, the phase shift θ_3 has been fixed at $\pi/2$. By changing the value of the phase shift, the variation in the gain margin and

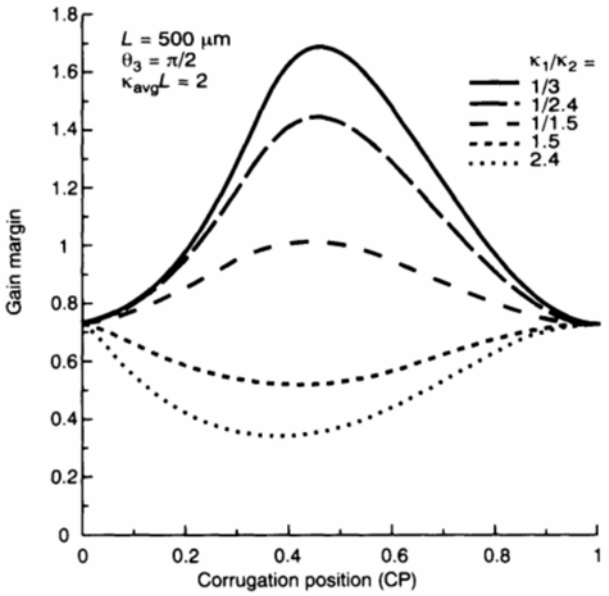

Figure 5.19 Variations in the gain margin versus CP for different coupling ratios.

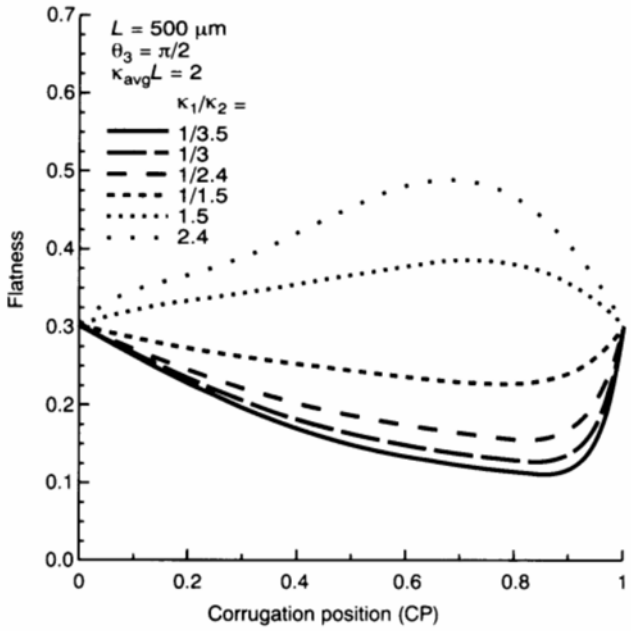

Figure 5.20 Variations in the flatness versus *CP* for different coupling coefficients.

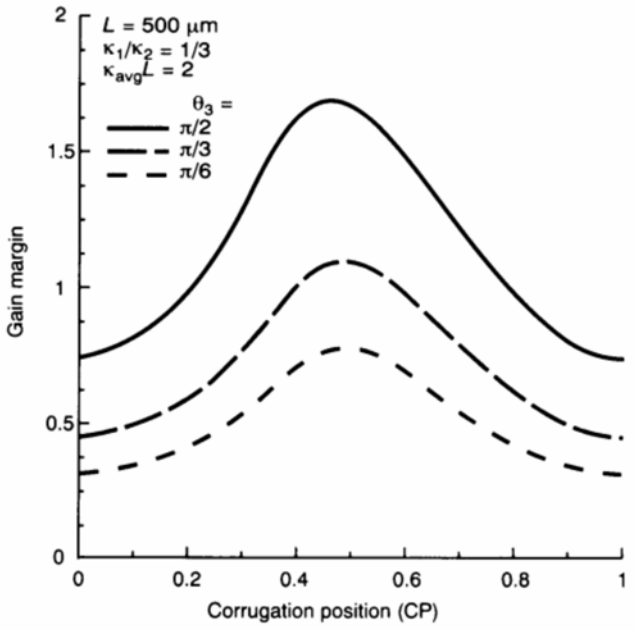

Figure 5.21 Variations in the gain margin versus *CP* for different values of the phase shift θ_3.

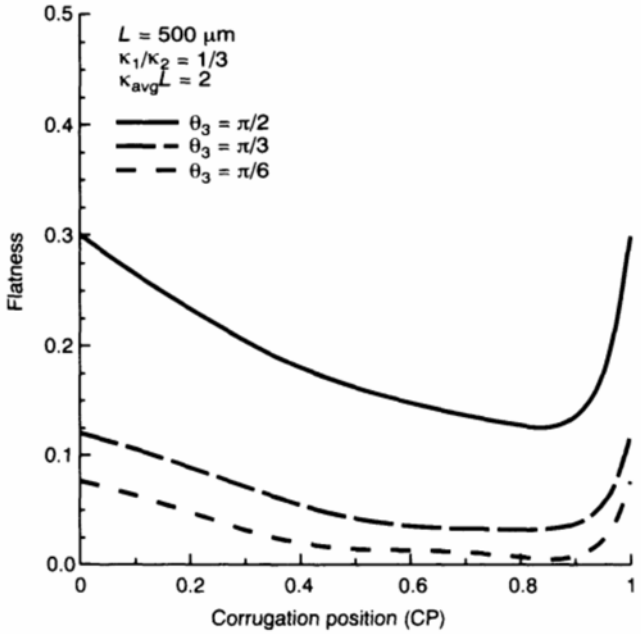

Figure 5.22 Variations in the flatness versus CP for different values of phase shift, θ_3.

the flatness are shown in Figures 5.21 and 5.22, respectively. In the analysis, $\kappa_1/\kappa_2 = 1/3$ and $\kappa_{avg} = 4.0$ mm are assumed.

5.5 THRESHOLD ANALYSIS OF THE DCC + 3PS DFB LASER STRUCTURE

From the previous section, the single QWS DFB laser with a non-uniform coupling coefficient shows significant improvement in both the threshold gain margin and flatness when compared with the uniform κ QWS DFB laser. With $\kappa_1/\kappa_2 = 1/3$ and $CP = 0.46$, oscillation at the Bragg wavelength is achieved when the lasing condition is reached. Despite the fact that there is a slight improvement in the flatness value, the large threshold gain margin strengthens the single mode oscillation in DCC DFB LDs. With more phase shifts introduced along the laser cavity, the 3PS structure was shown to have an improved field uniformity. In this section, the combined effect of both non-uniform κ and 3PS on the threshold characteristics of DFB LDs will be investigated.

A schematic diagram of such a combined DCC + 3PS DFB laser structure is shown in Figure 5.23. Bearing in mind that the use of the TMM in the threshold analysis requires all the physical parameters to be uniform within each transfer matrix section, six transfer matrices have to be used in this new structure. The three phase shifts shown in the figure have been defined following the N-section laser cavity model discussed in Chapter 4. In the

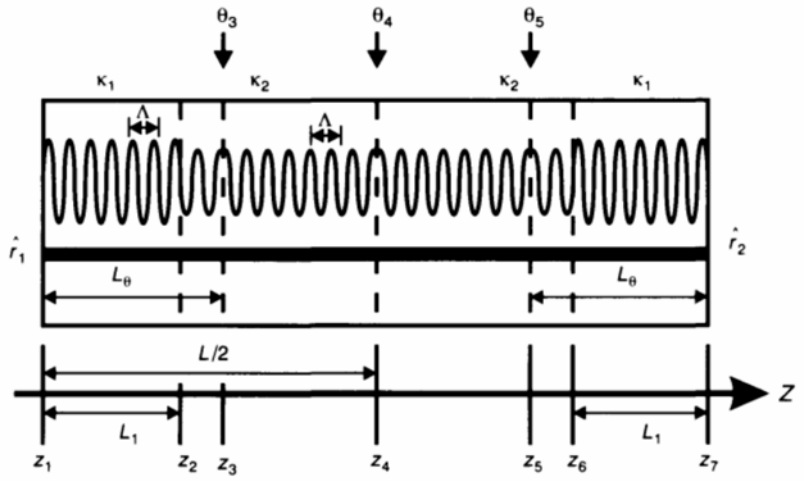

Figure 5.23 Schematic diagram of a distributed coupling coefficient DFB LD with three phase shifts (DCC + 3PS).

analysis, the overall laser cavity length is assumed to be 500 μm and $\kappa_{avg} = 4/mm$. The phase shift θ_4 is always fixed at the centre of the cavity while positions of θ_3 and θ_5 are allowed to change such that their actual phase shift positions (PSP) are defined as

$$\psi = PSP = 2L_0/L \tag{5.5.1}$$

Similarly, the change in the corrugation position follows the definition used in the DCC + QWS structure such that

$$CP = 2L_1/L \tag{5.5.2}$$

To find a suitable value for both the position and the value of the phase shift in the DCC + 3PS laser structure, the optimised design obtained from the uniform κ 3PS DFB laser was used. From the hatched areas shown in Figure 5.13, all phase shifts are assumed to be $\pi/3$, and $PSP = 0.5$ will be used in the analysis of the DCC + 3PS laser structure.

The variation in the normalised gain margin $\Delta\alpha L$ with respect to the CP is shown in Figure 5.24. In this figure, the values of the phase shifts are equal ($\theta_3 = \theta_4 = \theta_5 = \pi/3$) and three different sets of results are calculated with $\kappa_1/\kappa_2 = 1/3.5$, 1/3 and 1/2.5. In all three cases the highest gain margin is found at around $CP = 0.40$. As compared with the uniformly corrugated 3PS DFB laser (where $CP = 0$ and 1), the improvement in $\Delta\alpha L$ corresponds to a positive effect due to the presence of the non-uniform corrugation. At around $CP = 0.4$, the non-lasing side modes are suppressed to such an extent that an improved value of the gain margin ($\Delta\alpha L$) results. There are other regions of CP for which its corresponding gain margin is not as good as the uniformly corrugated 3PS structure. At $CP = 0.5$, where the place of corrugation change

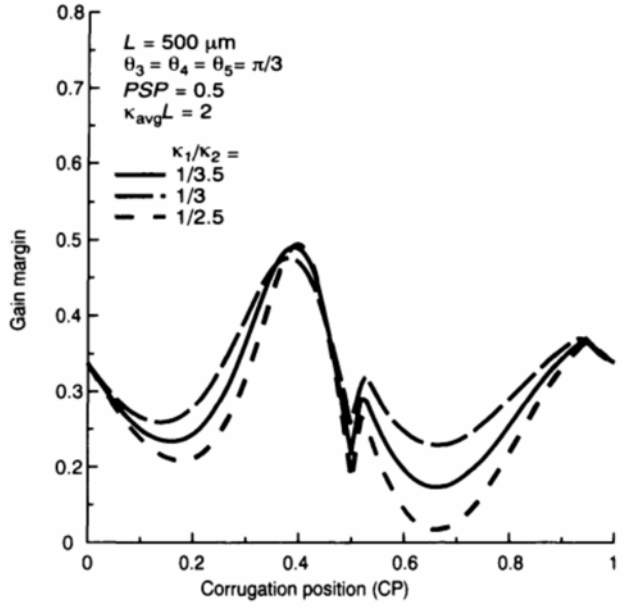

Figure 5.24 Variations in the gain margin versus CP for different values of κ_1/κ_2.

coincides with the position of the phase shift, it is interesting to show how $\Delta\alpha L$ drops to a local minimum.

Figure 5.25 shows the dependence of the flatness upon the corrugation position for different values of κ_1/κ_2. Similar to Figure 5.24, $\kappa_{avg} = 4/\text{mm}$ and $\theta_3 = \theta_4 = \theta_5$ are assumed. By changing the value of CP, the flatness of all three DCC + 3PS LDs used falls within the selection criterion of $F < 0.05$. There is only a minor change in F when the coupling ratio κ_1/κ_2 changes.

So far, the phase shifts used in the DCC + 3PS DFB LD have been fixed at $\pi/3$, and $\psi = 0.5$ is assumed. By changing the values of θ_3 and θ_5 as

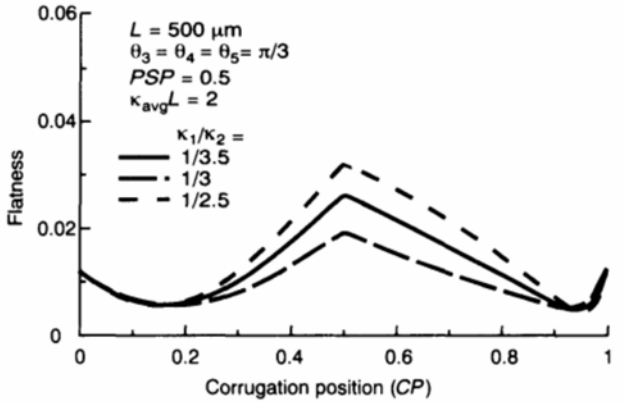

Figure 5.25 Variations in the flatness versus CP for different values of κ_1/κ_2.

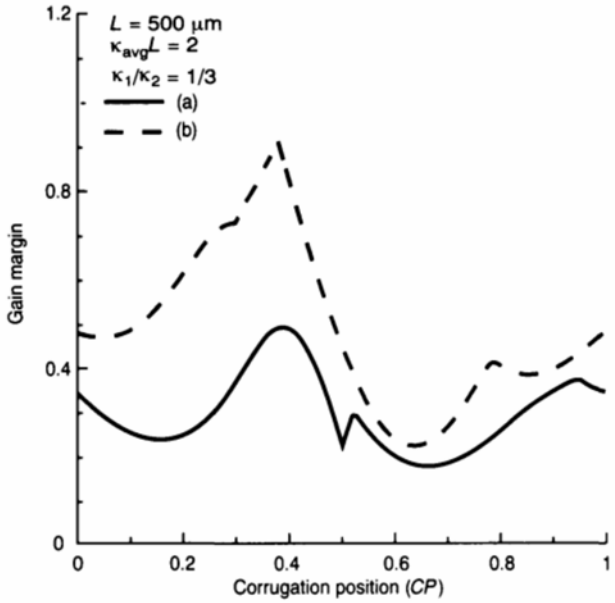

Figure 5.26 Variations in the gain margin for two DCC + 3PS DFB LDs. (a) $\theta_3 = \theta_5 = \pi/3$, $\theta_4 = \pi/9$ and $\psi = 0.3$; (b) $\theta_3 = \theta_4 = \theta_5 = \pi/3$ and $\psi = 0.5$.

well as the *PSP*, the variation in the normalised gain margin of one of these configurations is shown in Figure 5.26. In this configuration, $\theta_3 = \theta_5 = \pi/6$ and $\psi = 0.3$ are assumed [11]. For comparison purposes, the results obtained from a DCC + 3PS DFB LD with $\theta_3 = \theta_4 = \theta_5 = \pi/3$ and $\psi = 0.5$ are also shown. By altering both the position as well as the values of θ_3 and θ_5 along the laser cavity, DFB lasers show that there is an improvement in the threshold gain margin. A comprehensive optimisation on the DCC + 3PS structure is challenging since it involves the optimum design of five variables, namely the corrugation position, the PSP, the phase shifts, κ_1/κ_2 and κ_1. On the other hand, it is shown here that the N-section laser cavity model can be applied to the design of such a complicated structure. Of course, the use of the TMM has played a crucial role throughout the analysis.

The DCC + 3PS DFB laser structure, with $\theta_3 = \theta_4 = \theta_5 = \pi/3$, $CP = 0.39$, $\kappa_1/\kappa_2 = 1/3$ and $\psi = 0.5$, satisfies the threshold selection criteria on both $\Delta\alpha > 0.25$ and $F < 0.05$ for a 500 μm length cavity. This structure will be used in the next chapter to evaluate the above-threshold performance.

5.6 SUMMARY

In revealing the potential use of the TMM in the practical design of DFB LDs, the threshold analysis of various DFB laser structures, including the 3PS, DCC and DCC + 3PS, have been carried out. In an attempt to minimise the effects of SHB and hence to improve the maximum available single mode

output power, it is necessary that a stable SLM LD shows a high normalised gain margin ($\Delta\alpha L$) as well as a uniform field intensity (i.e. small value of F). On the basis of the lasing performance at threshold, selection criteria were set at $\Delta\alpha L > 0.25$ and $F < 0.05$ for a 500 μm length laser cavity.

With more phase shifts introduced along the laser cavity, a 3PS DFB LD was shown to have an improved field uniformity. By changing the corrugation height along the laser cavity, the DCC + QWS DFB LD showed an improved threshold gain and field flatness. The combined effect of having 3PS and a non-uniform coupling coefficient was investigated in a novel DCC + 3PS DFB laser structure. By changing the value of the phase shifts, the coupling coefficient and its corresponding positions, the gain margin ($\Delta\alpha L$) and the uniformity of the field distribution (F) of various DFB laser structures were evaluated. On the basis of the selection criteria $\Delta\alpha L > 0.25$ and $F < 0.05$ at the lasing threshold condition, optimised structures in the 3PS, DCC + QWS and DCC + 3PS DFB lasers were presented. Table 5.1 summarises the results obtained from the threshold characteristics of various DFB LDs. For comparison purposes, Figure 5.27 shows the field distribution of the DFB structures at threshold.

A conventional single QWS DFB was selected as standard for comparison purposes. This structure is characterised by an intense electric field at the centre of the cavity. Owing to the effects of SHB, the single mode oscillation deteriorates quickly as the biasing current increases. For the 3PS DFB LD, three $\pi/3$ phase shifts with a PSP factor of 0.5 fall within the selection criteria of $\Delta\alpha L$ and F. For the DCC + QWS DFB LD, a coupling ratio of $\kappa_1/\kappa_2 = 1/3$ and a corrugation change at 0.46 appears to be promising. This structure is characterised by a large threshold gain margin. In using both a non-uniform coupling coefficient and a 3PS laser structure, a DCC + 3PS DFB LD with $CP = 0.39$ and $PSP = 0.5$ satisfies the design criteria at threshold.

Throughout the analysis it was shown that the N-section laser cavity mode derived using the TMM facilitates both at and below-threshold (Chapter 3)

Table 5.1 Comparison of the threshold characteristics of various DFB LDs

DFB LD	PSP	CP	κ_1/κ_2	$\alpha_{th}L$	$\delta_{th}L$	$\Delta\alpha L$	F	I_{avg}
QWS	–	–	–	0.70	0.0	0.73	0.3006	1.43
3PS	0.5	–	–	0.98	0.91	0.34	0.0122	1.02
DCC + QWS	–	0.46	1/3	0.93	0.0	1.69	0.1678	1.08
DCC + 3PS	0.5	0.39	1/3	1.54	0.35	0.49	0.0164	0.65

3PS structure assumed $\theta_2 = \theta_3 = \theta_4 = \pi/3$.
DCC + 3PS structure assumed $\theta_3 = \theta_4 = \theta_5 = \pi/3$.

Laser structure:

QWS = quarterly wavelength shifted
3PS = three phase shift
DCC = distributed coupling coefficient

Other parameters:

CP = corrugation position, PSP = phase shift position, κ_1/κ_2 = coupling ratio, $\alpha_{th}L$ = normalised amplitude threshold gain, $\delta_{th}L$ = normalised detuning coefficient, $\Delta\alpha L$ = threshold gain margin, F = flatness, I_{avg} = average intensity.

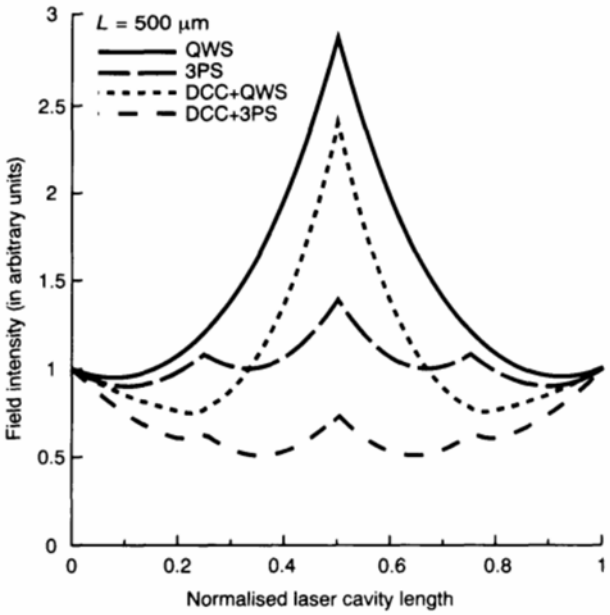

Figure 5.27 The internal field distribution of various DFB LDs as presented in Table 5.1.

analysis of DFB LDs. However, the TMM becomes inadequate in the above-threshold biasing regime when stimulated emission becomes dominant. For above-threshold analysis, such as the single mode stability and the spectral linewidth, the carrier rate equation must be considered. In the next chapter a new technique that combines the TMM with the carrier rate equation will be introduced and the above-threshold characteristics of those DFB laser structures summarised in Table 5.1 will be investigated.

5.7 REFERENCES

[1] Soda, H., Kotaki, Y., Sudo, H., Ishikawa, H., Yamakoshi, S. and Imai, H., "Stability in single longitudinal mode operation in InGaAsP/InP phase-adjusted DFB lasers", *IEEE J. Quantum Electron.*, **QE-23**, no. 6, pp. 804-814, 1987.

[2] Ghafouri-Shiraz, H. and Lo, B., "Structural dependence of three-phase-shift distributed feedback semiconductor laser diodes at threshold using the transfer-matrix method (TMM)", *Semi. Sci Technol.*, **8**, no. 5, pp. 1126-1132, 1994.

[3] Kimura, T. and Sugimura, A., "Coupled phase-shift distributed-feedback lasers for narrow linewidth operation", *IEEE J. Quantum Electron.*, **QE-25**, no. 4, pp. 678-683, 1989.

[4] Kimura, T. and Sugimura, A., "Narrow linewidth asymmetric coupled phase-shift DFB lasers", *Trans IEICE.*, **E 79**, no. 1, pp. 71-76, 1990.

[5] Ogita, S., Kotaki, Y., Hatsuda, M., Kuwahara, Y. and Ishikawa, H., "Long cavity multiple-phase shift distributed feedback laser diode for linewidth narrowing", *J. Lightwave Technol.*, **LT-8**, no. 10, pp. 1596-1603, 1990.

[6] Hoffman, J.D., *Numerical Methods for Engineers and Scientists*. New York: McGraw-Hill, 1992.

[7] Ketelsen, L.J.P., Hoshino, I. and Ackerman, D.A., "Experimental and theoretical evaluation of the CW suppression of TE side modes in conventional 1.55 μm InP-InGaAsP distributed feedback lasers", *IEEE J. Quantum Electron.*, **QE-27**, no. 4, pp. 965-975, 1991.

[8] Ong, B.S., Ghafouri-Shiraz, H. and Lo, B.S.K., "Design proposal of an asymmetric three phase shift distributed feedback laser diode", *Microwave Opt. Tech. Lett.*, in press.

[9] Kotaki, Y., Matsuda, M., Fujii, T. and Ishikawa, H., "MQW-DFB lasers with nonuniform-depth $\lambda/4$ shifted gratings", *Proc. ECOC/ICOC 91*, pp. 137-140, 1991.

[10] Okai, M., Tsuchiya, T., Uomi, K., Chinone, N. and Harada, T., "Corrugation-pitch-modulated MQW-DFB laser with narrow spectral linewidth (170 kHz)", *Photon. Tech. Lett.*, **2**, no. 8, pp. 529-530, 1991.

[11] Ong, B., Lo, B. and Ghafouri-Shiraz, H., "A proposal for the design of a three-phase-shift (3PS) distributed feedback (DFB) laser diode (LD)", *Trans. IEICE, Japan National Convention Record*, paper no. C-256, p. 4-256, March 1994.

6

ABOVE-THRESHOLD CHARACTERISTICS OF DFB LASER DIODES: A TMM APPROACH

6.1 INTRODUCTION

The flexibility of the transfer matrix method (TMM) allows us to evaluate the spectral behaviour of a corrugated optical filter/amplifier and the threshold characteristic of a laser source. To extend the analysis into the above-threshold biasing regime, the transfer matrix has to be modified to include the dominant stimulated emission.

On the basis of a novel numerical technique, the above-threshold distributed feedback (DFB) laser model will be presented. Using a modified transfer matrix, the lasing mode characteristics of DFB laser diodes (LDs) will be determined. The new algorithm is different from many other numerical methods in that no first-order derivative of the transfer matrix equation is necessary. As a result, the same algorithm can be applied easily to other DFB laser structures with only minor modification.

In section 6.2 the details of the above-threshold laser model will be presented. Taking into account the carrier rate equation, the dominant stimulated emission will be considered in building the transfer matrix. The numerical algorithm behind the lasing model will be discussed in section 6.3. Using the newly developed laser model, numerical results obtained from various DFB lasers including the quarterly wavelength shifted (QWS), three phase shift (3PS) and the distributed coupling coefficient (DCC) structures will be shown in section 6.4. Longitudinal varying parameters such as the carrier concentration, photon density, refractive index and the internal field intensity distributions will be presented with respect to biasing current

changes. Impacts due to the structural variation, in particular, will be discussed.

6.2 DETERMINATION OF THE ABOVE-THRESHOLD LASING MODE USING THE TMM

In above-threshold analysis, the lasing wavelength and the optical output power are important. For laser devices to be used in coherent communication systems, the single mode stability and the spectral linewidth should also be considered. Provided that the longitudinal distributions of the carrier, photon and other parameters are known, we can include the spatial hole-burning (SHB) effect as well as the non-linear gain [1] in the above-threshold analysis.

From the threshold characteristic of a DFB LD, a quasi-uniform gain model has been proposed that uses the perturbation technique [2]. However, in the analysis, a uniform gain profile along the cavity and a linear peak gain model were assumed. Using the TMM [3], the uniform gain profile was later improved by introducing a longitudinal dependence of gain along the cavity and an approximated carrier density was obtained for each subsection under a fixed biasing current. With the laser cavity represented by such a small number of subsections, impacts due to the localised SHB effect can only be shown in an approximate manner. For a more realistic laser model, the effects of SHB and any other non-linear gain saturation have to be considered.

In the previous chapter the flexibility of the TMM allowed us to evaluate a DFB laser design quickly, based on the threshold analysis. However, TMM fails to predict the above-threshold lasing characteristics after the lasing threshold condition is reached and stimulated photons become dominant. To take into account any change in the injection current, it is necessary to include the carrier rate equation in the analysis. In this section the relationship between the injection current (or carrier concentration) and the elements of the transfer matrix (mainly the amplitude gain α and the detuning factor δ) will be presented. From the output electric field obtained from the overall transfer matrix, the optical output power will then be evaluated. To include the localised effect in the TMM, a larger number of transfer matrices have to be used so that the length represented by each transfer matrix becomes much smaller. From the N-section DFB laser model, the physical parameters such as the carrier concentration and photon concentration are assumed to be homogeneous within an arbitrary subsection. As a result, information such as the localised carrier and photon concentration are obtained from each transfer matrix. Consequently, longitudinal distributions of the lasing mode carrier density, photon density, refractive index and the internal field distribution are obtained.

According to Chapter 4, the transfer matrix of an arbitrary section k, as shown in Figure 6.1, can be expressed as

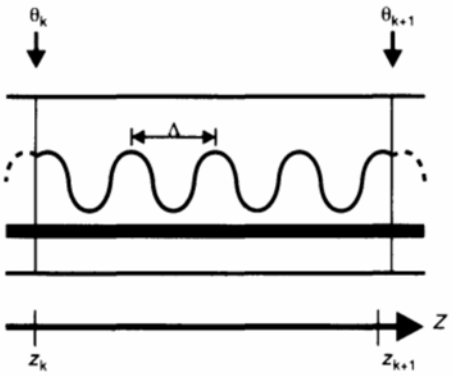

Figure 6.1 Schematic diagram showing a general section in a DFB LD cavity. θ_k shows the phase shift between sections k and $k-1$.

$$\begin{bmatrix} E_R(z_{k+1}) \\ E_S(z_{k+1}) \end{bmatrix} = \mathbf{F}(z_{k+1}|z_k) \cdot \begin{bmatrix} E_R(z_k) \\ E_S(z_k) \end{bmatrix} = \begin{bmatrix} f_{11} & f_{12} \\ f_{21} & f_{22} \end{bmatrix} \cdot \begin{bmatrix} E_R(z_k) \\ E_S(z_k) \end{bmatrix} \quad (6.2.1)$$

where $\mathbf{F}(z_{k+1}|z_k)$ is the transfer matrix of the corrugated section between $z = z_k$ and z_{k+1} whilst its elements f_{ij} $(i, j = 1, 2)$ are given as

$$f_{11} = (E - \rho^2 E^{-1}) \cdot e^{-j\beta_0(z_{k+1}-z_k)} e^{j\theta_k}/(1-\rho^2) \quad (6.2.2a)$$

$$f_{12} = -\rho(E - E^{-1}) \cdot e^{-j\Omega} e^{-j\beta_0(z_{k+1}+z_k)} e^{-j\theta_k}/(1-\rho^2) \quad (6.2.2b)$$

$$f_{21} = \rho(E - E^{-1}) \cdot e^{j\Omega} e^{j\beta_0(z_{k+1}+z_k)} e^{j\theta_k}/(1-\rho^2) \quad (6.2.2c)$$

$$f_{22} = -(\rho^2 E - E^{-1}) \cdot e^{j\beta_0(z_{k+1}-z_k)} e^{-j\theta_k}/(1-\rho^2) \quad (6.2.2d)$$

where Ω is the residue corrugation phase at $z = 0$ and θ_k is the phase discontinuity between sections k and $k-1$. The other parameters used are represented as

$$E = e^{\gamma(z_{k+1}-z_k)}, \qquad E^{-1} = e^{-\gamma(z_{k+1}-z_k)} \quad (6.2.3a)$$

$$\rho = j\kappa/(\alpha - j\delta + \gamma) \quad (6.2.3b)$$

For DFB lasers with a fixed cavity length, we must determine both the amplitude gain coefficient α and the detuning coefficient δ of the section k in order that the matrix element f_{ij} $(i, j = 1, 2)$, as shown in equation (6.2.2), can be determined. For first-order Bragg diffraction, it was shown in Chapter 2 that α and δ can be expressed as

$$\alpha = (\Gamma g - \alpha_{loss})/2 \quad (6.2.4)$$

$$\delta = \frac{2\pi}{\lambda} n - \frac{2\pi n_g}{\lambda \lambda_B}(\lambda - \lambda_B) - \frac{\pi}{\Lambda} \quad (6.2.5)$$

where Γ is the optical confinement factor, g is the material gain, α_{loss} includes the absorption in both the active and the cladding layers as well as any

scattering loss. In equation (6.2.5), n is the refractive index of section k and λ_B is the Bragg wavelength. To take into account any dispersion due to the difference between the actual wavelength and the Bragg wavelength [4], the group refractive index n_g is included in equation (6.2.5). From Chapter 2 that the material gain g of a bulk semiconductor device can be expressed as

$$g = A_0(N - N_0) - A_1[\lambda - (\lambda_0 - A_2(N - N_0))]^2 \tag{6.2.6}$$

where a parabolic model is assumed. In the above equation, A_0 is the differential gain, N_0 is the transparency carrier concentration and λ_0 is the wavelength of the peak gain at the transparency gain (i.e. $g = 0$). In the above equation, the variable A_1 determines the base width of the gain spectrum and A_2 corresponds to any change associated with the shift of the peak wavelength. Using a first-order approximation for the refractive index n, we obtain

$$n = n_{\text{ini}} + \Gamma \frac{\partial n}{\partial N} N \tag{6.2.7}$$

In the above equation, n_{ini} is the effective refractive index at zero carrier injection, Γ is the optical confinement factor and $\partial n/\partial N$ is the differential index. For a symmetric double heterostructure laser with an active laser width of w and thickness d [5], n_{ini} is approximated as

$$n_{\text{ini}}^2 \approx n_{\text{act}}^2 - X \log_{10}[1 + (n_{\text{act}}^2 - n_{\text{clad}}^2)/X] \tag{6.2.8}$$

where

$$X = \lambda_B^2/2\pi^2 d^2 \tag{6.2.9}$$

In the above equation a single transverse and lateral mode are assumed and n_{act} and n_{clad} are the refractive indices of the active and the cladding layers, respectively. From equations (6.2.6) and (6.2.7) it is clear that both g and n are related to the carrier concentration N. As mentioned in Chapter 2, the carrier concentration N and the stimulated photon density S are coupled together through the steady-state carrier rate equation ($\partial N/\partial t = 0$) which is shown here as

$$\frac{I}{qV} = R + R_{\text{st}} \tag{6.2.10}$$

where

$$R = N/\tau + BN^2 + CN^3 \tag{6.2.11a}$$

$$R_{\text{st}} = \frac{v_g g S}{1 + \varepsilon S} \tag{6.2.11b}$$

In the above equations R_{st} is the stimulated emission rate per unit volume and R is the rate of other non-coherent carrier recombinations. Other parameters used are listed as follows: I is the injection current, q is the electronic charge, V is the volume of the active layer, τ is the linear recombination lifetime, B is radiative spontaneous emission coefficient, C is the Auger

recombination coefficient and $v_g = c/n_g$ is the group velocity. To include any non-linearity and saturation effects, a non-linear coefficient ε has been introduced [6]. For strongly index-guided semiconductor structures like the buried heterostructure, the lasing mode is confined through the total internal reflection that occurs at the active and cladding layer interfaces. Both the active layer width w and thickness d are usually small compared with the diffusion length. As a result, the carrier density does not vary significantly along the transverse plane of the active layer dimensions and the carrier diffusion term in the carrier rate equation has been neglected [7]. In an index-coupled DFB laser cavity, the local photon density inside the cavity can be expressed as [8]

$$S(z) \approx \frac{2\varepsilon_0 n(z) n_g \lambda}{hc} \cdot c_0^2[|E_R(z)|^2 + |E_S(z)|^2] \tag{6.2.12}$$

where $\varepsilon_0 = 8.854 \times 10^{-12}$ F/m is the free space electric constant. From the escaping photon density at the output facet, the output power is then determined as

$$P(z_j) = \frac{dw}{\Gamma} v_g \frac{hc}{\lambda} S(z_j) \tag{6.2.13}$$

According to the general N-section DFB laser cavity model, $j = 1$ and $j = N + 1$ in the above equation correspond to the power output at the left and right facets, respectively. In equation (6.2.12), c_0 is a dimensionless coefficient that determines the total electric field $\overline{E}(z)$ as

$$\overline{E}(z) = c_0 E(z) = c_0[E_R(z) + E_S(z)] \tag{6.2.14}$$

where $E_R(z)$ and $E_S(z)$ are the normalised electric field components as shown in equation (4.4.6). Using the forward transfer matrix, it is important that both travelling electric fields $E_R(z)$ and $E_S(z)$ are normalised at the left facet ($z = z_1$) as

$$|E_R(z_1)|^2 + |E_S(z_1)|^2 = 1 \tag{6.2.15}$$

Of course, both $E_R(z_1)$ and $E_S(z_1)$ should satisfy the boundary conditions at the left facet such that

$$E_R(z_1)/E_S(z_1) = \hat{r}_1 \tag{6.2.16}$$

Both the amplitude threshold gain α_{th} and the detuning coefficient δ_{th} are determined from the threshold analysis. With virtually negligible numbers of coherent photons at the laser threshold, the threshold carrier concentration N_{th} can be determined from equations (6.2.4) and (6.2.6) such that

$$N_{th} = N_0 + (\alpha_{loss} + 2\alpha_{th})/\Gamma A_0 \tag{6.2.17}$$

where the peak gain is assumed at the threshold with $A_1 = A_2 = 0$. Consequently, the refractive index at the threshold can be found as

$$n_{th} = n_{ini} + \Gamma \frac{\partial n}{\partial N} N_{th} \tag{6.2.18}$$

By substituting $\delta = \delta_{th}$ in equation (6.2.5) at the threshold condition, the threshold wavelength λ_{th} can be obtained as

$$\lambda_{th} = \frac{2\pi\lambda_B(n_{th} + n_g)}{\delta_{th}\lambda_B + 2\pi n_g + \lambda_B\pi/\Lambda} \tag{6.2.19}$$

Consequently, the peak gain wavelength at zero gain transparency is found from equation (6.2.6) as

$$\lambda_0 = \lambda_{th} + A_2(N_{th} - N_0) \tag{6.2.20}$$

In the next section the features of the numerical process that help to determine the above-threshold characteristics will be discussed in a systematic way.

6.3 FEATURES OF NUMERICAL PROCESSING

To evaluate the longitudinal distribution of the carriers and the photons in the analysis, a large number of transfer matrices have been used. For a 500 μm length long QWS DFB laser, at least 5000 transfer matrices have been adopted to evaluate the above-threshold characteristics. To characterise the oscillation mode for such a non-uniform system, a numerical method such as the Newton–Raphson method will not be appropriate since it is almost impossible to find the required first-order derivative. The situation becomes worse when we realise that the oscillation characteristic depends on the laser structure.

In our analysis a novel numerical technique has been developed. Using this numerical technique it is not necessary to find a first-order derivative. Moreover, the algorithm has been designed such that with only minor changes it can be implemented easily in the design of various DFB laser structures. At a fixed above-threshold current, initial guesses on the lasing wavelength λ and the dimensionless coefficient c_0 are given. By matching the boundary condition at the right facet, the lasing characteristics such as the carrier density, photon density, refractive index distribution, optical output power and the lasing wavelength can be evaluated. Consequently, information such as the single mode stability and the spectral linewidth can be determined.

Figure 6.2 is a flow chart that helps to explain the numerical procedure. Features with regard to the novel numerical techniques will be highlighted as follows [9]:

(1) For a DFB LD with a specific structural design (e.g. a QWS, 3PS or a DCC DFB LD), the oscillation condition at the lasing threshold is first determined. A numerical method like the Newton–Raphson method is applied to determine the threshold characteristic. A reasonable number of roots near the Bragg wavelength are found on the complex plane. Each root $(\alpha_{th.}, \delta_{th})$ that represents an oscillation mode is sorted in rising order of α_{th}. The one showing the smallest α_{th} will become the lasing mode after the threshold condition is reached.

(2) Using equations (6.2.17)–(6.2.20), N_{th}, n_{th}, λ_{th} and λ_0 are evaluated from the threshold value of $(\alpha_{th.}, \delta_{th})$. Since there are virtually no

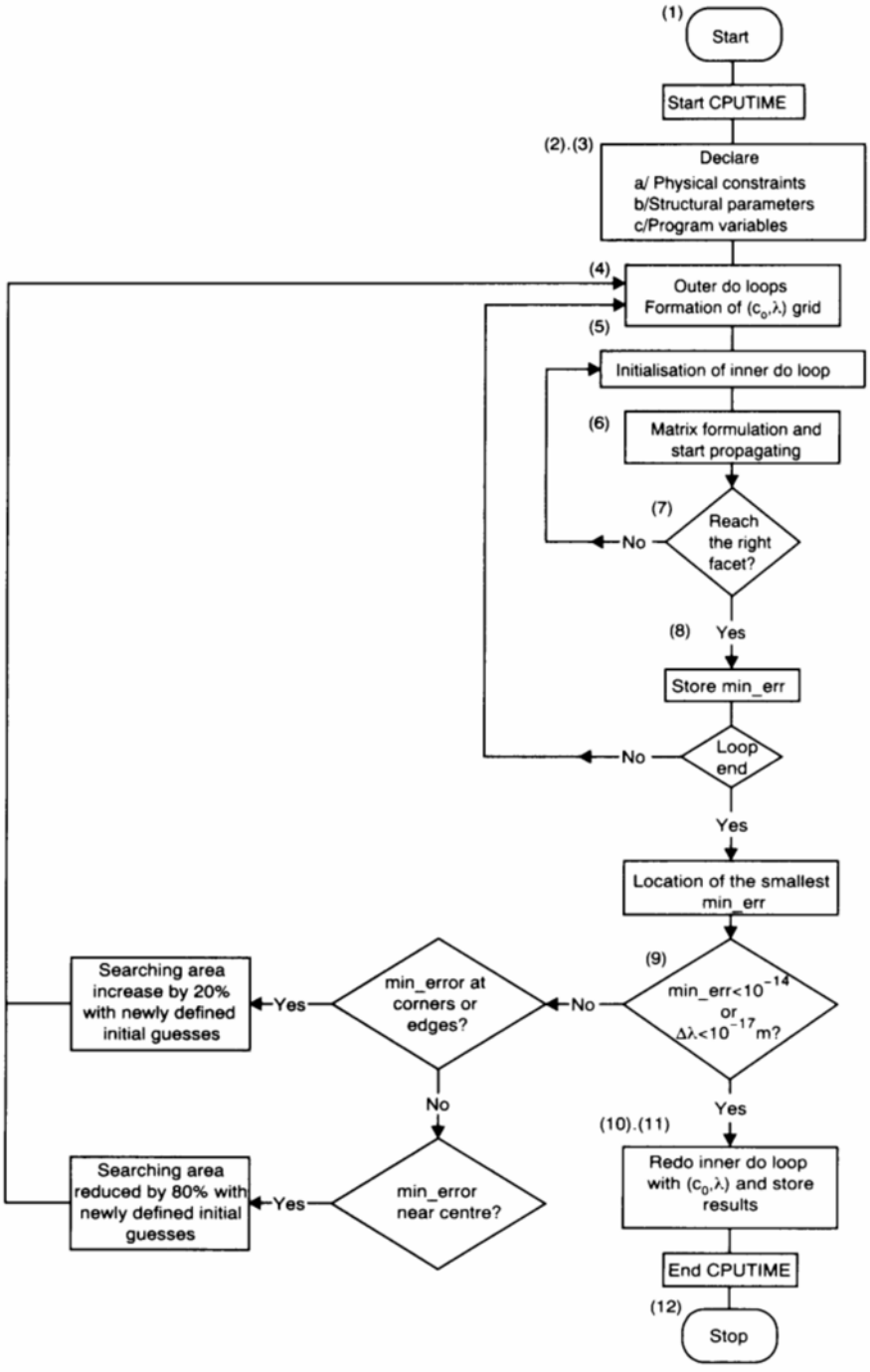

Figure 6.2 Flow chart showing the procedures in the numerical algorithm.

stimulated photons at the lasing threshold condition, the threshold current I_{th} is determined using equation (6.2.10).

(3) The DFB laser cavity is then subdivided into a large number of sections, each represented by a transfer matrix.

(4) An injection current that is normalised with respect to the threshold current is specified. To start the iteration, values of λ and c_0 are given as initial guesses such that a mathematical grid as shown in Figure 6.3, is built. Each intersection point on the grid (25 points all together) represents a pair of (c_0, λ) that will be used in the iteration.

(5) Using the forward transfer matrix, the photon density at the inner left facet is first determined. With no information on the carrier concentration, the threshold refractive index n_{th} is assumed. The carrier concentration N at the left facet is then found using equation (6.2.10), and subsequently the input components $E_R(z_1)$ and $E_S(z_1)$ are obtained according to equations (6.2.15) and (6.2.16).

(6) At this stage the photon density at the left facet can be found using equation (6.2.12). The carrier concentration is then evaluated by solving the carrier rate equation that includes the multi-carrier recombination. Subsequently, both α and δ of the first section and matrix elements f_{ij} $(i, j = 1, 2)$ of the first matrix are determined.

(7) Using the newly formed transfer matrix, the electric field at the output plane can be evaluated and hence the output photon density found. Both α and δ of the following section are then found and a new transfer matrix is formed. The whole process is then repeated until the output plane of the transfer matrix has reached the right facet. The discrepancy with the boundary condition is evaluated and stored (min_err).

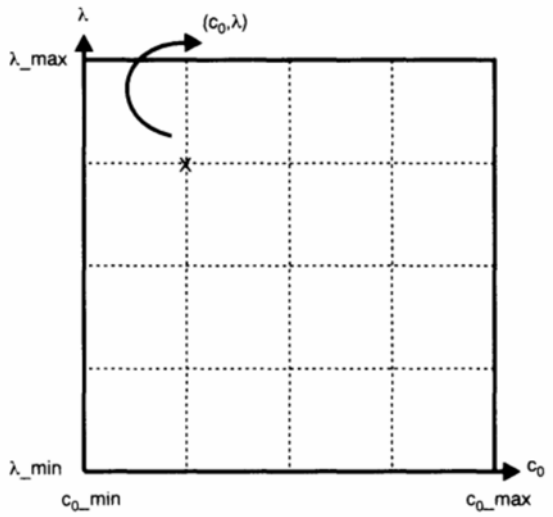

Figure 6.3 A 5 × 5 mathematical grid used in the above-threshold analysis.

(8) By repeating the same calculation for all other (c_0, λ) pairs obtained from the mathematical grid, the pair showing the smallest discrepancy will be selected. Depending on its position of the final point on the mathematical grid (it may be along the boundary, at the corner or near the centre), a new mathematical grid will be created. A possible quantization error must be considered when forming the new mathematical grid.

(9) Procedures (5)–(8) should be repeated until the boundary condition falls within a discrepancy of $< 10^{-14}$ or the iterative change of wavelength $(\Delta\lambda)$ falls below $< 10^{-17}$ m. The final pair $(c_0, \lambda)_{\text{final}}$ is then stored.

(10) The above-threshold characteristic of the DFB laser is determined by passing the $(c_0, \lambda)_{\text{final}}$ pair once again through the transfer matrix chain. From the photon density obtained at both facets, the output optical power is obtained. From each transfer matrix, the lasing mode distribution of the carrier concentration, $N(z)$, photon density, $S(z)$, refractive index, $n(z)$, amplitude gain, $\alpha(z)$, and detuning coefficient, $\delta(z)$, can be evaluated.

(11) The average values of $\bar{\alpha}_L$ and $\bar{\delta}_L$ associated with the lasing mode are then obtained from the corresponding longitudinal distribution as

$$\bar{\alpha}_L = \sum_{j=1}^{N} \alpha_j / N \tag{6.3.1}$$

$$\bar{\delta}_L = \sum_{j=1}^{N} \delta_j / N \tag{6.3.2}$$

where N is the total number of transfer matrices used and α_j and δ_j $(j = 1 \text{ to } N)$ are the amplitude gain and the detuning coefficients obtained from each transfer matrix, respectively.

(12) The whole iteration procedure is then repeated for other biasing current.

Using the numerical process described, the above-threshold lasing mode characteristics of various DFB LDs can be obtained. In the analysis, localised effects such as SHB have been included. With minor modifications, the same algorithm shown above can be implemented easily to find the above-threshold characteristics of various DFB laser designs. In the next section the lasing characteristics of various DFB laser structures including the QWS, the 3PS and DCC DFB LDs will be presented using the above-threshold model.

6.4 NUMERICAL RESULTS

The above-threshold model based on the TMM is applicable to various types of DFB laser structures. In this section, results obtained from the QWS, 3PS and the DCC DFB LDs are presented. Distributions of the spatially

Table 6.1 Parameters used in modelling the DFB laser diode.

Parameter	Symbol	Value	Unit
a) Material Parameters			
Spontaneous emission rate	τ^{-1}	2.5×10^{10}	s^{-1}
Bimolecular recombination coefficient	B	1×10^{-16}	m^3/s
Auger recombination coefficient	C	3×10^{-41}	m^6/s
Differential gain	A_0	2.7×10^{-20}	m^2
Gain curvature	A_1	0.15×10^{20}	m^{-3}
Differential peak wavelength	A_2	2.7×10^{-32}	m^3
Internal cavity loss	α_{loss}	4×10^3	m^{-1}
Refractive index at zero injection	n_0	3.41351524	
Carrier concentration at transparency	N_0	1.5×10^{24}	m^{-3}
Carrier concentration at threshold	N_{th}	—	
Differential index	dn/dN	-1.8×10^{-26}	m^3
Group velocity at Bragg wavelength	v_g	$3 \times 10^8/3.7$	m/s
Nonlinear gain coefficient	ε	1.5×10^{-23}	m^3
Peak gain wavelength at transparency	λ_0	1.63×10^{-6}	m
Lasing wavelength	λ	—	m
Lasing wavelength at threshold	λ_{th}	—	m
b) Structural Parameters			
Active layer width	d	1.2×10^{-7}	m
Active layer thickness	w	1.5×10^{-6}	m
Coupling coefficient	κ	4×10^3	m^{-1}
Laser cavity length	L	500×10^{-6}	m
Optical confinement factor	Γ	0.35	
Grating period	Λ	2.27039×10^{-7}	m
Grating phase at the left facet	Ω	—	rad
Bragg wavelength	$\lambda_B = 2\Lambda n_0$	1.55×10^{-6}	m
Threshold current density	J_{th}	—	A/m^2
Threshold current	I_{th}	—	A
Injection current	I	—	A

dependent parameters like the photon density and the carrier density will be shown. In Table 6.1 we summarise both the material and the structural parameters used in the analysis. These parameters are valid for bulk semiconductor lasing at around 1.55 μm. Unless otherwise stated, these parameters will be used throughout the analysis. Other structural parameters associated with each specific design (i.e. the plane of corrugation change, the phase shifts and their positions) will be listed accordingly.

6.4.1 Quarterly wavelength shifted (QWS) DFB LD

The QWS DFB LD with a uniform coupling coefficient has been used for some time because of its ease of fabrication, and because the Bragg oscillation can be achieved readily with a single $\pi/2$ phase shift [10]. From the threshold analysis, this DFB laser structure is characterised by a non-uniform field intensity which is vulnerable to the SHB effect. Experimental results [2]

have demonstrated that the gain margin deteriorates quickly when the biasing current increases. For a strongly coupled device (i.e. $\kappa L \geq 2$), the side mode on the shorter wavelength side (+1 mode) becomes dominant. For a 300 μm length cavity, two-mode operation at an output power of around 7.5 mW was observed at a biasing current of $2.25I_{th}$.

The SHB effect alters the lasing characteristics of the QWS DFB LD by changing the refractive index along the cavity. Under a uniform current injection, the light intensity inside the laser structure increases with biasing current. For strongly coupled laser devices, most light concentrates at the centre of the cavity. The carrier density at the centre is reduced remarkably as a result of stimulated recombination. Such a depleted carrier concentration induces the escalation of nearby injected carriers and consequently a spatially varying refractive index results.

Using the TMM based model, the above-threshold characteristics of the QWS DFB LD can be verified. In the analysis, a 500 μm long laser cavity with $\kappa L = 2$ is assumed and a phase shift of $\pi/2$ is located at the centre of the cavity. In Figure 6.4 the carrier concentration profile is shown with different injection currents. The depleted carrier concentration observed near the centre of the cavity arises from the severe SHB. It is also shown that the dynamic range of the carrier concentration increases with biasing current.

Figure 6.5 shows the spatial dependence of the photon density with biasing current changes. The photon distribution is fairly uniform when the biasing current is close to its threshold value. On the other hand, an overall increase in

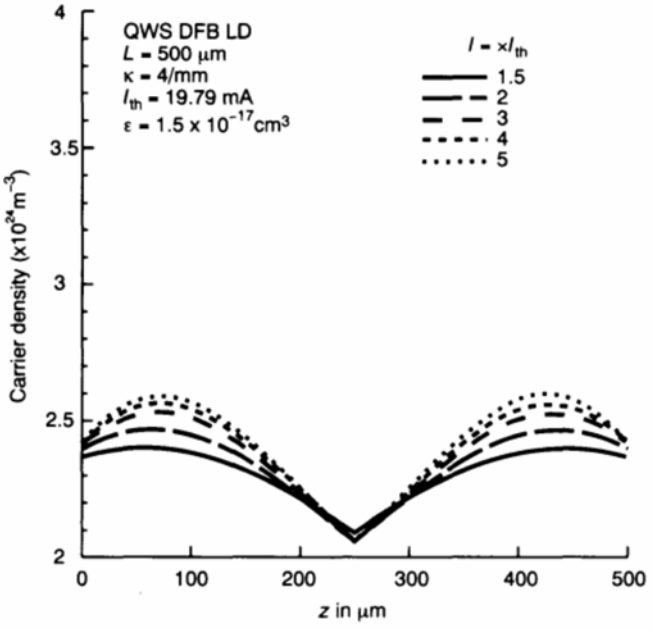

Figure 6.4 Longitudinal distribution of the carrier density in a QWS DFB LD for different injection currents.

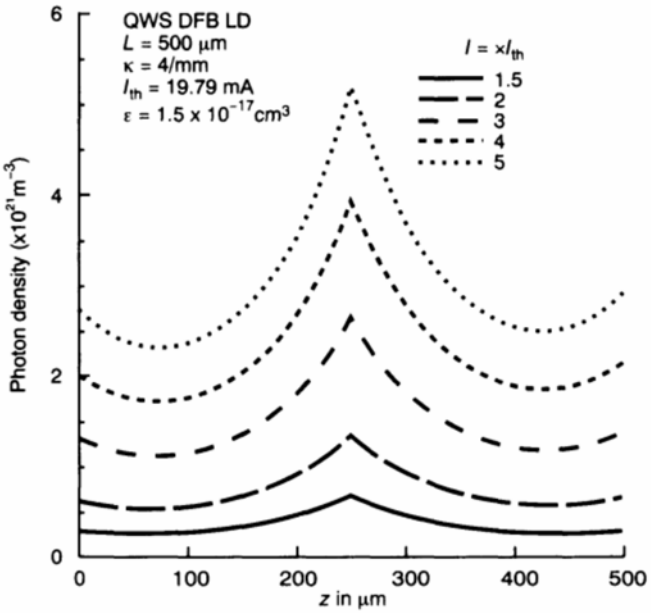

Figure 6.5 Longitudinal distribution of the photon density in a QWS DFB LD for different injection currents.

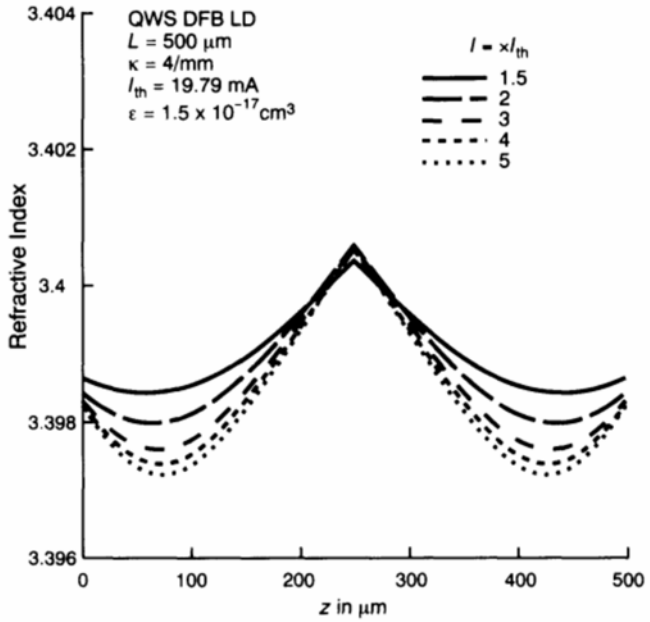

Figure 6.6 Longitudinal distribution of the refractive index in a QWS DFB LD for different injection currents.

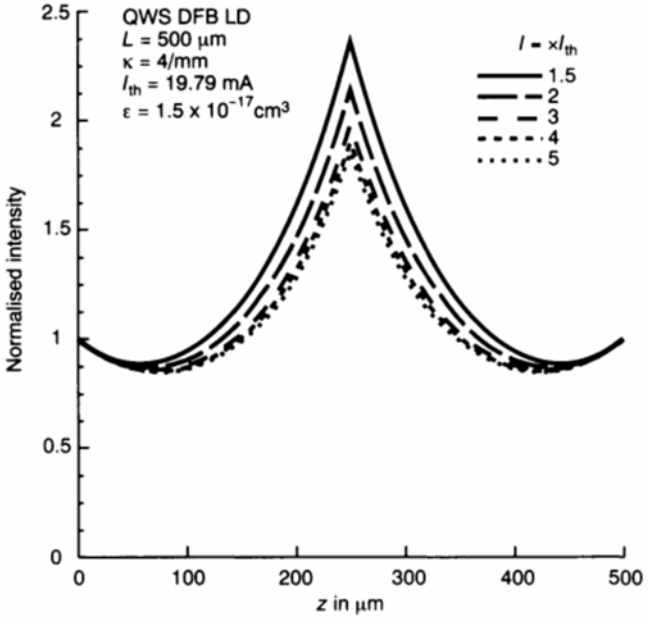

Figure 6.7 Longitudinal distribution of the normalised intensity in a QWS DFB LD for different injection currents.

the photon density is observed with increasing biasing current. At the centre of the cavity, in particular, a peak value of the photon density is expected in such a strongly coupled device. An increase in the dynamic range of the photon density is also shown when the biasing current increases.

The variations in the spatially distributed refractive index are shown in Figure 6.6. When the biasing current increases, the longitudinal span of the refractive index also increases. As we will discuss in the next chapter, this phenomena has a strong impact on the lasing mode characteristics and hence on the single mode stability of the QWS DFB LD. From Figure 6.6 it is also shown that the spatially distributed refractive index becomes saturated near the centre of the cavity at a high biasing current. As the photon density increases with biasing current, the photon density at the centre of the cavity becomes so high that the non-linear gain coefficient becomes dominant.

Figure 6.7 shows the dependence of the internal field intensity distribution with the biasing current changes. As the optical power increases, it is shown that the distribution profile becomes flattened.

6.4.2 Three phase shift (3PS) DFB LD

With more than a single phase shift introduced along the laser cavity, a 3PS DFB structure is characterised by a relatively more uniform field distribution. From the threshold analysis we know that a reasonable value of the gain margin ($\Delta\alpha L > 0.25$) as well as a relatively low value of the flatness

Table 6.2 Structural parameters used in the analysis of the 3PS DFB LD

$\kappa = 4/\text{mm}$
$\theta_2 = \theta_3 = \theta_4 = \pi/3$
PSP = 0.5

($F < 0.05$) can be achieved for a 500 μm length cavity. Using the TMM based above-threshold model, the above-threshold characteristics of 3PS DFB LDs will be presented. Table 6.2 listed the structural parameters used in the 3PS laser structure.

The variations in the carrier density distribution along the laser cavity are shown in Figure 6.8 for various biasing currents. Compared with the QWS DFB structure, the carrier density profile appears to be more uniform. An increase in the biasing current shows little change in the spatially distributed carrier distribution. Local minima can be seen at 125, 250 and 375 μm along the cavity, which correspond to the location of the three $\pi/3$ phase shifts.

The spatial dependences of the photon density, refractive index and the internal field distribution of the 3PS DFB LD are shown in Figures 6.9, 6.10 and 6.11, respectively. Similar to those obtained from the QWS structures, the averaged photon density increases with the biasing current. However, it can be seen that the introduction of more phase shifts flattens out the photon distribution. Rather than a single peak found at the centre of the cavity, local maxima can be seen in Figure 6.9 along with the phase shift position. The

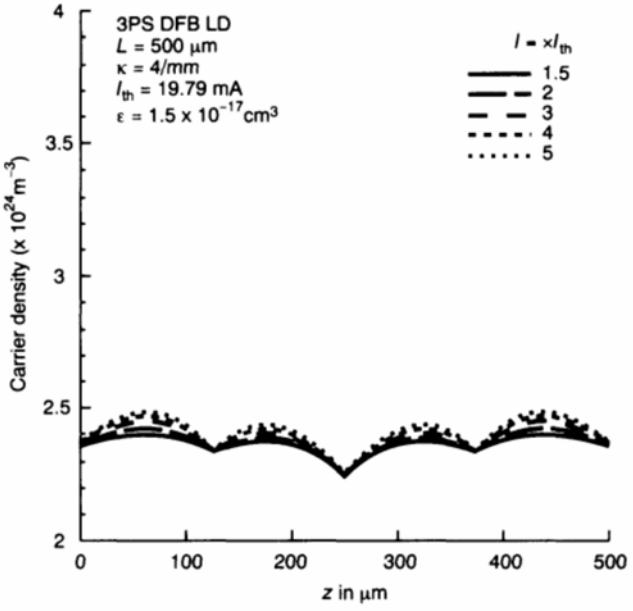

Figure 6.8 Longitudinal distribution of the carrier density in a 3PS DFB LD under different injection currents.

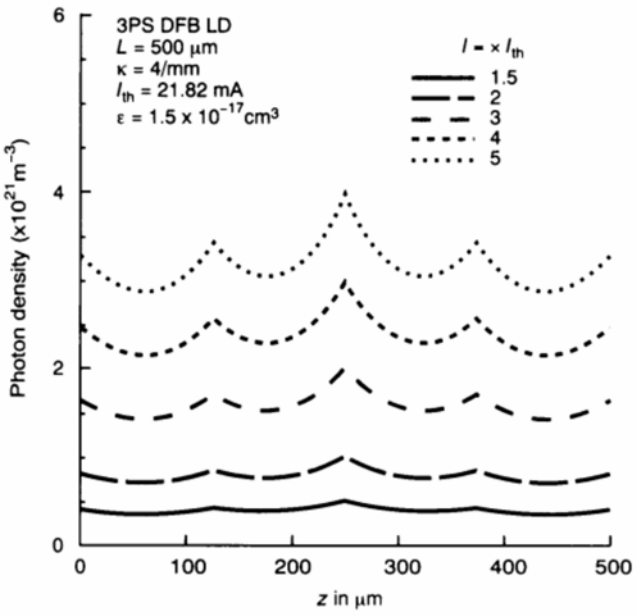

Figure 6.9 Longitudinal distribution of the photon density in a 3PS DFB LD for different injection currents.

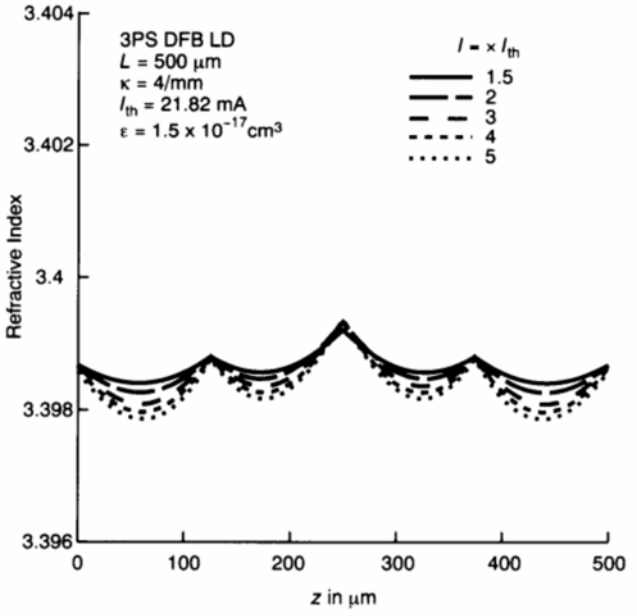

Figure 6.10 Longitudinal distribution of the refractive index inside a 3PS DFB LD under different injection currents.

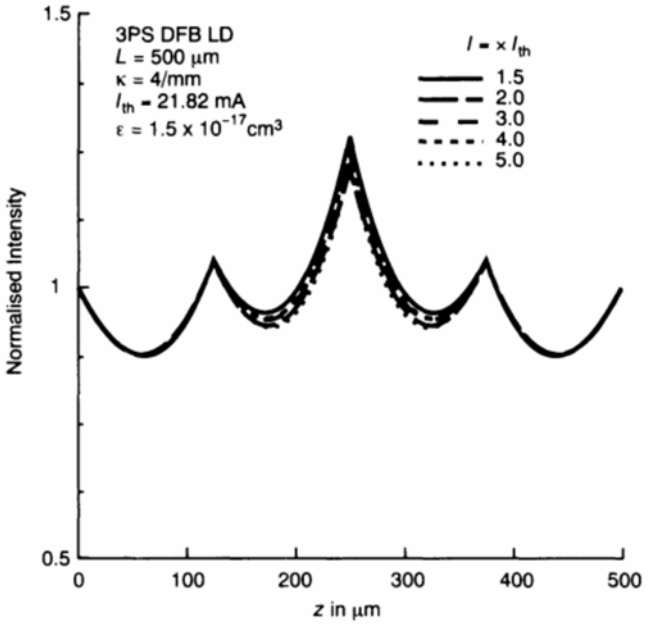

Figure 6.11 Longitudinal distribution of the normalised intensity inside a 3PS DFB LD under different injection currents.

uniform photon distribution also reduces the difference between the central photon density and the escaping photon density at the facet, especially at a high biasing current.

Compared with the QWS laser structure, a more uniform distribution can be seen in the case of the 3PS DFB structure. As shown in Figure 6.10, the refractive index at the phase shift position becomes saturated at high biasing currents. In Figure 6.11, the internal field distribution shows little change with increasing biasing current.

To summarise, the use of an optimised 3PS laser structure appears to be promising. With biasing current increases, the narrower span of the longitudinally distributed refractive index strengthens the single mode stability of the 3PS structure and hence reduces the threat from the SHB effect. This will be discussed further in the next chapter.

6.4.3 Distributed coupling coefficient with a quarterly phase-shifted (DCC + QWS) DFB LD

From the threshold analysis presented in the previous chapter we know that the introduction of a non-uniform coupling coefficient in the DCC + QWS structure can improve both the gain margin and the field uniformity when compared with the QWS structure having a uniform coupling coefficient. In this section the above-threshold characteristics of DCC + QWS laser

Table 6.3 Structural parameters used in the analysis of the DCC+QWS DFB LD

$\kappa_{avg} = 4/mm$
$\theta_3 = \pi/2$
Corrugation Position (CP) = 0.46
$\kappa_1/\kappa_2 = 1/3$

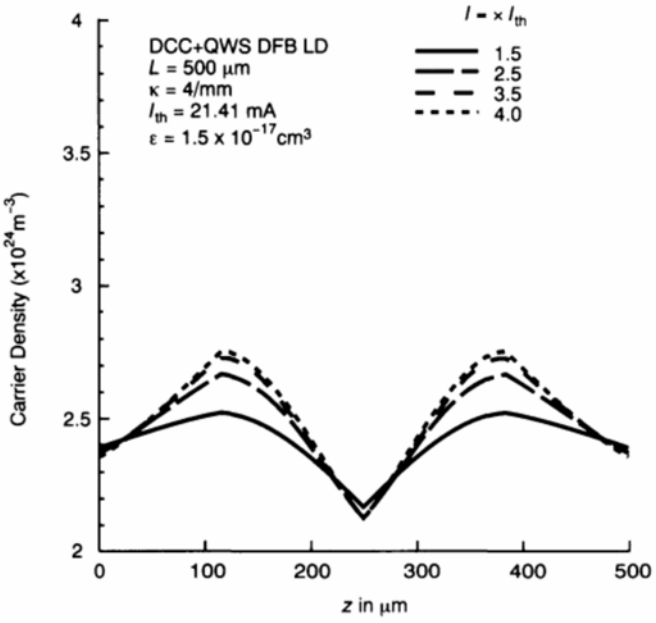

Figure 6.12 Longitudinal distribution of the carrier density in a DCC + QWS DFB LD under different injection currents.

structures, especially the longitudinally varying parameters, will be shown. Table 6.3 gives the structural parameters used.

The spatial dependence of the carrier concentration is shown in Figure 6.12 with respect to the biasing current. Compared with the QWS DFB LD with uniform κ, the DCC + QWS laser structure shows a comparable distribution. It can be seen that the carrier density near 115 and 385 μm along the laser cavity were boosted, especially at high injection currents. Such a change in carrier concentration is believed to be caused by a sudden change in the coupling coefficient.

The distributions of the photon density, refractive index and the internal field intensity are shown in Figures 6.13, 6.14 and 6.15, respectively, versus different biasing currents. As expected, all the figures show a similar distribution to the DFB LD except for the abrupt change seen near the plane of the corrugation change. In the photon density profile shown in Figure 6.13, the use of a smaller coupling coefficient near the facet has reduced the dynamic span of the photon density along the laser cavity.

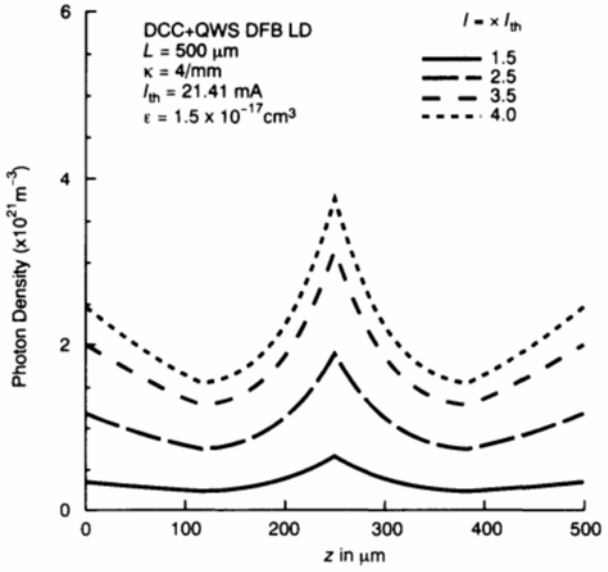

Figure 6.13 Longitudinal distribution of the photon density in a DCC + QWS DFB LD under different injection currents.

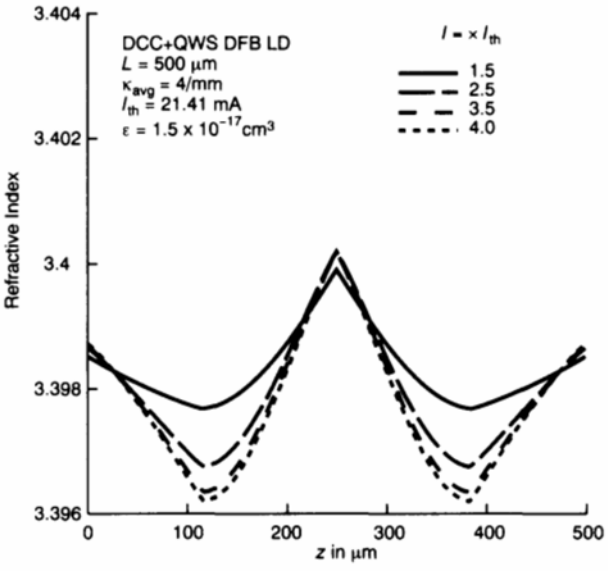

Figure 6.14 Longitudinal distribution of the refractive index in a DCC + QWS DFB LD under different injection currents.

Owing to the effects of SHB, it is evident that the refractive index distribution shows a larger dynamic range with increasing biasing current. On the other hand, it is demonstrated in the threshold analysis that the DCC + QWS laser structure is characterised by an improved threshold gain margin. As a result, the single mode stability of this structure could be maintained.

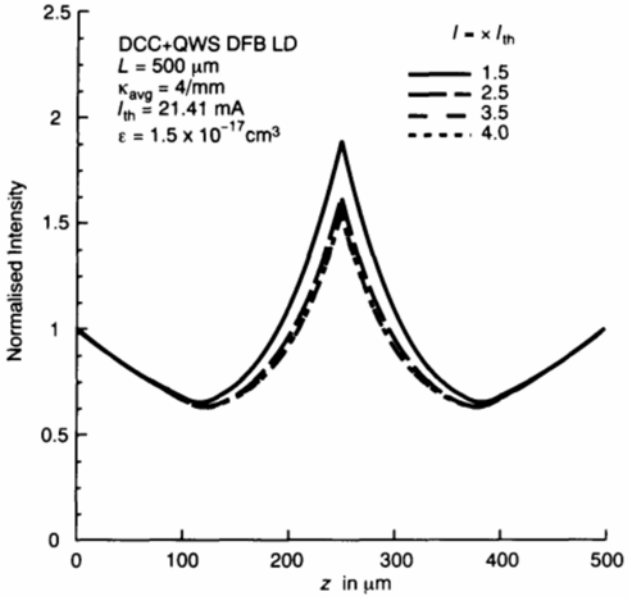

Figure 6.15 Longitudinal distribution of the normalised intensity in a DCC + QWS DFB LD under different injection currents.

The above-threshold single mode stability of this structure will be discussed further in the next chapter.

6.4.4 *Distributed coupling coefficient with a three phase shift (DCC + 3PS) DFB LD*

It is shown that both the carrier and photon densities are flattened when multiple phase shifts are introduced along the corrugation. Alternatively, the use of non-uniform coupling coefficients improves the value of the gain margin while a smaller value of κ near the facets reduces the dynamic change in the photon density.

In this section the above-threshold characteristics of the combined DCC with 3PS structure will be investigated. On the basis of the 3PS laser structure, a longitudinal variation in the coupling coefficient is introduced. In the analysis, the DFB laser diode structure used was exactly the same as the one presented in Chapter 5 with $\theta_3 = \theta_4 = \theta_5 = \pi/3$, $CP = 0.39$, $\kappa_1/\kappa_2 = 1/3$ and $\psi = 0.5$. Discontinuities associated with both the phase shift and the corrugation change enhance the spontaneous emission and hence a larger threshold current is expected. On the other hand, the potential and the capability of the above-threshold model can be demonstrated from the design of such a complicated device. Comparatively, the effect of the non-uniform coupling coefficient is expected to dominate since κ is one of the major parameters associated with coupled-wave equations. Table 6.4 lists the structural parameters used.

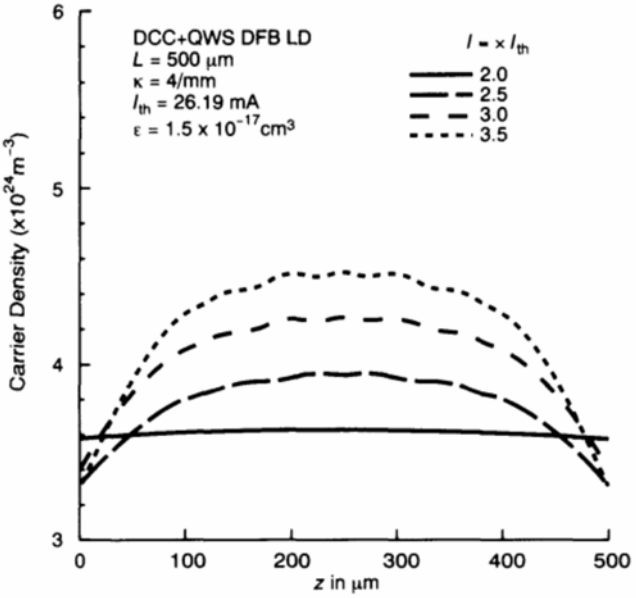

Figure 6.16 Longitudinal distribution of the carrier density in a DCC + 3PS DFB LD under different injection currents.

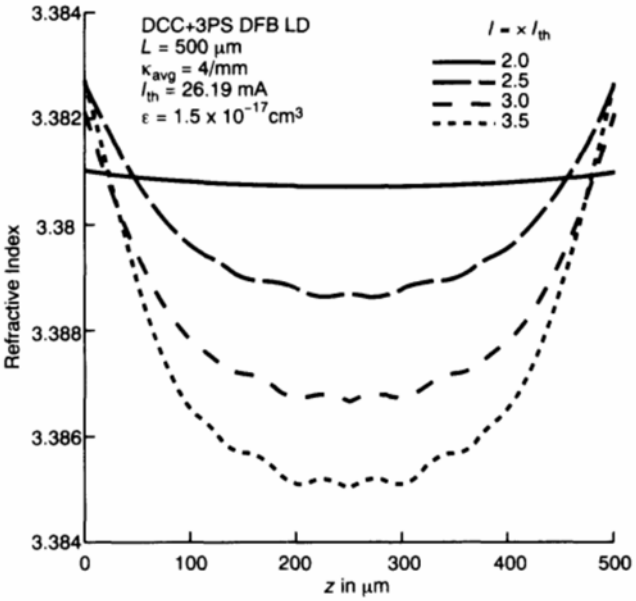

Figure 6.17 Longitudinal distribution of the refractive index in a DCC + 3PS DFB LD under different injection currents.

Table 6.4 Structural parameters used in the analysis of the DCC+3PS DFB LD

$\kappa_{avg} = 4/mm$
$\theta_2 = \theta_3 = \theta_4 = \pi/3$
$CP = 0.39$
$PSP = 0.5$
$\kappa_1/\kappa_2 = 1/3$

Figures 6.16 and 6.17 show the variations in the spatially distributed carrier density and refractive index with biasing current changes, respectively. It can be seen from both figures that the uniform distribution of curves deteriorates quickly when the biasing current increases from $2.5I_{th}$.

6.5 SUMMARY

In this chapter the above-threshold characteristics of various DFB LDs were investigated using a newly developed model based on the TMM. To take into account any changes in the biasing current, the carrier rate equation was included. In the analysis, multi-carrier recombination and a parabolic gain model were assumed. To include any gain saturation effects, a non-linear gain coefficient was introduced in the analysis. The algorithm used in the model was developed in such a way so that, with minor modifications, it can be applied to various laser structures.

The TMM based above-threshold laser model was applied to several DFB laser structures, including the QWS, 3PS and the DCC DFB LDs. The QWS DFB laser structure, which is characterised by its non-uniform field distribution, was shown to have a large dynamic change in the spatially distributed refractive index. Along the carrier concentration profile, a dip was shown at the centre of the cavity where the largest stimulated photon density is found.

The field distribution in the QWS DFB LD can be improved by introducing more phase shifts along the corrugation. In the analysis, a 3PS DFB LD with $\theta_2 = \theta_3 = \theta_4 = \pi/3$ and $PSP = 0.5$ were used. As compared with the QWS structure, uniform distributions were observed in the carrier density, photon density and the refractive index profiles.

With an improved threshold gain margin, the above-threshold characteristics of a QWS LD having non-uniform coupling coefficient were presented. As compared with the QWS structure, the introduction of the non-uniform coupling coefficient with $\kappa_1/\kappa_2 = 1/3$ and $CP = 0.46$ induced an increase in the localised carrier concentration near the corrugation change. We also found a significant reduction in the photon density difference between the central peak and the escaping photon density near the facet. Such a reduction improved the single mode stability of the DCC + QWS structure. This will be discussed in the next chapter.

The above-threshold lasing mode characteristics of a DCC + 3PS LD were also shown. As compared with the multiple phase shifts laser structure, it

was shown that the effect of the longitudinally varying coupling coefficient becomes dominant when the biasing current increases. In the next chapter the lasing mode characteristics obtained will be used to evaluate other characteristics such as the gain margin, the spontaneous emission spectrum and the spectral linewidth.

6.6 REFERENCES

[1] Pan, X., Olesen, H. and Tromborg, B., "Influence of nonlinear gain on DFB laser linewidth", *Electron. Lett.*, **26**, pp. 1074-1075, 1990.

[2] Soda, H., Kotaki, Y., Sudo, H., Ishikawa, H., Yamakoshi, S. and Imai, H., "Stability in single longitudinal mode operation in GaInAsP/InP phase-adjusted DFB lasers", *IEEE J. Quantum Electron.*, **QE-23**, no. 6, pp. 804-814, 1987.

[3] Orfanos, I., Sphicopoulos, T., Tsigopoulos A. and Caroubalos C., "A tractable above-threshold model for the design of DFB and phase-shifted DFB lasers", *IEEE J. Quantum Electron.*, **QE-27**, no. 4, pp. 946-957, 1991.

[4] Westbrook, L.D., "Measurement of dg/dN and dn/dN and their dependence on photon energy in $\lambda = 1.5$ μm InGaAsP laser diodes", *IEEE Proc. Pt. J*, **133**, no. 2, pp. 135-143, 1985.

[5] Chen, K.L. and Wang, S., "An approximate expression for the effective refractive index in symmetric DH lasers", *IEEE J. Quantum Electron.*, **QE-19**, no. 9, pp. 1354-1356, 1983.

[6] Huang, J and Casperson, L.W., "Gain and saturation in semiconductor lasers", *Opt Quantum Electron.*, **QE-27**, pp. 369-390, 1993.

[7] Agrawal, G.P. and Dutta, N.K., *Long-wavelength Semiconductor Lasers*. Princeton, NJ: Van Nostrand, 1986.

[8] Henry, C.H., "Theory of spontaneous emission noise in open resonator and its application to lasers and optical amplifiers", IEEE *J. Lightwave Technol.*, **LT-4**, no. 3, pp. 288-297, 1986.

[9] Lo, B.S.K. and Ghafouri-Shiraz, H., "A method to determine the above threshold characteristics of distributed feedback semiconductor laser diodes", *IEEE J. Lightwave Technol.*, IEEE/OSA J. Lightwave Technol., Vol. 13, No. 4, pp. 563-568, April 1995.

[10] Whiteaway, J.E.A., Thompson, G.H.B., Collar, A.J. and Armistead, C.J., "The design and assessment of $\lambda/4$ phase-shifted DFB laser structure", *IEEE J. Quantum Electron.*, **QE-25**, no. 6, pp. 1261-1279, 1989.

7

ABOVE-THRESHOLD ANALYSIS OF VARIOUS DFB LASER STRUCTURES USING THE TMM

7.1 INTRODUCTION

The above-threshold lasing characteristics of distributed feedback (DFB) semiconductor laser diodes (LDs) were presented in the previous chapter using a modified transfer matrix. Instead of using an average carrier concentration, the inclusion of the actual carrier distribution allows phenomena such as the spatial hole-burning effect (SHB) and the non-linear gain to be included. In the analysis, a parabolic gain model and high-order carrier recombination were assumed. The lasing mode characteristics such as the longitudinal distribution of the carrier density, the photon density, the refractive index and the internal field intensity were shown for various laser structures. In this chapter we use results obtained from the lasing mode characteristics to determine the mode stability and noise characteristics of DFB LDs.

For a coherent optical communication system, it is essential that the LD used oscillates at a stable single mode so that a narrow spectral linewidth is achieved. Using the information obtained for the lasing mode characteristics, a method derived from the above-threshold transfer matrix model is introduced in section 7.2, which allows the gain margin to be evaluated. By introducing an imaginary wavelength into the transfer matrix equation, the characteristics of other non-lasing side modes, can be evaluated and hence the single mode stability found. Numerical results obtained using this method are presented in section 7.3.

In section 7.4, an alternative method that allows the theoretical prediction of the above-threshold spontaneous emission will be presented. On the basis of the method of Green's function, transfer matrices help to determine the single mode stability of a DFB laser structure by inspecting the spectral components of the oscillating modes.

The transfer matrix method (TMM) also allows the noise characteristics of the DFB LD to be evaluated. In section 7.5 we show that various contributions to the spectral linewidth could be determined using the information obtained from the above-threshold transfer matrices. In the analysis, the effective linewidth enhancement factor [1] is used instead of the material-based linewidth enhancement [2]. Using a more realistic effective linewidth enhancement factor, impacts caused by structural changes can be investigated in a systematic way.

7.2 SINGLE MODE STABILITY IN A DFB LD

Using the TMM based above-threshold laser cavity model presented in the previous chapter, distributions of the carrier density, the photon density, the refractive index and the normalised internal field intensity were obtained from various DFB laser structures. From the emitting photon density at the facet, the output optical power is evaluated. Figure 7.1 summarises the results obtained for quarterly wavelength shifted (QWS), three phase shift (3PS) and distributed coupling coefficient with quarterly wavelength shifted (DCC + QWS) LDs with the biasing current as a parameter. Within the

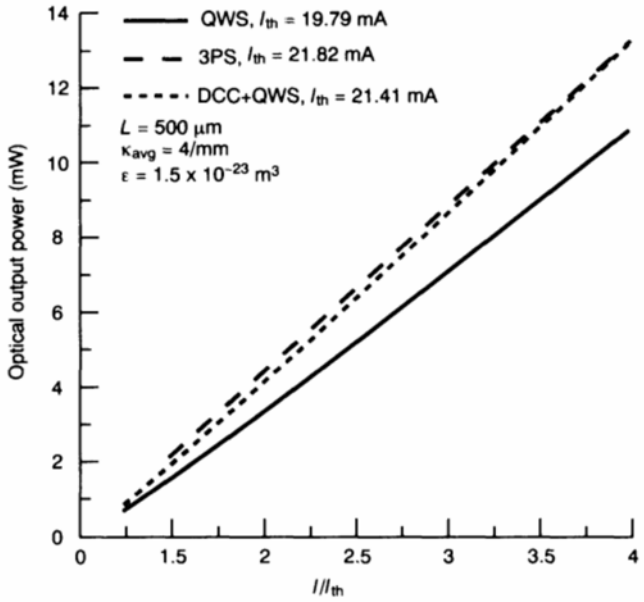

Figure 7.1 Variations in the optical output power versus I_{th} for three different types of DFB LDs.

range of the biasing current that we are interested in, no kink is observed in all three cases. Compared with the QWS structure, it seems that the introduction of multiple phase shifts along the 3PS laser cavity increases the overall cavity loss. It is also shown in the figure that the 3PS laser structure having the largest amplitude threshold gain has a relatively larger value of the threshold current. Among them, both the 3PS and the DCC + QWS structures appear to have relatively larger output power under the same normalised biasing current.

Semiconductor lasers having stable single longitudinal outputs and narrow spectral linewidths are indispensable in coherent optical communication systems. With a built-in wavelength selective corrugation, a DFB LD has a single longitudinal output. Other oscillation modes that fail to reach the threshold condition become non-lasing side modes. As the biasing current increases, the SHB effect becomes significant and mode competition between the lasing mode and the most probable non-lasing side mode may occur. Mode competition was observed from a QWS DFB laser [3–5], which resulted in multiple mode oscillations as the biasing current increased. In this section a numerical method that allows theoretical prediction of the above-threshold single mode stability of DFB LDs will be presented. In the analysis, it is assumed that the detailed lasing mode characteristics have been obtained from the above-threshold TMM, as discussed in the previous chapter.

Single mode stability implies suppression of the non-lasing side modes. There are two possible ways to demonstrate single mode stability in DFB LDs. The first approach involves evaluating the normalised gain margin $\Delta\alpha L$ between the lasing mode and the probable non-lasing side modes. The single mode stability is said to be threatened if the gain margin, $\Delta\alpha$, drops below 5/cm for a 500 μm length laser cavity. An alternative way to check the stability of the device involves the measurement of the spectral characteristics. With the help of an optical spectrum analyser, the measured intensity difference between the lasing mode and the side modes will give single mode stability. The second approach is often used to measure the single mode stability of DFB LDs. In this section we concentrate on the first approach which leads to the evaluation of the above-threshold gain margin.

From the numerical method discussed in the previous chapter, the oscillation characteristics of the lasing mode were obtained at a fixed biasing current. By dividing the DFB laser into a large number of smaller sections, longitudinal distributions like the carrier and photon densities were determined. Since the laser cavity is now dominated by the lasing mode, the characteristics of other non-lasing side modes should be derived from the lasing mode. To evaluate the characteristics of other non-lasing side modes, the dominant lasing mode has to suppressed in a mathematical way. In the analysis, an imaginary wavelength λ_i is introduced [6]. As a result, the complex wavelength λ_c of an unknown side mode becomes

$$\lambda_c = \lambda + j\lambda_i \tag{7.2.1}$$

where λ_i takes into account the mathematical gain the side mode may need to reach its threshold value and λ becomes the actual wavelength of the side mode. By changing the values of both λ and λ_i, the wavelengths of other non-lasing side modes can be evaluated

The numerical procedure involved in determining the characteristics of other non-lasing side modes is summarised as follows:

(1) A numerical procedure similar to the one discussed in section 6.2 is adopted. To initialise the iteration process, a 5×5 mathematical grid which consists of (λ, λ_i) is formed. Each of the (λ, λ_i) points will be used as an initial guess. Since the most probable non-lasing side mode is usually found near the lasing mode, it is advisable to start with those wavelengths that are close to that of the lasing mode.

(2) Lasing mode characteristics like the longitudinal distribution of the carrier, the photon density and the refractive index are retrieved from the data files obtained earlier. The matrix elements of each transfer matrix are then determined.

(3) From the boundary condition at the left facet, the electric fields $E_R(z_1)$ and $E_S(z_1)$ at the left facet are found and serve as the input electric field to the transfer matrix chain.

(4) By passing the electric field through the transfer matrix chain, the output electric field at the right laser facet is determined. The discrepancy with the right facet boundary condition is then evaluated and stored.

(5) Steps (2)–(4) are then repeated with other pairs of (λ, λ_i) obtained from the 5×5 mathematical grid. By comparing the discrepancy obtained from each of the (λ, λ_i) pairs, the one showing the minimum discrepancy is then selected. Depending on the position of the selected (λ, λ_i) found on the mathematical grid, a new mathematical grid is formed ready for the next iteration.

(6) The procedures shown above are then repeated until the discrepancy with the right facet boundary condition falls below 10^{-14}. The final λ obtained becomes the non-lasing side mode and the distributions of the amplitude gain $\alpha(z)$ and the detuning coefficient $\delta(z)$ are stored.

(7) The average values of $\bar{\alpha}_{SM}$ and $\bar{\delta}_{SM}$ associated with the side mode are evaluated from the corresponding longitudinal distribution as

$$\bar{\alpha}_{SM} = \sum_{j=1}^{N} \alpha_j / N \tag{7.2.2}$$

$$\bar{\delta}_{SM} = \sum_{j=1}^{N} \delta_j / N \tag{7.2.3}$$

where α_j and δ_j ($j = 1$ to N) are the amplitude gain value and the detuning value obtained from each transfer matrix, respectively, and N is the total number of transfer matrices.

(8) The whole numerical procedure can be repeated for other non-lasing side modes. All $\bar{\alpha}_{SM}$ obtained are then sorted in increasing order. The one showing the smallest value becomes the most probable side mode. The characteristics of the new dominant lasing mode must be loaded every time a new injection current is used.

From the result obtained, the gain margin between the lasing mode and the most probable non-lasing side mode can be evaluated as

$$\Delta\alpha = \bar{\alpha}_L - \bar{\alpha}_{SM} \tag{7.2.4}$$

To maintain a stable single mode oscillation, we need $\Delta\alpha L > 0.25$ for a 500 μm length laser cavity.

7.3 NUMERICAL RESULTS ON THE GAIN MARGIN OF DFB LDs

In this section we present the numerical results obtained from various DFB LDs including QWS, 3PS and DCC + QWS laser structures. Figure 7.2 shows the characteristics of the lasing mode (0) and side modes (±1) in the $(\bar{\delta}L, \bar{\alpha}L)$ plane. In the analysis, an anti-reflection coated QWS DFB structure with $\kappa L = 2$ is assumed for a 500 μm length cavity. For each oscillating mode shown in Figure 7.2, the cross and the black circle correspond to the oscillating mode at threshold and at $5I_{th}$, respectively. When the biasing current increases from the threshold value, an increase in the lasing mode amplitude gain and a

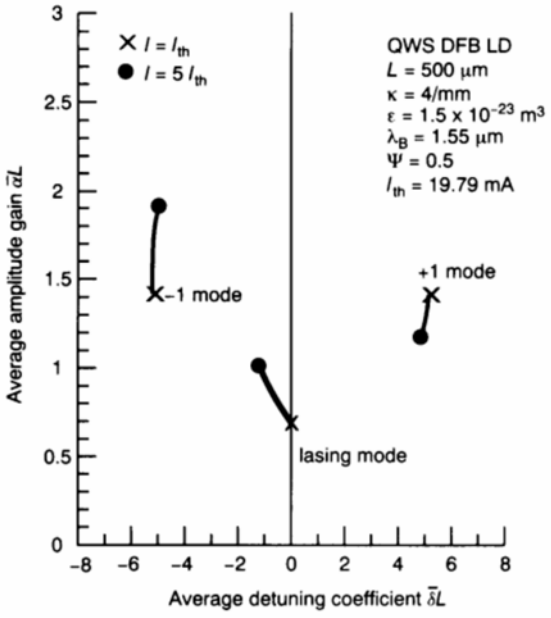

Figure 7.2 Lasing characteristics for the QWS DFB laser structure in the $(\bar{\delta}L, \bar{\alpha}L)$ plane showing two values of the normalised injection current.

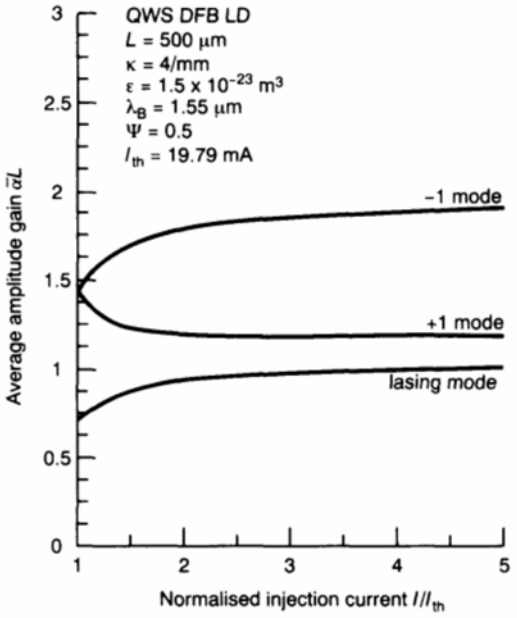

Figure 7.3 Average amplitude gain $\bar{\alpha}L$ of the QWS DFB laser structure versus the normalised injection current. Results for the lasing and non-lasing side modes (± 1) are shown.

corresponding reduction in the gain margin between the lasing mode and the $+1$ side mode can be seen. Such a phenomenon is well known to be induced by the SHB effect [5].

Figure 7.3 shows the normalised amplitude gain change in the QWS DFB LD with respect to the biasing current. The amplitude gain distribution for the lasing mode as well as for the non-lasing side modes are shown. It is obvious that the $\bar{\alpha}L$ value of each mode varies in a different way. When the biasing current increases from threshold, it is clear that the amplitude gain of the $+1$ mode reduces remarkably and approaches that of the lasing mode. However, the amplitude gain of the -1 mode becomes larger and hence becomes less significant. In Figure 7.4, for the same QWS structure, the variations in the normalised detuning coefficient $\bar{\delta}L$ are shown. In such a strongly coupled LD, both the lasing mode and the $+1$ side mode shift towards the shorter wavelength side (negative $\bar{\delta}L$) with increasing biasing current. Among the different modes shown, the shift in the lasing mode is stronger since it is found closer to the gain peak.

With multiple phase shifts introduced along the corrugation, the characteristics of the 3PS structure are as shown in Figure 7.5. In the analysis, the 3PS DFB is assumed to be anti-reflection coated. Phase shifts $\theta_2 = \theta_3 = \theta_4 = \pi/3$ and position factor $\psi = 0.5$ (see equation 5.2.3) are assumed for the 500 μm long cavity. Compared with the QWS structure, the 3PS structure shows a smaller shift in the mode characteristics. This will be clear when the variations in both the amplitude gain and the detuning coefficient are shown as

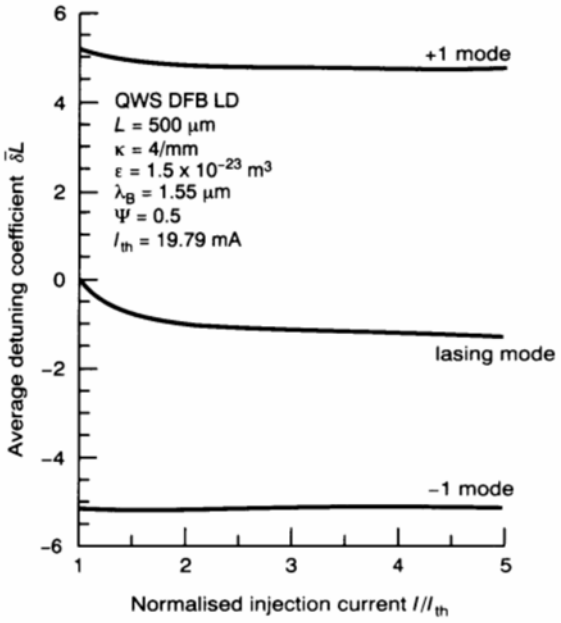

Figure 7.4 Average detuning coefficient $\bar{\delta}L$ of the QWS DFB laser structure versus the normalised injection current. Results for the lasing and the non-lasing side modes (± 1) are shown.

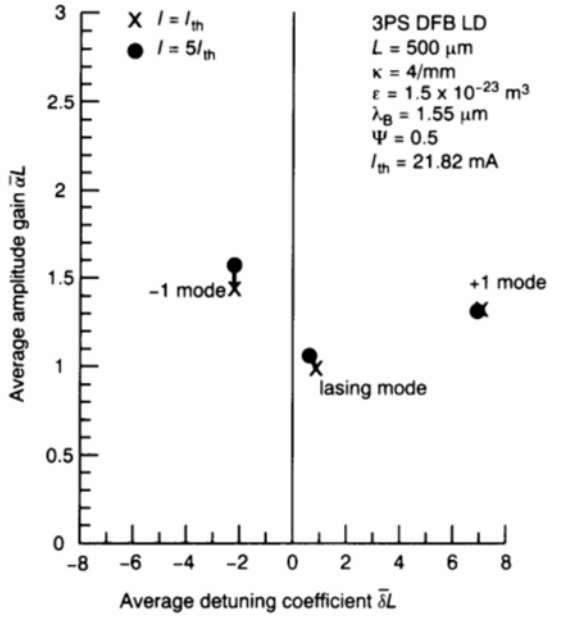

Figure 7.5 Lasing characteristics of the 3PS DFB laser structure in the $(\bar{\delta}L, \bar{\alpha}L)$ plane showing values of the normalised injection current.

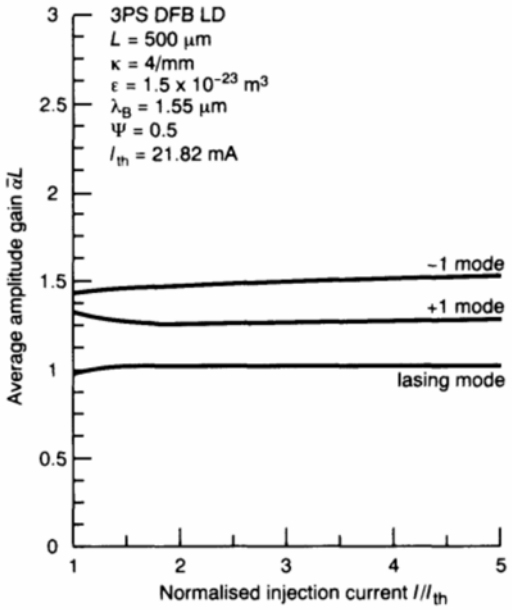

Figure 7.6 Average amplitude gain $\bar{\alpha}L$ for the 3PS DFB laser structure versus the normalised injection current. Results for the lasing and the non-lasing side modes (± 1) are shown.

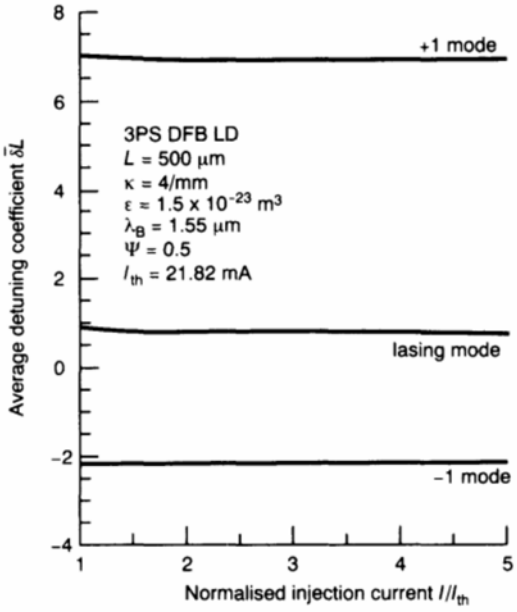

Figure 7.7 Average detuning coefficient $\bar{\delta}L$ of the 3PS DFB laser structure versus the normalised injection current. Results for both the lasing and the non-lasing side modes (± 1) are shown.

functions of the normalised injection current. From Figure 7.6, where the amplitude gain change is shown, the injection current alters the oscillating mode in a different way. It can be observed that the gain margin between the lasing mode and the most probable side mode (+1) shows little change. A similar situation can be seen in Figure 7.7, where the variations in the detuning coefficient are demonstrated. The lasing mode shown has a milder shift with increasing biasing current. On combining the results from both Figures 7.6 and 7.7 it appears that the 3PS laser structure is not seriously affected by the SHB effect. No severe reduction in the gain margin and only a fairly mild shift in the detuning coefficient are observed.

Results obtained from a DCC + QWS laser structure for the lasing characteristics, amplitude gain and the detuning coefficient are shown in Figures 7.8–7.10, respectively. A 500 μm length cavity is assumed. The other parameters used follow those adopted in the TMM based laser model discussed in the previous chapter. These parameters include $\kappa_1/\kappa_2 = 1/3$, $\kappa_{avg}L = 2$ and $CP = 0.46$. Owing to the effects of SHB, all figures appear to have a similar trend in the shape of their curve. However, the single mode stability in the DCC + QWS structure is improved owing to the presence of the DCC. As shown in Figure 7.9, the amplitude gain difference between the lasing mode and the +1 mode remains at a high value even at a high biasing current.

Figure 7.11 shows the normalised gain margin ($\Delta\alpha L$) between the lasing mode and the most probable side mode. Results obtained from QWS, 3PS and

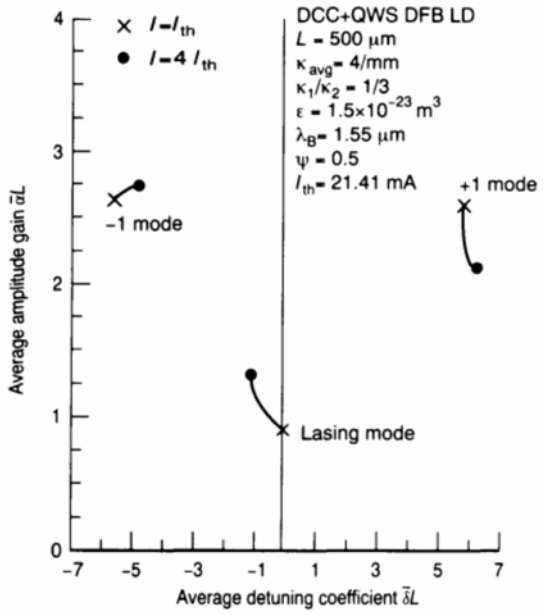

Figure 7.8 Lasing characteristics of the DCC + QWS DFB laser structure in the ($\bar{\delta}L$, $\bar{\alpha}L$) plane showing two values of the normalised injection current.

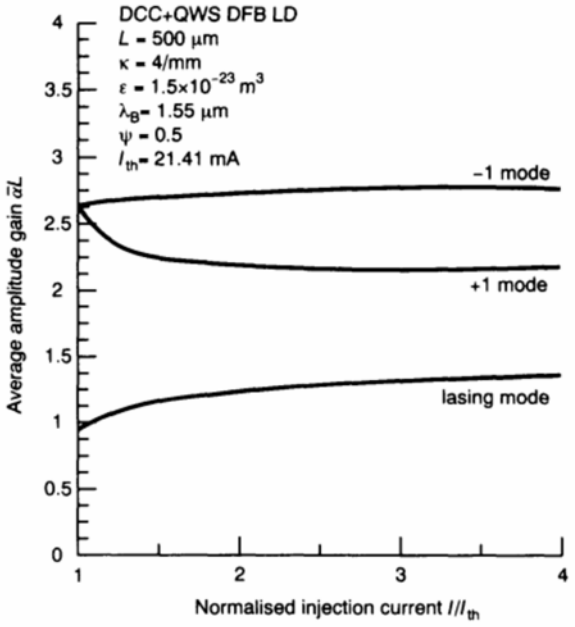

Figure 7.9 Normalised amplitude gain $\bar{\alpha}L$ of the DCC + QWS DFB laser structure versus the normalised injection current. Results for both the lasing and the non-lasing side modes (± 1) are shown.

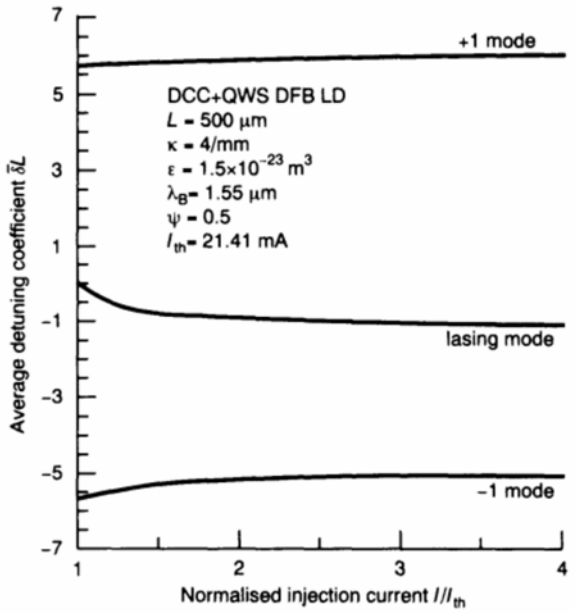

Figure 7.10 Normalised amplitude gain $\bar{\delta}L$ of the DCC + QWS DFB laser structure versus the normalised injection current. Results for both the lasing and the non-lasing side modes (± 1) are shown.

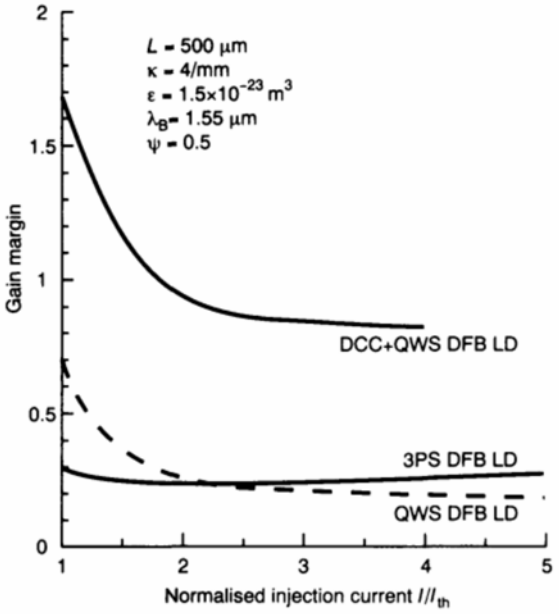

Figure 7.11 Variation in the gain margin with respect to changes in the injection current for different DFB LD structures.

the DCC + QWS structures are shown. The gain margin of both the QWS and the DCC + QWS structures reduce when the biasing current increases. From the above-threshold analysis, these structures were characterised by an intense electric field located at the centre of the cavity, and hence are affected by SHB. Nevertheless, the DCC + QWS laser structure can maintain the gain margin at a sufficiently high level, even under large biasing conditions. On the contrary, the gain margin of the 3PS shows little change over the range of biasing current. In all three cases the most dramatic change in the gain margin occurs when the biasing current is still close to that of the threshold value. At this biasing current, the photon density (as shown in the previous chapter) is still fairly uniform and the non-linear gain effect is still far from mature. It is believed that it is the dominant SHB effect that alters the characteristics of the oscillating modes. When the biasing current increases, the average photon density inside the laser cavity increases and so does its value found along the plane phase or corrugation discontinuities. Under such a high current injection, the non-linear gain effect becomes dominant.

A change in the lasing wavelength with respect to the injection current change is shown in Figure 7.12. Results obtained from the QWS, 3PS and the DCC + QWS structures are also shown. Among them, the 3PS structure shows relatively minor changes (~ 0.07 nm) with the biasing current. The introduction of multiple phase shifts along the corrugation suppresses the SHB effect to such an extent that the injection current hardly changes the refractive index and hence a less gradual change in the lasing wavelength is obtained. With such a stable output, it appears that the 3PS structure has potential use

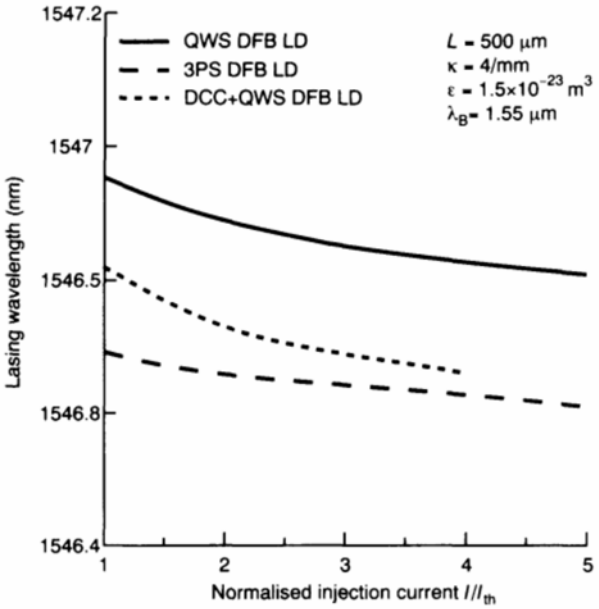

Figure 7.12 Variation in the lasing wavelength with respect to the injection current for different DFB LD structures.

as an optical carrier. On the contrary, structures like the DCC + QWS show a larger dynamic change in the lasing wavelength. A single mode continuous tuning of about 0.16 nm is achieved. It appears that this structure has potential application in the WDM optical network.

7.4 ABOVE-THRESHOLD SPONTANEOUS EMISSION SPECTRUM

By measuring the mode intensity difference from the spectrum, single mode stability can be determined. A minimum side mode suppression ratio of 25 dB is necessary for a stable single mode [7]. With the help of the method using Green's function, as discussed in Chapter 4, the above-threshold spontaneous emission spectrum can be evaluated using the transfer matrices. From the output of an individual transfer matrix, the contribution due to the distributed noise source is found.

From equation (4.4.8) in Chapter 4, the spontaneous emission power emitted for unity bandwidth ($\Delta\omega = 1$) at the right laser facet of an N-section mirrorless DFB laser cavity could be expressed in terms of the elements of the overall transfer matrix as

$$P_N(z_{N+1}) = \frac{hc}{\lambda} \cdot \frac{1}{|y_{22}(z_{N+1}|z_1)|^2} \int_{z_1}^{z_{N+1}} n_{sp} g[|y_{22}(z|z_1)|^2 + |y_{12}(z|z_1)|^2]\, dz \tag{7.4.1}$$

where $y_{22}(z_{N+1}|z_1)$ is a matrix element obtained from the overall transfer matrix $\mathbf{Y}(z_{N+1}|z_1)$ while $y_{22}(z|z_1)$ and $y_{12}(z|z_1)$ are elements of the matrix

$\mathbf{Y}(z|z_1)$ at arbitrary z. In the above equation, n_{sp} is the local population inversion factor which is usually approximated as [8]

$$n_{sp}(z) = N(z)/(N(z) - N_0) \tag{7.4.2}$$

with N_0 being the carrier concentration at zero gain transparency. In equation (7.4.1), the material gain term g becomes longitudinally dependent at the above-threshold biasing regime. In cases of below-threshold and at-threshold biasing conditions, a uniform distribution is expected. Using a sufficiently large number of transfer matrices, a numerical method such as the trapezoidal rule was applied to evaluate the above integral. As a result, the above integral can be approximated as

$$\int_{z_1}^{z_{N+1}} n_{sp} g[|y_{22}(z|z_1)|^2 + |y_{12}(z|z_1)|^2]\,dz \approx \frac{\Delta L}{2} \sum_{j=1}^{N} [Q(j) + Q(j+1)] \tag{7.4.3}$$

where $Q(j) = n_{sp}(z_j)g(z_j)\,[|y_{22}(z_j|z_1)|^2 + |y_{12}(z_j|z_1)|^2]$, N is the total number of transfer matrix used and $\Delta L = L/N$ is the length of each transfer matrix represented. From the matrices the matrix elements $y_{22}(z_j|z_1)$ and $y_{12}(z_j|z_1)$ at an arbitrary matrix output plane of $z = z_j$ can always be determined from those at $z = z_{j-1}$ as

$$\begin{bmatrix} y_{11} & y_{12} \\ y_{21} & y_{22} \end{bmatrix}_{(z_j|z_1)} = \begin{bmatrix} f_{11} & f_{12} \\ f_{21} & f_{22} \end{bmatrix}_{(z_j|z_{j-1})} \cdot \begin{bmatrix} y_{11} & y_{12} \\ y_{21} & y_{22} \end{bmatrix}_{(z_{j-1}|z_1)} \tag{7.4.4}$$

where $f_{ij}(i, j = 1, 2)$ are the matrix elements of the transfer matrix $\mathbf{F}$. When the biasing current increases, it is shown in the QWS DFB laser structure that the gain margin reduces significantly and the non-lasing side mode becomes significant. Mode competition is also revealed from the above-threshold spontaneous spectrum. Figure 7.13 shows the spectral characteristics of the QWS DFB laser structure with biasing current changes. In the analysis, a unity bandwidth is assumed. Along a fixed biasing current, distinct peaks can be seen along the spectrum which correspond to different oscillating modes. The lasing mode shown near 1546.85 nm becomes the lasing mode after the threshold condition is reached. When the biasing current increases, it can be seen that all peak wavelengths shift towards the shorter wavelength. The so-called "blue shift" in the wavelength follows the change in material gain with carrier concentration which has been demonstrated experimentally using a QWS DFB LD [9]. Apart from that, a reduction in the spectral amplitude difference is also shown between the lasing mode and the +1 mode which is located at the shorter wavelength side. At a biasing current of $5I_{th}$, the side mode suppression ratio (SMSR) is reduced to less than 25 dB. At such a SMSR value, the stability of the single mode oscillation is weakened and the presence of the +1 mode becomes significant in the case of a QWS DFB LD [10].

Figure 7.14 shows the spontaneous emission spectrum of a 3PS DFB LD. In the analysis, the 3PS laser structure used has phase shifts $\theta_2 = \theta_3 = \theta_4 =$

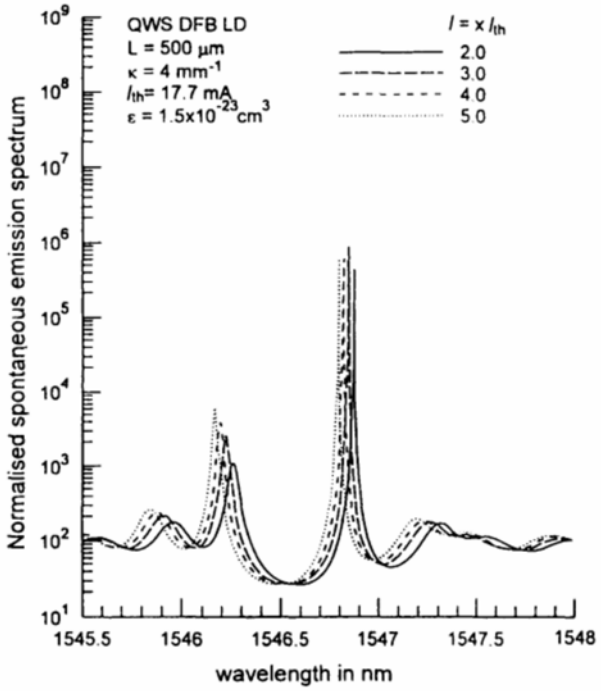

Figure 7.13 Normalised spontaneous emission spectra of a QWS DFB LD.

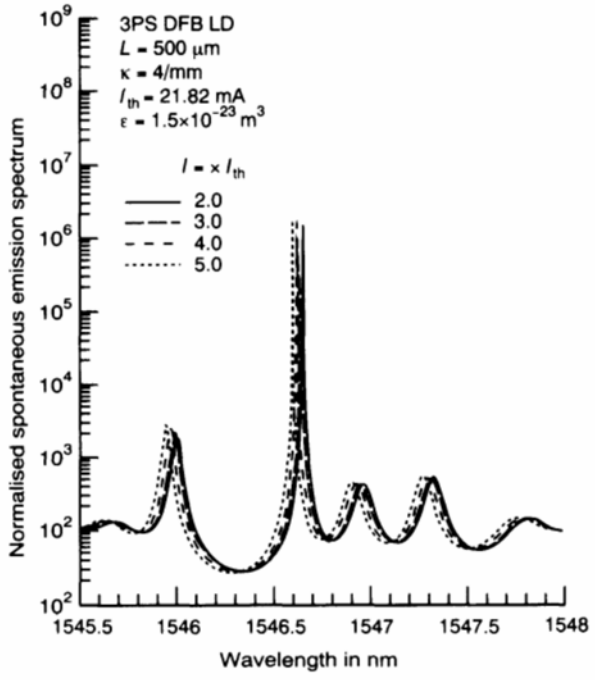

Figure 7.14 Normalised spontaneous emission spectra of a 3PS DFB LD.

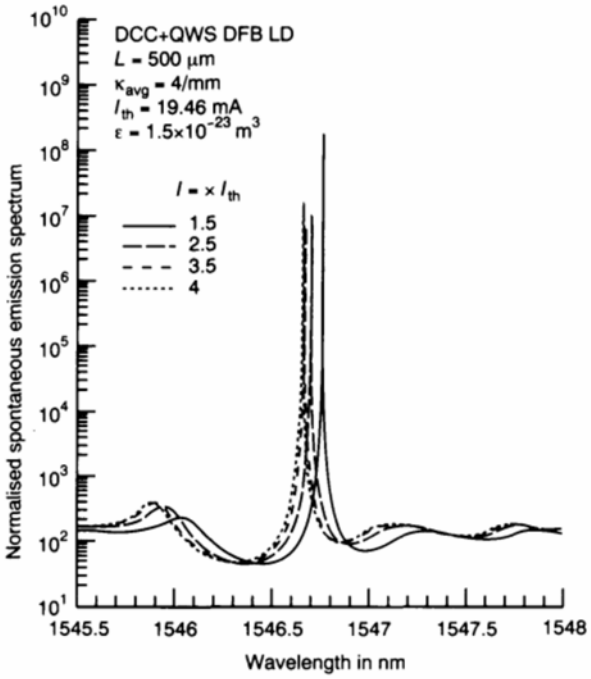

Figure 7.15 Normalised spontaneous emission spectra of a DCC + QWS DFB LD.

$\pi/3$ and $PSP = 0.5$ is assumed. The other parameters used are listed in the inset. Similar to the QWS laser structure, distinct peaks that correspond to different oscillating modes are observed along the spectrum. When the biasing current increases, the spectral amplitude of the dominant lasing mode found near 1546.6 nm shows no sign of a reduction and remains at a high value near 10^6. Compared with the QWS structure, the 3PS laser structure shows no severe mode competition and a SMSR of at least 25 dB is maintained throughout the range of biasing current.

The spectral characteristics of a DCC DFB LD with a single QWS are shown in Figure 7.15 under various biasing conditions. At a fixed biasing current, the central peak shown corresponds to the dominant lasing mode. Owing to the introduction of the DCC, mode competition has been reduced significantly with an improved SMSR between the lasing mode and the most probable non-lasing side mode [11]. Compared with the QWS and the 3PS LD, the DCC + QWS laser structure appears to have a more stable single mode oscillation and a SMSR of at least 35 dB.

7.5 SPECTRAL LINEWIDTH

In coherent optical communication systems it is important that the semiconductor laser LDs have narrow spectral linewidths. The finite spectral width measured at the output of a semiconductor laser [12] is the result

of spontaneous emission [13] which alters both the intensity and the phase components of the lasing mode. The mutual coupling between the intensity and the phase has been included by using an intrinsic linewidth enhancement factor, α_H [13]. Using the self-heterodyne method [14], the spectral linewidths of DFB LDs were measured [15]. Without including the SHB effect, their formulae, which is based on the α_H failed to predict the actual spectral linewidth when the biasing current increased. To obtain a more accurate linewidth prediction and hence a better understanding of the linewidth saturation and rebroadening effects [16,17], formulations based on an equivalent circuit theory were proposed [18,19]. On the basis of the scattering parameters commonly used in microwave engineering, the spectral linewidths of DFB LDs were determined. However, it is not straightforward to compare this approach with the carrier rate equation widely adopted in semiconductor lasers. Moreover, these analyses are only concerned with the above-threshold spectral linewidth and there is no formulation for any of the other characteristics. Another theory based on the open resonator has also been proposed [20]. Using the method of Green's function, the spontaneous emission rate and hence the spectral linewidths of DFB LDs were determined [21–24]. In this analysis the effective linewidth enhancement factor (α_{eff}) was considered; however, the analysis was limited to simple DFB laser structures. For complicated designs like the 3PS and DCC laser structures, it would be difficult to find the Green's function because of the mathematical complexity involved. In this section, results obtained from the TMM will be applied to evaluate the noise characteristics of the DFB LD. The linewidth formulae we have adopted are those obtained by Trombrog *et al.* [21,25]. The spectral linewidth ($\Delta\upsilon$) for a single frequency semiconductor laser is given as

$$\Delta\upsilon = \Delta\upsilon_{sp} + \Delta\upsilon_{NN} + \Delta\upsilon_{NS} \tag{7.5.1}$$

where $\Delta\upsilon_{sp}$ is the contribution owing to the spontaneous emission, $\Delta\upsilon_{NN}$ is the contribution due to the fluctuation of the local carrier density and $\Delta\upsilon_{NS}$ is due to the cross-correlation term between the fluctuation of the photon number and the carrier density. In the analysis a nearly single mode laser source is assumed and the effects due to the presence of other non-lasing side modes [26,27] have been ignored. For spontaneous emission, it is clear that [20]

$$\Delta\upsilon_{sp} = \frac{R_{sp}}{4\pi P_{num}}(1 + \alpha_{eff}{}^2) \tag{7.5.2}$$

where R_{sp} is the spontaneous emission factor, α_{eff} is the effective linewidth enhancement factor and P_{num} is the total number of photons found inside the DFB laser cavity.

According to Henry [20], the spontaneous emission rate R_{sp} of an open resonator like the DFB LD can be expressed in terms of the field intensity $|E^2(z)|$ as

$$R_{sp} = \frac{4\omega^2}{c^3} \cdot \frac{\int_{z_1}^{z_{N+1}} n_{sp} g n |E^2(z)| \, dz \cdot \int_{z_1}^{z_{N+1}} n_g n |E^2(z)| \, dz}{|\partial W/\partial\omega|^2} \tag{7.5.3}$$

where n_{sp} is the population inversion factor, g is the material gain, n is the refractive index, n_g is the group refractive index and $\partial W/\partial\omega$ is the derivative of the Wronskian term. According to equation (4.4.16), $\partial W/\partial\omega$ can be expressed in terms of the transfer matrix such that

$$\frac{\partial W}{\partial\omega} = -2j\beta_0 E_R(z_{N+1}|z) \left[\frac{\partial y_{22}}{\partial\omega} + \hat{r}_1 \frac{\partial y_{21}}{\partial\omega} - \hat{r}_2 \frac{\partial y_{12}}{\partial\omega} - \hat{r}_1 \hat{r}_2 \frac{\partial y_{11}}{\partial\omega} \right] \tag{7.5.4}$$

Owing to the fact that the matrix $\mathbf{Y}(z_{N+1}|z_1) = \mathbf{F}^{(N)} \cdot \mathbf{F}^{(N-1)} \cdot \mathbf{F}^{(N-2)} \ldots \mathbf{F}^{(2)} \cdot \mathbf{F}^{(1)}$, where $\mathbf{F}^{(j)}$ ($j = 1$ to N) is the transfer matrix of each smaller subsection, we can define $\partial\mathbf{Y}(z_{N+1}|z_1)/\partial\omega$ as

$$\frac{\partial \mathbf{Y}(z_{N+1}|z_1)}{\partial\omega} = \begin{bmatrix} \partial y_{11}/\partial\omega & \partial y_{12}/\partial\omega \\ \partial y_{21}/\partial\omega & \partial y_{22}/\partial\omega \end{bmatrix} \tag{7.5.5}$$

where

$$\frac{\partial \mathbf{Y}(z_{N+1}|z_1)}{\partial\omega} = \frac{\partial \mathbf{F}^{(N)}}{\partial\omega} \cdot \mathbf{F}^{(N-1)} \cdot \mathbf{F}^{(N-2)} \ldots \mathbf{F}^{(2)} \cdot \mathbf{F}^{(1)} + \cdots + \mathbf{F}^{(N)} \cdot \mathbf{F}^{(N-1)} \cdot \mathbf{F}^{(N-2)} \ldots \mathbf{F}^{(2)} \cdot \frac{\partial \mathbf{F}^{(1)}}{\partial\omega} \tag{7.5.6}$$

The individual transfer matrix $\partial\mathbf{F}^{(i)}/\partial\omega$ ($i = 1$ to N) is then obtained as

$$\frac{\partial \mathbf{F}^{(i)}}{\partial\omega} = \begin{bmatrix} \partial f_{11}^{(i)}/\partial\omega & \partial f_{12}^{(i)}/\partial\omega \\ \partial f_{21}^{(i)}/\partial\omega & \partial f_{22}^{(i)}/\partial\omega \end{bmatrix} \tag{7.5.7}$$

where

$$\partial f_{11}^{(i)}/\partial\omega = -j e^{-j\beta_0(\Delta z)} e^{j\theta_{(i)}} \mathbf{K}_{(1)}/v_g(1 - \rho_{(i)}{}^2)^2\gamma_{(i)} \tag{7.5.8a}$$

$$\partial f_{12}^{(i)}/\partial\omega = j e^{-j\beta_0(2z_{(i)}+\Delta z)} e^{-j\theta_{(i)}} e^{-j\Omega} \mathbf{K}_{(2)}/v_g(1 - \rho_{(i)}{}^2)^2\gamma_{(i)} \tag{7.5.8b}$$

$$\partial f_{21}^{(i)}/\partial\omega = -j e^{-j\beta_0(2z_{(i)}+\Delta z)} e^{j\theta_{(i)}} e^{j\Omega} \mathbf{K}_{(2)}/v_g(1 - \rho_{(i)}{}^2)^2\gamma_{(i)} \tag{7.5.8c}$$

$$\partial f_{22}^{(i)}/\partial\omega = j e^{j\beta_0(\Delta z)} e^{-j\theta_{(i)}} \mathbf{K}_{(3)}/v_g(1 - \rho_{(i)}{}^2)^2\gamma_{(i)} \tag{7.5.8d}$$

with

$$K_{(1)} = (1 - \rho_{(i)}^2)(E_{(i)} + \rho_{(i)}^2 E_{(i)}^{-1})(\alpha_{(i)} - j\delta_{(i)})(\Delta z) - 2\rho_{(i)}^2(E_{(i)} - E_{(i)}^{-1}) \tag{7.5.9a}$$

$$K_{(2)} = \rho_{(i)}(1 - \rho_{(i)}{}^2)(E_{(i)} + E_{(i)}{}^{-1})(\alpha_{(i)} - j\delta_{(i)})(\Delta z) - \rho_{(i)}(1 + \rho_{(i)}^2)(E_{(i)} - E_{(i)}{}^{-1}) \tag{7.5.9b}$$

$$K_{(3)} = (1 - \rho_{(i)}^2)(E_{(i)}^{-1} + \rho_{(i)}^2 E_{(i)})(\alpha_{(i)} - j\delta_{(i)})(\Delta z) - 2\rho_{(i)}^2(E_{(i)} - E_{(i)}^{-1}) \tag{7.5.9c}$$

$$\rho_{(i)} = j\kappa_{(i)}/(\alpha_{(i)} - j\delta_{(i)} + \gamma_{(i)}) \tag{7.5.9d}$$

$$\gamma_{(i)}^2 = (\alpha_{(i)} - j\delta_{(i)})^2 + \kappa_{(i)}^2 \tag{7.5.9e}$$

$$E_{(i)} = \mathrm{e}^{j\gamma_{(i)}\Delta z} \tag{7.5.9f}$$

$$E_{(i)}^{-1} = \mathrm{e}^{-j\gamma_{(i)}\Delta z} \tag{7.5.9g}$$

In the above equations, Δz is the length of each transfer matrix represented.

For a mirrorless DFB laser cavity with $\hat{r}_1 = \hat{r}_2 = 0$ the spontaneous emission rate R_{sp} in equation (7.5.3) is simplified to become

$$R_{\mathrm{sp}} = \frac{4\Lambda^2 n_{\mathrm{sp}}}{v_g \lambda^2} \cdot \frac{\displaystyle\int_{z_1}^{z_{N+1}} gn|E^2(z)|\,\mathrm{d}z \cdot \int_{z_1}^{z_{N+1}} n|E^2(z)|\,\mathrm{d}z}{|y_{12} \cdot \partial y_{22}/\partial\omega|^2} \tag{7.5.10}$$

where v_{g} is the group velocity. The denominator $|y_{12} \cdot \partial y_{22}/\partial\omega|^2$ in equation (7.5.10) is determined using the transfer matrices after following equations (7.5.5)–(7.5.9). Other integrals shown in the numerator can be found numerically from discrete sets of $n(z_i)$ and $g(z_i)$, and $|E^2(z_i)|$ ($i = 1$ to $N + 1$) are obtained from the above-threshold lasing cavity model as discussed in the previous chapter.

The effective linewidth enhancement factor α_{eff} used in the spontaneous emission linewidth is different from the intrinsic material linewidth enhancement factor [13,28]. By considering the effects due to the structural change [29] as well as the photon and carrier distributions [30–32], the effective linewidth enhancement factor is given as [25]

$$\alpha_{\mathrm{eff}} = \mathrm{Im}\{X\}/\,\mathrm{Re}\{X\} \tag{7.5.11}$$

where

$$X = \int_{z_1}^{z_{N+1}} S\left[C_{\mathrm{N}}\tau_{\mathrm{N}}\frac{\partial R_{\mathrm{st}}}{\partial S} - C_{\mathrm{s}}\right]\mathrm{d}z \tag{7.5.12}$$

In the above equation, $\tau_{\mathrm{N}} = \partial(R + R_{\mathrm{st}})/\partial N$ is the carrier recombination lifetime that includes spontaneous emission, stimulated emission and other non-radiative recombination; S is the photon distribution of the lasing mode. The parameter $\partial R_{\mathrm{st}}/\partial S$ is the rate of stimulated emission (s^{-1}) and is defined as

$$\frac{\partial R_{\mathrm{st}}}{\partial S} = \frac{v_{\mathrm{g}} g}{(1 + \varepsilon S)^2}(1 + \varepsilon S - Sg\varepsilon) \tag{7.5.13}$$

The weighted functions C_N and C_S used in equation (7.5.12) are defined as [21]

$$C_N(z) = \frac{v_g E^2(z)}{\int_{z_1}^{z_{N+1}} E^2 \, dz} \cdot \left(1 + \frac{j\alpha_H}{1 + \varepsilon S(z)}\right) \cdot \frac{A_0 - 2A_1A_2[\lambda - \lambda_0 + A_2(N(z) - N_0)]}{2(1 + \varepsilon S(z))} \tag{7.5.14a}$$

$$C_S(z) = \frac{v_g E^2(z)}{\int_{z_1}^{z_{N+1}} E^2 \, dz} \cdot \frac{-jg(z)\varepsilon}{2(1 + \varepsilon S(z))^2} \tag{7.5.14b}$$

where the intrinsic linewidth enhancement factor (α_H) can be expressed as

$$\alpha_H = -\frac{4\pi}{\lambda_B} \cdot \frac{\partial n / \partial N}{A_0} \tag{7.5.15}$$

From the set of discrete values $E(z_i)$ ($i = 1$ to $N + 1$) obtained from the TMM, the integral in both equations (7.5.14a) and (7.5.14b) is obtained and hence the value of α_{eff} can be evaluated. In a similar way, the total number of photons inside the laser cavity can be found as

$$P_{num} = \frac{wd}{\Gamma} \int_{z_1}^{z_{N+1}} S \, dz \tag{7.5.16}$$

where the integral is found numerically from the discrete set of $S(z_i)$ ($i = 1$ to $N + 1$).

There are other components, $\Delta\upsilon_{NN}$ and $\Delta\upsilon_{NS}$, which contribute to the spectral linewidth as well. Suppose we define the local frequency tuning efficiency K_{tn} as

$$K_{tn}(z) = \tau_N(z)\{\text{Im}\,(C_N(z)) - \alpha_{eff}\,\text{Re}\,(C_N(z))\} \tag{7.5.17}$$

With no pump noise suppression, $\Delta\upsilon_{NN}$ and $\Delta\upsilon_{NS}$ can be written as

$$\Delta V_{NN} = \frac{1}{\pi wd} \int_{z_1}^{z_{N+1}} (n_{sp} v_g g S + R + R_{st}) K_{tn}^2 \, dz \tag{7.5.18}$$

$$\Delta V_{NS} = \frac{R_{sp}\alpha_{eff}}{\pi P_{num}} \int_{z_1}^{z_{N+1}} S K_{tn} \, dz \tag{7.5.19}$$

where the integrals can be determined numerically using the discrete information provided by the TMM.

On the basis of the lasing mode characteristics obtained from the TMM of a DFB LD, sets of discrete values obtained on the carrier distribution, the photon distribution and refractive index distribution are applied in evaluating the spectral linewidth. The use of a transfer matrix enables spatially dependent factors such as the SHB effect and other longitudinally dependent parameters to be included in the analysis.

7.5.1 Numerical results on the spectral linewidth

For a QWS laser structure, the variations in the spectral linewidth with respect to the biasing current are shown in Figure 7.16. Changes in various components, including $\Delta\upsilon_{sp}$, $\Delta\upsilon_{NN}$ and $\Delta\upsilon_{NS}$, are also shown. In the analysis, a 500 μm long cavity and $\kappa L = 2.0$ are assumed. The other parameters used are listed in the inset of the figure. When the biasing current is still close to the threshold value, the dominant spontaneous emission remains the major contributor. When the biasing current increases, the value of $\Delta\upsilon_{sp}$ decreases dramatically, owing to the dominant stimulated emission, and the contribution of $\Delta\upsilon_{NN}$ becomes significant. Comparatively, the magnitude of $\Delta\upsilon_{NS}$ remains at a small value and can be neglected throughout the range of biasing currents.

By introducing multiple phase shifts along the corrugation of the laser cavity, a 3PS DFB LD is characterised by a relatively uniform field distribution and a reasonably stable single mode oscillation. Figure 7.17 demonstrates the variations in the spectral linewidth in a 3PS DFB LD. All structural parameters used in the analysis are identical to those for the QWS DFB laser except the phase shifts, which are assumed to be $\pi/3$ and $PSP = 0.5$. Compared with the QWS laser structure, the 3PS DFB LD shows a broader spectral linewidth under the same biasing condition. It was revealed in the threshold analysis that the 3PS DFB LD has a relatively larger amplitude threshold gain. As a result, a larger threshold current and hence a larger number of injected carriers are required before the threshold

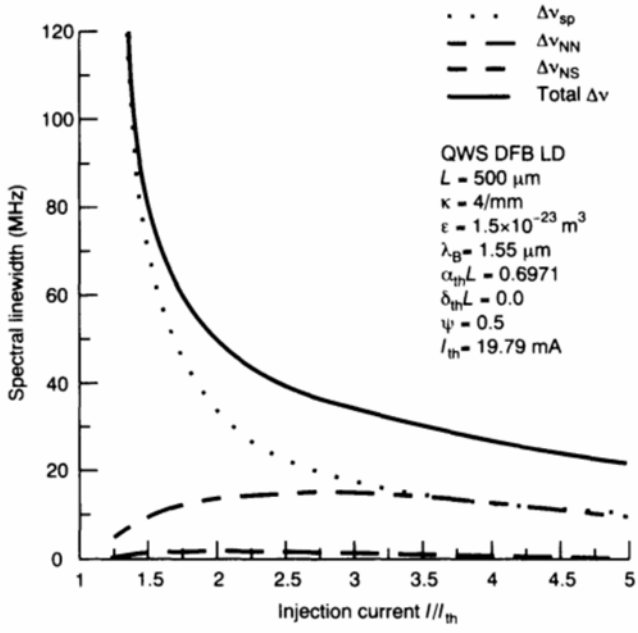

Figure 7.16 Variations in the spectral linewidth with respect to injection current for a QWS DFB LD.

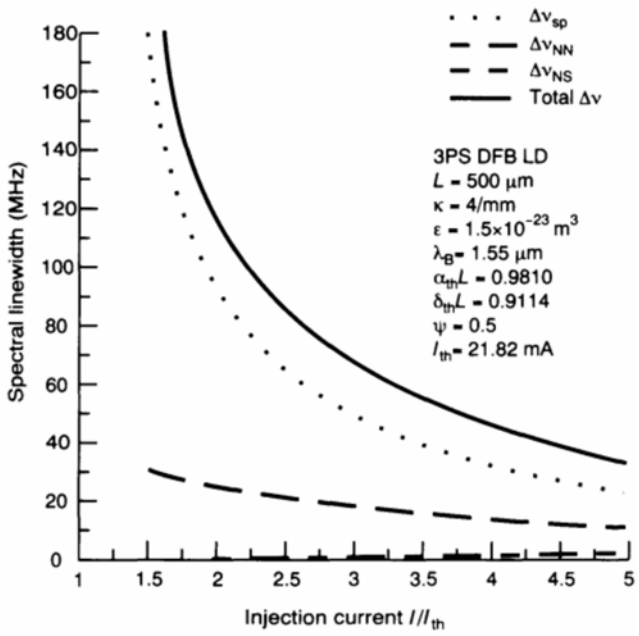

Figure 7.17 Variations in the spectral linewidth with respect to the injection current for a 3PS DFB LD.

condition is reached. In other words, a larger spontaneous emission rate, and consequently a larger $\Delta\upsilon_{sp}$, is expected. With increasing biasing current, the contribution of $\Delta\upsilon_{sp}$, is reduced and the $\Delta\upsilon_{NN}$ becomes influential.

By adopting a longitudinally dependent coupling coefficient κ, the gain margin and the field uniformity of the DCC + QWS DFB LD were shown to improve. Continuous tuning as far as 0.16 nm can be achieved with fairly stable single mode oscillations. The variations of the spectral linewidth of such a DCC + QWS structure are shown in Figure 7.18. In the analysis, we have used those structural parameters as presented in the previous chapter with $\kappa_1/\kappa_2 = 1/3$. A cavity length of 500 μm is assumed with $\kappa_{avg}L = 2$. Compared with other structures, the introduction of the longitudinally DCC is characterised by an overall increase in $\Delta\upsilon_{sp}$. The changes in the coupling coefficient along the corrugation result in an increase in the amplitude threshold gain and hence the spontaneous emission rate. Compared with the QWS structure, the influence of $\Delta\upsilon_{NN}$ becomes significant in the case of the DCC structure. When the biasing current increases, it is shown in the carrier density distribution that the carrier density increases near the plane of corrugation change. As a result, a stronger local carrier fluctuation is expected in this structure. With a further increase in the biasing current, the saturation of $\Delta\upsilon_{NN}$ may be a result of the non-linear gain effect. It is useful to mention that the validity of the TMM technique used to evaluate the spectral linewidth has been confirmed with experimental data reported for a single $\pi/2$ DFB laser structure [32].

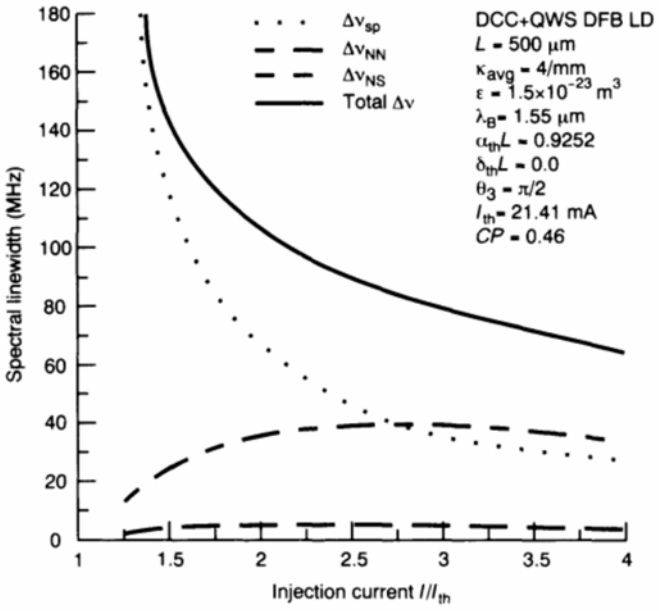

Figure 7.18 Variations in the spectral linewidth with respect to the injection current for a DCC + QWS DFB LD.

7.6 SUMMARY

In this chapter we applied the TMM based above-threshold model to evaluate the performance of various DFB LDs, including the QWS, 3PS and the DCC + QWS structures. From the lasing mode distributions of the carrier density, photon density, refractive index and the field intensity, characteristics like the single mode stability, the spontaneous emission spectrum and the spectral linewidth have been investigated. Throughout the analysis, all laser structures adopted are assumed to have a laser cavity length of 500 μm with κL or $\kappa_{avg}L = 2$. Table 7.1 summarises the results obtained for all three structures at a fixed biasing current of $4I_{th}$.

Table 7.1 Summary of results obtained from three DFB laser structures used at a biasing current of $4I_{th}$

	QWS	3PS	DCC + QWS
I_{th} (mA)	19.79	21.82	21.41
Power (mW)	10.79	13.13	13.10
$\Delta\alpha L$	0.1863	0.2452	0.8129
SMSR (dB)	22	28	45
Tuning range (nm)	0.14	0.07	0.16
$\Delta\upsilon_{total}$(MHz)	27.04	44.57	64.28
$\Delta\upsilon_{sp}$(MHz)	12.51	30.78	26.90
$\Delta\upsilon_{NN}$(MHz)	13.19	12.71	33.55

At a fixed biasing current, it was shown that the QWS structure showing the smallest threshold gain has the smallest spectral linewidth. However, this structure has a very poor single mode stability and the +1 non-lasing side mode becomes influential when the biasing current increases. From Table 7.1, the 3PS structure is shown to have one of the smallest changes in the lasing wavelength. With the introduction of multiple phase shifts along the corrugation, the internal field distribution becomes more uniform and hence a stable single mode oscillation results. Results obtained from the DCC + QWS structure show the largest gain margin. The introduction of the DCC has improved the single mode stability in such a way that the SMSR remained at a high value. A single mode continuous tuning as wide as 0.16 nm is achieved using the DCC + QWS laser structure. In this chapter, we showed that the complexity in the design of the DFB laser is apparent and it may well be that different designs are required for various applications. On the other hand, the TMM has proven to be a useful tool in handling such a problem.

7.7 REFERENCES

[1] Pan, X., Olesen, H. and Tromborg, B., "Spectral linewidth of DFB lasers including the effect of spatial holeburning and nonuniform current injection", *IEEE Photon Technol. Lett.*, **2**, no. 5, pp. 312-315, 1990.

[2] Henry, C.H., "Theory of the linewidth of semiconductor laser", *IEEE J. Quantum Electron.*, **QE-18**, no. 2, pp. 259-264, 1982.

[3] Soda, H., Kotaki, Y., Sudo, H., Ishikawa, H., Yamakoshi, S. and Imai, H., "Stability in single longitudinal mode operation in GaInAsP/InP phase-adjusted DFB lasers", *IEEE J. Quantum Electron.*, **QE-23**, no. 6, pp. 804-814, 1987.

[4] Ketelsen, L.J.P., Hoshino, I. and Ackerman, D.A., "The role of axially nonuniform carrier density in altering the TE-TE gain margin in InGaAsP-InP DFB lasers", *IEEE J. Quantum Electron.*, **QE-27**, no. 4, pp. 957-964, 1991.

[5] Ketelsen, L.J.P., Hoshino, I. and Ackerman, D.A., "Experimental and theoretical evaluation of the CW suppression of TE side modes in conventional 1.55 μm InP-InGaAsP distributed feedback lasers", *IEEE J. Quantum Electron.*, **QE-27**, no. 4, pp. 965-975, 1991.

[6] Lo, B.S.K. and Ghafouri-Shiraz, H., "A method to determine the above-threshold characteristics of distributed feedback semiconductor laser diodes", *IEEE J. Lightwave Technol.*, in press.

[7] Agrawal, G.P. and Dutta, N.K., *Long-wavelength Semiconductor Lasers*. Princeton, NJ: Van Nostrand, 1986.

[8] Bissessur, H., "Effects of hole burning, carrier-induced losses and the carrier-dependent differential gain on the static characteristics of DFB lasers", *J. Lightwave Technol.*, **LT-10**, no. 11, pp. 1617-1630, 1992.

[9] Ogita, S., Yano, M., Ishikawa, H. and Imai, H., "Linewidth reduction in DFB laser by detuning effect", *Electron. Lett.*, **23**, pp. 393-394, 1987.

[10] Krüger, U. and Petermann, K., "The semiconductor laser linewidth owing to the presence of side modes", *IEEE J. Quantum Electron.*, **QE-24**, no. 12, pp. 2355-2358, 1988.

[11] Lo, B.S.K. and Ghafouri-Shiraz, H., "Spectral characteristics of distributed feedback laser diodes with distributed coupling coefficient", *IEEE J. Lightwave Technol.*, **13**, no. 2, pp. 200-212, 1995.

[12] Fleming, M.W. and Mooradian, A., "Fundamental line broadening of single-mode (GaAs)As diode lasers", *Appl. Phys. Lett.*, **38**, no. 7, pp. 511-513, 1981.

[13] Henry, C.H., "Theory of the linewidth of semiconductor laser", *IEEE J. Quantum Electron.*, **QE-18**, no. 2, pp. 259-264, 1982.

[14] Okoshi, T. and Kikuchi, K. *Coherent Optical Fiber Communication*. Tokyo, Japan: KTK Scientific and Kluwer Academic Publishers, 1988.

[15] Kojima, K., Kyuma, K. and Nakayama, T., "Analysis of spectral linewidth of distributed feedback laser diodes", *J. Lightwave Technol.*, **LT-3**, no. 5, pp. 1048-1055, 1985.

[16] Amann, M.C. and Schimpe, R., "Excess linewidth broadening in wavelength-tunable laser diodes", *Electron. Lett.*, **26**, no. 5, pp. 279-280, 1990.

[17] Morthier, G., David, K. and Baets, R., "Linewidth rebroadening in DFB lasers owing to bias dependent dispersion of feedback", *Electron. Lett.*, **27**, no. 4, pp. 375-377, 1991.

[18] Björk, G. and Nilsson, O., "A tool to calculate the linewidth of complicated semiconductor lasers", *IEEE J. Quantum Electron.*, **QE-23**, no. 8, pp. 1303-1313, 1987.

[19] Chu, C.Y.J. and Ghafouri-Shiraz, H., "Equivalent circuit theory of spontaneous emission power in semiconductor laser optical amplifiers", *J. Lightwave Technol.*, **LT-12**, no. 2, pp. 760-767, 1994.

[20] Henry, C.H., "Theory of spontaneous emission noise in open resonator and its application to lasers and optical amplifiers", *J. Lightwave Technol.*, **LT-4**, no. 3, pp. 288-297, 1986.

[21] Pan, X., Olesen, H. and Tromborg, B., "Spectral linewidth of DFB lasers including the effect of spatial holeburning and nonuniform current injection", *IEEE Photon Technol. Lett.*, **2**, no. 5, pp. 312-315, 1990.

[22] Duan, G.H., Gallion, P. and Debarge, G., "Analysis of the phase-amplitude coupling factor and spectral linewidth of distributed feedback and composite-cavity semiconductor lasers", *IEEE J. Quantum Electron.*, **QE-26**, no. 1, pp. 32-44, 1990.

[23] Duan, G.H., Gallion, P. and Debarge, G., "Analysis of spontaneous emission rate of distributed feedback semiconductor lasers", *Electron. Lett.*, **25**, no. 5, pp. 342-343, 1989.

[24] Kojima, K. and Kyuma, K., "Analysis of the linewidth of distributed feedback laser diodes using Green's function method", *Japan J. Appl. Phys.*, **27**, pp. L1721-1723, 1988.

[25] Trombrog, B., Olesen, H. and Pan, X., "Theory of linewidth for multielectrode laser diode with spatially distributed noise sources", *IEEE J. Quantum Electron.*, **QE-27**, no. 2, pp. 178-192, 1991.

[26] Miller, S.E., "The influence of power level on injection laser linewidth and intensity fluctuations including side-mode contributions", *IEEE J. Quantum Electron.*, **QE-24**, no. 9, pp. 1837-1876, 1988.

[27] Krüger, U. and Petermann, K., "The semiconductor laser linewidth owing to the presence of side modes", *IEEE J. Quantum Electron.*, **QE-24**, no. 12, pp. 2355-2358, 1988.

[28] Osinski, M. and Buus, J., "Linewidth broadening factor in semiconductor lasers — an overview", *IEEE J. Quantum Electron.*, **QE-23**, no. 1, pp. 9-28, 1987.

[29] Furuya, K., "Dependence of linewidth enhancement factor α on waveguide structure in semiconductor lasers", *Electron. Lett.*, **21**, pp. 200-201, 1985.

[30] Vahala, K., Chiu, L.C., Margalit, S. and Yariv, A., "On the linewidth enhancement factor α in semiconductor injection lasers", *Appl. Phys. Lett.*, **42**, pp. 631-633, 1983.

[31] Wang, J., Schunk, N. and Petermann, K., "Linewidth enhancement factor for DFB lasers owing to longitudinal field dependence in the laser cavity", *Electron. Lett.*, **23**, pp. 715-717, 1987.

[32] Whiteaway, J.E.A., Thompson, G.H.B., Collar, A.J. and Armistead, C.J., "The design and assessment of $\lambda/4$ phase-shifted DFB laser structure", *IEEE J. Quantum Electron.*, **QE-25**, no. 6, pp. 1261-1279, 1989.

8

CONCLUSIONS

8.1 CONCLUSIONS

In this book the performance characteristics of distributed feedback (DFB) semiconductor laser diodes (LDs) have been investigated. As discussed in Chapter 1, these lasers can be used as optical sources and local oscillators in coherent optical communication networks in which a stable single mode (in both the transverse plane and the longitudinal direction) and a narrow spectral linewidth become crucial. On the basis of the interaction of electromagnetic radiation with a two-energy-band system, the operating principles of semiconductor lasers were reviewed in Chapter 2. With partially reflecting mirrors located at the laser facets, a Fabry–Perot (FP) laser forms the simplest type of optical resonator. However, owing to the broad gain spectrum, multi-mode oscillations and mode hopping are common in this type of laser. Nevertheless, single longitudinal mode operation becomes feasible with the use of a DFB LD. The characteristics of the DFB laser were explained using the coupled-wave equations. With a built-in periodic corrugation, travelling waves are formed along the direction of propagation in which a perturbed refractive index and/or gain are introduced. In fact, DFB lasers act as an optical bandpass filter so that only frequency components near the Bragg frequency are allowed to pass. The strength of the optical feedback is measured by the strength of the coupling coefficient. Based on the nature of the coupling coefficient, DFB semiconductor lasers can be classified into purely index-coupled, mixed-coupled and purely gain- or loss-coupled structures.

The discussion focused on the coupled-wave equations in Chapter 3. In the analysis, eigenvalue equations were derived for various structural configurations, and consequently their threshold currents and lasing wavelength were determined. From the lasing threshold characteristics, impacts due to the coupling coefficient, the laser cavity length, the facet reflectivities, the residue corrugation phases and the phase discontinuities were discussed in a systematic way. With a single $\pi/2$ phase shift introduced at the centre of the DFB cavity, the quarterly wavelength shifted (QWS) DFB LD oscillates

at the Bragg wavelength. However, owing to a non-uniform field distribution, the single mode stability of this structure deteriorates quickly when the biasing current increases. On the basis of a five-layer separate confinement heterostructure (SCH), the coupling coefficient of a trapezoidal corrugation was computed from which the coupling coefficients of other corrugation shapes, like the triangular and rectangular gratings, were also evaluated [1].

In Chapter 4 the idea of a transfer matrix (TM) was introduced and explored. Compared with the boundary matching approach in deriving the eigenvalue equation, the transfer matrix method (TMM) is more robust and flexible. By converting the coupled-wave equations into a matrix formation, the characteristics of a corrugated DFB laser section can be represented by a 2×2 matrix. This approach was extended to include phase discontinuity and the effect of residue reflection at the facets. By modifying the elements of the TM, TMM can also be used to represent other planar and corrugated structures including passive waveguides, the distributed Bragg reflector (DBR) and planar FP sections. Using the TMs as building blocks, a general N-section laser cavity model was constructed and the threshold analysis for such a laser model was discussed. With perfectly matched boundaries between consecutive TMs, the number of boundary conditions was reduced significantly. Only the boundary condition located at the laser facet remains to be matched. As compared with the eigenvalue equation, the TMM simplified the threshold analysis dramatically. In a similar way, the TM was also implemented to evaluate the below-threshold spontaneous emission power spectrum, P_N. By combining the Poynting vector with Green's function method, numerical results obtained from the three phase shift (3PS) DFB LD were presented and the structural impact on the spectral behaviour discussed [2].

In revealing the potential use of the TMM in the practical design of DFB LDs, the threshold analysis of various DFB laser structures, including the 3PS [3] and distributed coupling coefficient (DCC) [4], were carried out in Chapter 5. In an attempt to minimise the spatial hole-burning (SHB) effect and hence improve the maximum available single mode output power, it is necessary that a stable single longitudinal mode (SLM) LD shows a high normalised gain margin ($\Delta\alpha L$) and a uniform field intensity (i.e. a small flatness value, F). On the basis of the lasing performance at threshold, selection criteria were set at $\Delta\alpha L > 0.25$ and $F < 0.05$ for a 500 μm length laser cavity. Using these optimised structures, the complexities with respect to the design of DFB lasers may be reduced. By changing the value of the phase shifts, the coupling coefficient and their corresponding positions, results such as the gain margin ($\Delta\alpha L$) and the uniformity of the field distribution (F) were presented. A conventional single QWS DFB was selected for comparison purposes. This structure is characterised by an intense electric field at the centre of the cavity. With the introduction of multiple phase shifts along the laser cavity, a 3PS DFB LD with three $\pi/3$ phase shifts and a position factor of 0.5 falls within the selection criteria of $\Delta\alpha L$ and F. In an alternative

approach, the introduction of the DCC also appears to be promising. An improvement in the gain margin was shown for a DCC+QWS DFB laser structure with a coupling ratio of $\kappa_1/\kappa_2 = 1/3$ and a corrugation change at 0.46. Despite the fact that the flatness of this design does not match the requirements of the selection criteria, a high gain margin and oscillation at the Bragg wavelength still count as an advantage in the DCC DFB laser design.

The N-section laser cavity model was used to determine both the threshold and the below-threshold performance of DFB LDs. However, the TMM used had to be modified when the stimulated emission became dominant in the above-threshold biasing regime. In Chapter 6, a new technique [5] which combines the TMM with the carrier rate equation was introduced. In the model, multiple carrier recombination and a parabolic gain model were assumed. To include any gain saturation effects, a non-linear gain coefficient was introduced. The algorithm needed no first-order derivative and was developed in such a way that with minor modifications, the same algorithm could be applied to various laser structures. The TMM based above-threshold laser model was applied to several DFB laser structures including the QWS, 3PS and the DCC DFB LDs. The QWS DFB laser structure, which is characterised by its non-uniform field distribution was shown to have a large dynamic range of spatially distributed refractive index. Along the carrier concentration profile, a dip was shown at the centre of the cavity where the largest stimulated photon density was found. By introducing more phase shifts along the corrugation, results from a 3PS DFB LD with $\theta_2 = \theta_3 = \theta_4 = \pi/3$ and $PSP = 0.5$ were presented. Uniform distributions were observed in the carrier density, photon density and the refractive index profile. With an improved threshold gain margin, the above-threshold characteristics of a QWS LD having a non-uniform coupling coefficient were also shown. As compared with the QWS structure, the introduction of a non-uniform coupling coefficient with $\kappa_1/\kappa_2 = 1/3$ and $CP = 0.46$ increased the localised carrier concentration near the plane of the corrugation change. A significant reduction in the photon density difference between the central peak and the emitting photon density near the facet was also found.

On the basis of the TMM, in Chapter 7, the above-threshold model was extended and applied to evaluate the spectral and noise properties of DFB LDs. Based on the lasing mode distributions obtained for the carrier density, the photon density, the refractive index and the field intensity, characteristics like the single mode stability, the spontaneous emission spectrum and the spectral linewidth were investigated. At a fixed biasing current, the QWS structure having the smallest threshold gain was shown to have the smallest linewidth. On the other hand, the non-lasing +1 side mode became stronger with increased bias current. Comparatively, the 3PS structure was shown to show the smallest change in the lasing wavelength. With the introduction of multiple phase shifts along the corrugation, the internal field distribution became more uniform and hence a stable single mode oscillation resulted. It was shown that the DCC+QWS structure has the largest gain margin. The

introduction of a distributed coupling coefficient improved the single mode stability in such a way that the side mode suppression ratio (SMSR) remained at a high value. Wavelength tunability was also improved in this structure. From these results, it is apparent that the design of the DFB LD depends much on its applications. On the other hand, the TMM has proved to be a powerful tool when dealing with such a problem.

8.2 LIMITATIONS ON THE TMM ANALYSIS

In the analysis, the most important characteristics, namely the single mode stability, the spectral linewidth and the spectral behaviour of the DFB LDs, were investigated using the QWS, 3PS and DCC laser structures. The TMM has provided the flexibility we need in the design of DFB LDs. There are other dynamic characteristics, such as AM and FM responses [6–9] or the use of multiple electrode configuration [10,11], which are also important in the characterization of laser devices.

8.3 FUTURE RESEARCH

On the basis of the TMM, the characteristics of DFB LDs were investigated. Detailed analyses covering both below- and above-threshold biasing regimes were presented. There are at least three possible research directions which may be worth further investigation.

8.3.1 Extension to the analysis of quantum well (QW) devices

In this work, we have concentrated on bulk devices only. There is a potential to apply the same TMM technique to QW structures [12]. The major differences between QW lasers and bulk lasers, which we have been examining so far, will be on the recombination mechanism [13], material gain characteristics, band structure [14] and confinement factor [15]. We can replace some of the equations used in the bulk model with those appropriate for QW structures. The analysis and the algorithm will remain the same as for the bulk devices described earlier.

8.3.2 Extension to gain coupling devices

DFB LDs used in this work belong to the group of purely index-coupled devices. The wavelength filtering mechanism is solely caused by the perturbation of the refractive index. In recent years there has been a growing interest in the use of mixed-coupled and purely gain coupled devices [16–20]. With the coupling coefficient dependent on the material gain, it has been shown both in theory [21] and experiment [22] that these devices exhibit stable single mode oscillation at the Bragg wavelength. Even for a small degree of

gain coupling, a mixed coupled device shows an improvement in the gain margin. By introducing an imaginary term into the coupling coefficient used in the model, the characteristics of these devices could be investigated using the same methodology.

8.3.3 Further investigation of optical devices to be used in the wavelength division multiplex (WDM)

In this book, much of the analysis has been on the threshold and above-threshold analysis of various DFB laser structures. With the deployment of WDM techniques in optical communication networks [23], there is a growing demand for different types of optical devices. Optical filters that allow the end-user easy access to various information like TV or interactive digital services [24] are important. Recently, a four-channel notch filter based on a DCC DFB laser structure was demonstrated [25]. Channel cross-talk levels between 9 dB and 20 dB were obtained. In this area of application, the flexible and robust TMM may be used in the design of these devices.

8.3.4 Switching phenomena

In high-speed optical communication networks that employ a single mode semiconductor laser like the DFB LD, there is increasing attention towards phenomena associated with high-speed switching [26–28]. One of the system limitations is known to be the chirping effect induced by semiconductor lasers [29]. Owing to the strong coupling between the gain and the refractive index in the semiconductor, any switching in the form of an injection current results in a variation in the optical gain, and hence the refractive index of a semiconductor laser. A dynamic shift in the operating wavelength and the broadening of the spectral linewidth has been observed as a result of frequency chirping [29]. Owing to the dispersive nature of optical fibres, such a spectral broadening affects the pulse shape at the fibre output, and consequently degrades the overall system performance.

To overcome the problem of frequency chirping, a number of methods have been proposed, including the use of an external modulator [30], pre-shaping of the electrical signals [30], injection locking [31] and improvements in device structures [5]. Using the flexible TMM as a design tool, different structural designs of LDs can be tested systematically, and thus we can improve the performance of laser devices.

8.4 REFERENCES

[1] Ghafouri-Shiraz, H. and Lo, B.S.K., "Computation of coupling coefficient for a five-layer trapezoidal grating structure", *Opt. Laser Technol.*, **27**, no. 1, pp. 45–48, 1994.

[2] Ghafouri-Shiraz, H. and Lo, B.S.K.., "Structural impact on the below threshold spectral behavior of three phase shift (3PS) distributed feedback (DFB) lasers", *Microwave Opt. Tech. Lett.*, **7**, no. 6, pp. 296-299, 1994.

[3] Ghafouri-Shiraz, H. and Lo, B.S.K., "Structural dependence of three-phase-shift distributed feedback semiconductor laser diodes at threshold using the transfer-matrix method (TMM)", *Semi. Sci. Technol.*, **9**, no. 5, pp. 1126-1132, May 1994.

[4] Lo, B.S.K. and Ghafouri-Shiraz, H., "Spectral characteristics of distributed feedback laser diodes with distributed coupling coefficient", *IEEE J. Lightwave Technol.*, **13**, no. 2, pp. 200-212, 1995.

[5] Lo, B.S.K. and Ghafouri-Shiraz, H., "A method to determine the above threshold characteristics of distributed feedback semiconductor laser diodes", *IEEE J. Lightwave Technol.*, in press.

[6] Makino, T., "Transfer-matrix analysis of the intensity and phase noise of multi-section DFB semiconductor lasers", *IEEE J. Quantum Electron.*, **QE-27**, no. 11, pp. 2404-2415, 1991.

[7] Vankwikelberge, P., Morthier, G. and Baets, R.,"CLADDISS — A longitudinal multimode model for the analysis of the static, dynamic and stochastic behaviour of diode lasers", *IEEE J. Quantum Electron.*, **QE-26**, no. 10, pp. 1728-1741, 1990.

[8] Yoshikuni, Y. and Motosugi, G., "Multielectrode distributed feedback laser for pure frequency modulation and chirping suppressed amplitude modulation", *J. Lightwave Technol.*, **LT-5**, pp. 516-522, 1987.

[9] Kikuchi, K. and Okoshi, T., "Measurement of FM noise, AM noise and field spectra of 1.3 μm InGaAsP/InP DFB lasers and determination of their linewidth enhancement factor", *IEEE J. Quantum Electron.*, **QE-21**, no. 6, pp. 1814-1818, 1985.

[10] Kikuchi, K. and Tomofuji, H., "Analysis of oscillation characteristics of separated-electrode DFB laser diodes", *IEEE J. Quantum Electron.*, **QE-26**, no. 10, pp. 1717-1727, 1985.

[11] Kikuchi, K. and Tomofuji, H., "Performance analysis of separated-electrode DFB laser diode", *Electron. Lett.*, **25**, no. 2, pp. 162-163, 1989.

[12] Zory, P.S., Jr., *Quantum Well Lasers*. New York: Academic Press, 1993.

[13] Agrawal, G.P. and Dutta, N.K., *Long-wavelength Semiconductor Lasers*. Princeton, NJ: Van Nostrand, 1986.

[14] Yariv, A., *Optical Electronics*, 4th edition. Orlando, FL: Saunders College Publishing, 1991.

[15] Ghafouri-Shiraz, H. and Tsuji, S., "Strain effects on refractive index and confinement factor of $In_xGa_{(1-x)}$ laser diodes", *Microwave Opt. Tech. Lett.*, **7**, no. 3, pp. 113-119, 1994.

[16] David, K., Buus, J. and Baets, R., "Basic analysis of AR-coated, partly gain-coupled DFB lasers: The standing wave effect", *IEEE J. Quantum Electron.*, **28**, no. 2, pp. 427-433, 1992.

[17] David, K., Morthier, G., Vankvikelberge, P., Baets, R., Wolf, T. and Borchert, B., "Gain-coupled DFB lasers versus index-coupled and phase-shifted DFB lasers: A comparison based on spatial hole burning corrected yield", *IEEE J. Quantum Electron.*, **27**, no. 6, pp. 1714-1724, 1991.

[18] David, K., Buus, J., Morthier, G. and Baets, R., "Coupling coefficient in gain-coupled DFB lasers: Inherent compromise between strength and loss", *Photon. Technol. Lett.*, **3**, no. 5, pp. 439-441, 1991.

[19] Luo, Y., Nakano, Y., Tada, K., Inoue, T., Homsomatsu, H. and Iwaoka, H., "Fabrication and characteristics of gain-coupled distributed feedback semiconductor lasers with a corrugated active layer", *IEEE J. Quantum Electron.*, **QE-27**, no. 6, pp. 1724-1732, 1991.

[20] Makino, T., "Transfer matrix analysis of the spectral linewidth of a partly gain-coupled MQW DFB laser", *Optical Quantum Electron.*, **25**, pp. 473-481, 1993.

[21] Kogelnik, H. and Shank, C.V., "Coupled-wave theory of distributed feedback lasers", *J. Appl. Phys.*, **43**, no. 5, pp. 2327-2335, 1972.

[22] Luo, Y., Nakano, Y. and Tada, K., "Purely gain-coupled distributed feedback semiconductor lasers", *Appl. Phys. Lett.*, **56**, no. 17, pp. 1620-1622, 1990.

[23] Lee, T.P. and Zah, C.N., "Wavelength-tunable and single frequency semiconductor lasers for photonic communications networks", *IEEE Commun. Mag.*, pp. 42-52, 73, 1989.

[24] Van Heijnngen, P., Muys, W., Van der Platts, J. and Willems, F., "Crosstalk in a fibre access network demonstrator carrying television and interactive digital services", *Electron. Commun. Eng. J.*, **6**, pp. 49-55, 1994.

[25] Weber, J.P., Stoltz, B., Dasler, M. and Koek, B., "Four channel tunable optical notch filter using InGaAsP/InP reflection gratings", *IEEE Photon. Technol. Lett.* **6**, no. 1, pp. 77-82, 1994.

[26] Lidoyne, O., Gallion, P., Chabran, C. and Debarge, G., "Locking range, phase noise and power spectrum of an injection-locked semiconductor laser," *IEEE Proc. Pt. J.*, **137**, pp. 147-153, 1990.

[27] Cartledge, J.C., "Improved transmission performance resulting from the reduced chirp of a semiconductor laser coupled to an external high-Q resonator", *J. Lightwave Technol.*, **8**, pp. 716-721, 1990.

[28] Mohrdiek, S., Burkhard, H. and Walter, H., "Chirp reduction of directly modulated semiconductor lasers at 10 Gb/s by strong CW light injection", *J. Lightwave Technol.*, **12**, pp. 418-424, 1994.

[29] Linke, R.A., "Modulation induced transient chirping in single frequency lasers", *IEEE J. Quantum Electron.*, **QE-21**, pp. 593-597, 1985.

[30] Petermann, K. *Laser Diode Modulation and Noise*. Tokyo, Japan: KTK Scientific and Kluwer Academic Publishers, 1988.

[31] Hui, R., D'Ottavi D., Mecozzi, A. and Spano, P., "Injection locking in distributed feedback semiconductor lasers," *IEEE J. Quantum Electron.*, **QE-27**, pp. 344-351, 1931.